Tracing the evolution of protoplanetary disks

Proefschrift

ter verkrijging van
de graad van Doctor aan de Universiteit van Leiden,
op gezag van Rector Magnificus prof. mr. C.J.J.M. Stolker,
volgens besluit van het College voor Promoties
te verdedigen op maandag 23 juni 2014
klokke 15:00 uur

door

Koen Maarten Maaskant

geboren te Naarden, Nederland,
in 1985.

Promotiecommissie:

Promotoren:	prof. dr. A.G.G.M. Tielens
	prof. dr. L.B.F.M. Waters
	prof. dr. C. Dominik
Overige leden:	prof. dr. C. Dullemond
	prof. dr. I. Kamp
	prof. dr. H.J.A. Röttgering
	dr. M.R. Hogerheijde

Faculteit der Natuurwetenschappen, Wiskunde en Informatica.

ISBN: 978-94-6259-213-1
Contact e-mail: info@koenmaaskant.nl

Front and back cover: A selection of figures and photos are shown representing the content of this thesis. The film rolls illustrate the mission of this thesis: connecting the frames and making a story of the evolution of protoplanetary disks. Scientific figures are adapted from several papers and are referred to in the bibliography. References to the telescope photos and the artist illustrations can be find in the introduction.

Remember kids, the only difference between screwing around and science is writing it down.

ADAM SAVAGE

Contents

CHAPTER 1

Introduction

1.1 Protoplanetary disk evolution

The universe is an entity in which everything seems to be in motion. The birthplace of our solar system is no exception to this general principle. Planet Earth formed $\sim$ 4.57 billion years ago out of a rotating protoplanetary disk. Together with the other planets and celestial bodies in our solar system, it has been rotating around the sun ever since. The study of protoplanetary disks aims to characterize the evolution of disks towards mature planetary systems such as our solar system. This thesis aims to contribute to our understanding of protoplanetary disk evolution. It focuses on gas and dust in protoplanetary disks around intermediate mass stars (stars which are $\sim 2-10$ times more massive than the sun). These objects are also known as Herbig stars, named after their discoverer, George Herbig (1920 – 2013).

The objective of this thesis is tracing the structure and evolution of protoplanetary disks through the infrared emission of dust and gas. In the next sections of this introduction, the general properties of protoplanetary disks are reviewed. The basic tools used in the study of disks are discussed: observations from telescopes and physical models. Thereafter the topics covered in this thesis are discussed: the geometry of protoplanetary disks, ionization of polycyclic aromatic hydrocarbons (PAHs), and the location of forsterite dust in the disk. The introduction ends with a brief outlook on some of the next key questions in the context of this thesis.

1.1.1 Why do we study protoplanetary disks?

In the past decades, discoveries of exoplanets around other stars have ignited a revolution in astronomy. As turned out, not only our own sun, but also other stars have planets orbiting around them. Finding exoplanets is not an easy task. Planets are very small and are fainter than their central star. However, clever observation techniques have overcome these problem and have been, and continue to be, successful in finding new exoplanets. To date, more than thousand exoplanets have been found[1]. Based on extrapolations of these observations, it is predicted that billions of exoplanets may reside in our galaxy (Howard et al., 2010). Even exoplanetary atmospheres are currently being investigated. The new era of exoplanetary science enables scientists to answer numerous questions. What kind of exoplanets do we see? Are there any other habitable exoplanets like Earth? How do planets form? Answering these big questions takes patience and requires joint efforts of many scientists working in different disciplines like astronomy, physics, chemistry and computer sciences. To this end, important insights can be obtained by zooming in on one of the earliest phases of the formation of planetary systems: the *protoplanetary disk*.

1.1.2 From clouds, to protoplanetary disks, to planetary systems

The formation of a star and a planetary system starts with a giant cloud consisting of gas, more complex molecules, and dust. An example, of such a cloud is the Orion nebula (Figure 1.1), in which stars and planets are currently forming. When the gravity of (fragments of) the cloud exceeds the supporting gas pressure, the cloud starts to collapse and the material slowly falls to the center. However, since the cloud has some initial rotation, it carries angular momentum. Because angular momentum is a conserved quantity, the angular velocity of the material will increase during infall. As a result, not all the gas and dust can directly fall on the central star because the material is rotating too fast. For that reason, a protoplanetary disk is formed. Eventually, the material in the protoplanetary disk may clump together to form planets. Characterizing this planet formation process is currently one of the main challenges in the study of protoplanetary disks.

Protoplanetary disks are round and are often observed to be $\sim 5-10$ times larger than our solar system (see Williams & Cieza 2011 for a review of the properties of protoplanetary disks). Atomic gas, molecules and dust particles are the major observable constituents that build up the disk. Estimates of disk masses range between $\sim 10^{-4}-10^{-1}$ $M_\odot$. For comparison, the cumulative mass of all the planets in our solar system is 1.3×10^{-3} $M_\odot$. Thus, a fraction of the material in the disk may be expected to clump together into planets. The rest of the mass is either accreted onto the central star or is repelled from the system by other mechanisms such as outflows and jets (see right panel of Figure 1.1).

[1]NASA exoplanet archive: http://exoplanetarchive.ipac.caltech.edu/

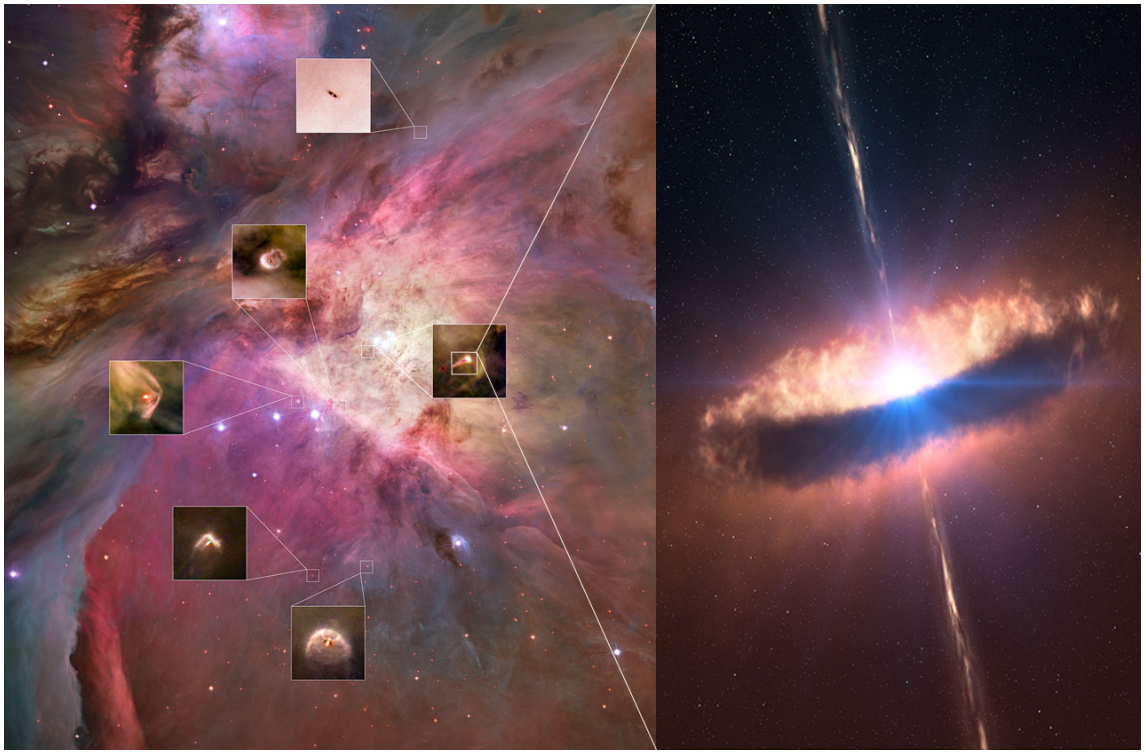

Figure 1.1: ***Left:*** *Hubble telescope image of the Orion nebula. Inside this cloud of gas and dust, hundreds of new stars are born. This image highlights several 'proplyds', in which protoplanetary disks can be detected as dark silhouettes in the center of excited material. Credits: NASA, ESA, M. Robberto (Space Telescope Science Institute/ESA), the Hubble Space Telescope Orion Treasury Project Team and L. Ricci (ESO)* ***Right:*** *Artist impression of a protoplanetary disk rotating around the star. In roughly 10 million years, the material in the disk can either clump together to form planets, it can be accreted onto the central star, or it can be blown out by outflows and jets as shown by the streams perpendicular to the disk. Credit: ESO/L. Calcada/M. Kornmesser*

Modeling protoplanetary disks is essential for the interpretation of telescope observations. A great leap forward came when Shakura & Sunyaev (1973) proposed a recipe to describe the inward transfer of accreting material and outward transfer of angular momentum in a disk. These authors found an analytical model to describe the basic physical structure of a steady state accretion disk. When the Infrared Astronomical Satellite (IRAS) telescope began to observe protoplanetary disks at mid- to far-infrared wavelengths, it was quickly realized that the outer parts of the disk were producing more emission than what was expected for flat disks (Adams et al., 1987). Kenyon & Hartmann (1987) suggested that the gas and dust in planetary disks are actually in hydrostatic equilibrium (i.e. the density in the disk is set by an equilibrium between the pressure of the gas and the vertical component of the stellar gravity). Because the temperature gradient and the gradient of stellar gravity are both decreasing towards larger distances from the star, their interplay results in a flaring disk structure (i.e. a thicker disk outward). This explanation was further improved by Chiang & Goldreich (1997) and has become standard in state of the art disk models. A sketch of a flaring disk is shown in Figure 1.2.

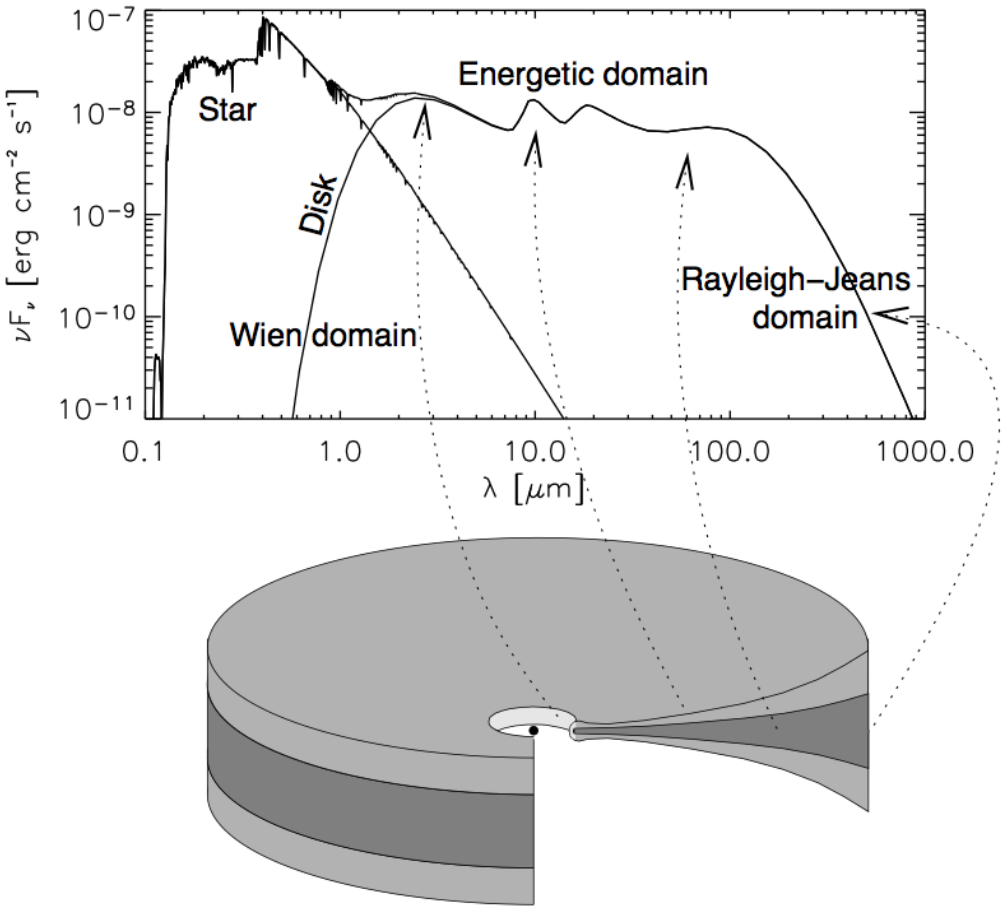

Figure 1.2: *A sketch of a flaring protoplanetary disk (Dullemond et al., 2007b). The central star dominates the emission (expressed in the flux quantity νF_ν) at optical wavelengths ($\lambda \lesssim 1$ μm). The inner disk ($T \sim 1500$ K) can be traced at near-infrared wavelengths ($1 \lesssim \lambda \lesssim 5$ μm). The surface of the disk ($T \sim 100 - 500$ K) is best studied at mid-infrared wavelengths ($5 \lesssim \lambda \lesssim 50$ μm). The colder ($T \lesssim 100$ K) outer parts of the disk are traced though observations in the far-infrared up to millimetre wavelengths ($\lambda \gtrsim 50$ μm). Not shown on this SED is that accretion columns and/or accretion spots on the star can have temperatures of $\sim 10^4$ K or more leading to an excess at ultraviolet wavelengths.*

Studies of disks around young stars in clusters suggested that most stars lose their disk in $\sim$ 10 million years (e.g. Mamajek 2009). This means that compared to the total lifetime of the star ($\sim$10 billion years for a sun-like star), the evolution of the disk is a rapid process. Turbulent motions inside protoplanetary disks may induce planet formation (Weidenschilling, 1980). Due to these motions, small dust particles collide, stick together, grow to larger planetesimals and eventually may form planets with sizes similar to to the Earth. When the planet grows to even larger sizes, it becomes so massive that it starts accreting gas from the disk and transforms into a gas giant such as Jupiter. This scenario

is known as the core-accretion scenario (Pollack et al., 1996). Evidence for this planet formation process can be found by carefully analyzing the emission we observe from the disks. If the system is close enough, than the disk may be spatially resolved and structures can potentially reveal disk processes. Figure 1.2 shows how we can trace different parts of the disk by observing at different wavelengths. This flux versus wavelength diagram is known as the spectral energy distribution (SED) and displays the total emission per wavelength, which trace different parts of the disks. The emission we observe from the star and the disk shows up on an SED. In this thesis, the SED is used as an important diagnostic tool to study the evolution of disks.

1.1.3 Disk evolution: self-shadowed and transitional disks

A general picture of disk evolution of protoplanetary disks is shown in figure 1.3. It starts as a massive flaring disk, and through evolutionary processes such as grain growth, grain settling and planet formation, the disk eventually transforms into a debris disk. In this thesis it is proposed that in this evolutionary sequence, two types of protoplanetary disks represent the most important disk structures observed in the sample of Herbig stars: self shadowed ('flat') disks and transitional ('flaring') disks. Note that it is yet unknown whether transitional disks form out of self-shadowed disks, or that both disks types represent independent pathways of disk evolution.

Self-shadowed disks are thought to have a disk geometry which is high (puffed up) close to the star but flatter outwards. A typical SED shows strong near-infrared excess, but little emission at far-infrared wavelengths. Among Herbig stars, the SED types were identified as groups by Meeus et al. (2001). An interpretation of their disk structure quickly followed. Dullemond & Dominik (2004a,b, 2005) proposed that the flatness of the outer disk was the result of dust particles which stick together and grow in size. If the dust grains become more massive, they settle down to the mid-plane and the disk becomes flatter. Another important factor is that the inner disk is believed to 'puff up' because it receives a relatively large amount of stellar radiation at the inner edge of the disk (Dullemond et al., 2001). The increase of the inner disk temperature causes the inner disk to increase its vertical scaleheight. As a result, the thick inner disk casts a shadow which decreases the emission from the outer disk.

The second subclass consist of the transitional disks (e.g. Calvet et al. 2005). These protoplanetary disks have a smaller excess at near-infrared wavelengths, but still significant excess at longer wavelengths (Strom et al., 1989). These types of disks are characterized by large, empty regions, depleted of gas and dust. These empty regions are called 'gaps' and have a ring like (i.e., annular) shape. As an example, Figure 1.4 shows the transitional disk of HD 169142 (studied in detail in Chapter 2). If the gap is located close to the star, it is also known as an 'inner hole'. It is widely believed that these gaps are a result of the formation of planets. When all the material in the disk at a certain radius from the star is being accreted onto a planet, a gap is formed in the disk (e.g., Armitage 2011).

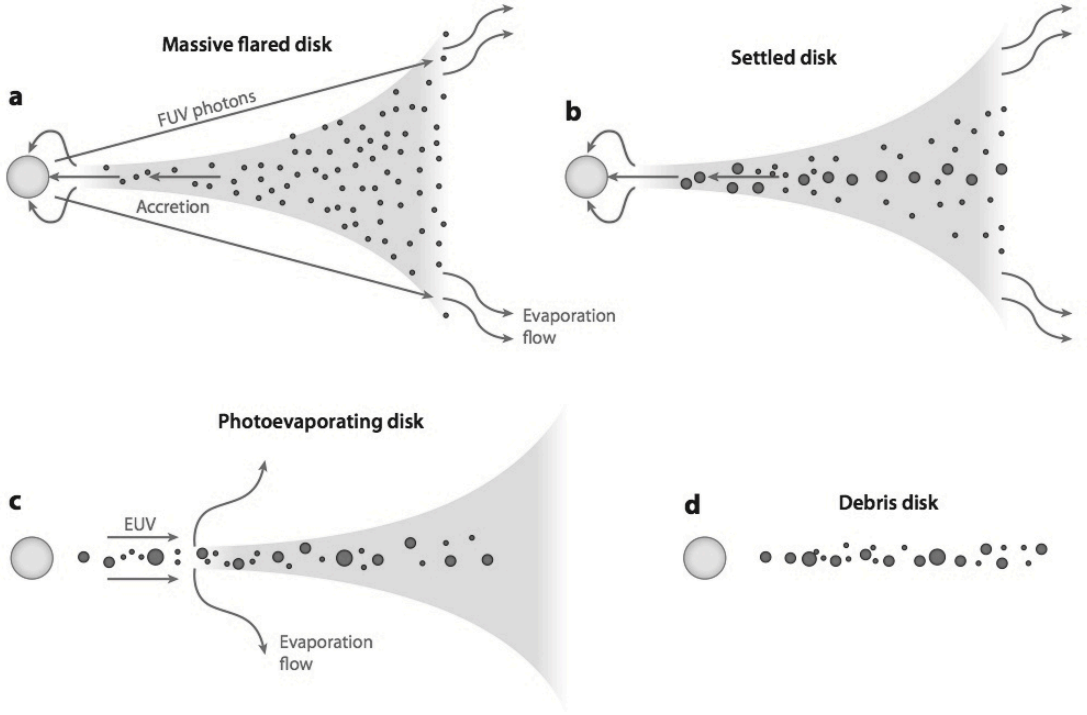

Figure 1.3: *This sketch shows several processes in the evolution of a typical disk.* ***(a)*** *A massive flaring disk early in its evolution. The disk loses mass through accretion onto the star and photoevaporation of the outer disk.* ***(b)*** *A flat, self-shadowed disk. Grains grow into larger bodies that settle to the mid-plane of the disk.* ***(c)*** *A transitional disk. As the disk mass and accretion rate decrease, the outer disk no longer replenishes the inner disk. Material in the inner disk sticks together to form planets, or photoevaporation removes all material by radiation pressure.* ***(d)*** *The debris disk, which has a very low mass and is not always detectable. The small grains are removed by radiation pressure and Poynting-Robertson drag. Only large grains, planetesimals, and/or planets are left. Figure adapted from Williams & Cieza (2011).*

There are also physical mechanisms, other than planet formation, that are responsible for the evolution of disks. For example, photo-evaporation by high energetic UV and X-ray emission can also create gaps and inner holes (e.g. Alexander et al. 2006, Gorti et al. 2009). Together with mechanisms such as viscous accretion by the magneto-rotational instability (e.g. Hartmann et al. 1998, Chiang & Murray-Clay 2007), and dynamical interactions between the disk and stellar or substellar companions (Artymowicz & Lubow, 1994), physical processes in the disk may be responsible for a variety of observational appearances of the protoplanetary disk. Disentangling their effects is a challenging task and requires both analytic models as well as high spectral and spatial resolution observations.

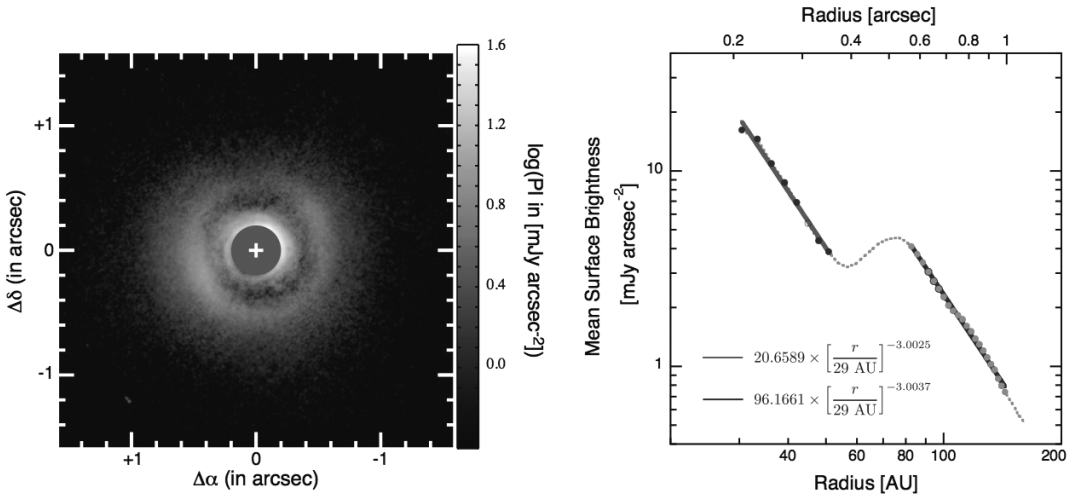

Figure 1.4: *Left: the polarized intensity image of the transitional disk around HD 169142 observed pole-on in the H-band ($\lambda \sim 1.6\ \mu m$) with Subaru/HiCIAO (Momose et al., 2013). A large empty ring (i.e. a 'gap') can be seen between $\sim 60 - 80$ AU. Right: the averaged radial distribution of the intensity. The disk structure of HD 169142 is studied in Chapter 2.*

1.2 Observations and models of protoplanetary disks

Stars with protoplanetary disks reveal themselves through electromagnetic radiation from X-ray up to millimetre wavelengths. To be able to understand how disks evolve, a combination of observations from high quality telescopes and analytic and numerical models is required. This thesis uses observations of state-of-the-art infrared telescopes. In particular observations from the Spitzer and Herschel space telescopes are an important observational input for this thesis. We now briefly discuss a short history and future prospects of space based infrared observatories.

1.2.1 New generations of telescopes

New insights in astronomy are often the result of new generations of telescopes. In 1983, the Infrared Astronomical Satellite (IRAS) was the first space telescope to perform a survey of the entire sky at infrared wavelengths (Figure 1.5). IRAS triggered the first systematic studies on the variety of SEDs of protoplanetary disks. Follow-up space based infrared telescopes further opened up of the infrared sky, improving in spatial and spectral resolution and sensitivity. In 1995, the Infrared Space Observatory (ISO) was the first to reveal the incredible richness of the mid-IR spectrum. Most notably, the characteristic emission features from polycyclic aromatic hydrocarbon and silicate dust grains could be studied in detail. The analysis of these spectral features provides insight into the physical processes in disks. Less than a decade later, ISO was followed up in 2003 by the Spitzer Space Observatory. Spitzer improved the infrared view of protoplanetary disks

Figure 1.5: *Six generations of space based infrared telescopes. New telescopes often improve spatial resolution, spectral resolution and sensitivity. Top, from left to right: the Infrared Astronomical Satellite (IRAS) launched in 1983, the Infrared Space Observatory (ISO) launched in 1995 and the Spitzer Space Observatory launched in 2003. Bottom, from left to right: the Herschel space telescope launched in 2009, and the James Webb Space Telescope (JWST), with a proposed launch in 2018 and the Space Infrared Telescope for Cosmology and Astrophysics (SPICA), with a proposed launch in 2025.*

with unprecedented sensitivity and became the first telescope to directly capture the infrared light from extrasolar planets: the 'hot Jupiters' TrES-1 (Charbonneau et al., 2005) and HD 209458b (Ballester et al., 2007). On May, 14, 2009, the next space telescope was launched towards its operational orbit: Herschel. Three instruments on board of Herschel performed imaging photometry and spectroscopy in the far-infrared and sub-millimeter part of the spectrum (55–672 μm). Herschel provided the spectral resolution and sensitivity to study the spectral features at 69 μm from crystallised silicate dust grain called forsterite. The James Webb Space Telescope (JWST) and the Space Infrared Telescope for Cosmology and Astrophysics (SPICA) are the next telescopes capable of observing at infrared wavelengths, and are scheduled to be launched in 2018 and 2025 respectively. JWST and SPICA have even larger mirrors and more sensitive instruments which will provide unprecedented resolution and sensitivity from the near- to to far-infrared.

Space based telescopes have the advantage that they do not suffer from atmospheric absorption (especially at wavelengths above $\lambda \sim 1$ μm) and turbulence. However, their mirror sizes are limited to a few meter because they require expensive rockets to launch them into space. Another disadvantage is their limited life-time: infrared space observatories typically only last for a couple of years due to depletion of the cooling system. Ground based telescopes can be made much larger and are easier to maintain. The world

today counts hundreds of professional ground-based telescopes. Obviously, the bigger the better. Examples of impressive telescopes which are currently the most important deliverers of protoplanetary disk observations are the Subaru telescope on Mauna Kea in Hawaii, and the Very Large Telescope (VLT) and the Atacama Large Millimeter/submillimeter Array (ALMA), both in the Atacama Desert of northern Chili.

New telescopes often improve observations in three ways: the spatial resolution, the spectral resolution and the sensitivity. A higher spatial resolution enables the telescope to zoom in and observe smaller structures. A better spectral resolution allows telescopes to better observe emission profiles of gas lines and substructure in solid state features. Finally, if the instrument has a higher sensitivity, a telescope can observe in a shorter time, fainter objects, often located at greater distances in space, with a better signal to noise. For this thesis, all three dimensions are important. Chapters 2, 3 and 4 present high spatial resolution images taken at 18.8 and 24.5 μm from the Subaru, VLT and Gemini North and South telescopes. Chapter 5 presents a study of detailed study of sensitive PAH features, with a high signal to noise ratio, for a large sample of Herbig stars. In Chapter 6 the improved spectral resolution of the Herschel space telescope is used to analyze the spectral shape of the forsterite 69 μm feature.

1.2.2 From observations to physical models

It is important to understand the physical processes which are responsible for the radiation emitted by the materials around young stars. The most relevant emission processes in disks are from the interaction of stellar light with atomic gas, molecules and dust.

For atomic and molecular gas, the interaction with incident energy carriers (i.e. such as photons from the central star or energetic particles like cosmic rays) can produce strong emission lines at specific wavelengths. The wavelengths of these emission lines are defined by internal energy transitions, either discretely or continuously distributed over energy. Furthermore, the emission is influenced by macroscopic properties such as the density (i.e. pressure, surface, volume, number of particles and temperature). Groups of atoms can build up molecules which are more complex in terms of their structure and their emission spectrum. Simple molecules such as CO have ro-vibrational band structures that can be resolved with very high spectral resolution spectrographs. At some size, molecules start to behave partly like a solid (surface) in that they show band structure. Because internal rotational and vibrational modes between the atoms in the molecule can result in emission features which are blended. This generates so-called emission feature complexes. An example of such features are the mid-infrared emission profiles of very large molecules such as the PAHs.

In protoplanetary disks, the absorption at mid-infrared wavelengths is dominated by dust grains. Silicate dust grains dominate the radiation in the low energy regime. The thermal emission profile of silicate dust as a function of wavelength is characterised by the temperature and the material properties such as size and composition. In this way, the characteristic mid-infrared spectral features of silicate grains have important diagnostic value for constraining properties like the chemical composition and sizes of dust grains.

Comparing telescope observations to analytic and numerical models is essential to provide a quantitative interpretation. Ideally, a model is as simple as possible, though the level of complexity often grows as the resolution of the observations increases. Whether observations are needed to test the model, or vice versa, depends on the nature of the scientist. An example of a very simple disk model is one that assumes that the SED of a disk can be fitted by a distribution of blackbodies within a certain temperature range. While this model may give a relatively good fit to the SED, it fails to explain the underlying physics (i.e. the structure of the disk). Thus, more realistic models involve detailed particle properties, radiative transfer, chemical descriptions and more complex physics to understand and predict observations. The analysis of protoplanetary disks must include a computational code which can follow the photon paths in disks and produce model images and SEDs which are used to compare to the observations. Throughout this thesis, this has been done using the Monte Carlo radiative transfer code MCMax (Min et al., 2009).

1.3 Topics in this thesis

In the next sections, it is discussed how in this thesis observations and models are combined to give a better understanding of the structure and evolution of protoplanetary disks. The infrared emission of dust and gas are considered: amorphous silicate dust grains to trace the structure of the disk, neutral versus ionized PAHs in gas flows through the gap, and crystalline dust (forsterite) in the inner and outer regions of protoplanetary disks.

1.3.1 Emission from dust grains around disk gaps

Dust grains provide the material from which terrestrial planets and the cores of the giant planets (in the core accretion model) are made. In the diffuse interstellar medium (ISM), dust is mainly composed of silicates with sizes ~ 0.1 μm (Draine, 2003). During the evolution from the ISM to protoplanetary disks to planets, dust undergoes significant processing. Molecules freeze out from the gas phase onto dust grain surfaces and form icy mantles (Bergin & Tafalla, 2007). Dust grains stick together and grow and thereby become more massive and settle down to the mid-plane of the disk (Dullemond & Dominik, 2004a, 2005). Small dust grains are replenished in the disk by fragmentation processes. The dust size distribution in the disk is therefore determined by a complex balance between dust coagulation and fragmentation (Dullemond & Dominik, 2008). To study the disk geometry and composition we need to understand the observational appearance of the silicates grains in the disk: a class of materials also commonly found on Earth (i.e. 90 % of the Earths crust consists of silicates).

1.3.1.1 Imaging the geometry of the disk

Silicate dust particles are the dominant absorbers and scatterers in disks and re-radiate stellar light in the 1 μm to 1 mm range. Amorphous silicates are easily identified through

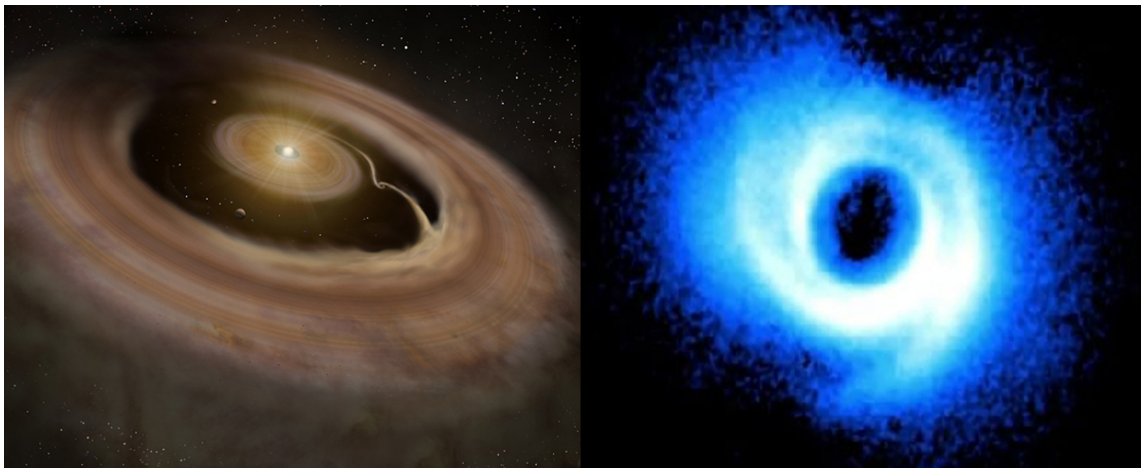

Figure 1.6: *Left: artist impression of a transitional disk. A stream of material is flowing inward through the gap, accreting onto the planet, and replenishing the inner disk. Credit: The Graduate University for Advanced Studies, Japan. Right: Subaru/HiCiAO observations of the transitional disk HD 135344 B (Muto et al., 2012). Obvious spiral arms can be seen in this disk.*

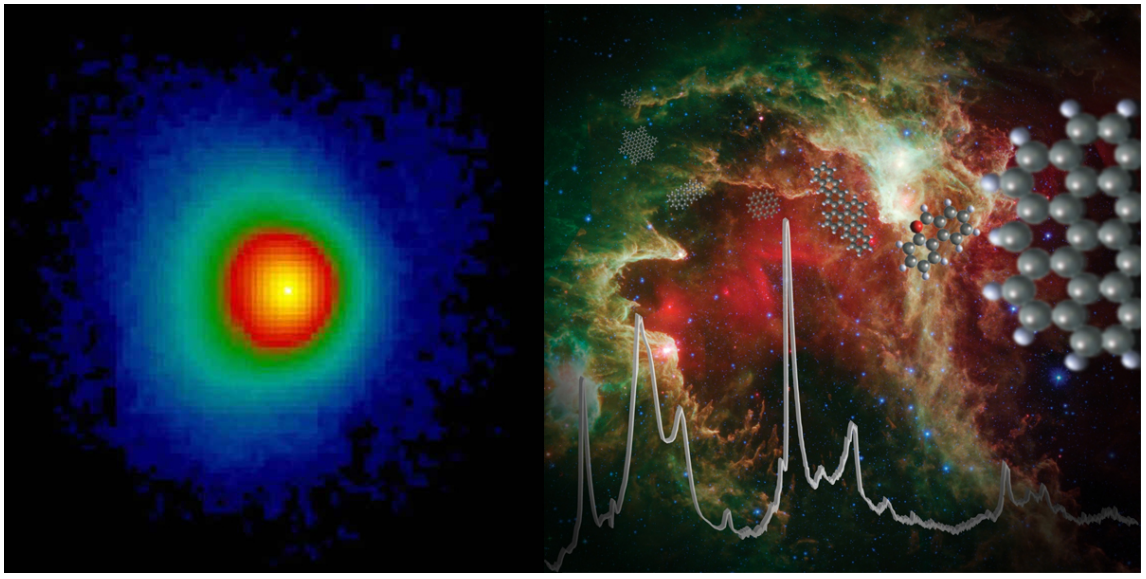

Figure 1.7: *Left: HD 97048 observed by VLT/VISIR in the PAH filter (Lagage et al., 2006). The PAHs on the surface of the disk emit at mid-infrared wavelengths, and the disk surface can be traced. Right: an interstellar nebula showing the emission from PAHs in red. Over plotted are some PAH molecular structures and a typical interstellar PAH infrared spectrum.*

broad spectral bands at 10 and 18 μm (see e.g. Henning 2010 for a review on cosmic silicates). Because the temperature of the dust decreases with the distance from the central star, different wavelengths trace different disk radii. As gaps form, possibly due to planet formation, a decrease of radiation is detected in both the SED and in resolved images. Another effect of the formation of a disk gap is that the vertical wall (i.e. the inner edge of the outer disk) is now exposed to the star and increases in brightness because it receives the emission which would otherwise fall on the disk. Depending on the location (i.e. temperature range) and size of the gap in the disk, the gap may be identified in the SED. A typical gap can be seen in the SED by a decreased emission dip at wavelengths corresponding to the temperature range where the gap is residing. This dip is directly followed by an increase of emission at longer wavelengths, originating from the wall of the outer disk.

An SED can be used as an indirect indicator of the presence of a disk gap. However, an SED is inconclusive in determining the location of the disk gap because the temperature of the inner edge of the outer disk also depends on the luminosity of the star, the grain properties and the opaqueness of the inner disk structure. By imaging protoplanetary disks with high spatial resolution, it is possible to lift this degeneracy, directly observe disk gaps, and thereby constrain the radius of the gap. In addition, with sufficient spatial resolution, it is also possible to observe the structures of the material around the gap such as banana shapes (e.g. in HD 142527, Fujiwara et al. 2006, Casassus et al. 2013) and spiral arms (e.g. in HD 135344 B, Muto et al. 2012, Figure 1.6).

1.3.2 Emission from polycyclic aromatic hydrocarbons

Many astrophysical objects show a rich spectrum of infrared emission features associated with polycyclic aromatic hydrocarbons (PAHs, Leger & Puget 1984, Allamandola et al. 1985). With respect to their size, PAHs can be considered as gas. However, their opacities and broad emission features are more characteristic of dust. They exchange charge in collisions with the gas and can break up or release some subgroups if they interact with energetic radiation. PAH features are ubiquitous in space, for example in H II regions, reflection nebulae, young stellar objects, planetary nebulae, post-asymptotic giant branch objects, nuclei of galaxies, and ultra-luminous infrared galaxies (Tielens 2008 and references therein). Peeters et al. (2002) classified PAH emission profiles in three different classes based on the positions of their feature centers, class A: representing interstellar material illuminated by a star, such as HII regions, reflection nebulae, and the general ISM of the Milky Way and other galaxies, class B: sources associated with circumstellar material and include PNe and a variety of post-AGB objects, and Herbig AeBe stars, and class C: a few extreme carbon-rich post-AGB objects. This classification appears to be tracing the extent to which PAH molecules have been processed by their environments, particularly the stellar radiation field. PAHs in disks have been used to trace the disk structure. Observations presented by Lagage et al. (2006) and Doucet et al. (2006) demonstrated that PAH emission can be used to derive the flaring angle of the disk of HD 97048 (Figure 1.7, left). Figure 1.7 (right) shows a composite image of PAH emission in an interstellar nebula, the structure of some PAH molecules, and a typical infrared PAH

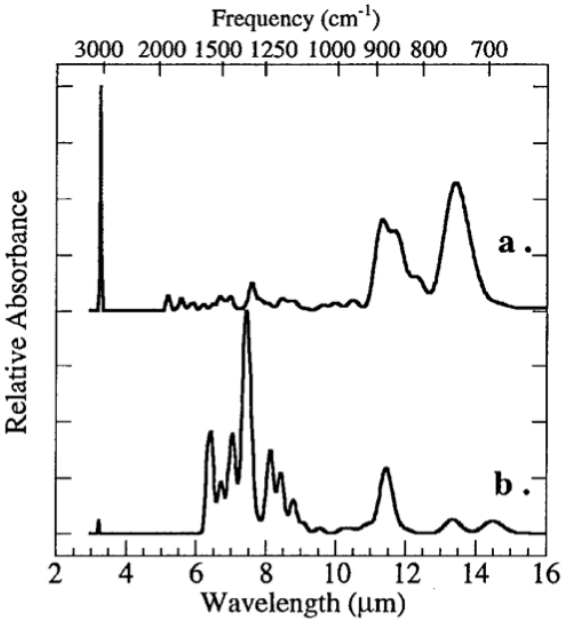

Figure 1.8: *The absorption spectrum produced by neutral PAHs (top) compared with the spectrum produced by the same PAHs but ionized (bottom). The ionization state has a strong effect on the relative intensities (Allamandola et al., 1989).*

spectrum. PAHs account for a significant part of all cosmic carbon (Snow & Witt, 1995, Puget & Leger, 1989, Allamandola et al., 1989). They have been detected in cometary material during the Deep Impact mission (Lisse et al., 2006) and were brought back to Earth by the Stardust mission (Sandford et al., 2006). It is therefore believed that carbon bearing species such as PAHs are also important constituents of planets in habitable zones (Kasting et al., 1993).

1.3.2.1 PAH ionization

Nearly 50% of Herbig Ae/Be stars have strong PAH emission (e.g. Meeus et al. 2001, Acke & van den Ancker 2004). A variety of PAH emission intensities and ionization fractions have been found (Sloan et al., 2005, Boersma et al., 2008). The ionization balance is predominantly set by the incident UV radiation field, which ionizes the PAHs, and the density of electrons, which can recombine with the PAHs to their neutral state. The peak ratio of the $I_{6.2}/I_{11.3}$ μm PAH features can be used as a measure for the ratio of neutral versus ionized PAH (Allamandola et al. 1989, see Figure 1.8). Ionized PAHs have a higher $I_{6.2}/I_{11.3}$ μm ratio, whereas neutral PAHs emit stronger in the 11.3 band.

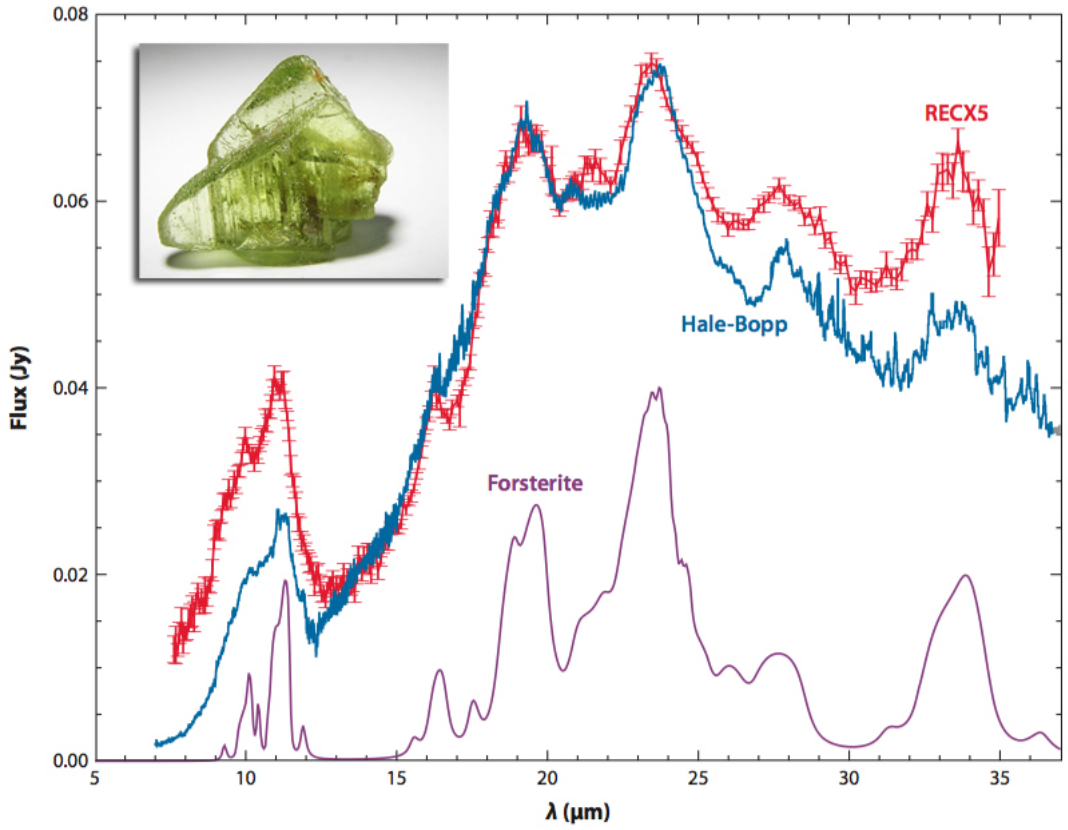

Figure 1.9: *This figure shows the striking similarity between a laboratory forsterite spectrum and the spectrum from the comet Hale-Bopp and the spectrum from the protoplanetary disk RECX5. On the upper right corner a figure is shown of a forsterite rock. Figure adopted from Henning (2010).*

1.3.3 Emission from forsterite grains

In the ISO spectra of Herbig Ae/Be systems, dust species such as silicates, both crystalline as well as amorphous, metallic iron, iron oxide, carbonaceous grains and water ice, have been identified (e.g. Malfait et al. 1998, Bouwman et al. 2000). Since dust in the ISM is largely amorphous (Kemper et al., 2004), substantial dust processing takes place in the protoplanetary disks surrounding protostars. At high temperatures ($T \gtrsim 1000$ K), forsterite is formed by condensation from the gas phase or by thermal annealing of amorphous silicates. The crystallisation products are mainly enstatite and forsterite, producing stronger and narrower features. They have the same chemical composition as the amorphous silicates. However, their atoms are ordered in a lattice with long range order. The emission features at about 10 and 18 μm, correspond to Si–O stretching and O–Si–O bending vibrations respectively. The 69 μm feature can be attributed to translational motions of the metal cations and complex translations involving metal and Si atoms. Forsterite shows narrower spectral features which carry information of the chemical composition as well as the grain size (Figure 1.9). By comparing the mid-infrared spectra

with laboratory spectra of dust material (e.g. Koike et al. 2003, 2006, Suto et al. 2006), the individual dust species can be identified. With observations from the ISO, Spitzer and Herschel telescopes, enormous progress has been made in determining both the dust composition as well as the processes that govern this composition in protoplanetary disks.

1.3.3.1 The forsterite 69 μm feature

The most recent insights in the characteristics of forsterite are made possible by observations from the Herschel space telescope. Information about the temperature, grain size and iron fraction can be derived from the shape of the 69 μm feature. The forsterite 69 μm feature has been observed and analysed by Sturm et al. (2010), Mulders et al. (2011) and Sturm et al. (2013). The widths and peak positions of the 69 μm detections indicate low temperature ($\sim$ 200 K) forsterite. This indicates that forsterite must be located at regions where it is significantly colder as compared to the location where they are formed (T$\gtrsim$ 1000K). This is consistent with earlier analysis of forsterite in protoplanetary disks by Bouwman et al. (2008), Juhász et al. (2010). Either efficient radial mixing from warmer regions in the inner disk, or in situ formation by a local process such as shocks or parent body processing must be responsible.

1.4 Outline of this thesis

The study of protoplanetary disks is 'in motion'. The work in this thesis spans over a timescale of four years, and already during these years, many new insights of protoplanetary disks have been presented. This thesis aims to contribute to the key question 'How do planets form?'. It focuses on the characterisation of several elements in the earliest phases of planet formation in protoplanetary disks: the connection between the SED and disk gaps (Chapters 2, 3 and 4), PAHs in the gas flows in disk gaps (Chapter 5) and dust processing of forsterite in evolving protoplanetary disks (Chapter 6).

In Chapters 2, 3 and 4, Q-band ($\lambda = 18.8$ μm and $\lambda = 24.5$ μm) observations have been analysed using the radiative transfer code MCMax to constrain the location of the gap. Sizes of the large gaps are identified in the transitional objects HD 97048, HD 169142, HD 135344 B, Oph IRS 48, HD 34282 and HD 100453. None of these objects show broad amorphous silicate features in the SED. By using direct imaging we confirm the presence of gaps in the disks and constrain their location. The main conclusion is therefore that the absence of the silicate feature can be used as a tracer of large size gaps in the temperature regime $\sim 200 - 500$ K. A second conclusion is that almost all flaring disks, within the sample of well known Herbig stars, are actually transitional disks. It thus seems that there are distinct ways in which disk can evolve: from flaring to flat disks (by grain growth and settling), from flaring to transitional disks (likely due to the formation of planets), or a combination of both: from flaring to flat to transitional.

In Chapter 5 an analysis is presented of the ionization balance of PAHs in Herbig stars. An analytic model for the ionization balance of PAHs is implemented in the radiative transfer code MCMax. The model was applied to four key objects for which spatial information was available about the location of PAHs in the disk. It is found that the PAHs are ionized when they are located in the gas flows through protoplanetary disk gaps. This is because in the low density, optically thin disk gaps, the local UV field is high, while the electron density is low. It is found that PAHs in the high density, optically thick disks are neutral, independent of the distance to the central star. The main conclusion is therefore that the band strength ratio $I_{6.2}/I_{11.3}$ can be used as a tracer of gas flows through protoplanetary disk gaps.

The analysis of forsterite spectra from disks must include radiative transfer models to properly study the influence of the disk geometry and different radial distributions of forsterite grains in the disk. In addition, optical depth effects can be taken into account. In Chapter 6 all the Herbig stars of which the 69 μm wavelength domain have been observed by Herschel/PACS are studied. The consistency between the forsterite features in the Spitzer/IRS and Herschel/PACS spectra are tested. For all objects, independent estimates of the forsterite temperature are made using the I_{23}/I_{69} feature ratio and the shape of the 69 μm feature. For the evolved transitional objects HD 141569 and Oph IRS 48, it is found that the 69 μm features may indicate larger grain sizes. This could be a result of substantial grain processing. The non-detections and general weakness of the 69 μm feature in flat disks indicate that the forsterite temperature is high ($T \gtrsim 300$ K). The location of the forsterite in these types of disks must be close to the star. This is consistent with the hypothesis that radial mixing is not very efficient in flat disks. This may be connected with the flatness of the disk, which can be a sign of low turbulence.

1.5 Future outlook

The final answers to many key questions are still ahead of us. And of course, as soon as they have been answered, they will be replaced by new questions. In the study of protoplanetary disk towards planetary systems, an important role will be taken by new generations of telescopes. ALMA has just started to explore the millimetre sky with great spatial resolution and sensitivity. And with the JWST and SPICA on their way, the future of infrared astronomy may be expected to boost again. In the context of this thesis, there are several relevant science questions waiting to be further explored:

- Is the emission from PAHs in disk gaps of Herbig stars indeed largely ionized? Will JWST be able to confirm this prediction?
- What is the influence of PAHs on heating and cooling events in the disk gaps? How are other gas/molecule diagnostics sensitive for the PAHs? The PAHs have a strong effect of the photoelectric heating in the disk. However, the interaction between the PAHs and the other material in the disk must be studied in more detail. This will allow us to understand whether the observational variety of PAH spectral signatures are a consequence of the disk structure, and vice versa.

- How radially extended are flat disks? The high sensitivity of ALMA is needed to observe the outer regions of flat disks. In addition, is there a relation between the mid-infrared (MIR) spectral index $F_{30}/F_{13.5}$ (i.e. the degree of self-shadowing, Acke et al. 2009) and the mm luminosity for flat disks? If grains in flat disks continue to drift inwards, where they accrete onto the star, and thus make the disk 'small and fat', the disk gets smaller over time. This may be indicated by the disk sizes of HD 163296 and HD HD31648 which are several hundreds of AU in size and have high mm luminosities, while the disk of HD 104237 is only $\sim$70 AU large and has a much lower mm luminosity.

- Are flat disks precursors of transitional disks? If a planet would form in a flat disk, could it increase the scale-height of the grains in the outer disk (e.g., increase the turbulence), and/or are small grains from inner disk blown outward and do they 'land' on the outer disk? A modeling study could investigate such scenarios.

- What are the differences between Herbig and T Tauri objects? We can study the influence of stellar properties on the disks by comparing full disks and transitional disks of T Tauri and Herbig stars. In this way, the consistency of their gap size characteristics and connection to mid- to far- infrared spectral colors can be studied. Herbig stars are known for their strong near-infrared (NIR) excess as compared to T Tauri stars. Is there a significant difference between the NIR excess of Herbig and T Tauri systems? If so, this may be attributed to the higher ultraviolet (UV) luminosity in Herbig stars. Including stochastically heated VSG in the disk could be examined as a solution. There is a strong correlation between the absence of the silicate feature and the $F_{30}/F_{13.5}$ ratio. Is this correlation also present in T-Tauri objects? In addition, most Herbig Be stars are self-shadowed/flat, while for T Taui stars, there does not seem to be a clear distinction between full/flat and transitional/flaring disks. Does the mass of the central star influence the structure of the disk?

- Are dust grains within the snow-line (i.e. where the temperature is $\gtrsim$ 150 K) significantly smaller? Test models show that the grain population needed to model a typical disk with silicate feature (group Ia) has a much higher abundance of small grains as compared to the grain population needed to fit a typical disk which does not show silicate features (group Ib). Possibly, this may reflect that the coagulation/-fragmentation balance of dust grains in the inner region lies more toward smaller sizes than in the outer disks. Remarkably, the transition between group Ia and Ib seems to be indicated by the presence of small grains above $\sim$150 K (Chapter 4). It would be interesting to study whether this is caused by the properties of the grains. Could particles in the outer disk stick together more easily due to icy mantles around the dust grain?

- Can laboratory measurements characterize the broadening of the 69 μm feature width as a function of grain size and low ($\sim 0-1$ %) fractions of iron inclusion?

The study of the chemistry and mineralogy inside protoplanetary disks is rapidly advancing. New modeling studies focus on to improve their description of the interaction

between the gas, the molecules and the dust in protoplanetary disks. New observations of dusty grains and ices originating in protoplanetary disks will gain further insights on the physical processes that alter the chemical composition and sizes of the grains in the disk. Perhaps we may soon find a better understanding between the variety of chondrites found in and around Earth, and the physical formation history of our solar system. With many new telescopes approaching, and excellent collaborations made between scientists all over the world, the future of exoplanetary science looks promising.

CHAPTER 2

Mid-IR imaging of the disk of HD169142: Measuring the size of the gap

M. Honda, K.M. Maaskant, Y. K. Okamoto, H. Kataza, M. Fukagawa, L. B. F. M. Waters, C. Dominik, A. G. G. M. Tielens, G. D. Mulders, M. Min, T. Yamashita, T. Fujiyoshi, T. Miyata, S. Sako, I. Sakon, H. Fujiwara, and T. Onaka
The Astrophysical Journal, Volume 752 (2012)

Abstract

The disk around the Herbig Ae star HD 169142 was imaged and resolved at 18.8 and 24.5 μm using Subaru/COMICS. We interpret the observations using a 2D radiative transfer model and find evidence for the presence of a large gap. The MIR images trace dust that emits at the onset of the strong rise in the spectral energy distribution (SED) at 20 μm, therefore are very sensitive to the location and characteristics of the inner wall of the outer disk and its dust. We determine the location of the wall to be 23^{+3}_{-5} AU from the star. An extra component of hot dust must exist close to the star. We find that a hydrostatic optically thick inner disk does not produce enough flux in the NIR and an optically thin geometrically thick component is our solution to fit the SED. Considering the recent findings of gaps and holes in a number of Herbig Ae/Be group I disks, we suggest that such disk structures may be common in group I sources. Classification as group I should be considered a support for classification as a transitional disk, though improved imaging surveys are needed to support this speculation.

2.1 Introduction

Transitional disks are a class of protoplanetary disks whose inner regions are devoid of small dust grains. These disks have been attracting attention recently, since such cleared inner regions or gaps may be related to on-going planet formation. The presence of an inner hole/gap has been suggested for the disk around the Herbig Ae star HD 169142 by Grady et al. (2007) and Meeus et al. (2010), mostly based on the analysis of the spectral energy distribution (SED). Both groups conclude that the steep rise in flux at $\sim$20 μm in the SED reflects emission from the wall of the outer disk. The location of the wall (i.e. the inner edge of the outer disk) has not been determined conclusively – Meeus et al. (2010) used 20 AU while Grady et al. (2007) suggested 44 AU. Observations of HD 169142 at various wavelengths have so far not been able to constrain the inner cavity radius directly and accurately.

One of the limitation of SED modeling is the inability to locate and prove the existence of gaps in proto-planetary disks. For instance, gaps may not be revealed in the SED because the inner disk can partially obscure large parts of the outer disk (Acke et al., 2009) and gaps hidden under that shadow do not leave a fingerprint in the SED. Clever SED modeling can reproduce SEDs of truly transitional disks without the need of a gap. The transitional disk LkCa 15 has an outer disk starting at 46 AU as seen at 1.4 and 2.8 mm wavelengths (Piétu et al., 2006). However, Isella et al. (2009) show that a model approach with a smooth distribution of material from a few stellar radii to about 240 AU can sometimes reproduce both the observed spectral energy distribution and the spatially resolved continuum emission at millimeter wavelengths for this object. Only from direct imaging it is possible to directly constrain the radial density structure of dust in a proto-planetary disk.

Dust in proto-planetary disks covers a temperature range from $\sim$1500 K at the inner dust sublimation radius to a few Kelvin in the outer parts of the disk. Direct mid-infrared (MIR) imaging at 18.8 and 24.5 μm is most sensitive for 100-150 K blackbody dust, though strong contributions from dust elsewhere in the disk at lower and higher temperatures can also be present. If the disk has a very strong NIR component such as HD 135344, the inner region may still be strongly represented in the center of the image at 18 micron. On the other hand, for disks with a larger gap or an inner hole, the image size will be a sensitive tracer to the location of the inner radius of the outer disk (Verhoeff et al., 2011).

In this paper, we present direct MIR imaging observations of HD 169142 at 18.8 and 24.5 μm, using COMICS on the 8.2m Subaru telescope. We confirm the result found by Mariñas et al. (2011) and find that the disk shows extended emission at 18 μm. In addition we find that the disk is also resolved at 24.5 μm. By constructing a radiative transfer disk model that fits both the SED and the imaging results, we find that the size of the source at MIR wavelengths is most naturally explained by a disk with a large inner gap, i.e. transitional disk. We discuss the structure of the disk, and the implications for its nature.

Table 2.1: *Observations Summary*

object	filter	Date (UT)	Integ. time [s] used/total (%)	AirMass	Direct FWHM
δOph	Q24.5	2004/07/11	195/243 sec (80 %)	1.254-1.354	$0.628'' \pm 0.007''$
HD 169142	Q24.5	2004/07/11	345/802 sec (43 %)	1.541-1.542	$0.680'' \pm 0.034''$
αHer	Q18.8	2004/07/12	83/83 sec (100 %)	1.081-1.115	$0.493'' \pm 0.006''$
HD 169142	Q18.8	2004/07/12	215/360 sec (60 %)	1.553-1.559	$0.604'' \pm 0.017''$

2.2 Observations and Data Reduction

Observations were conducted using COMICS (Cooled Mid-Infrared Camera and Spectrometer; Kataza et al., 2000, Okamoto et al., 2003, Sako et al., 2003) on the 8.2 m Subaru Telescope on Mauna Kea, Hawaii. HD 169142 was observed using the Q24.5-NEW (λ=24.5 μm, $\Delta\lambda$=0.75 μm) and Q18.8(λ=18.8 μm, $\Delta\lambda$=0.9 μm) filters. The plate scale of the COMICS camera is $0.13''$ per pixel. The chopping throw was $10''$ and the position angle of chopping direction was 0 degree. The chopping frequency was 0.45 Hz. The total integration time for Q24.5 and Q18.8 observations were 802 s and 360 s, respectively. Just before and after observing HD 169142, we took data of PSF reference and photometric standard stars. We used δ Oph for Q24.5 and α Her for Q18.8. The total integration times for the reference stars were 243 s and 83 s, respectively. A summary of the observations is given in Table 2.1.

We processed the data using a shift-and-add method to improve the blurring caused by atmosphere, tracking errors, mis-registration, etc. The imaging data consists of 0.98 s on-source integration frames. First, the thermal background and the dark current signals were removed through the subtraction of the chopped pair frames. The object and the PSF star are bright enough to be recognized even in 0.98 s chop-subtracted frames, so we searched the centroid of the object. We then shifted the frames so as to align the centroid position, and summed up the frames. However, we excluded frames which were blurred by atmospheric seeing. We rejected frames whose radius of 78.4% encircled energy ($r_{78.4}$) is larger than threshold radius (r_c) which covers 95% of the wavefronts whose Strehl ratio is 0.9. These threshold values are determined as $r_c = 1.131''$ at 18.8 μm and $r_c = 1.482''$ at 24.5 μm by Monte Carlo simulation of ideal unresolved point source. Due to this rejection of lower quality data, the effective integration time of HD 169142 was reduced to 345 s and 215 s for Q24.5 and Q18.8, respectively. The same procedure was applied to the PSF images taken before and after HD 169142, where the effective integration time became to 195 s and 83 s, respectively. Since HD 169142 shows marginal extension compared to the PSF and the rejection criterion r_c is determined for the ideal unresolved point source, frame rejection rates of HD 169142 are higher than those of PSF stars. It means that the effective rejection criterion is slightly more stringent for HD 169142 than for PSF stars, however, it does not overestimate the extension of HD 169142.

For flux calibration we used template spectrum provided by Engelke et al. (2006). Using the standard stars observed over the two nights, an airmass correction was applied

for Q24.5 photometry. For Q18.8 photometry, we could not find a significant airmass dependence during the night. A standard aperture photometry was applied and the resultant flux density of HD 169142 was 10.5 ± 0.4 Jy at 18.8 μm and 13.0 ± 0.5 Jy at 24.5 μm. The final images of the PSF and HD 169142 are shown in Figure 2.1.

2.3 Results

2.3.1 Source size of HD 169142 in 18.8 and 24.5 μm

The azimuthally-averaged radial brightness profiles of HD 169142 and the PSF stars at 18.8 and 24.5 μm are shown in Figure 2.2. It is clear that HD 169142 is extended at these wavelengths. At 18.8 μm the direct FWHM of the shift-and-added images of HD 169142 and of the PSF stars were $0.604'' \pm 0.017''$ and $0.493'' \pm 0.006''$, respectively. At 24.5 μm, the corresponding numbers are $0.680'' \pm 0.034''$ and $0.628'' \pm 0.007''$ (see Table 2.1). It is surprising that the size of HD169142 is not increasing with wavelength. For a continuous flaring disk, one would expect the size of the image to scale roughly with the PSF (Meijer, 2007). Our images therefore give a first indication that the radial density structure is not continuous. The FWHMs of the PSF references are comparable to the predicted value of the diffraction limited performance of the telescope. As a rough estimate of the intrinsic source size of HD 169142, we applied the quadratic subtraction method as described by Mariñas et al. (2011). The derived source FWHMs were $0.349'' \pm 0.014''$ at 18.8 μm and $0.261'' \pm 0.025''$ at 24.5 μm. Since Mariñas et al. (2011) observed the FWHM of this source to be $0.32'' \pm 0.05''$ at 18.0 μm, our measurement at 18.8 μm is in good agreement with their results within the uncertainties.

2.4 Modeling

2.4.1 Observational constraints

Complementary views of the disk structure and the dust properties of HD 169142 are obtained by adopting photometric data at various wavelengths from the literature (van den Ancker et al., 1998, Cutri et al., 2003, Zacharias et al., 2004, Sylvester et al., 1996, Meeus et al., 2010) and MIR spectra from ISO (Meeus et al., 2001) and Spitzer/IRS (Juhász et al., 2010). These datasets reflect the disk brightness as a function of wavelength and are a result of the disk structure defined by the density distribution, composition, inclination, and inner and outer radius of the disk and by the properties of the central star. An outer disk radius of 235 AU is taken from Panić et al. (2008). An inner disk radius of 0.1 AU is set at the location where the dust reaches 1500 K and starts to sublimate. With an inclination of 13° (Raman et al., 2006), the system is nearly pole-on and, therefore, deviations from axial symmetry caused by projection effects can be neglected in our images. The stellar spectrum is described by a Kurucz model with an effective temperature of 8200

K (Dunkin et al., 1997), luminosity of 15.3 $L_\odot$ and extinction A_V=0.46 (van den Ancker et al., 1998). The system is set at a distance of 145 pc (de Zeeuw et al., 1999). All stellar and disk parameters used in this paper are shown in table 2.2.

2.4.2 Radiative transfer code MCMax

We construct a geometrical model of the disk of HD 169142 and fit it to both the radial surface brightness profile (RBP) of our observed images and to the SED. For the model we use the radiative transfer code MCMax (Min et al., 2009), which is able to solve temperature and density structures in very optically thick circumstellar disks. This code has been compared to other radiative transfer codes by Pinte et al. (2009) and has been applied successfully in previous studies (e.g. Verhoeff et al., 2011, Mulders et al., 2011). We assume an axisymmetric dust distribution in which the optical properties of the grains are computed using a distribution of hollow spheres (DHS; Min et al., 2005). We consider all dust species in the disk to be in thermal contact, and calculate their respective opacities from the optical constants as if they were separate particles. Furthermore we assume the gas temperature to be set by the dust temperature. We adopted grains with sizes according to the power-law $f(a) \propto a^{-3.5}$. The power-law index is that of interstellar grains (Mathis et al., 1977) and is consistent with collisional fragmentation considerations (Hellyer, 1970). Under the assumption that the system is in hydrostatic equilibrium, the vertical density distribution of the disk is solved by iterating the density and temperature structures until they become self-consistent (e.g. Dullemond et al., 2007b).

We assume a grain population consisting of 30% carbon and 70% silicates (we refer to Mulders et al. (2011) for references of the optical properties of this dust composition). The contribution of warm small (< 10 μm) amorphous silicate grains to the spectrum must be low, since the flux level at 10 μm is very low compared to that at 20 μm. We model this change in flux level by replacing the amorphous silicate dust in the inner disk with dust with a higher continuum opacity. We here use carbon, but other dust species such as metallic iron may give the same result. This treatment is consistent with van Boekel et al. (2004) who find that grain growth in the innermost regions has proceeded further than in the outer disk regions. We have not attempted to fit the PAH features in detail, though we implement them into our model to fit the SED. Scattered light contribution is also included and the fraction of the scattered light to the total flux density in 18.8 and 24.5 μm is 22–26% in this model.

2.4.3 The best fit model

We fit the SED as well as the 18.8 and 24.5 μm images simultaneously by using the disk parameters shown in Table 2.2. The RBPs and SED of our final best fit model are shown by the the purple dashed lines in Figures 2.2 and 2.3. A cartoon sketch is given in Figure 2.4. In this section we will first discuss the geometrical characteristics of the location of the gap and the outer disk properties. Thereafter we discuss the constraints we find to the inner disk structure of the best fitting model.

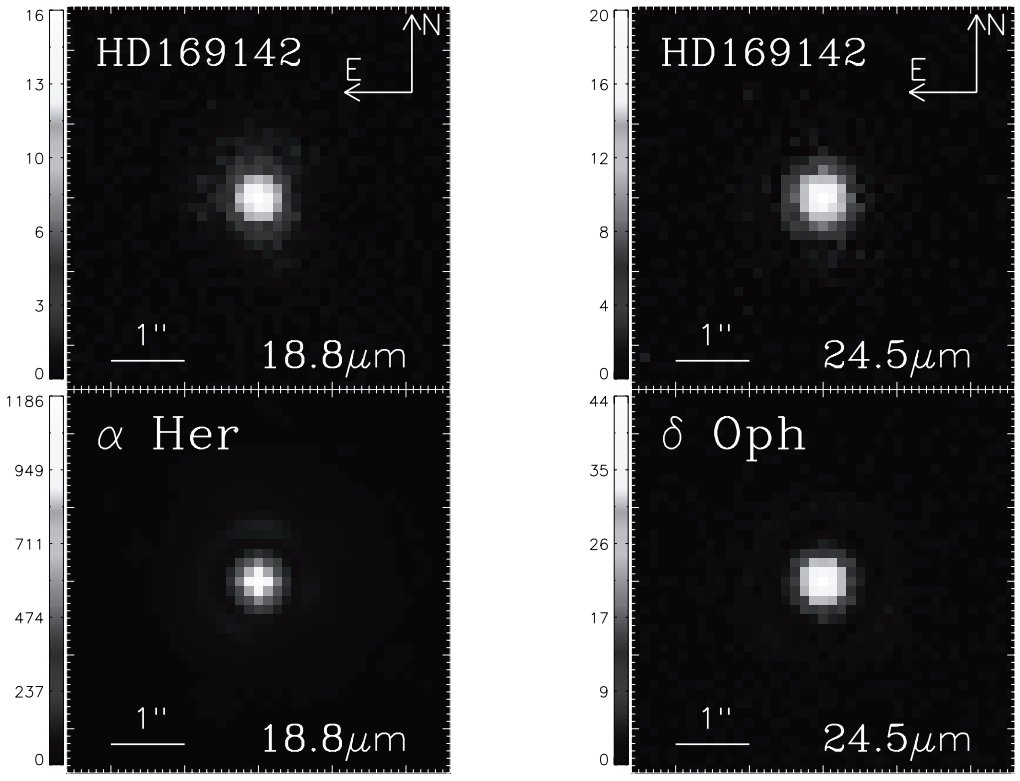

Figure 2.1: *Shift-and-added image of HD 169142 (top) and PSF star (bottom) at 18.8 and 24.5 μm. Brightness unit is in Jy/arcsec^2 and scaled from 0 to the peak value in the image. North is up and the east is to the left*

2.4.3.1 Fitting the SED

Previous SED modeling by Meeus et al. (2010) and Grady et al. (2007)suggested a gap in the disk with an outer radius of 20 and 44 AU respectively. We confirm and improve on this result by our test modeling for HD169142: disks without a gap fail to fit the SED, despite various attempts within the physically reasonably parameter space. So already the SED fitting gives a strong indication for the presence of a gap (confirming the results by Meeus et al. (2010) and Grady et al. (2007), even though its size is not well constrained at all from the SED alone. We incorporate this result and include a gap in our model. The effect of the discontinuity in the radial density structure is that a large fraction of the stellar light now falls on the vertical wall at the inner edge of the outer disk. Emission from this wall is clearly distinguishable in the SED (Figure 2.3, illustrated by the red dotted-line). In addition, Figure 2.3 shows that the flux contribution from the inner edge (between 23-26 AU) dominates at 18.8 and 24.5 μm and that flux contributions from the inner regions and from the outer disk are negligible at these wavelengths. Therefore, our Subaru/COMICS images at 18.8 and 24.5 μm are sensitive tracers of the radius where the outer disk starts. Another insight to understand the dominance of the wall is given by the radial density and temperature plots of the outer disk of this model in Figure 2.5. The dotted lines show that the densest regions are largely optically thick. Therefore the

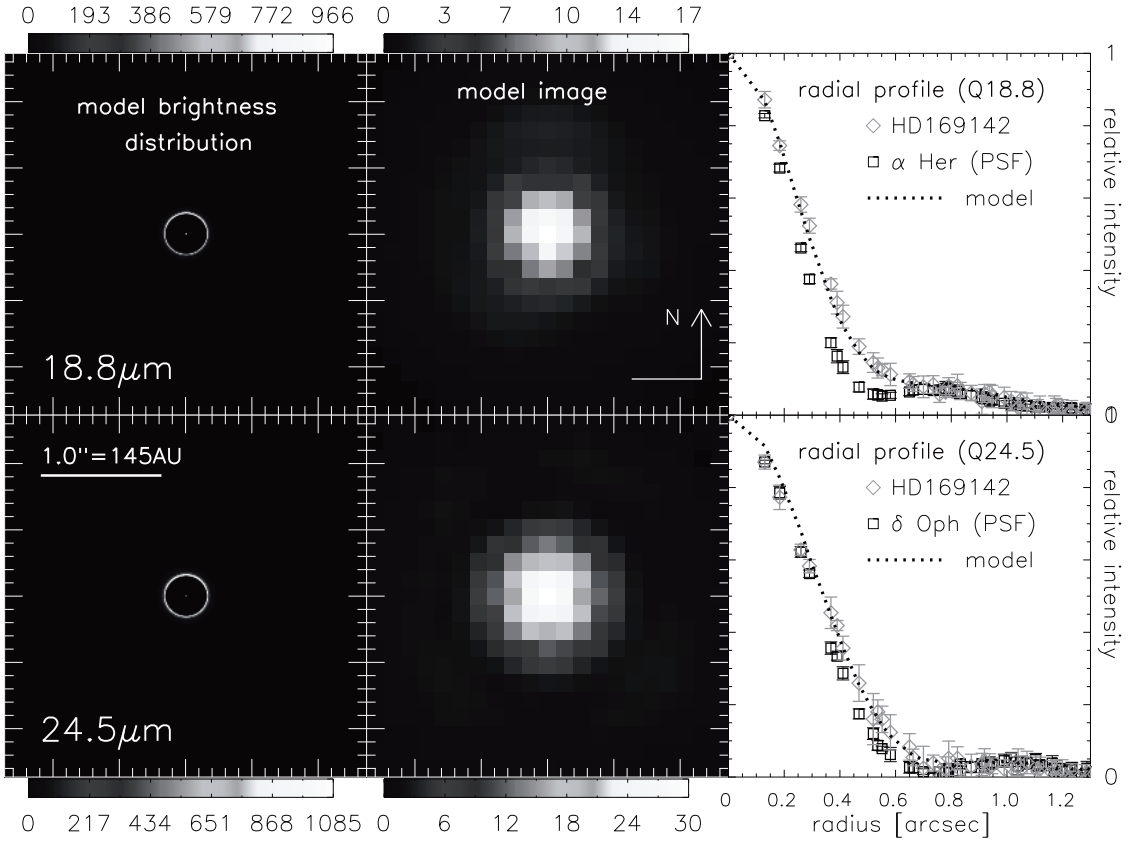

Figure 2.2: *Left and middle panels are model brightness distribution of final model and model image after convolved by Subaru/COMICS PSF (middle), respectively, shown in Jy/arcsec^2. Right panels represents the peak-normalized azimuthally-averaged radial brightness profiles relative to the centroid of the image (right). Top panels are in the Q18.8 and the bottom panels are in the Q24.5 filters. In the radial profile plots (right), the observation of HD 169142 is shown by the diamonds, and the corresponding PSF of the calibrators is shown by the squares. The final model convolved with the PSF is shown by the dotted line.*

temperature of the disk mid-plane decreases rapidly as a function of radius. Thus 18.8 and 24.5 μm photons are mostly produced at the inner few AU radii of the outer disk.

The radius where the outer disk starts is not well constrained by SED modeling. Because the disk structure is degenerate by uncertainties of many parameters like the stellar temperature and luminosity, the interstellar extinction, the grain size population of the dust, the vertical density structure and so on. Only by fitting our model to the resolved MIR observations we can unambiguously confirm the existence of a gap and constrain the location of the wall of the outer disk.

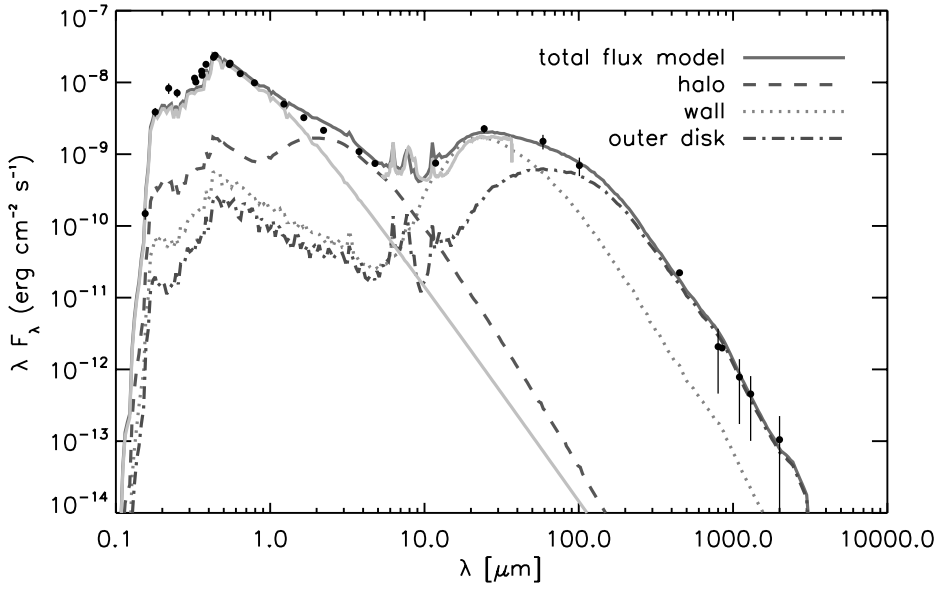

Figure 2.3: *Spectral energy distribution of HD 169142. The solid grey lines represent the Kuruczand the Spitzer/IRS [5.3 - 37 μm] spectra respectively. The dashed line shows the geometrically thick, optically thin halo-like dust cloud component. The dotted line gives the flux contribution from the innermost part of the outer disk (23-26 AU). The flux from the remainder of the outer disk (26-237 AU) is given by the dashed-dotted line. The sum of the components is given by the solid line. It is clear that at both 18.8 and 24.5 μm, the SED is dominated by flux coming from the inner edge of the outer disk.*

2.4.3.2 Fitting the MIR-images, constraining the location of the wall

After convolving our best fit model with the PSFs of the calibrators, we find that the imaging data is fitted best with an inner edge of the outer disk of 23^{+3}_{-5} AU (see Fig.2.2). The uncertainty on this radius is determined by fitting the uncertainty of the azimuthally averaged flux level at ± 1 sigma. This result is consistent with a wall radius of 20 AU (Meeus et al., 2010) but excludes the model with a wall at 44 AU (Grady et al., 2007).

We have performed a small parameter study where we have examined the robustness of our final model to fit the RBPs at MIR wavelengths. We have varied the following parameters: the surface density powerlaw between {-0.5, -1.5}, the grain size distribution powerlaw {-2.5, -4.5}, the dust settling factor {0.5, 1}, the stellar temperature {8000 K, 8500 K} and luminosity {13 $L_\odot$, 17 $L_\odot$} and the distance {130 pc, 160 pc}. While the RPB only vary slightly in this parameter study (all within the 1 sigma error of the measurements), the SED fit becomes significantly worse. We conclude that the radius of the wall is the only free parameter which significantly influences the broadness of the RBP. Therefore our fit to the RBP is robust in constraining the radius of the inner edge of the outer disk at 23^{+3}_{-5} AU.

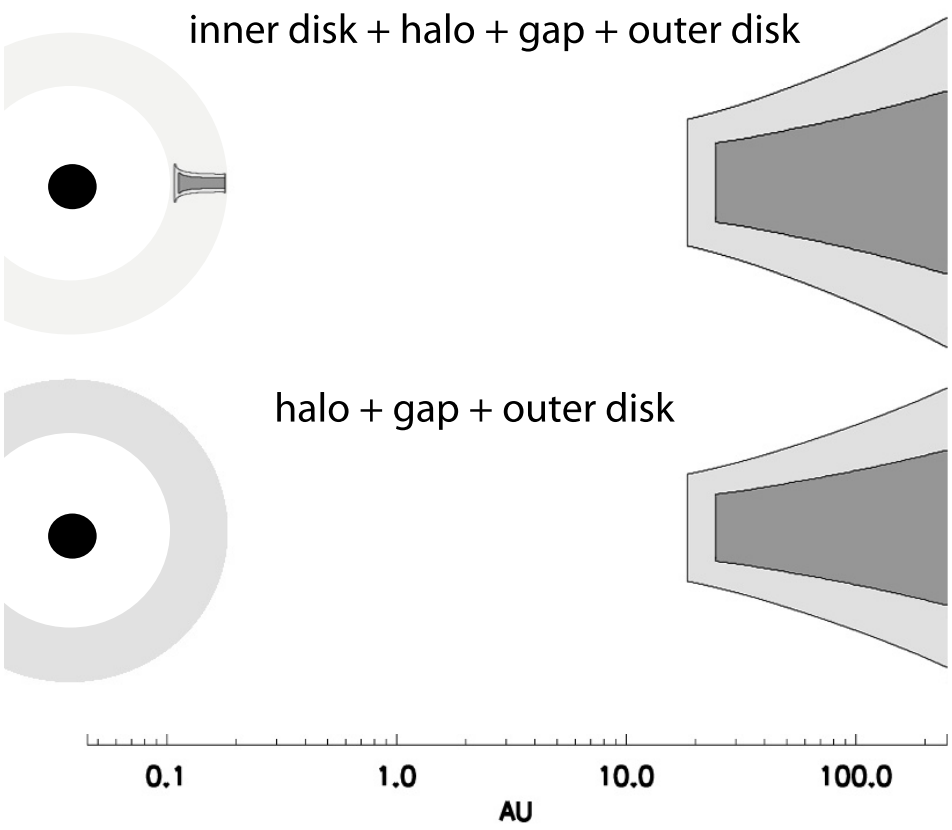

Figure 2.4: *Sketch of our final model with two possible structures for the inner regions. Top: the model with a flat inner disk, a optically thin halo and an outer disk. Bottom: the model with a denser but still optically thin halo, and an outer disk in which the scale-height of the dust is decreased. Both geometries give an equally good fit to the SED and the images. Although we can not distinguish between these models with our dataset, we choose the bottom model as our final model described in the text.*

2.4.3.3 The inner disk

In this section we explain in more detail the implications for the inner disk structure. Modeling shows that an optically thick hydrostatic inner disk does not produce enough flux to fit the SED. Scaling up the vertical height of the inner disk would not be a solution because if the inner disk is higher than Z/r $\sim$ 0.1 it covers the outer disk for more than $\sim$50% in direct and scattered light. This inner disk then casts a too large shadow on the outer disk to be able to reproduce the SED at wavelengths longer than $\sim$10 μm. To solve this problem we include a geometrically thick, *optically thin* halo-like dust cloud to the inner regions ($<$ 0.5 AU, see Figure 2.5) to fit the SED in the NIR and to avoid a shadowing effect on the outer disk. The physical origin is not certain at this moment, though other observational studies show that an optically thin component close to the star provides a good fit as well (Grady et al., 2007, Benisty et al., 2011, Verhoeff et al., 2011, Mulders et al., 2010). Furthermore, fitting the Herbig stars' median SED requires such a halo (Mulders et al., 2012). Further high spatial resolution observations such as infrared

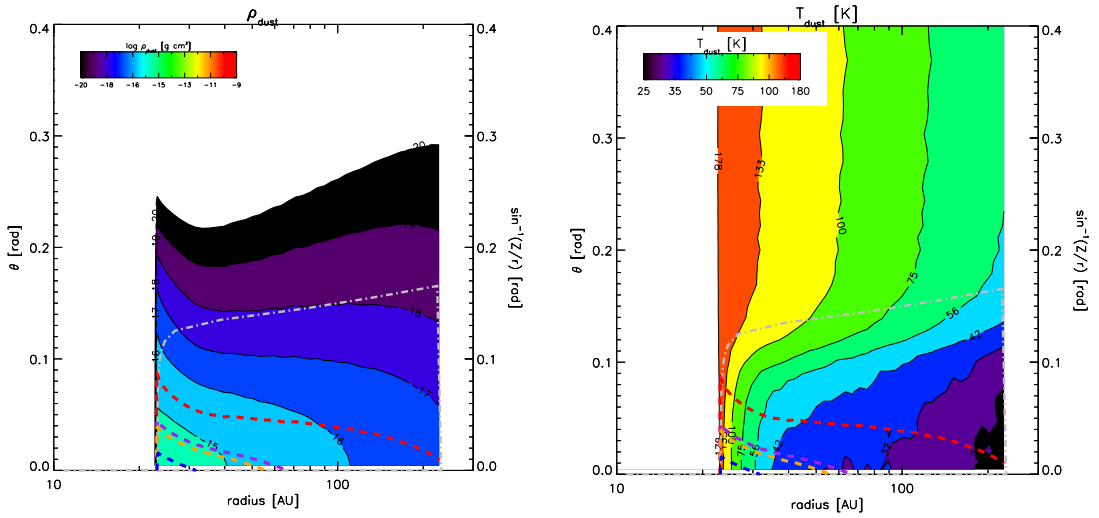

Figure 2.5: *Left: the dust density $\rho_{\rm dust}$ in g cm^{-3} of the outer disk as a function of radius and angle θ for our best fitting model. The lower and upper density cut-offs are 10^{-20} and 10^{-9} g cm^{-3} respectively. Right: the temperature structure of the outer disk as a function of radius and angle θ for our best fitting model. The inner edge of the outer disk starts at a temperature of 180 K. For small θ the angle is approximately Z/r. The grey dot-dashed line shows the τ=1 surface in radial direction in scattered light (λ=0.5 μm). The dashed lines represent the τ=1 surfaces as seen perpendicular from the disk. From top to bottom the colors are red, purple, orange and blue and represent the wavelengths 0.5, 18.8, 24.5, 70 μm.*

interferometry will be necessary to reveal the inner disk structure.

If there is no shadowing effect from the inner disk, the wall of the outer disk is too luminous. To fit the SED again, we can either settle the grains in the outer disk by scaling down the dust density scaleheight by a factor of 0.6 or we can scale down the abundance of small (< 1 µm) grains by one order of magnitude. These adjustments are consistent with dust settling and grain growth (Dullemond & Dominik, 2005), however, it is uncertain to what extent these effects are present in the disk. The influence of other effects like dynamical scattering of larger dust grains may also play a role in the vertical grain size distribution. Alternatively, we can *combine* a halo-like dust cloud and a flat inner disk and consequently perform no settling or removal of small dust grains. So we conclude that there are two possible inner disk geometries (as illustrated in the cartoon in Figure 2.4) which give an equally good fit to the SED and the RBP.

Without an optically thick inner disk, the RBP is still reproduced with the inner radius of the outer disk at 23^{+3}_{-5} AU. The final model can be interpreted as an inner halo-like dust cloud (Krijt & Dominik, 2011) and a gas-rich outer disk structure, so truly a transitional disk.

Table 2.2: *Parameters of HD 169142 system used in our best-fit model*

parameter	value	Remarks
Spectral type	A5Ve	Dunkin et al. (1997)
Extinction A_V	0.46±0.05	van den Ancker et al. (1998)
log g	4.22	van den Ancker et al. (1998)
Temperature	8200K	Dunkin et al. (1997)
Distance	145±15 pc	de Zeeuw et al. (1999)
Age	6^{+6}_{-3} Myr	Grady et al. (2007)
Stellar luminosity	15.33±2.17 $L_\odot$	van den Ancker et al. (1998)
Stellar Mass	2.28±0.23 $M_\odot$	van den Ancker et al. (1998)
Stellar Radius	1.94±0.14 $R_\odot$	van den Ancker et al. (1998)
Gas disk mass	(0.16–3.0)×10^{-2} $M_\odot$	Panić et al. (2008)
Dust disk mass	4×10^{-4} $M_\odot$	fit to the sub mm photometry
Inclination	13^o	Raman et al. (2006), Dent et al. (2005)
accretion rate	$\leq 10^{-9} M_\odot$ yr^{-1}	Grady et al. (2007)
R_{halo}	0.1-0.2 AU	geometrically heigh, optically thin component
R_{in}	23^{+3}_{-5} AU	fit to RBP of Subaru/COMICS data
R_{out}	235 AU	Panić et al. (2008)
surface density exponent	-1.0	Hydrostatic equilibrium
Particle size	a ={0.03μm,1cm}	powerlaw distribution of -3.5
Silicates	70%	similar to Mulders et al. (2011)
Amorphous carbon	30%	Zubko et al. (1996)
M_{PAH}	0.45 × 10^{-7} $M_\odot$	uniform PAH distribution
M_{halo}	0.28 × 10^{-10} $M_\odot$	only carbon
M_{disk}	0.3 × 10^{-3} $M_\odot$	dust mass, a ={0.03μm, 1cm}

2.5 Discussion

2.5.1 Inner hole/gap are common for Meeus's group I sources ?

We have shown observational evidence for the presence of an inner hole or gap in the HD 169142 disk. A similar structure is also indicated for other Herbig Ae/Be stars such as AB Aur (Honda et al., 2010), HD 142527 (Fukagawa et al., 2006, Fujiwara et al., 2006, Verhoeff et al., 2011), HD 135344 (Brown et al., 2009), HD 36112 (Isella et al., 2010), HD 100546 (Bouwman et al., 2003, Benisty et al., 2010, Mulders et al., 2011). All of these objects have been classified as group I according to the definition introduced by Meeus et al. (2001). Since the strong far infrared excess is a characteristic of group I sources, we speculate that this component may come from the emission from the inner-edge of the outer disk. Consequently, we suggest that the inner hole or gap structure may be common for group I sources. If this is true, the hypothesis that the group I flared disks evolves into the group II flat disks due to dust sedimentation should be reconsidered, because the difference of group I and II is not only the degree of disk flaring or grain growth, but also the presence of cleared inner regions (holes and gaps) in the disk.

As we have shown in the above analysis, the spatial extent of a Herbig Ae/Be disk at MIR wavelengths, often described by a FWHM, is strongly influenced by the position and temperature of the wall. Previous studies showed that group I sources are likely to

be more extended than group II sources in the MIR wavelengths, and suggested that the disk geometry (flaring or flat disk) may play an important role in the thermal structure and MIR emission of the disk (Leinert et al., 2004, Mariñas et al., 2011). Our 24.5 μm imaging survey of Herbig Ae/Be stars with Subaru/COMICS (Honda et al. in preparation) also confirms that many group I sources are extended, however, their spatial extent shows a great diversity, from marginally to remarkably extended. Such diversity in the spatial extent in the MIR can be understood in terms of the distance, the inner disk structure and the location of the wall of the outer disk. In fact, the temperature of the wall both in the AB Aur and HD 142527 systems appears to be relatively cool (70-100 K) and its wall radius also tends to be at some distance away from the central star ($\sim$100 AU in AB Aur; $\sim$170 AU in HD 142527; Fujiwara et al. 2006). The wall in HD 169142 is at a smaller distance (23AU), thus the spatial extent is not so large compared to that of AB Aur and HD142527. We suggest that not only the geometry (flared or flat) of the disk, but also the inner gap and a wall-like inner edge of the outer disk are important for understanding the spatial extent of Herbig Ae/Be disks in the MIR.

2.5.2 Origin of the inner hole of HD 169142 disk

Gaps seem to be a common characteristic of the group I flaring disks (Honda et al., 2010, Fukagawa et al., 2006, Fujiwara et al., 2006, Verhoeff et al., 2011, Brown et al., 2009, Isella et al., 2010, Bouwman et al., 2003, Benisty et al., 2010, Mulders et al., 2011). An inner hole or gap in the disk has been explained by several mechanisms, including (1) photoevaporation of the disk (Alexander et al., 2006), (2) geometric shadowing (Dullemond & Dominik, 2004a), (3) grain growth in the inner disk causing a lower dust opacity zone (van Boekel et al., 2005), and (4) the presence of another body in the disk that dynamically creates a gap and decouples the inner disk from the outer disk (Augereau & Papaloizou, 2004). We prefer solution (4) since this also provides a natural explanation for a inner halo-like dust cloud in the inner disk. The presence of a halo likely requires some dynamical interactions with planetary bodies since new generations of dust can than be created in situ up to large disk heights (Krijt & Dominik, 2011). Grain growth can not explain the presence of a gap and a wall. Furthermore, our test models show that geometric shadowing (i.e. varying scaleheights, surface density powerlaws) of a part of the disk at several AU can not reproduce the SED and the RBP of the images. We recognize that planetary companions have not yet been detected in the transitional disk around HD 169142, though recent direct detection of the planets around A type stars (e.g. HR8799; Marois et al. 2008, βPic; Lagrange et al. 2010) leads support for such hypothesis. Thus we suggest that the HD 169142 system is an excellent candidate to look for newly-formed planets in the protoplanetary disk.

2.6 Conclusions

We arrive at the following conclusions:

1. HD 169142 is extended at MIR wavelengths with the Subaru/COMICS instrument. The derived source sizes from quadratic PSF reference subtraction are $0.349'' \pm 0.014''$ at 18.8 μm and $0.261'' \pm 0.025''$ at 24.5 μm, respectively.

2. The observed sizes as well as the steep rise of the SED near 20 μm require a disk model with an inner hole the size of 23^{+3}_{-5} AU, making HD 169142 a transitional disk.

3. HD 169142 is one of a growing number of Herbig Ae disks that are classified as group I source and that *also* require the presence of a large inner gap. It appears that many if not all group I sources may be strong candidates for classification as transitional disks.

Acknowledgements: *We are grateful to all of the staff members of the Subaru Telescope. We also thank Ms. Hitomi Kobayashi and Dr. Yuji Ikeda at Kyoto-Nijikoubou Co., Ltd.. KM is supported by a grant from the Netherlands Research School for Astronomy (NOVA). This research was partially supported by KAKENHI (Grant-in-Aid for Young Scientists B: 21740141) by the Ministry of Education, Culture, Sports, Science and Technology (MEXT) of Japan.*

CHAPTER 3

Identifying gaps in flaring Herbig Ae/Be disks using spatially resolved mid-infrared imaging. Are all group I disks transitional?

K. M. Maaskant, M. Honda, L.B.F.M. Waters, A.G.G.M. Tielens, C. Dominik, M. Min, A. Verhoeff, G. Meeus, and M. E. van den Ancker
Astronomy & Astrophysics, Volume 555 (2013)

Abstract

The evolution of young massive protoplanetary disks toward planetary systems is expected to correspond to structural changes in observational appearance, which includes the formation of gaps and the depletion of dust and gas. A special group of disks around Herbig Ae/Be stars do not show prominent silicate emission features, although they still bear signs of flaring disks, the presence of gas, and small grains. We focus our attention on four key Herbig Ae/Be stars to understand the structural properties responsible for the absence of silicate feature emission. We investigate Q- and N-band images taken with Subaru/COMICS, Gemini South/T-ReCS and VLT/VISIR. We perform radiative transfer modeling to examine the radial distribution of dust and PAHs. Our solutions require a separation of inner- and outer- disks by a large gap. From this we characterize the radial density structure of dust and PAHs in the disk. The inner edge of the outer disk has a high surface brightness and a typical temperature between $\sim$100–150 K and therefore dominates the emission in the Q-band. All four disks are characterized by large gaps. We derive radii of the inner edge of the outer disk of 34^{+4}_{-4}, 23^{+3}_{-5}, 30^{+5}_{-3} and 63^{+4}_{-4} AU for HD 97048, HD 169142, HD 135344 B and Oph IRS 48 respectively. For HD 97048 this is the first detection of a disk gap. The large gaps deplete the entire population of silicate particles with temperatures suitable for prominent mid-infrared feature emission, while small carbonaceous grains and PAHs can

still show prominent emission at mid-infrared wavelengths. The continuum emission in the N-band is not due to emission in the wings of PAHs. This continuum emission can be due to VSGs or to thermal emission from the inner disk. We find that PAH emission is not always dominated by PAHs on the surface of the outer disk. The absence of silicate emission features is due to the presence of large gaps in the critical temperature regime. Many, if not all Herbig disks with Spectral Energy Distribution (SED) classification 'group I' are disks with large gaps and can be characterized as (pre-) transitional. An evolutionary path from the observed group I to the observed group II sources seems no longer likely. Instead, both might derive from a common ancestor.

3.1 Introduction

Planetary systems form in the dusty disks around pre-main-sequence stars. The structure and evolution of these disks depend upon a wide range of parameters, such as the initial mass, size, and chemical characteristics of the disk and the properties of the central star. In addition, evolutionary processes such as grain growth, grain settling, photo-evaporation and planet formation can take place in disks. Their interplay will eventually transform gas rich disks into debris disks with possibly planetary systems, such as in Fomalhaut (Boley et al., 2012), β Pictoris (Lagrange et al., 2010) or HR8799 (Marois et al., 2010). Characterization of pathways toward mature planetary systems are key in understanding protoplanetary disks evolution.

The evolution of intermediate-mass pre-main-sequence stars, known as Herbig Ae/Be stars, is different from that of lower- and higher-mass stars due to the differences in stellar and circumstellar physics (Natta et al., 2007). Meeus et al. (2001) classified the Herbig Ae/Be stars into two groups: group I sources, which require blackbody components up to far-infrared wavelengths to fit the SED, and group II sources, which can be well fitted with only a single power law at mid- to far-infrared wavelengths.

Several explanations have been proposed to understand the evolutionary link between group I and group II objects. Dullemond & Dominik (2004b, 2005) showed that spectral energy distributions (SEDs) of group I sources can be interpreted by hydrostatic disks with a flaring geometry while group II sources are thought to be the evolved version of group I sources: as dust grains coagulate and settle to the mid-plane, the disk becomes flatter producing the steeper, bluer mid- to far-infrared SEDs. Additionally, a decrease of mid-to far-infrared flux in the SED can be explained by a puffed-up inner disk that shadows large parts of the outer disk (Dullemond & Dominik, 2004a).

Gaps have been found in an increasing number of Group I sources such as in AB Aur (Honda et al., 2010), HD 142527 (Fukagawa et al., 2006, Fujiwara et al., 2006), HD 135344 (Brown et al., 2009), HD 36112 (Isella et al., 2010), HD 169142 (Honda et al., 2012), Oph IRS 48 (Geers et al., 2007a) and HD 100546 (Bouwman et al., 2003, Benisty et al., 2010). Recently, Honda et al. (2012) proposed that the classification as a group I source could mean a disk geometry with a strongly depleted inner disk (i.e. a transitional

disk). Due to gaps and inner holes, huge vertical walls arise at the edge of the outer disk and significantly contribute to the mid-to far-infrared flux. In view of the possibility that all group I disks are transitional disks, the relation between group I and group II sources may have to be revisited.

To get a better understanding of the geometry of group I disks and the use of PAHs to trace the geometry of disks, we examine a representative set of four group I objects: HD 97048, HD 169142, HD 135344 B and IRS48 for which we have obtained a homogeneous set of N- and Q-band data. These targets have been observed and resolved before in the N- and Q-band by Mariñas et al. (2011) and Geers et al. (2007a). Our study adds a careful examination of the disk sizes in the continuum and in the PAH filter at 11.2 μm by comparing to radiative transfer models. In Section 3.2, we introduce the sources in our sample. Thereafter we describe the observations, which are used as an input for the analysis in Section 6.2. We start in Section 3.5 by fitting the Q-band size and demonstrate that the flux at 18.8 and 24.5 μm is dominated by the inner edge of the outer disk and thus gives a solid constraint on the location where the outer disk starts. In Section 3.6, we show that the disk size in the N-band at 10.5 μm is given by emission from the inner disk, outer disk, and very small grains and is therefore less suitable to derive the gap radius. We show in Section 3.6.5 that the FWHM of the 8.6 and 11.2 μm PAH features in our sample do not correlate with the disk geometry which implies that imaging in the PAH bands cannot always be used as a reliable tracer of the disk structure. In Section 6.6, we discuss the implications of our findings. Section 6.7 summarizes our conclusions.

3.2 The sample

We selected a sample of four Herbig Ae/Be objects for study: HD 97048, HD 169142, HD 135344 B, and Oph IRS 48. The SEDs are shown in Figures 3.1 and 3.2. We collected a comprehensive data set for these objects, which consists of Spitzer IRS spectra and photometry. See Appendix 3.9 for an overview of available photometric UV, optical, infrared, and millimeter data and their references. Spitzer IRS spectra are taken from Juhász et al. (2010). The Spitzer IRS spectrum of Oph IRS 48 has been reduced with the latest calibration version (S18.18.0, Sturm et al. 2013). These four sources are representative for the sample of flaring Herbig Ae/Be objects, which lack the silicate features in their spectra. We have chosen these stars, since we could acquire a homogeneous set of MIR

Table 3.1: *Star & disk parameters used in this study*

Object	R.A. (J2000) h m s	Decl. (J2000) ° ′ ″	Teff [K] [K]	L_* [$L_\odot$]	Av	d [pc]	M_* [$M_\odot$]	i [°]
HD 97048	11 08 03.32	-77 39 17.48	10 010	40.70±5.9	1.21	158^{+16}_{-14}	1.84	43°
HD 169142	18 24 29.79	-29 46 49.22	8200	15.33±2.17	0.46	145^{+15}_{-15}	2.28	13°
HD 135344 B	15 15 48.40	-37 08 55.86	6590	8.26±1.17	0.32	140^{+14}_{-14}	3.30	11°
Oph IRS 48	16 27 37.19	-24 30 34.80	9000	14.3±5	11.50	120^{+5}_{-5}	2.0	48°

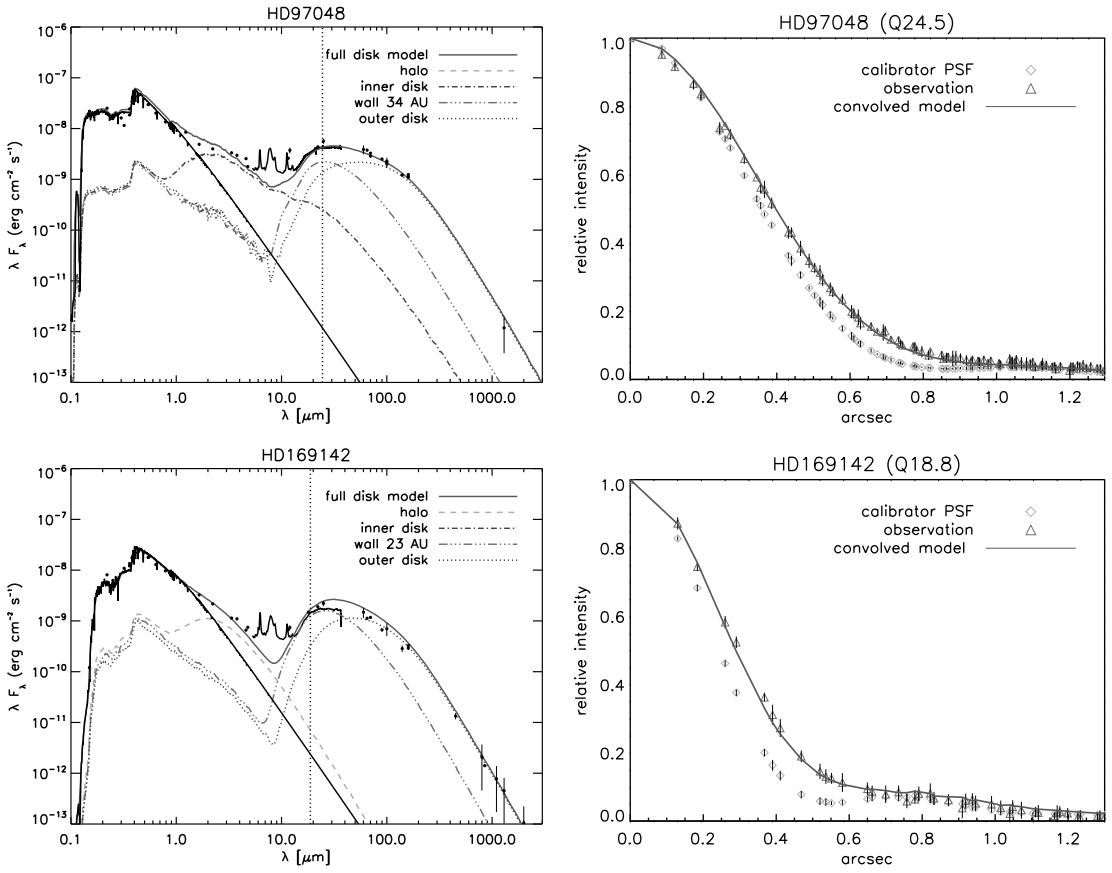

Figure 3.1: *Left: decomposed SEDs. The solid lines show the Kurucz models and the Spitzer IRS spectra. The dots represent the observed photometry corrected for extinction (See also Appendix 3.9.). The solid line is the sum of the flux of all the components. The dashed and dashed-dotted lines are the halo and inner disk components, respectively. The triple dotted dashed line indicates the emission from the wall (from the wall radius to 3 AU outwards). The dotted line shows the emission from the rest of the outer disk. Note that the IRAS photometry and Spitzer spectrum do not match very well for HD 97048, this may be caused by the difference in beam sizes. Right: azimuthally averaged radial brightness profiles of the Q-band relative to the maximum flux. The central wavelengths is 18.8 μm for HD 169142 and and 24.5 μm for HD 97048. The 24.5 μm fit to HD 169142 can be found in Honda et al. (2012). The diamonds indicate the PSF of the calibration star. The triangles show the observation of the science targets. The error bars indicate the one sigma error on the azimuthally averaged radial brightness profiles. The solid line shows our best fit model.*

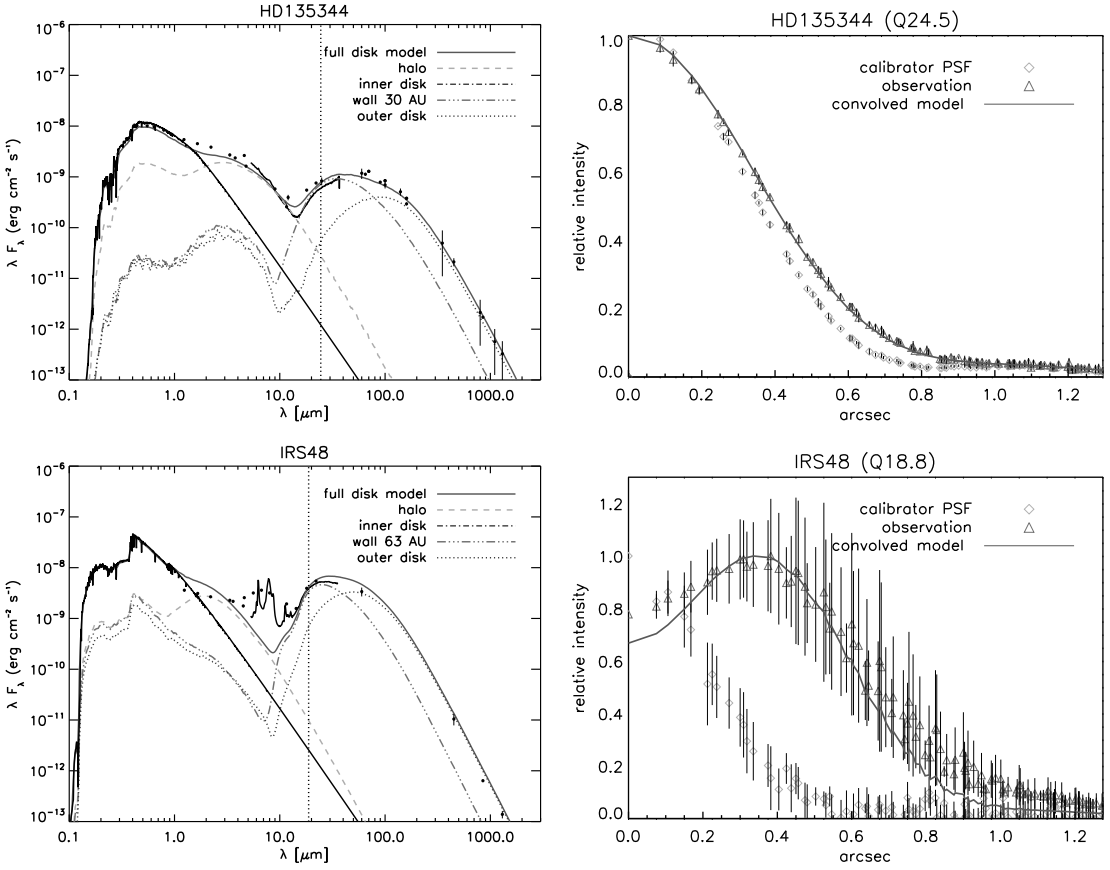

Figure 3.2: *Left: decomposed SEDs. The solid lines show the Kurucz models and the Spitzer IRS spectra. The dots represent the observed photometry corrected for extinction (See also Appendix 3.9.). The solid line is the sum of the flux of all the components. The dashed and dashed-dotted lines are the halo and inner disk components, respectively. The triple dotted dashed line indicates the emission from the wall (from the wall radius to 3 AU outwards). The dotted line shows the emission from the rest of the outer disk. Right: azimuthally averaged radial brightness profiles of the Q-band relative to the maximum flux. The central wavelengths of these images are 18.8 μm for Oph IRS 48 and 24.5 μm for HD 135344 B. The diamonds indicate the PSF of the calibration star. The triangles show the observation of the science targets. The error bars indicate the one sigma error on the azimuthally averaged radial brightness profiles. The solid line shows our best fit model.*

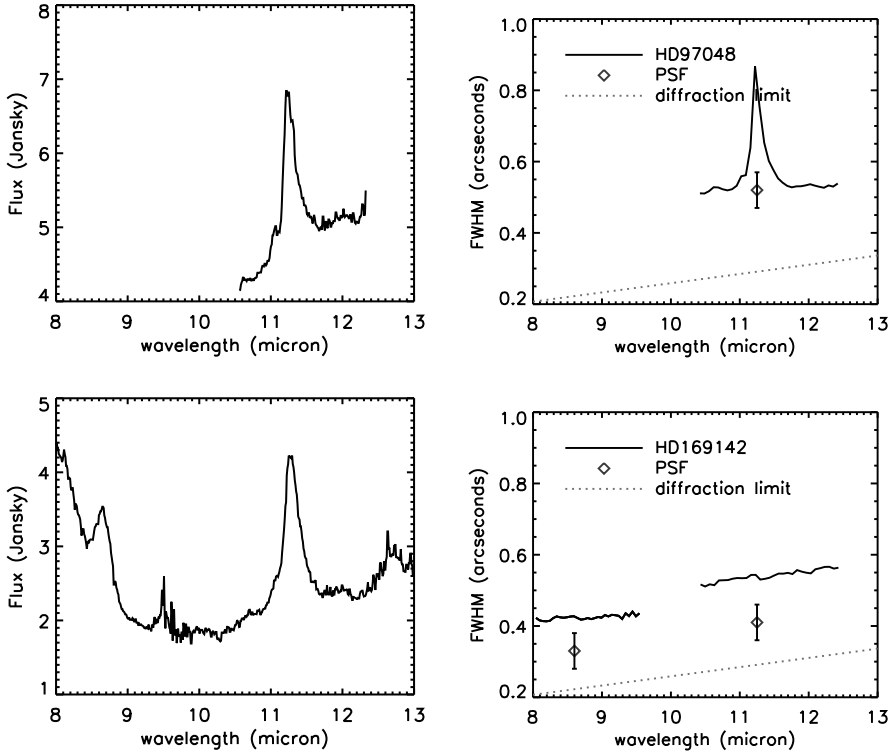

Figure 3.3: *VISIR observations in the N-band. Left: the observed spectra, right: the corresponding FWHM (in arcseconds) as a function of wavelength. Top: HD 97048, bottom: HD 169142. The dotted line shows the diffraction limit for a 8.2 m telescope; the diamonds show the PSF values of the statistical calibrator. The 11.2µm PAH feature in HD97048 is more extended than the continuum (which is unresolved) and as large as the continuum for HD 169142.*

data for study. The four selected stars are listed in Table 6.2 with the adopted spectral types, temperatures, luminosities, visual extinctions, distances, stellar masses, and disk inclinations. The SEDs are bright at mid- to far-infrared and sub-mm wavelengths and all show a similar 'bump' of excess emission at ∼20 micron. Detailed radiative transfer modeling suggests that this kind of SEDs are consistent with disks with partially depleted inner region (i.e., a cavity or a gap), while a wall-like structure at the outer edge of this region can be responsible for the abrupt rise of the SED at MIR (Bouwman et al., 2003, Calvet et al., 2005, Espaillat et al., 2007). In the remainder of this paper, we present and discuss the targets ordered by their sub-mm emission above the photosphere, which is strongest for HD 97048, followed by HD 169142, HD 135344 B and Oph IRS 48. With all other properties being equal, the sub-mm excess can be used as a crude estimate of the total disk mass. Thought we are aware that the sub-mm excess is sensitive for some other properties, such as the differences in stellar temperature, luminosity and the temperatures and opacities in the outer disk, we use the sub-mm excess as a rough indication of its evolutionary position between a massive young flaring disk towards an evolved debris disk.

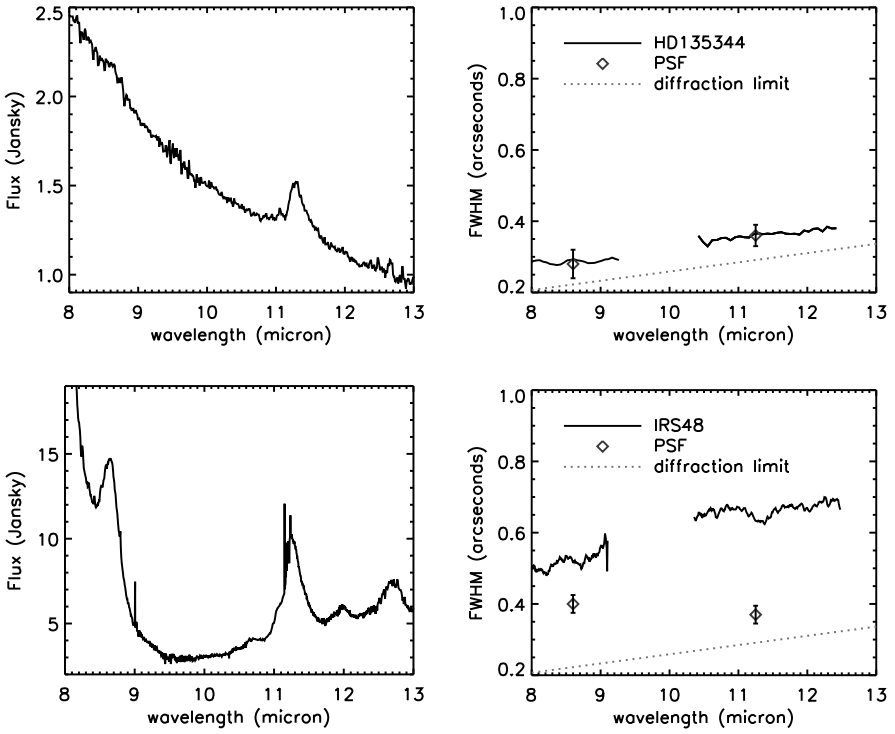

Figure 3.4: *VISIR observations in the N-band. Left: the observed spectra, right: the corresponding FWHM (in arcseconds) as a function of wavelength. Top: HD 135344 B, bottom: Oph IRS 48. The dotted line shows the diffraction limit for a 8.2 m telescope; the diamonds show the PSF values of the statistical calibrator. For HD 135344 B, the continuum and PAH features are both unresolved. The 11.2µm PAH feature is smaller than the continuum in Oph IRS 48.*

3.2.1 HD 97048

TIMMI2 observations by van Boekel et al. (2004) resolved the disk at 8-13 µm. They suggested that the dominating source of continuum emission is from very small carbonaceous grains since thermal emission from grains in the outermost region of the disk are too cold to dominate the SED in the continuum. Resolved VISIR images in the N-band (Lagage et al., 2006, Doucet et al., 2007) showed a detection of the circumstellar disk with an inclination of i $\sim$43° from pole-on. It was shown that the extended PAH emission at 8.6 µm could be explained by surface emission from a hydrostatic disk model with a flaring geometry. HST/ACS V-band images (Doering et al., 2007) revealed scattered light out to a radial distance of $\sim 4''$ in almost all directions. Recent polarimetric differential imaging detected polarized scattered light emission between $\sim 0.1'' - 1.0''$ ($\sim 16 - 160$ AU) (Quanz et al., 2012). No detection of dust depleted inner regions have been yet reported.

Several gas emission lines ([OI], CO, and H2) have been detected and were, at least partly, spectrally and spatially resolved (Acke & van den Ancker, 2006, van der Plas et al., 2009, Martin-Zaïdi et al., 2007, Carmona et al., 2011). The spatial distribution of gas is peculiar: analysis of the CO emission profile shows that the CO gas sets in at greater than

11 AU, while 80% of the [OI] emission originates between $0.8 < R < 20$ AU. This was taken as a possible sign of photo-dissociation of CO in the inner regions and heating by high-energy UV and X-ray photons.

3.2.2 HD 169142

The disk around HD 169142 has been resolved with Subaru/COMICS in the Q-band (Honda et al., 2012). Fitting the Q-band images with radiative transfer models, they derive an inner radius of 23^{+3}_{-5} AU for the outer disk, which is in agreement with SED modeling by Meeus et al. (2010). H-band VLT/NACO polarized light images (Quanz et al., 2013) confirmed this result where it is shown that the inner disk ($\lesssim$ 20 AU) appears to be depleted of scattered dust grains and an unresolved disk rim is imaged at $\sim$25 AU. In addition Quanz et al. (2012) found an extra gap extending from $\sim$40 – 70 AU. Modeling of the 1.3 mm continuum emission and CO line emission shows that the disk has an outer radius of $\sim$235 AU and is viewed close to pole-on with an inclination of i $\sim$13° (Raman et al., 2006, Panić et al., 2008). This is in agreement with scattered light detected out to $\sim$200 AU with differential polarimetry (Kuhn et al., 2001), HST/ASC observations (Grady et al., 2007), and polarized light images (Quanz et al., 2013). The PAH emission feature at 3.3 μm is extended with a FWHM of 0.3″ ($\sim$50 AU) (Habart et al., 2006), though the underlaying continuum is not.

Near-infrared (NIR) excess emission indicates that the inner region (<23 AU) is not empty of dust and gas. Modeling by Honda et al. (2012) favored the idea that an optically thin, but geometrically thick component close to the star is the best dust-solution to model the NIR excess. Detections of [OI] Acke et al. (2005), Hα (Dunkin et al., 1997) and Brγ (Garcia Lopez et al., 2006) emission indicate the presence of gas in the inner disk of HD 169142. Higher resolution interferometric observations are needed for a better understanding of the inner disk.

3.2.3 HD 135344 B

The disk of HD 135344 B (SAO 206462) has recently been imaged in the H-band with Subaru/HiCIAO (Muto et al., 2012). Scattered light components with two small-scale spiral structures are observed close to 0.2″ ($\sim$ 28 AU) from the central star. This result was surprising since SMA sub-mm imaging (Brown et al., 2009) showed a larger inner hole of $\sim$ 39 AU. These different radii of the beginning of the outer disk may indicate different radial distributions of small and large grains (Dong et al., 2012, Pinilla et al., 2012). Observations of CO line profiles (Dent et al., 2005, Pontoppidan et al., 2008, Lyo et al., 2011) indicate an almost pole-on geometry (i $\sim$11°). From 20.5μm imaging, Doucet et al. (2006) derived an outer radius of 200 AU for the dust disk.

Compared to the other sources in our sample, the MIR spectrum of HD 135344 B shows relatively weak PAH features. This has been attributed to its lower stellar temperature and thus lower UV field (e.g. Acke et al. 2010). For our study, HD 135344 B

serves as a perfect comparison object of a protoplanetary disk in which emission from the stochastically heated PAHs and very small grains is significantly weaker.

For the inner disk structure, interferometric N-band observations (Fedele et al., 2008) suggested a much higher inclination (53°–61°) with estimated inner and outer radii of 0.05 and 1.8 AU respectively. Pontoppidan et al. (2008) observed molecular CO gas (λ = 4.7 μm) at 0.3–15 AU. Though variabilities in the NIR (Sitko et al., 2012) may indicate planet-disk interactions, the physical origin of the inner disk remains unclear.

3.2.4 Oph IRS 48

The disk around the Herbig Ae star Oph IRS 48 (WLY 2-48) in the ρ Ophiuchi star formation region was imaged and resolved using VLT/VISIR (Geers et al., 2007a). A distance of 120 pc has been derived for the ρ Ophiuchi star formation region (Loinard et al., 2008). The 18.8 μm image reveals a ring structure with an $\sim 1''$ diameter (120 AU). From the east-west orientation of the continuum image an inclination of 48° was derived. The brightness distribution of the image is not symmetric, the flux on the east side of the star is ∼30% higher than on the west side. The spectral type of A0±3 has been derived from optical spectroscopy by McClure et al. (2010).

The size of the gap is unclear as observations at 18.8 μm dust continuum, PAH emission and 4.6 μm CO all indicate very different gap sizes. Geers et al. 2007b found that the PAH emission at 8.6, 9.0 and 11.2 μm peaks closer towards the central star than the dust continuum ring at 18.8 μm. A study by Brown et al. (2012a) using high spatial and spectral resolution VLT/CRIRES data found vibrationally excited CO gas in a ringlike structure at 30 AU around the star. No CO was found closer than 30 AU from the star. SMA observations by Brown et al. (2012b) show a 12.9 AU inner hole radius at 880 μm. Observations of higher spatial resolution are needed to differentiate between potential scenarios to explain the different radial distributions of CO gas and large and small dust grains.

3.3 Observations

3.3.1 Q-band imaging

All objects in our sample are resolved in the Q-band. An overview of the observed sizes is included in Table 3.2 and Figure 3.5. Images at 24.5μm for HD 97048 and HD 135344 B were obtained with the T-ReCS on the Gemini South telescope on UT 2011 June 28 and 14, and the total integration times were 637 s and 1361 s, respectively. The calibration stars used for PSF measurements were Gamma Cru for HD 97048 and Alpha Cen for HD 135344 B. The filter used for the T-ReCS observation is Qb centered at 24.56 μm ($\Delta\lambda$ = 1.92μm). For T-ReCS imaging data, the chop and nod technique was used. The reduction of the T-ReCS imaging data has been done using the pipeline in the Gemini

Table 3.2: *FWHM sizes*

Object		FWHM 10.5μm [″]	FWHM 11.2μm [″]	FWHM 18.8μm [″]	FWHM 24.5μm [″]
HD 97048	PSF	0.270±0.015 [a]	0.55±0.05[b]	...	0.720±0.006 [e]
	obs	0.330±0.015 [a]	0.83±0.05[b]	...	0.789±0.017 [e]
HD 169142	PSF	0.40 ±0.05[b]	0.33±0.05[b]	0.493±0.006 [d]	0.628±0.007 [d]
	obs	0.50 ±0.05[b]	0.50±0.05 [b]	0.604±0.017 [d]	0.680±0.034 [d]
HD 135344 B	PSF	0.30 ±0.03 [b]	0.30±0.03 [b]	...	0.719±0.004 [e]
	obs	0.30 ±0.03 [b]	0.30±0.03 [b]	...	0.802±0.007 [e]
IRS48	PSF	0.41±0.025[c]	0.41±0.025 [c]	0.5±0.1 [c]	...
	obs	0.66±0.025[c]	0.63±0.025[c]	0.7 ±0.1[c]	...

References: a) Doucet et al. (2007) **b)** Verhoeff (2009) **c)** Geers et al. (2007b) **d)** Honda et al. (2012) **e)** This study

IRAF MIDIR package provided by Gemini. Each observation is accompanied with the PSF (Point Spread Function) references obtained just before or after the main object. In all the PSF data taken with Gemini/T-ReCS in 24.56 μm during the observing runs, the FWHM size is relatively stable ($0.72'' \pm 0.03''$). Images at 18.8 μm and 24.5 μm for HD 169142 were taken from (Honda et al., 2012), which were observed using COMICS on the 8.2 m Subaru Telescope on Mauna Kea, Hawaii. An 18.8μm image of Oph IRS 48 is published in Geers et al. (2007a), which was taken with VISIR on VLT.

3.3.2 N-band VLT/VISIR

During the nights of March 26, 2005 and June 16, 2005, and July 9, 2007, HD 169142, HD 97048, HD 135344 B have been observed respectively with the VLT Imager and Spectrometer for the mid-IR (VISIR, Lagage et al. 2004). These observations were part of the VISIR GTO program on circumstellar disks (see e.g. Verhoeff 2009). Long-slit low-resolution (R≈300) spectroscopy was performed using the 8.8 and 11.4 μm setting with a 0.75arcsec slit in the North-South direction. For HD 135344 B the 8.5 μm setting was used. Standard parallel chopping and nodding was employed with a chopper throw of 8arcsec to correct for the atmospheric background. The observing conditions were good for HD 169142 and HD 135344 in which the airmass was in between 1.0-1.1 and the optical seeing ∼0.6arcsec and ∼0.8arcsec respectively, and poor for HD 97048 in which the airmass was in between 1.6-1.7 and the optical seeing ∼1.3arcsec. The spatial FWHM of the spectra and their PSF was extracted with the method described in Verhoeff et al. (2012). VLT/VISIR data of Oph IRS 48 is taken from Geers et al. (2007b). In this study, we do not fit the absolute sizes of the N-band VISIR observations because of the large uncertainty of the statistical calibrator. However, relative size differences in the observations can be trusted. The spectra and FWHM are shown on Figures 3.3 and 3.4.

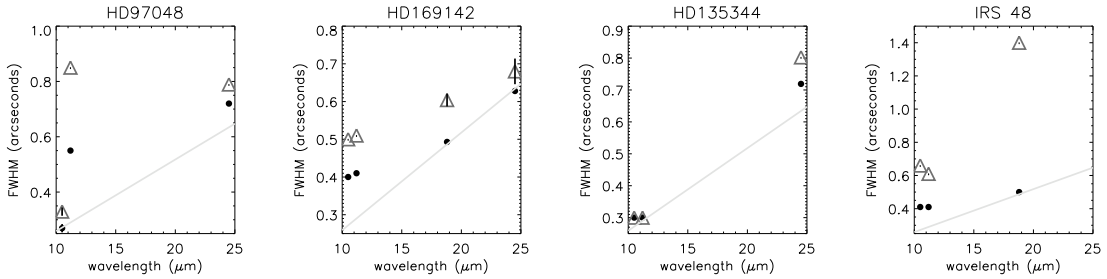

Figure 3.5: *The FWHM of the four targets as function of wavelengths are given by the triangles. Their corresponding PSF is given by the black dots. The FWHM sizes are taken from different observations (references are given in Table 3.2.). The solid line is the FWHM size of the diffraction limit of a 8.2 m telescope.*

3.4 Description of the model

For modeling the disks, we use the radiative transfer tool MCMax (Min et al., 2009). MCMax uses an axially symmetric density setup and performs 3D Monte Carlo radiative transfer using the scheme outlined by Bjorkman & Wood (2001a) to solve the temperature structure and scattering of light in the disk. MCMax has been successfully applied to model observations of protoplanetary disks over a large range of wavelengths and observational techniques (e.g. Verhoeff et al. 2011, Honda et al. 2012). It is successfully benchmarked against a large number of radiative transfer codes (Pinte et al., 2009). The mass accretion rates of the disks that we study is sufficiently low to ignore viscous heating through accretion. Thereby, our only energy source is the central star, which is described by a Kurucz model for the stellar photosphere using the stellar parameters listed in Table 1.

For the radial density profile we use the so-called similarity solution (Hughes et al., 2008, Andrews et al., 2011),

$$\Sigma(r) \propto r^{-p} \exp\left\{-\left(\frac{r}{R_0}\right)^{2-p}\right\}, \tag{3.1}$$

for $r < R_{\rm out}$. Here R_0 is the turnover point from where an exponential decay of the surface density sets in and p sets the power law in the inner region. We fix this to $p = 1$, which is a commonly used value (see e.g. Dullemond et al., 2006). We allow for a gap in the radial surface density profile. We solve for the vertical structure of the disk assuming vertical hydrostatic equilibrium. We assume turbulence is sufficiently high such that the gas and dust are well mixed and there is no size dependent dust settling.

The hydrostatic equilibrium causes the inner edge of a disk to be puffed up, because it is directly irradiated by the central star. This is not only true for the innermost disk edge but also for the inner edge of the outer disk. This allows such a wall to capture and reprocess significant amounts of radiation at a single temperature.

To compute the optical properties of the dust grains in the disk, we use the distribution of hollow spheres (DHS; see Min et al., 2005) with an 'irregularity parameter' $f_{\max} = 0.8$. This method simulates the properties of irregularly shaped particles by breaking the symmetry of a homogeneous sphere. For the grain composition we take a simple dust mixture of 80% silicates (Dorschner et al., 1995, Henning & Stognienko, 1996, Mutschke et al., 1998) and 20% amorphous carbon (Preibisch et al., 1993). Scattered light contribution is included in the total flux, and for simplicity, we have assumed isotropic scattering. Opacities are calculated from the optical constants using a size distribution from a_{min} to a_{max} proportional to $f(a) \propto a^{-p}$. For each object, we choose a maximum grain size of 1 mm and fit the minimum grain size (between 0.1 and 1.0 μm) to the SED. Dust larger than millimeter grains do not leave signatures on the observed SED and are therefore of little relevance. The size distribution of the grains is fitted to the observed spectral slope from the far-IR to the submm using power-laws of $p = -3.5$ and $p = -4.0$. The power-law index is close to the size distributions ($p = -3.5$) of interstellar grains (Mathis et al., 1977).

The PAHs and VSGs optical properties are taken from Draine & Li (2007). The spectral feature profiles of the PAH and VSG models are based on observations that attempt to mimic the spectra for the central regions of galaxies in the SINGS galaxy sample (Smith et al., 2007) at wavelengths $\lambda > 5.5\mu$m. We used a PAH and VSG size of 0.001 μm ($N_{\rm C} \sim 460$) and 0.01μm ($N_{\rm C} \sim 4.6 \times 10^4$) respectively. We have chosen single sized PAHs and VSGs to be able to distinguish their effect to the spectrum. Draine & Li (2007) note that the broad feature seen in the opacity profile of VSG near 30 μm may not apply to realistic carbonaceous grains since the measured absorption in amorphous carbon grains does not appear to show a peak near 30 μm (Tanabe et al., 1983, Mennella et al., 1999). However, studies of well-developed PDRs, such as the Orion Bar and the reflection nebula NGC 2023 have indicated that $\sim 20 - 30$ *Å* VSG ($N_{\rm C} \sim 10^3 - 10^4$) may be responsible for a 25 μm cirrus (Tielens, 2008). There is yet no clear evidence for this broad feature in protoplanetary disks.

In the radiative transfer code, the PAHs and VSGs are treated as transiently heated particles in the temperature distribution approximation. This means that the particles are heated using single photon events. We use the cooling timescale of the particles to determine the average temperature distribution before the next photon hits the particles. In this way, we get a temperature distribution function for these transiently heated grains that can be used to compute their emissivity. This emissivity is used again in the Monte Carlo radiative transfer to include these grains fully self-consistently. This procedure included multiphoton events (i.e., a photon hits the particle before it is fully cooled down), which are important close to the star. Note that it is needed to iterate the procedure to get a self-consistent solution since the emissivity of the PAHs and VSGs depend on the local radiation field that is determined by the radiative transfer. However, convergence is very fast since most of the heating of these grains is done by direct UV radiation from the star.

Examples of the computed optical properties used in our model are shown in Figure 5.5. The halo component in the models consists of 100% carbon. For the disk components, we used a composition of 80% silicates and 20% amorphous carbon in the entire disk. Thus the opacity is dominated by silicate grains in the UV and mid- to far-IR

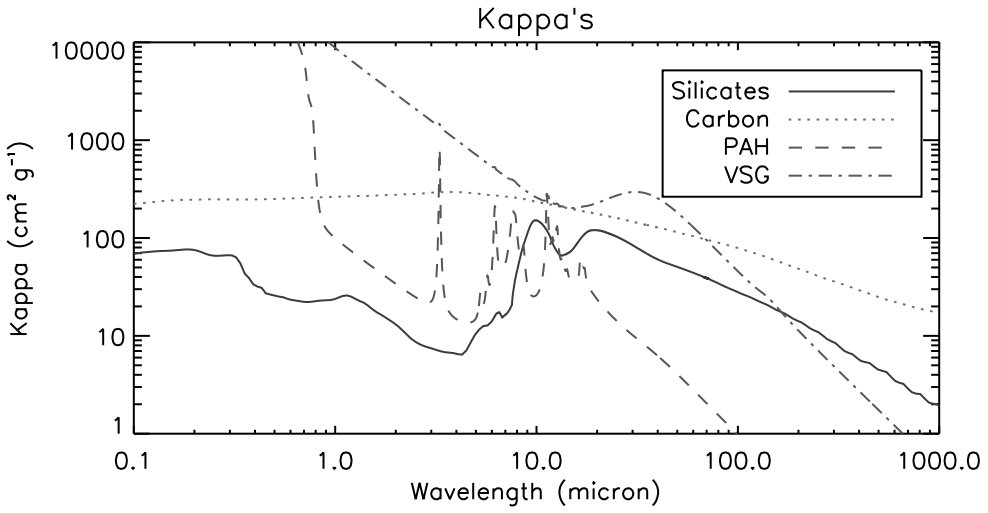

Figure 3.6: *Examples of absorption crosssection per unit mass used in this paper for amorphous olivine (0.1*μ*m – 1mm, $p = -3.5$) and amorphous carbon (0.1*μ*m – 1mm, $p = -3.5$) and PAHs and VSGs with sizes of 0.001 and 0.01* μ*m respectively. The halo consists of 100% carbon. For the disk components, we used a composition of 80% silicates and 20% amorphous carbon in the entire disk.*

wavelength domain while at optical, NIR and mm wavelengths, the carbon grains dominate the opacity.

3.5 The disk size in the Q-band

3.5.1 Modeling goal

Our goal is to reproduce the SEDs and the azimuthally averaged Q-band brightness profile shown in Figures 3.1 and 3.2. In this section, we will first show that a disk with a continuous density distribution fails to fit the data. Instead, a multiple-component disk model, which includes an inner disk or an inner halo, a gap, a wall, and an outer disk fits the observations best. We find that the inner edges of the outer disks are located in a temperature range of $\sim$100–150 K and dominate the emission in the Q-band. Therefore, we robustly constrain the location of this wall by fitting our model to the observed Q-band images. We will discuss the results for each object individually. In the end of this section, we briefly discuss the free parameters, assumptions and other possible degeneracies.

3.5.2 Models with a continuous density distribution fail

It is well known that the model fits to SEDs are highly degenerate in the derived geometry (e.g. Andrews et al. 2011). However, resolved images in the Q-band can break this

degeneracy. Fitting the observed Q-band size provides a solid measurement of the location of the inner edge of the outer disk dominated by micronsized grains. We have explored a wide range of parameters but fail to reproduce the observed Q-band sizes and SEDs using models with a continuous density distribution (i.e., no gap or depleted inner region). Test-modeling shows that the emission at Q-band wavelengths originates in dust located in the inner $\lesssim$10 AU for disks with a continuous density profile from the inner rim at the dust-sublimation radius up to the outer disk. This implies the convolved Q-band sizes of such disk models have a similar size as the PSF and are thus not resolved that for an observation taken with an 8 meter class telescope of a disk located at $\sim$150 pc. For a diffraction limit observation, these sizes are 0.50″ at 18.8 μm and 0.63″ at 24.5 μm. Since all the sources in our sample are significantly resolved in the Q-band images, we consistently fail to reproduce our imaging data with continuous disk models.

Another possible solution to broaden the Q-band size is to include stochastically heated VSG to the disk. For HD 97048, only a very high abundance ($\gtrsim 3 \times 10^{-6}$ $M_\odot$) of VSGs broadens the Q-band image to the observed size. However, this model gives a very bad fit to the shape of the SED: the flux is over-predicted in the MIR range, and the shape of the SED is too flat (i.e., especially since the characteristic emission bump between $\sim$15-30 μm is poorly fitted). For HD 169142 and HD 135344 B, we fail to reproduce the observed Q-band size with any abundance of VSG. We conclude that continuous density models fail to simultaneously fit the SED and Q-band size and consider the gapless disk solution unlikely.

3.5.3 Fitting strategy for a multiple-component disk model

We find that an inner hole/gap (i.e., a depletion of $\gtrsim 10^2$ of the surface density in the inner region) is required to fit the Q-band size and SED. The effect of a gap is that the inner edge of the outer disk has a high surface brightness and a higher temperature at larger distances from the star. The MIR bumps at $\sim$20 μm seen in all SEDs hint that the inner and outer disks are decoupled. These bumps follow the shape of a modified black-body with a temperature of $\sim$150 K, suggesting that a disk component with a similar temperature is dominating the SED. Our fitting procedure can be summarized as follows:

1. Start with a disk with a continuous density profile and fit the Far-Infrared (FIR) to mm photometry to a grain size power-law index of p between 3.0 and 4.0.
2. Make a gap in the disk by decreasing the surface density by 15 orders of magnitude. This will result in a "wall" structure at the inner edge of the outer disk. Choose the radius of the inner edge of the outer disk, so that the convolved model image fits the observed Q-band image size.
3. Put in an optically thick inner disk. This will increase the flux in the NIR but casts a shadow on the outer disk and therefore reduces the flux at MIR and FIR wavelengths.

4. If an optically thick inner disk fails to produce enough NIR flux or casts too much shadow on the outer disk, add or replace with an optically thin inner halo to fit the NIR flux.

5. Choose the minimum size (between 0.1 μm and 1 μm) of the grains in the disk to fit the flux in the MIR and FIR to the SED.

We have tested various different approaches and find that we are able to fit the data by using this procedure using a largely similar set of free parameters and assumptions for the grains and in the physical structure of the disk (see also Section 3.4). This disk fitting procedure allows us to fit all the Q-band images and SEDs (Figures 3.1 and 3.2). The N-band is not yet considered, since there are multiple candidates to be responsible for the emission. These candidates will be discussed in Section 3.6, and it will be shown that we follow a valid approach, since it does not influence the Q-band size.

The spatial resolution and sensitivity of our Q-band data is not sufficient to study the effects of asymmetries in the brightness profile for which could be caused by the inclination or complex structures of the disk wall. Therefore we *azimuthally average* the radial brightness profiles in order to compare the observed and model images (see Figures 3.1 and 3.2). With the assumption that the wall of the outer disk has a vertical shape, we fit the radius of the inner edge of the outer disk, so that the convolved model image fits the observed brightness profile. The model image is convolved with the PSF (i.e., the observed calibration star). The uncertainty in the distance of the objects translates into the dominant uncertainty in constraining the radius of the wall.

The inner disk structure is not well known in Herbig Ae/Be stars. It has been found that the NIR flux is often much higher than expected for an inner dusty disk in hydrostatic equilibrium (Acke et al., 2009). As a solution, we use an optically thin but geometrically thick shell of dust around the star to fit the NIR flux. Replacing the optically thick inner disk with an optically thin halo does not affect the Q-band size of the models. We assume a 100% amorphous carbon distribution in the halo because it has a steep opacity profile and thus gives the best fit to the SED. Alternatively, large ($\gtrsim 10\mu$m) silicate grains or metallic iron can also be used. Although the physical nature of a halo is not yet understood, it has some useful properties. While a puffed up inner disk could also be used as a solution to fit the NIR flux of the disk, test modeling shows that it casts a significant shadow and

Table 3.3: *Best-fit model parameters*

Object	M_{dust} [$M_\odot$]	M_{halo} [$M_\odot$]	$R_{innerdisk/halo}$ [AU]	R_{wall} [AU]	R_{out} [AU]	a [a_{min}, a_{max}]	p
HD 97048	6.0×10^{-4}	...	0.3 - 2.5	34^{+4}_{-4}	500	{0.5μm, 1mm}	-3.5
HD 169142	0.8×10^{-4}	0.31×10^{-12}	0.1- 0.2	23^{+4}_{-4}	235	{0.5μm, 1mm}	-3.5
HD 135344 B	1.0×10^{-4}	0.47×10^{-12}	0.1- 0.3	30^{+4}_{-3}	200	{1.0μm, 1mm}	-4.0
Oph IRS 48	3.0×10^{-5}	0.50×10^{-12}	0.1 -0.3	63^{+4}_{-4}	235	{0.1μm, 1mm}	-4.0

therefore requires the entire outer disk to have a pressure scale-height, which is $\sim 2-3$ times higher than for a hydrostatic disk. A halo does not cast a significant shadow on the outer disk so that the temperature is kept high by direct irradiation and thereby the scale height remains high in the outer disk. We prefer to maintain hydrostatic equilibrium in the outer disks of our models. We note that the use of a halo instead of an inner disk does not have an influence on the derived gap size. See Honda et al. (2012) for more discussion of the use of a halo in our disk modeling. An extended review about the inner regions of protoplanetary disks can be found in Dullemond & Monnier (2010).

Table 3.3 shows an overview of the basic parameters used in our best-fit models. The wavelength range between $\sim 5-14$ μm (including the N-band continuum and PAH emission) is studied in Section 3.6.

3.5.4 Results of the Model Fitting

Below, we review the fitting procedure for each source individually and discuss their uncertainties. The decomposed SEDs and Q-band fits are shown in Figures 3.1 and 3.2, and the radial temperature and density structure are shown in Figure 3.7. The star and disk parameters for the best-fitting models are given in Table 3.3.

3.5.4.1 Best-fit model HD 97048

We find the best-fitting model with the radius of the inner edge of the outer disk set at 34^{+4}_{-4} AU. This is the first time that a disk gap has been reported for HD 97048. An optically thick inner disk with inner and outer radii of $0.3-2.5$ AU fits the NIR flux in a natural way so no halo is required.

We can compare our best-fit model to observations at other wavelengths. Polarimetric differential images in the H and K band by Quanz et al. (2012) show emission from $\sim 0.1''-1.0''$ (~ 16 up to 160 AU). We have computed theoretical images of the disk of HD 97048 in polarized scattered light using the disk parameters derived from the fitting of the SED and the Q-band image. We find that the convolved polarized scattered light image of our best-fit model does not match the observed brightness profile. Up to $\sim 0.175''$, our models predict a reduced brightness due to the gap. At 34 AU ($\sim 0.22''$), our model shows a bump due to the higher surface area of the inner edge of the outer disk. From 55 AU ($\sim 0.35''$), the surface brightness of the outer disk starts to dominate and decreases further as a constant power-law. A possible solution to this discrepancy between the observed scattered light images and our predictions may be that the gap is not entirely empty but filled with small ($< 1\mu$m) particles that scatter efficiently. This solution has been suggested to explain the missing cavities in the polarized scattered light images of transitional disks, while SMA observations detected large gaps (Grady et al., 2013, Dong et al., 2012).

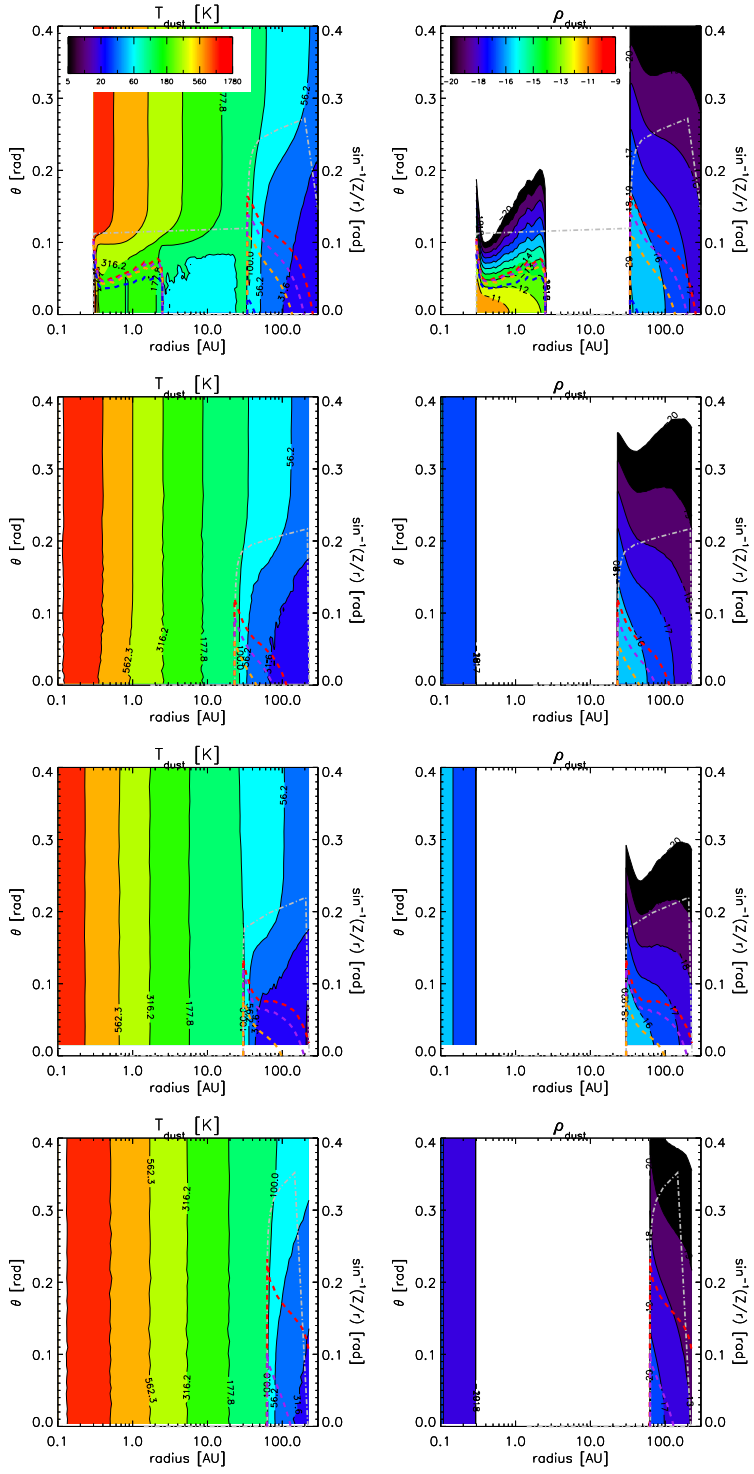

Figure 3.7: *Left: radial temperature distribution (K). Right: density (g cm^3) structures of the disks. Top to bottom: HD 97048, HD 169142, HD 135344 B and Oph IRS 48. The dashed lines represent the $\tau = 1$ surfaces as seen perpendicular from the disk. From top to bottom, the colors are red, purple, orange, and blue and represent the wavelengths 1, 20, 70, and 1000 µm. The gray dot-dashed line shows the $\tau = 1$ surface in radial direction in scattered light ($\lambda = 0.5$ µm). Note that HD 97048 has a thick inner disk, and therefore the radial $\tau = 1$ surface starts at the rim of the inner disk.*

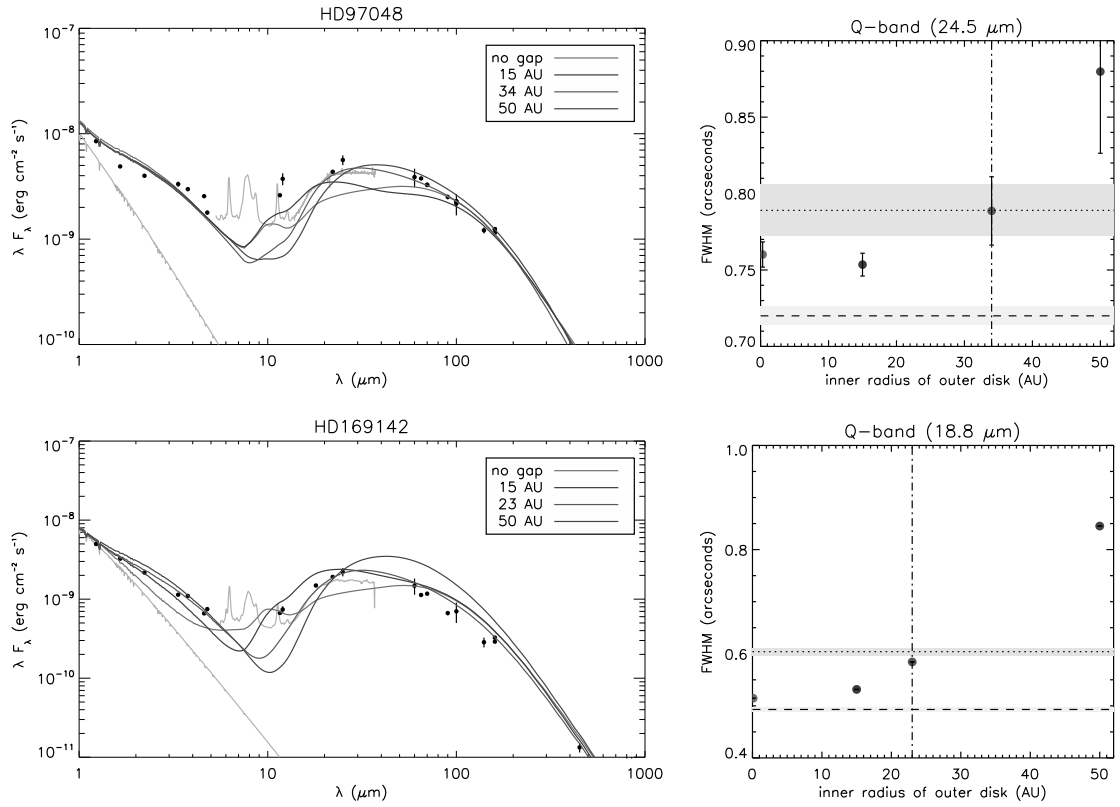

Figure 3.8: *Parameter study showing the SED and Q-band FWHM as a function of the inner radius of the outer disk. Top: HD 97048, bottom: HD 169142. Left: the SEDs of models with a different location of the inner edge of the outer disk. Right: the FWHM sizes of these four models as a function of the location of the outer disk wall, given for the Q-band at 18.8 μm (HD 169142) and 24.5 μm (HD 97048). The horizontal dotted and dashed lines give the FWHM sizes of the observations and calibration stars (PSFs) respectively. The $\pm 1\sigma$ variation in the FWHM as a function of the position angle is given by top and bottom boxes (observation and PSF respectively) and the error bars of the models. The vertical dashed-dotted line shows the chosen parameter of our best-fit model.*

3.5.4.2 Best-fit model HD 169142

The averaged size of the Subaru/COMICS 18.8 and 24.5 μm images are best fitted with the wall of the outer disk set at 23^{+3}_{-5} AU (Honda et al., 2012). We note that this radius is a compromise to the fit to both wavelengths since it predicts a slightly smaller size than observed at 18.8 μm and slightly overpredicts the size at 24.5 μm. The discrepancy between the 18.8 and 24.5 μm observations has been considered in the derived error.

An optically thick inner disk does not produce enough flux to fit the NIR flux in the SED; therefore, we added a halo close to the star. There are currently no other observations in the literature with sufficient spatial resolution to test our results.

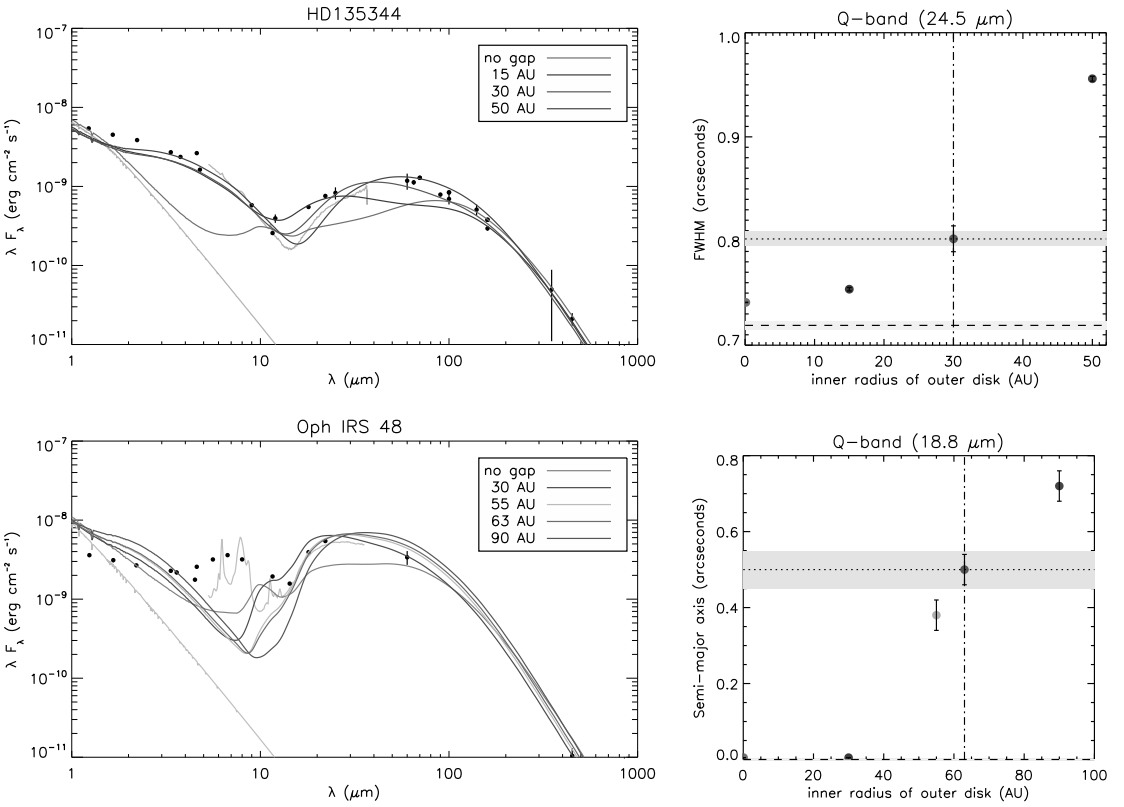

Figure 3.9: *Parameter study showing the SED and Q-band FWHM as a function of the inner radius of the outer disk. Top: HD 135344 B, bottom: Oph IRS 48. Left: the SEDs of models with a different location of the inner edge of the outer disk. Right: the FWHM sizes of these four models as a function of the location of the outer disk wall, given for the Q-band at 18.8 μm (Oph IRS 48) and 24.5 μm (HD 97048). The horizontal dotted and dashed lines give the FWHM sizes of the observations and calibration stars (PSFs) respectively. The $\pm 1\sigma$ variation in the FWHM as a function of the position angle is given by the top and bottom boxes (observation and PSF respectively) and the error bars of the models. The vertical dashed-dotted line shows the chosen parameter of our best-fit model. We note that for Oph IRS 48 the semi-major axis of the MIR image is fitted, but not the FWHM.*

3.5.4.3 Best-fit model HD135344B

The radial brightness profile is best fitted with the inner edge of the outer disk set at 30^{+5}_{-3} AU. The Spitzer spectrum clearly shows two different temperature components. This shape is consistent with the NIR excess originating from a remarkably strong component of T$\sim$1500 K. Since the SED between $\sim$ 5-10 μm follows a Rayleight-Jeans slope, there is no strong contribution in the NIR from lower temperature ($<$1000 K) dust.

Subaru/HiCIAO images by Muto et al. (2012) shows scattered light emission as close as $0.2''$ ($\sim$28 AU) from the star while SMA sub-mm imaging by Brown et al. (2009) showed a gap size of $\sim$39 AU. Our Q-band size is consistent with the HiCIAO disk size. The origin and significance of the differences in derived radii are still unclear. However,

a model solution is easily found, since the Q-band is dominated by micron-sized grains and the sub-mm by large (>100 μm) particles. Removing the millimeter-sized grains in the disk below 39 AU does not affect the fit in the Q-band or the SED.

3.5.4.4 Best-fit model Oph IRS 48

Due to a larger gap size relative to the other stars in the sample, the observed Q-band image of Oph IRS 48 shows a clear extended ring of emission peaking at $\sim 0.55''$ (Geers et al., 2007a) from the center. The radius from the center to the peak of this ring represents the location of the inner edge of the outer disk from the star. We have fitted the inner edge of the outer disk of our model to the radius of the peak position of the observed ring (the semi-major axis). The images are best fitted with the inner edge of the outer disk at 63^{+4}_{-4} AU. We do not attempt to fit the asymmetry in brightness which could be caused by e.g. Rossby wave instabilities (Li et al., 2001) causing axial asymmetries and differences in grain sizes in the disk. The calibration star taken during the observation (the PSF) is of low quality. Therefore we have fitted a Gaussian to the calibration star and used this to convolve the theoretical model image.

The star has a high extinction (Av$\approx$11 – 13) and no photometry is available in the optical, therefore de-reddening introduces a large uncertainty in the luminosity of the star (Brown et al., 2012a, McClure et al., 2010). Since the luminosity directly affects the temperature distribution of the outer disk, this translates to an uncertainty in fitting the SED. Modeling shows, however, that the relative brightness distribution at 18.8 μm is not influenced by a factor of 2-3 higher or lower in stellar luminosity. So the derived wall radius does not change.

We note that the observed radial brightness profile (Figures 3.1 and 3.2) is significantly brighter than our model at a radius of $\sim 0.6 - 0.8''$ from the star. This could be explained by a larger PSF during the observations, a higher stellar luminosity, differences in grain properties as a function of radius or by a complex disk asymmetric structure of the outer disk.

The outer radius of the disk is unknown, so we choose an outer radius of 235 AU similar to HD 169142. The modeling is not sensitive to this choice. SMA observations at 880μm of Brown et al. (2012b) indicate a hole up to ∼13 AU. SMA and new ALMA 690 GHz observations (van der Marel et al. in prep) of this source at sub mm wavelengths are in conflict with each other. While SMA images indicate a hole at 13 AU, there is no indication of this in recent ALMA observations. ALMA reveals a highly asymmetric dust structure, indicating that the SMA image is actually misaligned due to its vertically elongated beam and thus interpreted differently.

3.5.5 Short summary of Q-band analysis

We have applied a similar modeling approach to all four sources and derived the outer radius of the disk gap from the Q-band imaging. The decomposed SEDs (Figures 3.1

and 3.2) show that the wall component (the first 3 AU of the outer disk) dominates the emission at Q-band wavelengths. Therefore, the size of the resolved Q-band images are a sensitive diagnostics for the radius where the emission is emitted. For transition disks with a typical distance of $\sim$150 pc and observed with an 8 meter class telescope, resolved Q-band images can be a good tracer of the gap size if the dust in the wall reaches temperatures of $\sim$100–150 K.

To study the robustness of our results we have performed a parameter study. We have taken the best-fit models and studied the effect of variations in the following parameters: the location of the inner edge of the outer disk, the size of the inner disk, the surface density power-law, the stellar luminosity, the distance, the minimum grain size and the silicate-to-carbon ratio. We discuss the influence of VSG in Section 3.6. We find that the angular size of the Q-band image is only sensitive to the angular size of the wall radius, where, of course, the absolute radius of the wall depends directly on the adopted distance. Figures 3.8 and 3.9 quantify the results of the parameter study on the location where the outer disk starts. The models show that the FWHM of the Q-band generally increases as the inner wall of the outer disk moves outward. The distance uncertainty results in the dominant error on the fit to the radius of the wall, which is typically in the order of a few AU.

3.6 The disk size in the N-band

3.6.1 The origin of emission in the N-band

The spatial resolution of a diffraction-limited observation in the N-band is a factor of two higher than in the Q-band. However, while the flux in the Q-band comes predominantly from micron-sized grains in the wall of the outer disk, the origin of flux in the N-band is more difficult to constrain, since it is a composite of a) thermal dust from the inner and outer disk, b) stochastically heated very small carbonaceous grains (VSGs), and c) polycyclic aromatic hydrocarbons (PAHs). In this section we demonstrate that the N-band cannot be used as a reliable tracer for the gap size.

We use VLT/VISIR data (see section 3.3.2) to study the N-band sizes. Figures 3.3 and 3.4 show the FWHM profiles of the VISIR observations in our sample. From this profile, the radial extent of the 8.6 and 11.2 μm PAH features compared to the continuum can be studied. We study the general trends of the N-band sizes caused by dust, VSGs, and PAHs and study the relation to the disk geometry.

It is important to emphasize that the plateau of continuum emission between the strong PAH features at 8.6 and 11.2 μm is not from PAH emission. This is illustrated by the VLT/VISIR observations of the FWHM profile of HD 97048 in the N-band (see Figures 3.3 and 3.4). The FWHM increases by $\sim$11 μm, peaks at 11.2 μm and decreases back to the continuum size at 11.6 μm. If the plateau of continuum emission at 10.5 μm would also originate in PAH molecules, then the FWHM size would not be different compared to the size at 11.2 μm.

Below, we first discuss two possible origins of continuum emission between the PAH features; thereafter, we compare their sizes with the disk size in the PAH 8.6 and 11.2 μm filters.

3.6.2 Thermal dust continuum

Thermal emission from dust grains with a temperature of ∼200–400 peaks in the N-band. Depending on the stellar temperature, luminosity, the disk structure and grain size, dust of this temperature is typically located in the inner $\lesssim$15 AU in the disk. In the best-fit models of the transitional disks of our sample, we have assumed that the gaps are depleted in dust. Continuum emission in the N-band, therefore, originates in the Rayleight-Jeans and Wiens tails of the inner and outer disk respectively. This is illustrated by the decomposed SEDs in Figures 3.1 and 3.2, in which the separated disk components are shown. In this scenario, the FWHM size in the N-band is a measure for the relative contribution of the inner disk versus the outer disk.

HD 135344 B is not resolved with respect to the PSF. In the decomposed SEDs in Figures 3.1 and 3.2 the flux at 10.5μm for HD 135344 B is dominated by the halo. Since the halo is very close to the star (0.1–0.3 AU), the N-band is also not resolved in our best-fit model and is in agreement with the observations.

The size of the continuum emission in the N-band is influenced by the radial size of the inner disk. In Figure 3.10, we show a small parameter study for HD 97048 in which the outer radius of the inner disk is increased. We compare the FWHM of our models with the (Doucet et al., 2006) observations of HD 97048 since they are of better quality and have a low seeing (their observation of the PSF is diffraction limited). If the contribution from the inner disk becomes larger in the N-band, the FWHM of the model image decreases. For small inner disks of $\lesssim$5 AU, this has no effect on the Q-band size. However, the N-band is nearly as small as the PSF and the Q-band also decreases (see Figures 3.8 and 3.9) for models with a larger inner disk or no gap. We can fit the observed N-band size by choosing an inner disk from 0.3 to 2.5 AU, though an inner disk of this size does not fit the SED (see Figure 3.10).

3.6.3 Continuum emission from Very Small Grains

Besides the inner disk, emission in the N-band can also originate in stochastically heated, very small carbonaceous grains that can be transiently warm far from the star. Similar to PAH molecules, VSG are excited by UV photons and re-emit at longer wavelengths. These very small grains are expected in the size range of ∼20–30 $\AA$. For comparison, recall that a typical 50 C-atom interstellar PAH molecule is ∼6 $\AA$, and the interstellar dust grains have sizes of ∼50–3000 $\AA$ (Tielens, 2005). For a disk with a high abundance of VSGs, the image size is influenced by the radial density distribution of VSGs in the disk

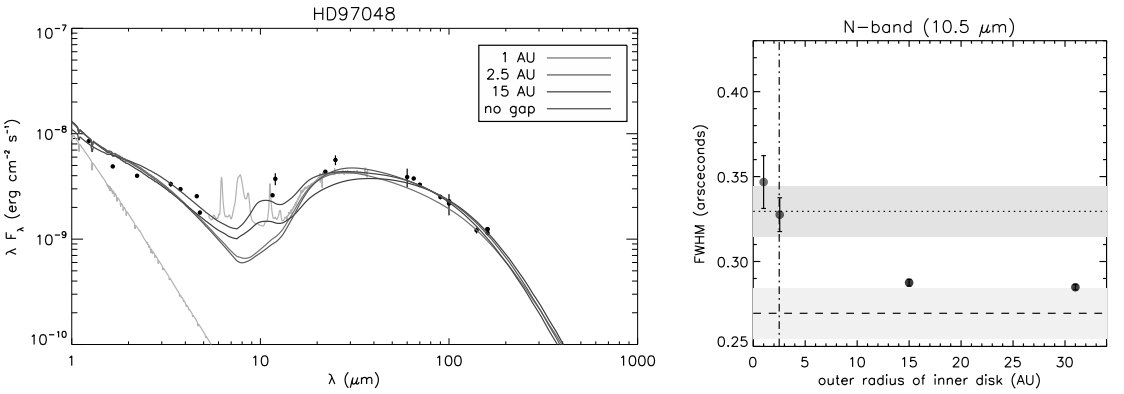

Figure 3.10: *Models of HD 97048 with increasing size for the outer radius of the inner disk. The larger the inner disk, the smaller the N-band size. The top and bottom boxes and the error bars indicate the $\pm 1\sigma$ error on the FWHM of the azimuthally averaged radial brightness profiles for the target and PSF, respectively. Observed data of HD 97048 is from Doucet et al. (2006)*

and the number of UV photons that interact with the VSGs. Thus, the N-band size becomes larger for an increasing abundance of VSG in the outer regions of a protoplanetary disk.

To demonstrate the effect of VSG on the disk size, we have performed a small parameter study using the best-fit model for HD 97048 with a larger (0.3-5 AU) contribution from the inner disk and an abundance of VSGs in the entire disk. Figure 3.11 shows the SEDs and FWHM sizes in the N-band of these models. We can compensate for an increased contribution from a larger inner disk (which makes the disk size in the N-band smaller) by including VSG, which emits at 10 μm in the outer disk and hence fit the observed N-band size (Doucet et al., 2006) as well as the SED. The VSG increase the Q-band size but only negligibly ($\sim 0.005''$). Hence, the derived radii of the outer disks through the analysis of the Q-band (See Section 3.5) is not affected by including or neglecting VSG emission in the Q band.

The spectrum of HD 135344 B serves as an ideal example of an SED with very weak PAH and VSG emission. It has a stellar temperature of 6590 K, and as a result, its UV field is low compared to the other sources in our sample, which may explain the weakness of the PAH features. The contribution of VSG seems low, since all the N-band excess observed in the spectrum is originating from the hot inner disk.

3.6.4 N-band continuum summary

We conclude that it is difficult to constrain the origin of emission in the N-band. An improved fit to the SED and the N-band image was found in Section 3.6.3 for HD 97048 by assuming a larger inner disk size and by including VSG in the modeling. Since we do not have information on the actual size, structure and dust composition of the inner disk however, we are degenerate in determining to what degree thermal dust or VSG are

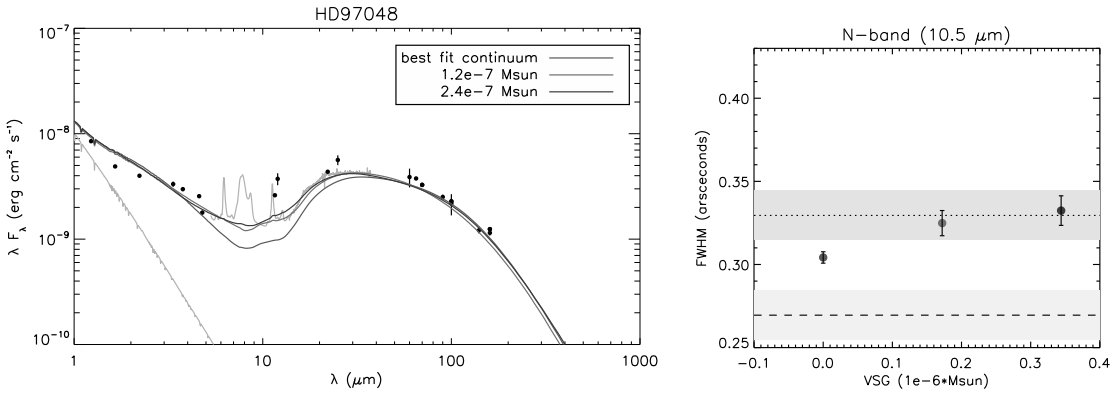

Figure 3.11: *Models of HD 97048 with very small grains added to the disk. We note that a larger inner disk of 0.3-5 AU is chosen in this modeling grid to fit the observations. The higher the abundance of VSG, the larger the N-band size. The top and bottom boxes and the error bars indicate the* $\pm 1\sigma$ *error on the FWHM of the azimuthally averaged radial brightness profiles for the target and PSF, respectively. Observed data of HD 97048 is from Doucet et al. (2006).*

responsible for emission in the SED and the disk sizes in the N-band. Detailed analysis of multiwavelength data with sufficient spatial resolution may provide more insight on this issue. The most important insight of our modeling effort in this section is that the Q-band is a more reliable tracer for disk gaps than the N-band for the sources in our sample (i.e. group Ib Herbig stars at a distance of $\sim$150 pc).

3.6.5 The disk size in the PAH features

PAHs are the carriers of the characteristic features observed in the 5–15μm range. Studies of the relative emission profiles have been carried out to find a relationship between the chemical and physical characteristics of these large molecules (e.g., size, charge state and excitation) and the physical conditions of a region (e.g., density, temperature, radiation field and metallicity). After direct irradiation from the photospheric UV radiation field, PAH molecules presumably located on the surfaces and/or inner rims of protoplanetary disks cool through emission in their mid-IR vibrational modes. PAH molecules are thought to be co-spatial with the gas. PAH emission is often found spatially extended in protoplanetary disks of Herbig stars (van Boekel et al., 2004, Habart et al., 2006). If PAH molecules in the outer disk are illuminated by UV photons, they can be excellent tracers of the outer disk structure. As Lagage et al. (2006) and Doucet et al. (2007) show for HD 97048, imaging in the PAH filter can be used to derive the (flaring) structure of the disk surface.

Using spatially resolved VLT/VISIR observations, we compare the sizes of the PAH emitting regions in the N-band for the objects in our sample. Figures 3.3 and 3.4 show the FWHM plots as a function of wavelength in the N-band. For HD 97048, the FWHM size in the PAH feature is larger than in the continuum as expected. However, this behavior is

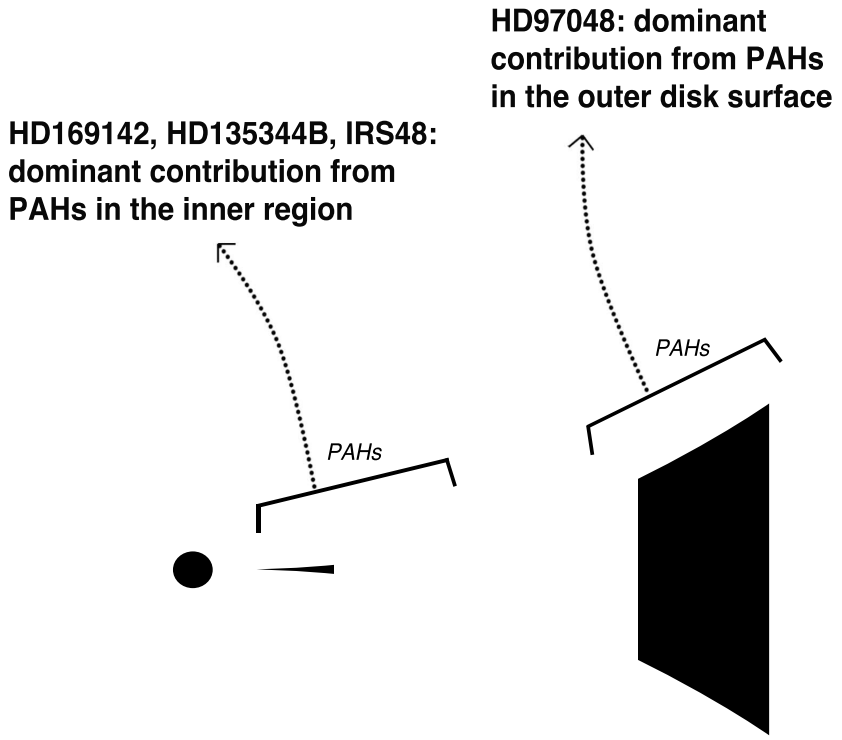

Figure 3.12: *Sketch of a Herbig group Ib star. In the VISIR data, we find that PAH emission in the spectra of HD 169142, HD 135344 B, and Oph IRS 48 is dominated by PAHs located in the inner region (i.e. $\lesssim$50 AU). While in HD 97048, the PAH emission is dominated by PAHs in the outer disk surface (as shown by Lagage et al. 2006, Doucet et al. 2007).*

not observed in the other sources: the sizes of the PAH features in HD 169142 are as large as the continuum; they are unresolved in HD 135344 B; and most surprisingly, the FWHM of the 11.3 μm PAH feature in Oph IRS 48 is smaller than the continuum (Geers et al., 2007b,a). We recall that the 3.3μm PAH feature is extended in HD 97048, HD 169142 and Oph IRS 48 (Habart et al., 2006, Geers et al., 2007b). Can we understand the very different behavior of our sample in the spatial extent of the emission in the PAH bands and the 10 micron continuum?

We have examined the scenario that PAH emission is emitted from the disk surface (i.e., not from the halo). We have fitted the peak fluxes of the observed PAH features by adding PAH molecules in the disk with a fixed abundance with respect to the other dust components. See Section 3.4 for details of the PAH implementation in the radiative transfer code. For HD 97048, HD 169142, HD 135344 B, and Oph IRS 48, the abundance ratio (fraction of total dust mass) fitting the observations are respectively $\{3.5, 5, 10, 100\}$ $\times 10^{-4}$, and the is result in a total mass in PAHs are respectively $\{1.7, 0.4, 1.0, 3.0\}$ $\times 10^{-7}$ $M_{\odot}$. If no VSG are included, we find that the FWHM sizes at the PAH wavelengths are resolved and significantly larger than the continuum. Except for HD 97048, these models are not consistent with the FWHM observations from VISIR. If VSG are included and

have a large contribution to the continuum emission in the N-band as explained in Section 3.6.3, the observed angular size in the PAH band is still larger compared to the continuum. This is because the contrast between the flux from PAHs and the continuum from thermal dust is higher than the contrast between emission from VSG and thermal dust. Therefore, the angular size of the disk is larger in the PAH band than in the N-band continuum for any of these models include PAHs and fit the SED.

For HD 97048, PAH emission has a dominant contribution from PAHs in the outer disk and thus have a larger observed size in the PAH bands of VISIR. A closer look at the brightness distribution of the 11.2μm VISIR image of HD 97048 (Doucet et al., 2007) shows no clear sign of a gap. Instead, it shows a relatively strong inner component between $0-0.2''$ ($0-30$ AU). The PAH model in Doucet et al. (2007), which assumes a continuous density in the disk and no gaps in the inner disk structure, overpredicts the PAH surface brightness of the outer disk by a factor of 2 between $0.2-1.5''$ ($30-240$ AU). This suggests that there is a significant contribution from the inner disk to the PAH flux, so the relative contribution from inner and outer disk to the PAH flux seems to be different from what Doucet et al. (2007) modeled. However, the observed FWHM of the disk in the PAH band still has to come out larger than the continuum.

The VISIR observations of HD 169142 show that the observed FWHM of the continuum and the PAH features are similar in size. The contrast between the size in the PAH filter and the continuum can be decreased, if VSG are added to the disk and dominate the continuum emission in the N-band. In that case, the continuum size also increases and the difference between the size in the PAH filter versus the continuum becomes smaller. However, the addition of VSG does not result in a equal disk size between the continuum and the PAH band; therefore, an extra component of PAHs in the inner disk is needed.

For HD 135344 B, the PAH features are fitted with a higher abundance ratio than for HD 97048. Because the UV field of HD 135344 B is lower, the line fluxes of the PAH features are also weaker. Our disk model with PAH emission dominated by PAHs in the outer disk predicts that the PAH features would be spatially resolved by VISIR. This is, however, not seen in our VISIR data in Figures 3.3 and 3.4 No PAH features were also observed within the correlated flux spectrum of HD 135344 B measured with MIDI (Fedele et al., 2008), leading these authors to draw the conclusion that the PAH emission must be more extended than the continuum (i.e. $\gtrsim$5–10 AU). These measurements can only be reconciled with our VISIR data in a situation in which the bulk of the N-band continuum emission comes from a narrow ring very close to the star (0.05-1.8 AU), and that the emitting PAHs are located in another ring/structure small enough not be be resolved by VISIR outside this region.

In Oph IRS 48, the FWHM of the 11.3 μm PAH feature is even smaller than the continuum (Geers et al., 2007b). Direct imaging observations by VISIR in the PAH band at 11.3 μm Geers et al. (2007a) show that the PAHs are centrally located and do no show a similar ring structure as seen at 18.8 μm continuum, which traces the outer disk. This can only be explained if PAH emission has a higher contribution from PAHs located in the inner regions (possibly from within the gap) compared to PAHs in the surface of the outer disk.

3.6.6 PAH-band summary

Modeling the N-band FWHM sizes of the 11.3 μm PAH feature of our sample has demonstrated that PAH emission is not always dominated by emission from PAHs in the outer disk surface. A strong contribution from PAHs in the inner regions (probably including the gap itself) can explain the small FWHM of the VISIR 11.3 μm PAH feature of HD 169142, HD 135344 B and Oph IRS 48. Measuring the size of a disk in the PAH filter does contain information about the disk size. However, the relative contributions to the total PAH flux from the inner and outer disks can vary strongly from source to source, making PAHs a more complex tracer of disk structure than previously assumed. See Figure 3.12 for a sketch of this geometry.

3.7 Discussion

3.7.1 The weakness of silicate emission features in some sources is caused by large disk gaps

Spectroscopic ISO/SWS (Meeus et al., 2001) and Spitzer/IRS observations (Juhász et al., 2010) revealed that the 10 μm silicate feature is detected in the majority of the Herbig Ae/Be stars (8 out of 53 lack the feature in the Spitzer sample). Flaring and flat objects with silicate features are respectively called group Ia and group IIa; those without silicate features are called group Ib and group IIb. Although this may be a consequence of the limited number of Herbig stars in the sample, objects without evidence of silicate emission are so far *only* found among flaring group I sources.

Until now, it was not well understood how the absence of these features is connected to the physical disk structure. An explanation supported by our study is because of the geometry: the (sub-) micron-sized silicate dust suitable for prominent feature emission (T$\sim$200–400 K) are depleted in the disk due to the large size of inner holes or gaps. Objects *without* silicate features are only found in group I Herbig Ae/Be stars, which suggests that gaps are connected to the flaring geometry. Since we found that Herbig Ae/Be stars in our sample are best fitted with large gaps separating the inner and outer disk, we suggest that a decreasing strength of the silicate feature is related to the severe depletion of (sub-) micron-sized silicate grains of $\sim$200–400 K. Its weakness can serve as a tracer of large dust-depleted inner regions of protoplanetary disks. Figure 3.13 shows a sketch of this scenario for transitional group I objects. Group Ia sources that have a gap show silicate features, because the inner disk (e.g. HD 142527, Verhoeff et al. 2011) and/or the outer disk wall (e.g. HD 100546, Mulders et al. 2011) still have a sufficient amount of silicate dust in the critical temperature regime ($\sim$200–400 K region). In group Ib objects (the objects in our sample: HD 97048, HD 169142, HD 135344B, and IRS 48), our study shows that the silicate dust is severely depleted in this region.

HD 97048 is a prototypical group I source, and so far no gap has been reported. Now that our study finds an inner gap (or a region of lower dust density), it strengthens the case

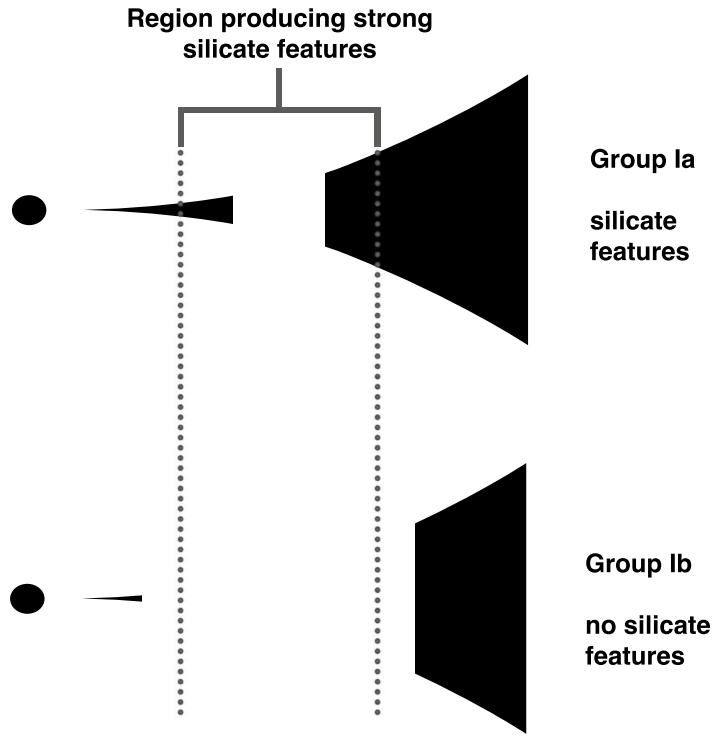

Figure 3.13: *Sketch showing the region where (sub-) micron-sized silicate grains have a temperature (T∼200–400 K) where they produce strong silicate features. Transitional group Ia sources (top) show silicate features, because the inner disk and/or the outer disk wall have a sufficient amount of silicate dust in this region. In the group Ib objects of our sample (bottom), the silicate dust is severely depleted in this region, and thus, no silicate features are produced.*

for disk gaps as the reason for the absence of the silicate features in the spectra of group Ib, and more generally, the classification of group I sources as transitional disks.

3.7.2 Gaps in Herbig Ae/Be objects

It was already suggested by Waelkens et al. (1994) based on SED analysis that disks around Herbig Ae/Be stars may have large gaps separating an inner and outer disk. It was proposed that larger circumstellar bodies could form in these gaps, typically, in the temperature range of 200 to 500 K. With the improved spatial resolution of current telescopes, the prediction of large gaps as a common feature in Herbig Ae/Be stars seems to be confirmed.

Other group I Herbig stars *without* silicate features that are not included in our sample are HD 100453, HD 34282, and HD 141569 (with distances of 112, 164, and 99 parsec, respectively). The first two sources are also resolved in the Q-band by Gemini/T-ReCS

observations (Mariñas et al., 2011). HD 141569 has generated much debate in the literature, but it is now believed that this disk is in transition to a debris disk (Wyatt 2005, Reche et al. 2009). Our analysis outlined in Section 3.5 suggests that significantly resolved Q-band images of Herbig Ib stars indicate disk gaps. Since all Herbig Ib stars are resolved in the Q-band, we suggest that all Herbig Ib objects have similar disk structures with large gaps between the inner and outer disk.

Flaring Herbig Ae/Be stars *with* silicate features and detected gaps are AB Aur (Honda et al., 2010), HD 142527 (Fukagawa et al., 2006, Fujiwara et al., 2006), HD 36112 (Isella et al., 2010), and HD 100546 (Bouwman et al., 2003, Benisty et al., 2010). These stars still do have silicate emission, despite a gap.

In recent years there has been much speculation about Herbig group I objects being transitional disks. However, there are also many flaring Herbig Ae/Be stars for which no gaps are yet reported. Most of these objects are located at larger distances and therefore more difficult to spatially resolve. Other targets are just not yet observed at full resolution and/or have not been subject to detailed radiative transfer analysis.

There is only limited information available on the spatial structure of flat (group II) disks. Mariñas et al. (2011) reported faint extended emission at 12μm from HD 144668 and HD 163296, but no resolved group II objects in the Q-band[1]. The disks of HD 163296 and HD 31648 (MWC 480) are spatially resolved in the sub-mm (Sandell et al., 2011) and observed in scattered light (Wisniewski et al., 2008, Kusakabe et al., 2012); however, no gaps are reported. Since they show the highest sub-mm excess among flat objects and show CO gas lines in the sub-mm (Dent et al., 2005, Mannings & Sargent, 1997, Qi et al., 2011), they are considered as transitional between flaring and flat. UV observations of HD 104237 point also indirectly, towards a small disk; for example, obscuration of a background microjet in the UV constrained the circumstellar disk to $r < 0.6''$ (70 AU). There are no other flat disks identified in the literature with observational evidence of the disk structure beyond $\gtrsim$50 AU.

It is still an open question whether the inner disk structures of flaring group I and flat group II disks are different. However, there are observations that may indicate that flat group II sources could have optically thicker inner disks. First, there are no group II objects *without* silicate features. Thus, group II sources do not seem to have large gaps in the temperature range of ∼200–400 K (see Section 3.7.1). Second, a photometric study of Acke et al. (2009) demonstrated a correlation between higher optically thick inner rims which resulted in lower outer disk brightness due to shadowing effects. This correlation is strongest in flat group II sources suggesting that their inner disks are optically thicker than in flaring group I objects. Third PAH and other gas lines in flat group II sources, such as far-IR CO (Meeus et al., 2012), milimeter CO (Dent et al., 2005) and near-IR H2 (Carmona et al., 2011) emission are much weaker or not present. While a lower far-IR continuum flux can be ascribed to dust settling, it is not yet understood why gas lines are much weaker in group II sources. Opposite to what is observed, modeling by Dullemond et al. (2007a) predicts that PAH features become *stronger* as the dust settles down to the

[1]We follow the classification in Juhász et al. (2010) of HD 34282 as a group Ib source. Thus, no group II source in the sample of Mariñas et al. (2011) is resolved in the Q-band.

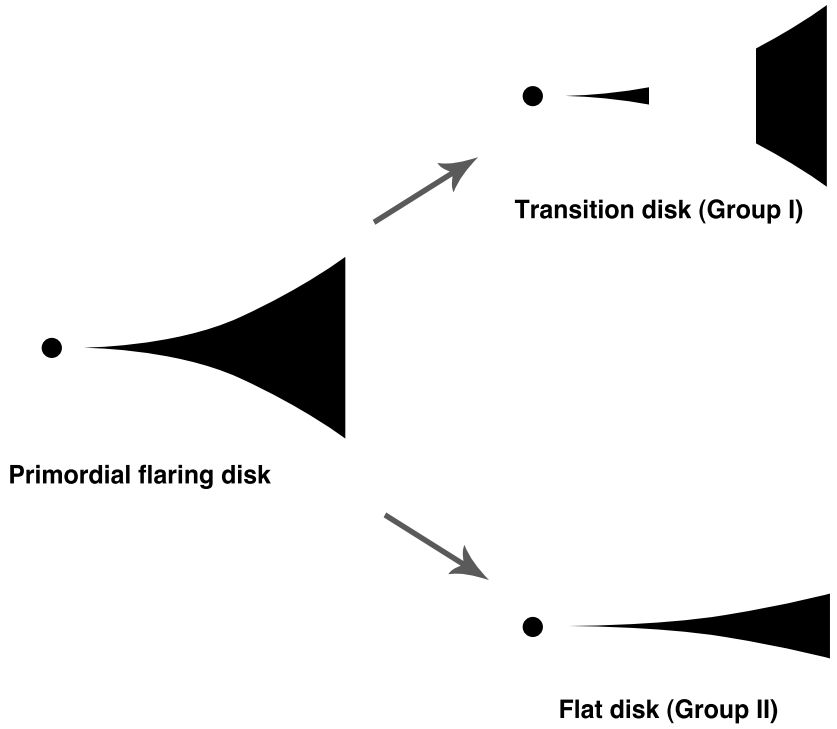

Figure 3.14: *Sketch of an evolutionary scenario for disk evolution in Herbig Ae/Be objects (after Currie 2010). Both groups have evolved from a common ancestor (i.e. primordial, possibly embedded, flaring disk structure). In transitional group I objects, gap formation proceeds the collapse of the outer disk. In group II objects, grain growth and dust settling have flattened the outer disk.*

mid-plane. A possible solution may be that group II sources have optically thicker inner disks casting a greater shadow on the outer disk, thereby reducing the strength of the gas lines and the FIR continuum flux even more.

3.7.3 Consequences for the evolutionary link between group I and group II

While gaps are found in an increasing number of group I Herbig stars, there is no evidence of gaps in group II sources. Since it is likely that the gap is formed by a low mass companion, which is probably a planet (Pollack et al., 1996), this planet will maintain the gap throughout the further evolution of the disk (e.g. Armitage 2007). If group II objects do not have gaps then the evolutionary link from group I to group II is no longer evident. As a solution to this problem, we suggest that a typical 'primordial flaring disk' with a continuous density distribution (i.e. no gaps) in the disk may be a 'common ancestor' for transitional group I and flat group II objects (See the sketch in Figure 3.14). From that starting point, a flaring disk can evolve into transitional group I objects by gap-formation or a self-shadowed group II source in which the outer disk has collapsed. We stress that

this scenario is very speculative but may however help to redefine the evolutionary link between Herbig group I and II sources. A similar scenario for T-Tauri stars has been proposed by Currie (2010).

Not included in Figure 3.14 is the hypothetical possibility of a disk in which both effects are present (planet formation and the collapse of the outer disk). New key questions need to be addressed to understand any putative evolutionary link between group I and group II objects. Can transitional group I sources with large gaps still evolve to flat group II? Or reversely, can flat group II objects become group I sources when/if gaps form? Better constraints on the structure of group II disks by direct imaging are essential to address these issues.

The SED and spectral characteristics of group I sources seem to indicate the dominant presence of a high wall irradiated by the star. As more and more Q-band observations have become available, it has become clear that these walls are indicative of gaps in the disk structure. As we do not observe similar characteristics of walls in group II sources, we infer that these sources do not have disks with gaps.

More insight into the different evolutionary pathways of Herbig stars can be obtained by examining the color-magnitude diagram on Figure 3.15. The objects are taken from the sample of Acke et al. (2010) for which sub-mm photometric data was available. The filled symbols indicate the Herbig stars for which gaps have been reported in the literature. This diagram can be used to compare the inner and outer disk evolution among Herbig stars. The y-axis shows the flux at 1.3 mm that is widely used in estimates for the total disk mass in milimeter grains (e.g., Andrews & Williams 2005, 2007). As disks lose their mass during their evolution, they will move down in this diagram. There is no significant difference between group I (red dots and orange triangles, $F_{30}/F_{13.5} \gtrsim 2.2$) and group II (blue squares) in disk mass. On the x-axis however, the absence of silicate features (orange triangles) is strongly correlated with the MIR spectral index ($F_{30}/F_{13.5} \gtrsim 5.1$), as expected for a disk with a large gap and a vertical wall of T$\sim$100–150 K at the inner edge of the outer disk. Since no gaps have yet been observed in group II objects, it seems unlikely that group Ib objects (with large inner cavities and no silicate features) continue their evolutionary path on this diagram as group IIa objects (with silicate features). Instead, the end-stage of the evolution of a group Ib object is likely to be represented by a group IIb object (though group IIb objects have so far not been identified in infrared spectral surveys of Herbig Ae/Be stars) or a disk/debris system, such as HD 141569.

Candidates for the 'common ancestor' group may be Herbig group Ia objects without gaps. Since many group I objects are too far away to be spatially resolved, improved spatial resolution is needed to identify whether these objects are transitional or have continuous disks. Other candidates are heavily embedded YSOs (i.e. Lada Class I sources). Examples may be present in an ISO study of 46 Herbig Ae/Be stars (Acke & van den Ancker, 2004) where a small sample of six objects has been identified (labeled as group III) and display the amorphous 10 micron feature in absorption. It was believed that these objects possess disks whose luminosity is dominated by viscous dissipation of energy due to accretion. These objects are deeply embedded systems and hence, are fundamentally different from the other sample stars.

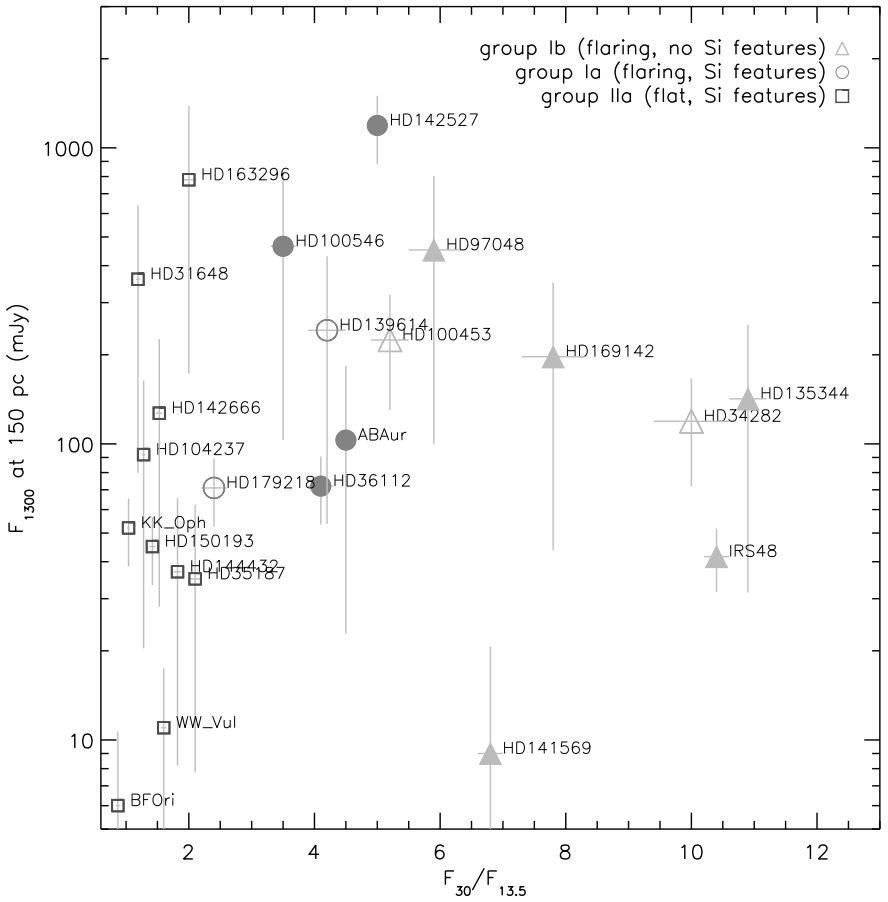

Figure 3.15: *For a sample of Herbig stars, the sub-mm flux at 1.3 mm (normalized at a distance of 150 pc) is compared to the MIR spectral index given by the flux ratio at 30.0 and 13.5 μm. Filled symbols indicate sources for which gaps have been reported in the literature. The sub-mm flux can be used as a proxy for the disk mass while the MIR spectral slope may trace gaps in the temperature range T∼200–400 K. Because gaps are found in most group I objects, the evolutionary link from group I to group II is no longer obvious.*

T-Tauri stars are more numerous than Herbig objects, and therefore, better statistics are available in studies of the SED shape in the context of star and disk properties. In recent Spitzer studies, large samples of T-Tauri stars have been studied (e.g. Cieza et al. 2010, 2012, Currie & Sicilia-Aguilar 2011, Oliveira et al. 2013). SEDs classifications of T-Tauri stars reveal a similar variety as for Herbig Ae/Be stars. Using radiative transfer modeling, these SEDs are identified as objects with large inner cavities, transitional disks with obvious gaps and objects with homologously depleted (flattened) outer disks. However, the dust mineralogy (grain sizes, temperatures and crystallinity fractions) does not show any correlation to either stellar and disk characteristics or mean cluster age in the 1–10 Myr range as shown by (Oliveira et al., 2013).

A variety of effects are thought to be responsible for disk evolution. Such as planet formation (Lissauer 1993, Boss 1997), grain growth and settling (Dullemond & Dominik,

2004b, 2005), photo-evaporation (e.g. Alexander et al. 2006, Gorti et al. 2009), viscous accretion (Hartmann et al., 1998), the magneto-rotational instability (Chiang & Murray-Clay, 2007), and dynamical interactions between the disk and stellar or substellar companions (Artymowicz & Lubow, 1994). The timescales and strengths of these disk clearing mechanisms highly depend on intrinsic disk properties such as initial disk mass, composition and angular momentum. Properties are poorly constrained and likely have a large dispersion. The duration and stability of each evolutionary phase, with either a cleared inner gap or a flattened outer disk are therefore currently one of the main challenges of the disk-evolution field.

3.8 Conclusions

We have modeled the spectral energy distribution and N- and Q-band imaging of type Ib Herbig AeBe stars using the radiative transfer code MCMax. The best-fitting models of the protoplanetary disks indicate that the inner regions of these disks contain large gaps. As a consequence, directly irradiated vertically extended outer disk walls emerge on the inner edge of the outer disk. We conclude:

- We observed HD 97048 and HD 135344 B with the T-ReCS instrument on the Gemini South telescope. Both sources are extended at 24.5μm with respect to the calibration stars. The derived source sizes are $0.789 \pm 0.017''$ and $0.802 \pm 0.007''$, respectively.
- For all four sources in our sample, the observed Q-band sizes require disk models with an inner-hole/gap, making them transitional disks. We fail to model the Q-band images using models with a continuous density distribution (i.e. no gaps). Although SED modeling is degenerate in terms of the source structure, our study suggests that the typical SEDs of Herbig group Ib sources is an indicator of gaps. We find that Q-band images are required to unambiguously infer the presence and sizes of gaps.
- Radiative transfer modeling constrains the radius of the inner edge of the outer disk at 34^{+4}_{-5} AU for HD 97048, 23^{+3}_{-5} AU for HD 169142, 30^{+2}_{-1} AU for HD 135344 B and 63^{+4}_{-4} AU for Oph IRS 48 .
- We have selected Herbig group Ib sources that show a pronounced increase in flux at about 20μm and are resolved in the Q-band. Hence, the emitting dust temperature of the wall is typically ∼100–150 K.
- The absence of silicate features in Herbig Ib objects is a natural consequence of the presence of large gaps in the inner disks of our models. The depletion of dust in the inner regions results in weaker silicate features.
- The observations show that the continuum emission in the N-band is not due to emission in the wings of PAHs. In general, this continuum emission can be due to

VSGs or to thermal emission from the inner or outer disk. For most of our sources, we cannot decide which of these is the dominant source of emission. Therefore, Q-band imaging is a more reliable tracer of gaps.

- Disks with PAH emission do not automatically imply a disk structure, where PAH emission is dominated by PAHs on the surface of the outer disk.
- If the conclusion holds up that all group I sources are transitional and group II sources have no gaps, then the evolutionary link from group I to group II is no longer obvious. A possible solution is that both groups have evolved from a common ancestor (i.e., gapless flaring-disk structure). In transitional group I objects, gap formation has proceeded the collapse of the outer disk while grain growth and dust settling have flattened the outer disk in flat group II objects.

Acknowledgements: *The authors thank Vincent Geers for providing the reduced data from his 2007 papers. K.M. is supported by a grant from the Netherlands Research School for Astronomy (NOVA). Based on observations collected at the European Southern Observatory, Chile under program IDs, 075.C-0540A, 075.C-0540C and 079.C-0602A. M.M. acknowledges funding from the EU FP7-2011 under Grant Agreement nr. 284405. We are grateful to all of the staff members of the Subaru Telescope. We also thank Ms. Hitomi Kobayashi and Dr. Yuji Ikeda at Kyoto-Nijikoubou Co., Ltd. This research was partially supported by KAKENHI (Grant-in-Aid for Young Scientists B: 21740141) by the Ministry of Education, Culture, Sports, Science and Technology (MEXT) of Japan. This publication makes use of data products from the Wide-field Infrared Survey Explorer, which is a joint project of the University of California, Los Angeles, and the Jet Propulsion Laboratory/California Institute of Technology, funded by the National Aeronautics and Space Administration. This publication makes use of data products from the Two Micron All Sky Survey, which is a joint project of the University of Massachusetts and the Infrared Processing and Analysis Center/California Institute of Technology, funded by the National Aeronautics and Space Administration and the National Science Foundation.*

3.9 Appendix A: photometry

Herschel/PACS: For HD 97048 and HD 135344 B far-IR photometry was derived from Herschel/PACS scan maps at 70, 100 and 160 micron. The PACS photometric data were reduced with the mini scanmap pipeline in HIPE version 8.1.0 (calTree version 32). The photometry was extracted using apertures of 12", 15" en 20" for 70, 100 and 160 micron, respectively. The fluxes were aperture and color-corrected, and have a maximum error of 5%, according to the PACS manual.

Other photometry is collected from the literature. The photometric data is presented in Tables 3.4 for HD 97048, 3.5 for HD 169142, 3.6 for HD 135344 B and 3.7 for Oph IRS 48. Upper limits and erroneous data are not included. The photometry is sorted by the central wavelengths of the photometric filters. Magnitudes have been converted to fluxes (in Jansky) for comparison in the SED. The conversion has been done using zero

Table 3.4: *Photometric data HD 97048 (not corrected for extinction) used in this study*

band ID	λ [μm]	F_ν [Jansky]	reference
IUE 15	0.15	0.053 ± 0.001	a
IUE 18	0.18	0.066 ± 0.001	a
IUE 22	0.22	0.054 ± 0.002	a
IUE 25	0.25	0.091 ± 0.002	a
IUE 30	0.30	0.192 ± 0.004	a
Walraven W	0.32	0.163 ± 0.003	b
Johnson U	0.36	0.458 ± 0.010	b
Walraven U	0.36	0.350 ± 0.005	b
Walraven L	0.38	0.724 ± 0.017	b
Walraven B	0.43	1.216 ± 0.014	b
Johnson B	0.44	1.374 ± 0.018	b
Walraven V	0.54	1.531 ± 0.014	b
Johnson V	0.55	1.629 ± 0.015	b
Cousins R	0.64	1.574 ± 0.021	b
Cousins I	0.79	1.667 ± 0.035	b
Near-IR J	1.23	2.280 ± 0.042	b
Near-IR H	1.65	1.967 ± 0.037	b
Near-IR K	2.22	2.301 ± 0.043	b
WISE 1	3.35	3.039 ± 0.195	c
Near-IR L	3.77	3.089 ± 0.146	b
WISE 2	4.60	3.273 ± 0.127	c
Near-IR M	4.78	2.382 ± 0.112	b
WISE 3	11.60	8.690 ± 0.088	c
IRAS 12	12.00	12.88 ± 1.91	d
WISE 4	22.10	27.923 ± 0.332	c
IRAS 25	25.00	40.89 ± 4.99	d
IRAS 60	60.00	67.93 ± 15.64	d
AKARI S65	65.00	71.36 ± 2.40	e
PACS 70	70.00	66.91 ± 3.35	f
AKARI S90	90.00	66.04 ± 3.80	e
PACS 100	100.00	66.75 ± 3.34	f
IRAS 100	100.00	63.54 ± 16.45	d
AKARI S140	140.00	49.58 ± 3.72	e
AKARI S160	160.00	53.67 ± 3.56	e
PACS 160	160.00	58.21 ± 2.91	f
1300 micron	1300.00	0.452 ± 0.352	g

References: a) IUE archival data **b)** de Winter et al. 2001 **c)** WISE All-Sky Data Release **d)** IRAS Point-source catalogue **e)** AKARI/IRC mid-IR all-sky Survey **f)** This paper **g)** Henning et al. 1994

magnitudes provided in the instrument documentations and, where possible the spectral index were considered. The photometry listed in the tables is not corrected for extinction, while the photometry presented in the SEDs in Figures 3.1 and 3.2 are corrected, according to the stellar extinction given in Table 6.2, the parameter $R = 3.1$ and the extinction law presented in Fitzpatrick (1999).

Table 3.5: *Photometric data HD 169142 (not corrected for extinction) used in this study*

band ID	λ [μm]	F_ν [Jansky]	reference
ANS 15	0.15	0.002 ± 0.0002	a
ANS 18	0.18	0.077 ± 0.001	a
ANS 22	0.22	0.163 ± 0.003	a
ANS 25	0.25	0.199 ± 0.004	a
Walraven W	0.32	0.566 ± 0.012	b
ANS 33	0.33	0.519 ± 0.010	a
Johnson U	0.36	0.841 ± 0.019	c
Walraven U	0.36	0.758 ± 0.011	b
Walraven L	0.38	1.183 ± 0.028	b
Walraven B	0.43	1.794 ± 0.021	b
Johnson B	0.44	1.986 ± 0.026	c
Walraven V	0.54	2.084 ± 0.019	b
Johnson V	0.55	2.207 ± 0.020	c
Cousins R	0.64	1.963 ± 0.026	c
Cousins I	0.79	2.004 ± 0.041	c
Near-IR J	1.23	1.828 ± 0.034	c
Near-IR H	1.65	1.667 ± 0.031	c
Near-IR K	2.22	1.534 ± 0.029	c
WISE 1	3.35	1.238 ± 0.047	d
Near-IR L	3.77	1.349 ± 0.064	c
WISE 2	4.60	0.995 ± 0.021	d
Near-IR M	4.78	1.172 ± 0.055	c
WISE 3	11.60	2.575 ± 0.028	d
IRAS 12	12.00	2.95 ± 0.29	e
AKARI S18	18.00	8.90 ± 0.23	f
WISE 4	22.10	14.021 ± 0.103	d
IRAS 25	25.00	18.39 ± 2.24	e
IRAS 60	60.00	29.57 ± 6.81	e
AKARI S65	65.00	24.45 ± 0.10	f
PACS 70	70.00	27.35 ± 0.03	g
AKARI S90	90.00	19.99 ± 1.23	f
IRAS 100	100.00	23.37 ± 6.74	e
AKARI S140	140.00	13.32 ± 1.89	f
AKARI S160	160.00	15.47 ± 0.46	f
PACS 160	160.00	17.39 ± 0.05	g
450 micron	450.00	2.00 ± 0.275	h
800 micron	800.00	0.553 ± 0.431	c
850 micron	850.00	0.40 ± 0.02	h
1100 micron	1100.00	0.286 ± 0.223	c
1300 micron	1300.00	0.197 ± 0.153	c
2000 micron	2000.00	0.070 ± 0.079	c

References: a) a) IUE archival data **b)** van der Veen et al. 1989 **c)** Sylvester et al. 1996 **d)** WISE All-Sky Data Release **e)** IRAS Point-source catalogue **f)** AKARI/IRC mid-IR all-sky Survey **g)** Meeus et al. 2010 **h)** Di Francesco et al. 2008

Table 3.6: *Photometric data HD 135344 B (not corrected for extinction) used in this study*

band ID	λ [μm]	F_ν [Jansky]	reference
Johnson U	0.35	0.414 ± 0.009	a
Johnson B	0.44	1.023 ± 0.014	a
Johnson V	0.55	1.393 ± 0.013	a
Cousins R	0.64	1.633 ± 0.022	a
Cousins I	0.79	1.862 ± 0.039	a
Near-IR J	1.23	2.060 ± 0.038	a
Near-IR H	1.65	2.365 ± 0.044	a
Near-IR K	2.22	2.766 ± 0.051	a
WISE 1	3.35	2.967 ± 0.183	b
Near-IR L	3.77	2.923 ± 0.138	a
WISE 2	4.60	3.994 ± 0.169	b
Near-IR M	4.78	2.564 ± 0.121	a
AKARI S09	9.00	1.727 ± 0.063	c
WISE 3	11.60	0.990 ± 0.013	b
IRAS 12	12.00	1.57 ± 0.19	d
AKARI S18	18.00	3.29 ± 0.014	c
WISE 4	22.10	5.571 ± 0.056	b
IRAS 25	25.00	6.89 ± 1.21	d
IRAS 60	60.00	23.59 ± 5.43	d
AKARI S65	65.00	24.41 ± 1.68	c
PACS 70	70.00	30.00 ± 1.50	e
AKARI S90	90.00	23.65 ± 1.23	c
PACS 100	100.00	28.01 ± 1.40	e
IRAS 100	100.00	23.15 ± 3.43	d
AKARI S140	140.00	23.73 ± 3.81	c
AKARI S160	160.00	15.69 ± 0.95	c
PACS 160	160.00	20.21 ± 1.01	e
350 micron	350.00	5.794 ± 4.509	f
450 micron	450.00	3.175 ± 0.575	a
800 micron	800.00	0.569 ± 0.443	a
850 micron	850.00	0.489 ± 0.024	a
1100 micron	1100.00	0.208 ± 0.162	a
1300 micron	1300.00	0.142 ± 0.110	a

References: **a)** Sylvester et al. 1996 **b)** WISE All-Sky Data Release **c)** AKARI/IRC mid-IR all-sky Survey **d)** IRAS Point-source catalogue **e)** This paper **f)** Gezari et al. 1999

Table 3.7: *Photometric data Oph IRS 48 (not corrected for extinction) used in this study*

band ID	λ [μm]	F_ν [Jansky]	reference
2MASS J	1.24	0.0946 ± 0.0025	a
2MASS H	1.66	0.3050 ± 0.0182	a
2MASS K	2.20	0.6182 ± 0.0146	a
WISE 3.3	3.35	1.294 ± 0.062	b
IRAC 1	3.60	1.400 ± 0.075	c
IRAC 2	4.50	1.630 ± 0.082	c
WISE 4.6	4.60	2.454 ± 0.102	b
IRAC 3	5.60	4.050 ± 0.022	c
ISOCAM	6.70	5.87 ± 0.110	d
IRAC 4	8.00	6.530 ± 0.035	c
WISE 11	11.60	6.262 ± 0.069	b
ISOCAM	14.30	6.49 ± 0.099	d
AKARI S18	18.00	21.04 ± 0.049	e
WISE 4	22.10	36.472 ± 0.467	b
IRAS 60	60.00	65.46 ± 13.01	f
450 micron	450.00	1.56 ± 0.39	g
850 micron	850.00	0.18 ± 0.01	g
1300 micron	1300.00	0.06 ± 0.01	g

References: **a)** 2MASS All-Sky Catalog of Point Sources **b)** WISE All-Sky Data Release **c)** Cieza et al. 2009 **d)** Bontemps et al. 2001 **e)** AKARI/IRC mid-IR all-sky Survey **f)** IRAS Point-source catalogue **g)** Andrews & Williams 2007

CHAPTER 4

Large gaps in the transitional disks of HD 100453 and HD 34282. Connecting gap sizes to spectral energy distributions

S. Khalafinejad, K. M. Maaskant, N. Mariñas, A.G.G.M Tielens
Submitted to Astronomy & Astrophysics

Abstract

The formation of gaps in protoplanetary disks is one of the most important signposts of disk evolution and possibly the formation of planets. We aim to characterize the 'flaring' disk structure around the Herbig Ae/Be stars HD 100453 and HD 34282. Their spectral energy distributions (SEDs) show an emission excess between $15-40$ μm, but very weak (HD 100453) and no (HD 34282) signs of the 10 and 20 μm amorphous silicate features. We investigate whether this implies the presence of large gaps. Spatially resolved mid-infrared Q-band images taken with Gemini North/MICHELLE are investigated. We perform radiative transfer modeling and examine the radial distribution of dust. We simultaneously fit the Q-band images and SEDs of HD 100453 and HD 34282. Our solutions require that the inner-halos and outer-disks are separated by large dust depleted gaps. The inner edges of the outer disks of HD 100453 and HD 34282 have temperatures of ~ 160 K and ~ 60 K respectively. Because of the high surface brightnesses of these walls, they dominate the emission in the Q-band. Their radii are therefore well constrained at 17^{+2}_{-2} AU and 79^{+31}_{-17} AU, respectively. HD 100453 and HD 34282 have large disk gaps. We find that the locations and sizes of disk gaps are connected to the SED, as traced by the mid-infrared flux ratio $F_{30}/F_{13.5}$. The absence of amorphous silicate features in the observed SEDs is caused by the depletion of small ($\lesssim 1$ μm) silicate dust at temperatures above $\gtrsim 160$ K.

4.1 Introduction

Transitional disks have dust depleted gaps and inner holes in their dust distribution and form a special class of protoplanetary disks (Williams & Cieza, 2011). The presence of gaps and inner holes may be indicators that planets are forming in the disks. To search for evidence of planet formation and characterize their physical and chemical conditions, the location and sizes of gaps in protoplanetary disks have to be investigated.

Transitional disks can be identified on the basis of their low near infrared excess (e.g. Calvet et al. 2005, Espaillat et al. 2007, Najita et al. 2007). Analysis of their spectral energy distribution (SED) may indicate that their inner regions are depleted of dust. However, modeling the radial disk structure by fitting only the SED is highly degenerate. Direct imaging of a protoplanetary disks is essential to derive the radial and azimuthal density structure. High spatial resolution observations of transitional disks reveal complex disk structures and can be used to study the interaction between gaps and proto-planets (e.g. van der Marel et al. 2013, Casassus et al. 2013, Quanz et al. 2013). Characterizing the connection between the radial structure and the SED is thus important to gain insight in the role of planet formation in the evolution of protoplanetary disks.

Herbig Ae/Be stars are intermediate mass stars with circumstellar disks (e.g. Natta et al. 2007). The SEDs of Herbig Ae/Be stars fall apart into two groups (Meeus et al., 2001). Group I, with strong excess at mid- to far-infrared wavelengths, and group II, without strong excess at mid- to far-infrared, but with a remarkable similarity in spectral shape. A first interpretation for the evolutionary link between these groups was proposed by Dullemond & Dominik (2004b, 2005). These authors suggested that grain growth and settling cause the mid- to far-infrared excess to decrease. It was proposed that in this scenario, the disk structure evolves from flaring (group I) to flat (group II). However, recent studies indicate that almost all group I objects have large gaps (Grady et al., 2005, Honda et al., 2012, Maaskant et al., 2013). This implies that it is unlikely that group I sources with large gaps can evolve to group II disks, where no large gaps are found. To solve this issue, Maaskant et al. (2013) suggested that both groups evolve from a primordial continuous flaring disk, but may follow different pathways. The disks of group I objects are flaring/transitional due to the formation of large gaps. The disks of group II objects are self-shadowed because grain growth and vertical settling have flattened the outer disk.

In this paper, we investigate spatially resolved direct imaging mid-infrared observations of two protoplanetary disks presented in Mariñas et al. (2011). As these images are most sensitive to thermal emission of micron sized grains, they are suitable to study the radial density structure of transitional disks with large dust depleted gaps. To derive the properties of the disk, we perform a similar analysis of Q-band images as carried out in Maaskant et al. (2013).

The content of this paper is outlined in the following way. In Section 4.2, we introduce the Herbig stars HD 100453 and HD 34282. In Section 6.2 we discuss the Q-band observations and photometric properties of our sample. Section 4.4 describes the radiative transfer code MCMax and the dust model. In section 5.4 we derive the properties of the

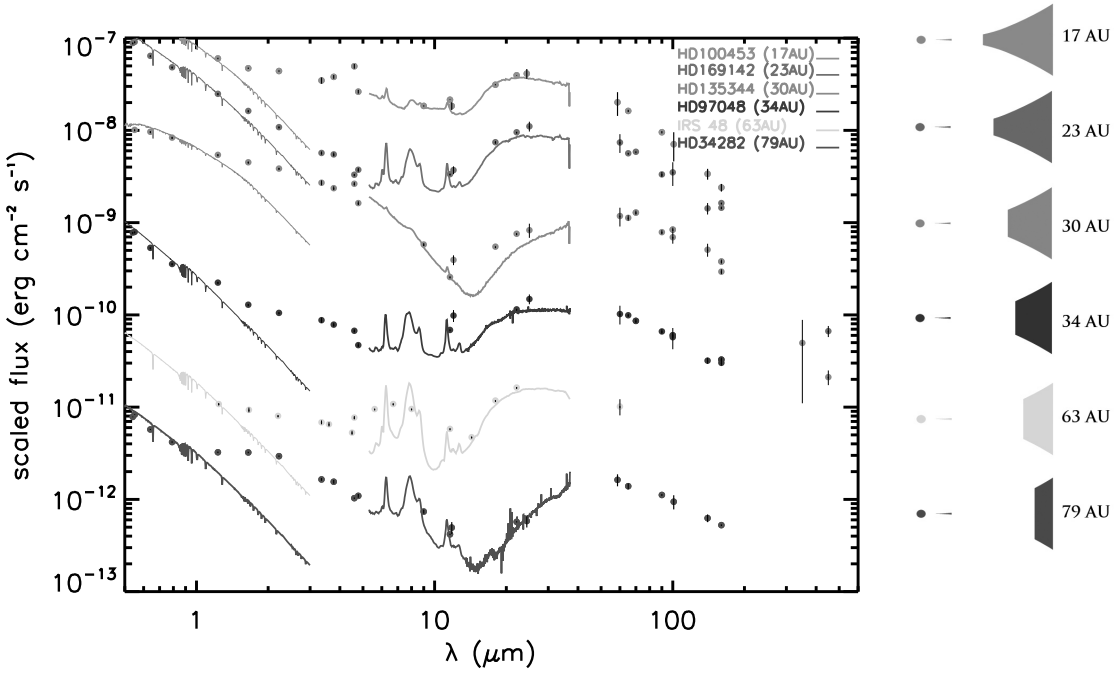

Figure 4.1: *The SEDs of group Ib Herbig Ae/Be stars in the sample of Maaskant et al. (2014). There is a great similarity in the shape of the SEDs. The fluxes are scaled so that the objects are sorted by gap size, with the smallest gap radius on top and the largest gap radius on the bottom. The flux scaling factors for the objects from top to bottom are respectively 10, 5, 1, 0.03, 0.003, 0.003.*

disk structures and constrain the radii of the inner edges of the outer disks. The discussion and conclusions are given in Sections 6.6 and 6.7.

4.2 The sample

The Herbig Ae/Be objects HD 100453 and HD 34282 are studied in this paper. In this section, we present a brief summary. The SEDs of HD 100453 and HD 34282 are characterized by a strong excess of MIR emission at $\sim 15-40\ \mu$m (Figure 4.1). HD 100453 may show a very weak sign of amorphous silicate features (Figure 4.2), while in HD 34282 they are totally absent. The spectra of HD 100453 and HD 34282 show PAH emission bands. Their $I_{6.2}/I_{11.3}$ feature ratios are respectively 2.25 and 1.82 and relatively high, possibly indicating optically thin gas flows through the disk gaps (Maaskant et al., 2014).

4.2.1 HD 100453

HD 100453 is thought to be in transition between a gas rich protoplanetary disk and a gas poor debris disk (Collins et al., 2009). Observations of spatially resolved Q-band imaging (Mariñas et al., 2011), the SED and the absence of the silicate feature are indications

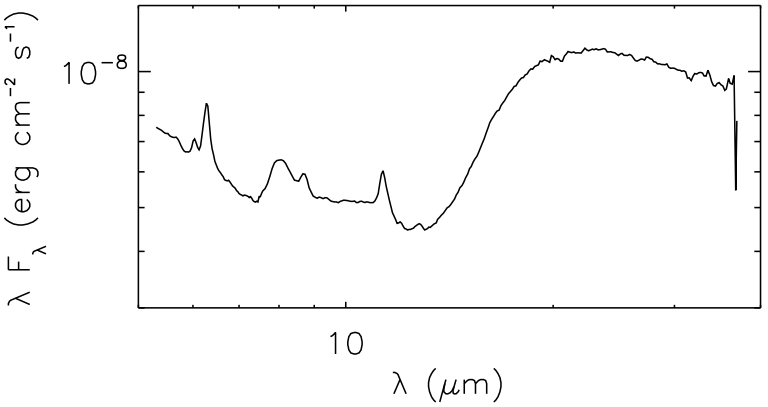

Figure 4.2: *A close up of the Spitzer/IRS spectrum of HD 100453 shows a tentative detection of the 10 and 20 μm silicate features.*

of a gap Maaskant et al. (2013). HD 100453 has a close M-type companion (projected distance of 120 AU), the connection of the companion with the disk structure is not well understood (Collins et al., 2009). The stellar properties are taken from Meeus et al. (2001), where a the distance 114^{+11}_{-9} pc is adopted based on Hipparcos measurements.

4.2.2 HD 34282

Acke et al. (2009) already suggested that the disk around HD 34282 has a large opacity gap based on the near IR excess and far IR color. Rotational J=3-2 CO emission (Greaves et al., 2000), but no rovibrational CO emission (Carmona et al., 2005) was detected in this source, which is consistent with an evacuated inner disk but gas rich outer disk. We adopt the stellar properties derived by Merín et al. (2004) putting this source at a distance of 348^{+129}_{-77} pc.

4.3 Observations

We collect data of HD 100453 and HD 34282 which we use for the analysis of this paper. The SEDs and Q-band radial brightness profiles (RBPs) are shown in Figures 4.3 and 4.4. In addition, we compare these two objects to other similar transitional disks of the sample of Herbig stars presented in Maaskant et al. (2013, 2014).

4.3.1 Data

HD 100453 and HD 34282 were observed as part of a larger high-resolution imaging survey of protoplantary disks around Herbig Ae/Be stars (Mariñas et al., 2011). Q-band

Table 4.1: *Stellar parameters used in this study. The parameters of HD 100453 are taken from van den Ancker et al. (1998) and the stellar properties of HD 34282 are taken from Merín et al. (2004).*

parameter	unit	HD 100453	HD 34282
R.A.	(J2000)	11:33:05.58	05:16:00.48
Dec.	(J2000)	-54:19:28.5	-09:48:35.4
T	K	7400	8625
L_*	$L_\odot$	10.0	13.6
d	pc	114^{+11}_{-9}	348^{+129}_{-77} pc
M_*	$M_\odot$	1.66	1.59

images (18.1 μm, $\Delta\lambda = 1.1$) were obtained using MICHELLE on the Gemini North telescope on February 2^{nd}, 2006 for HD100453 and December 4^{th}, 2003 for HD34282. The pixel scale of the observations was $0.089''$. The standard chop-and-nod technique was used to remove thermal background from the sky and the telescope. A point-spread-function (PSF) star, selected from the Positions and Proper Motions (PPM) Catalogue, was observed before and after each science target observation to assess image quality. Mid-infrared standard stars Sirius and HD133774 were used for image calibration and airmass correction. All data was reduced using IDL (Interactive Data Language). The observations of the disks around the Herbig stars HD 100453 and HD 34282 are resolved with respect to their point spread functions derived from observations of the calibration stars with FWHM sizes of respectively $0.23 \pm 0.06''$ and $0.34 \pm 0.07''$. For all observational details we refer to Mariñas et al. (2011).

The MIR spectra of the disks are obtained by the Spitzer/IRS telescope and are adopted from Juhász et al. (2010) and Acke et al. (2010). The photometric data is taken from the literature and shown in Tables 4.2 and 4.3. The central star is described by a Kurucz model with the stellar parameters presented in table 4.1. Figures 4.3 and 4.4 show the SEDs and RBPs. The inclination of the disks are not well constrained, therefore we have adopted inclinations of 45 degrees for both sources.

4.3.2 The SEDs of transitional disks

The mid-IR parts of the SEDs of group Ib Herbig Ae/Be stars show similar shapes (see Figure 4.1). All objects show an emission bump at $\sim$20 μm and PAH features. In HD 100453, a weak signature of the amorphous 10 and 20 μm silicate features can be seen (Figure 4.2). All other sources show no sign of amorphous silicate features. In the next section we will characterise the gaps in the disks of HD 100453 and HD 34282 and confirm that the weakness of the silicate feature is connected to the presence of large gaps. The detailed shape of the SED is degenerate as it depends on parameters such as temperature and density structure as well as the composition of the disk. Though, the 'bump' in the the SED at MIR wavelengths for these objects is an indicator of large gaps in the disks

Table 4.2: *Photometric data HD 100453 (not corrected for extinction) used in this study*

band ID	λ [μm]	F_ν [Jansky]	reference
IUE 15	0.15	0.002 ± 0.000	a
IUE 18	0.18	0.066 ± 0.001	a
IUE 22	0.22	0.167 ± 0.003	a
IUE 25	0.25	0.172 ± 0.003	a
IUE 30	0.30	0.503 ± 0.009	a
Johnson U	0.36	1.079 ± 0.025	b
Johnson B	0.44	2.717 ± 0.036	b
Johnson V	0.55	2.993 ± 0.028	b
Near-IR J	1.23	2.433 ± 0.045	b
Near-IR H	1.65	2.571 ± 0.048	b
Near-IR K	2.22	3.237 ± 0.060	b
WISE 1	3.35	3.868 ± 0.304	c
Near-IR L	3.77	4.766 ± 0.225	b
WISE 2	4.60	7.582 ± 0.441	c
Near-IR M	4.78	4.180 ± 0.197	b
AKARI S09	9.00	5.518 ± 0.077	d
WISE 3	11.60	8.308 ± 0.053	c
IRAS 12	11.80	7.234 ± 0.698	e
AKARI S18	18.00	18.740 ± 0.248	d
WISE 4	22.10	29.131 ± 0.187	c
IRAS 25	25.00	33.533 ± 4.092	e
IRAS 60	60.00	39.379 ± 11.351	e
AKARI S65	65.00	35.230 ± 0.965	d
AKARI S90	90.00	28.650 ± 0.812	d
IRAS 100	100.00	23.822 ± 8.313	e
AKARI S140	140.00	15.770 ± 2.120	d
AKARI S160	160.00	12.810 ± 1.220	d
SIMBA 1.2 mm	1200.00	0.265 ± 0.021	f

References: **a)** IUE archival data **b)** Malfait et al. 1998 **c)** WISE All-Sky Data Release **d)** AKARI/IRC mid-IR all-sky Survey **e)** IRAS Point-source catalogue **f)** Meeus et al. 2003

of group Ib Herbig Ae/Be stars. Radiative transfer modeling of the Q-band is needed to constrain the radii of the inner edges of the outer disks of HD 100453 and HD 34282.

4.4 Modeling

In this section we introduce the radiative transfer code MCMax and the dust model. We discuss the modeling approach and outline the parameters that we study in this paper.

4.4.1 Radiative transfer code MCMax

For the modelling of the disks, we use MCMax dust modelling and radiative transfer tool (Min et al., 2009). MCMax performs radiative transfer using a Mont Carlo recipe outlined by Bjorkman & Wood (2001a). It solves the temperature structure and density structure

Table 4.3: *Photometric data HD 34282 (not corrected for extinction) used in this study*

band ID	λ [μm]	F_ν [Jansky]	reference
Walraven W	0.32	0.095 ± 0.002	a
Johnson U	0.36	0.162 ± 0.004	b
Walraven U	0.36	0.125 ± 0.002	a
Walraven L	0.38	0.231 ± 0.006	a
Walraven B	0.43	0.392 ± 0.005	a
Johnson B	0.44	0.443 ± 0.006	b
Walraven V	0.54	0.408 ± 0.004	a
Johnson V	0.55	0.441 ± 0.004	b
Cousins R	0.64	0.364 ± 0.005	a
Cousins I	0.79	0.339 ± 0.007	a
Near-IR J	1.23	0.427 ± 0.008	b
Near-IR H	1.65	0.578 ± 0.011	b
Near-IR K	2.22	0.715 ± 0.013	b
WISE 1	3.35	0.607 ± 0.021	c
Near-IR L	3.77	0.646 ± 0.030	b
WISE 2	4.60	0.524 ± 0.009	c
Near-IR M	4.78	0.577 ± 0.027	b
AKARI S09	9.00	0.736 ± 0.038	d
WISE 3	11.60	0.538 ± 0.008	c
IRAS 12	11.80	0.647 ± 0.096	e
WISE 4	22.10	1.401 ± 0.020	c
IRAS 25	25.00	1.577 ± 0.234	e
IRAS 60	60.00	10.604 ± 1.571	e
AKARI S65	65.00	10.040 ± 0.726	d
AKARI S90	90.00	11.170 ± 0.261	d
IRAS 100	100.00	10.584 ± 1.851	e
AKARI S140	140.00	9.745 ± 0.932	d
AKARI S160	160.00	9.353 ± 0.186	d
450 micron	450.00	1.611 ± 0.826	b
800 micron	800.00	0.409 ± 0.318	b
1100 micron	1100.00	0.183 ± 0.142	b
PDB 1.3	1300.00	0.100 ± 0.023	g
2600 micron	2600.00	0.024 ± 0.019	f
PDB 3.2	3200.00	0.0055 ± 0.001	g

References: a) de Winter et al. 2001 **b)** Sylvester et al. 1996 **c)** WISE All-Sky Data Release **d)** AKARI/IRC mid-IR all-sky Survey **e)** IRAS Point-source catalogue **f)** Mannings & Sargent 2000 **g)** Natta et al. 2004

assuming a 2-D geometry. It is used for modelling of circumstellar material including high optical depth regions. Our aim is to fit models to the observed Q-band images and SEDs of our sample stars to derive the disk structure. Therefore, we azimuthally average the Q-band brightness profiles and evaluate the radial extent of the disk emission. An extensive description of the modeling approach can be found in Maaskant et al. (2013).

4.4.2 Dust model

The composition of the grains in the disk are 20 % carbon and 80 % silicates. The standard dust composition with reference to the optical constants, is 32% $MgSiO_3$ (Dorschner et al.,

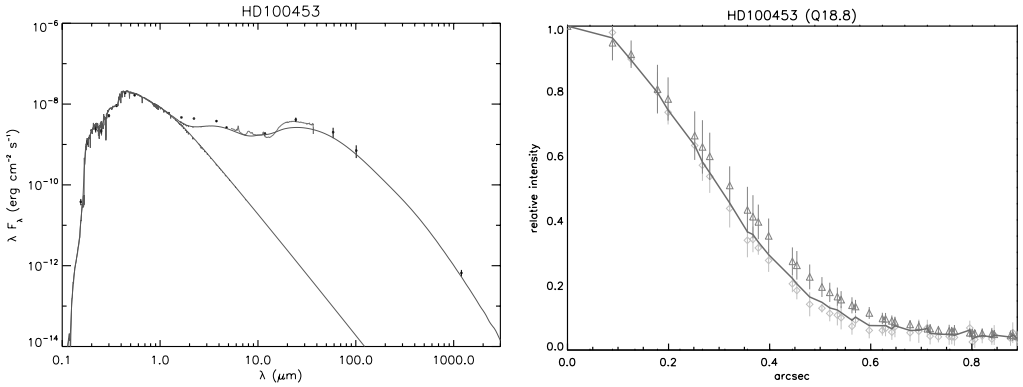

Figure 4.3: *This figure presents the model for HD 100453 where a continuous disk is assumed (i.e. no gap). The model fit to the SED seems reasonable, although the detailed spectral shape at ∼20 μm is not well fitted, though, the convolved model image does not fit the observed radial brightness profile.* ***Left:*** *The solid lines show the stellar Kurucz models and Spitzer/IRS spectra. The dots represent the observed photometry. The solid lines show the total fluxes.* ***Right:*** *azimuthally averaged radial brightness profiles of the Q-band relative to the maximum flux for HD 100453 (top) and HD 34282 (bottom). The central wavelengths of these images are* 18.8μm *for both of the stars. The diamonds indicate the PSF of the calibration star. The triangles show the observation of the science targets. The error bars indicate the one sigma error on the azimuthally averaged radial brightness profiles. The solid line shows our best-fit model.*

1995), 34% Mg_2SiO_4 (Henning & Stognienko, 1996), 12% $MgFeSiO_4$ (Dorschner et al., 1995), 2% $NaAlSi_2O_6$ (Mutschke et al., 1998), 20% C (Preibisch et al., 1993). The shape of our particles is irregular and approximated using a distribution of hollow spheres (DHS, Min et al. 2005) using a vacuum fraction of 0.7.

4.5 Results

In this section we describe the disk parameters that we constrain by fitting the size of the Q-band image. Thereafter we present the best fitting radiative transfer models to the Q-band sizes and the SEDs of HD 100453 and HD 34282.

4.5.1 Constraining the gap size

It has been shown by Maaskant et al. (2013) that the disk parameter that is constrained by fitting the Q-band size is the inner radius of the outer disk (i.e. the location of the wall). We perform a modeling study in Appendix 4.8 to study the effect to the SED of the inner and outer radii of the outer disk, the mass of the outer disk and the grain properties. We confirm that only the inner radius of the outer disk substantially effects the Q-band size. In the remainder of this section we fit the Q-band and SED of HD 100453 and HD 34282.

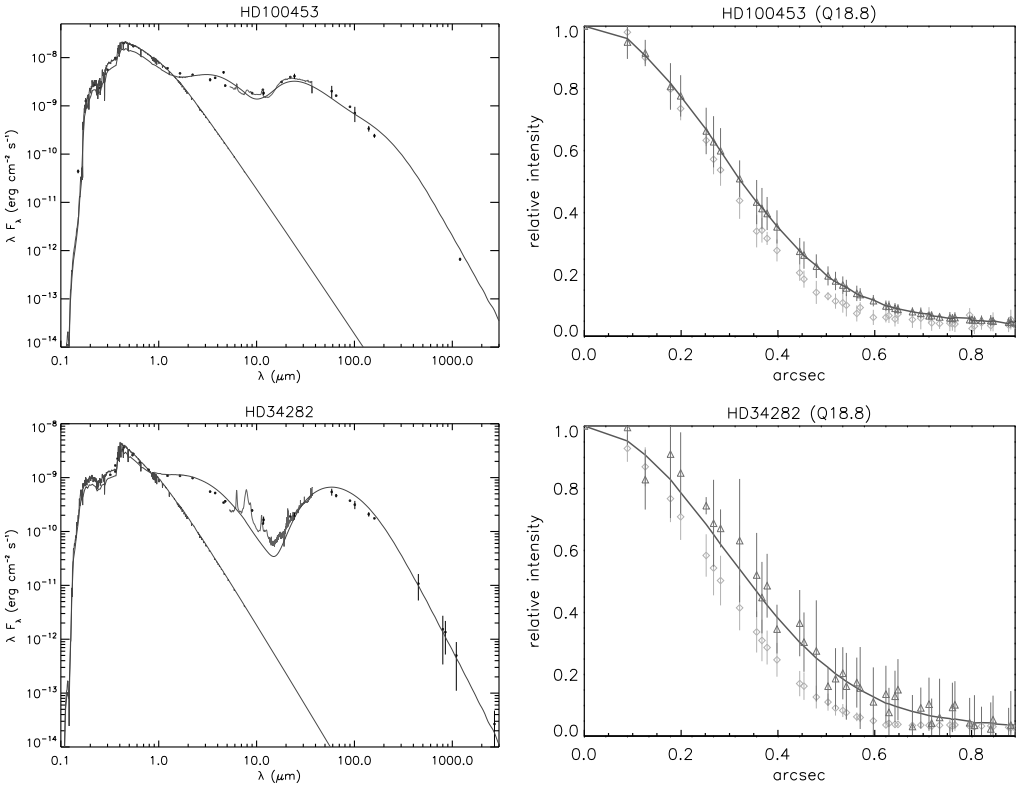

Figure 4.4: *The SED (right) and Q-band (left) of the best fit models for HD 100453 (top) and HD 34282 (bottom). See the caption of Figure 4.3 for a description of the lines and symbols shown in this figure.*

To fit the SED as well as the Q-band size we follow the fitting procedure as outlined in Maaskant et al. (2013). We summarize the procedure briefly here. As a first step, we start with a disk which has a continuous density profile. We assume that the disk is in hydrostatic equilibrium and that the radial dependence of the surface density drops off proportional to a powerlaw of -1. We fit the far-Infrared (FIR) to mm photometry to a grain size powerlaw index of p between 3.0 and 4.0. If this does not fit the Q-band size, than we insert a gap in the disk. We decrease the surface density in the gap by 15 orders of magnitude. This will result in a "wall" structure at the inner edge of the outer disk. Now we choose the radius of the inner edge of the outer disk, so that the convolved model image fits the observed Q-band image size. Then, we fit the emission in the NIR by including an optically thick inner disk. This will increase the flux in the NIR but casts a shadow on the outer disk and therefore reduces the flux at MIR and FIR wavelengths. In the case that an optically thick inner disk does not produce enough NIR flux or casts too much shadow on the outer disk, we add or replace an optically thin inner spherical halo to fit the NIR flux. As a final step, we choose the minimum size (between 0.1 μm and 1 μm) of the grains in the disk to fit the flux in the MIR and FIR to the SED.

Table 4.4: *Best-fit model parameters and comparison to the previous values by Maaskant et al. 2013*

Object	M_{dust} $M_\odot$	M_{halo} $M_\odot$	$R_{innerdisk/halo}$ AU	R_{wall} AU	R_{out} AU	$a_{min} - a_{max}$	a_{pow}
HD100453	3.2×10^{-4}	0.15×10^{-9}	0.1-1.7	17^{+2}_{-2}	200	0.5 μm - 1mm	-3.5
HD 3428	6.1×10^{-4}	5.5×10^{-11}	0.05-1.3	79^{+31}_{-17}	900	0.5 μm - 1mm	-3.5
HD 97048	6.0×10^{-4}	...	0.3 - 2.5	34^{+4}_{-4}	500	0.5 μm - 1mm	-3.5
HD 169142	0.8×10^{-4}	0.31×10^{-12}	0.1- 0.2	23^{+4}_{-4}	235	0.5 μm - 1mm	-3.5
HD 135344 B	1.0×10^{-4}	0.47×10^{-12}	0.1- 0.3	30^{+4}_{-3}	200	1.0 μm - 1mm	-4.0
Oph IRS 48	3.0×10^{-5}	0.50×10^{-12}	0.1 -0.3	63^{+4}_{-4}	235	0.1 μm - 1mm	-4.0

4.5.2 Best-fit model HD 100453

We first explore models without a gap in the disk. This seems to fit the SED reasonably well, though it always fails to fit the size of the Q-band image (see Figure 4.3, right panel). We find that this is because for a continuous disk, the disk surface which is emitting in the Q-band is much closer to the star (i.e. $\lesssim 10$ AU). Therefore, the model Q-band image is barely resolved with respect to the PSF (Figure 4.3). We can only fit the size of the Q-band by including a gap in the disk.

The model that gives us the best-fitted SED (Figure 4.4-left) and radial brightness profile (Figure 4.4-right) has a gap in the disk. We find that the inner edge of the outer disk has a very high surface brightness and dominates the emission in the Q-band. For this reason, the Q-band size is very sensitive for the location of the inner edge of the outer disk. We constrain its location at 17^{+2}_{-2} AU. The error is dominated by the uncertainty in the distance. As can be seen in Figure 4.4-right, the convolved image that is modelled using these input parameters fits well with this observation. The average temperature of the inner edge ($17-20$ AU) of the outer disk is $\sim$160 K.

The structure of the inner disk is poorly constrained by our data. Therefore we have modelled the inner circumstellar region by spherical halos which are optically thin, but geometrically high. To fit the near-infrared (NIR) emission we adopt a halo from 0.1 to 1.7 AU with a mass of 0.15×10^{-9} $M_\odot$. As there are many uncertainties in the structure of the inner disk (e.g. Dullemond & Monnier 2010), we only use the halo in our model in order to reproduce the amount of produced NIR emission from the disk. To account for the absence of silicate features at 10 and 20 μm, we assume a dust specie in the halo which does not show any features. We adopt 100% amorphous carbon, but alternatively, larger silicate grains or metallic iron may yield similar results.

Clearly, the absence of small silicate grains in the inner region of protoplanetary disks is remarkable. Similar dust compositional solutions have been inferred for a number of other transitional disks (e.g. T Cha: Olofsson et al. 2013, HD 135344 B: Carmona et al. 2014), however, no satisfactory explanation have been found to explain the depletion of small silicate grains. So not only the correlation with the presence of gaps, but also the assumption that there are no small silicate grains in the optically thin halo, causes the absence of silicate features in the SED.

The values of the best-fit parameters are listed in Table 4.4 and also compared with the values obtained for four other Herbig star by Maaskant et al. (2013).

4.5.3 Best-fit model HD 34282

For the the Herbig star HD 34282, we follow the same procedure as HD 100453. We find that we can not find a fit to the SED and Q-band size by using a disk with a continuous density structure. Therefore we adopt a gap in the disk. The best SED fit can be seen in Figure 4.4-right and its radial brightness profile is shown in Figure 4.4-right. The location of the inner radius of the outer disk is constrained to 79^{+31}_{-17} AU. Although the signal to noise of the Q-band observation is of worse than that of HD 100453, the error is still dominated by the uncertainty in the distance.

The model of the disk includes a halo that is extended from 0.02 to 1.3 AU and has a mass of 2.4×10^{-11} $M_{\odot}$. The dust grains in the halo are made of carbon and they have the size of 0.5 μm to 1 mm with an size distribution power law of -3.5. The mass of the outer disk is considered to be 0.83×10^{-4} $M_{\odot}$.

4.5.4 Summary

By using radiative transfer models, we have studied the Q-band sizes and SEDs of HD 100453 and HD 34282. We fail to find solutions with a continuous density structure. Thus we find that is is required to include large gaps in the disk to simultaneously fit the Q-band size and SED. The inner edge of the outer disks of HD 100453 and HD 34282 are respectively 17^{+2}_{-2} AU and 79^{+31}_{-17} AU.

4.6 Discussion

For HD 100453 and HD 34282, radii of the inner edges of the outer disks have been derived from the best-fit models. These values are in the same range as the wall radii of disks around other group Ib Herbig stars. We now discuss the implications of these results.

4.6.1 New Meeus group classification based on the $F_{30}/F_{13.5}$ continuum flux ratio

We compare the photometric properties of HD 100453 and HD 34282 to other Herbig stars. Figure 4.5 shows the color-magnitude and classification of a sample of Herbig stars. It shows luminosities at 1.3 mm compared to flux ratios at 30.0 and 13.5 μm for Herbig stars from the sample of Maaskant et al. (2014). As disks lose their mass during

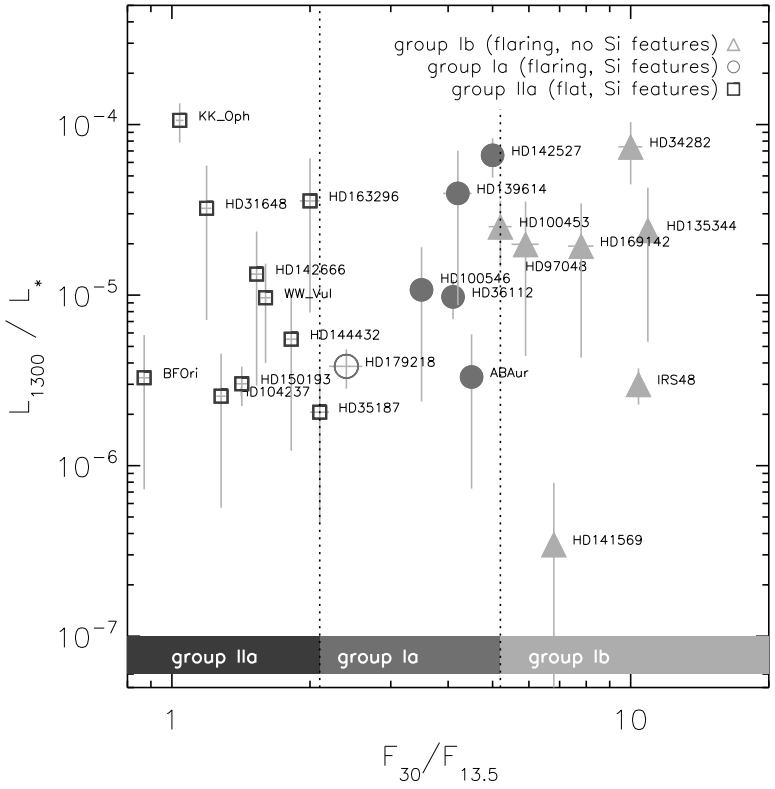

Figure 4.5: *The luminosities at 1.3 mm is compared to the flux ratio at 30.0 and 13.5 µm. The filled symbols indicate whether large gaps have been detected in the literature. The L_{1300}/L_* can be used as a proxy of the disk mass. We confirm the connection between the gap size and its location, with the $F_{30}/F_{13.5}$ ratio. The groups are divided by $2.1 < F_{30}/F_{13.5} < 5.1$. All the objects in this diagram are taken from the sample of Maaskant et al. (2014).*

their evolution, they move down in this diagram. This diagram seems to indicate that there is no trend between group I and group II disks with regard to the disk mass. Previous studies (Acke et al., 2009, Maaskant et al., 2013, 2014) have indicated a strong correlation between the $F_{30}/F_{13.5}$ continuum flux ratio and the group classification based on (Meeus et al., 2001). The transitions between group Ia, Ib and group IIa may be more easily expressed by the the $F_{30}/F_{13.5}$ ratios. For flat sources with amorphous silicate features (group IIa) that implies $F_{30}/F_{13.5} \leqslant 2.1$. For transitional/flaring objects with amorphous silicate features (group Ia) we find $2.1 < F_{30}/F_{13.5} < 5.1$. The transitional/flaring objects which do not have silicate feature (group Ib) have $F_{30}/F_{13.5} \geqslant 5.1$. The Meeus groups are well separated by the new criteria based on the mid-infrared flux ratio 4.5.

4.6.2 Correlation between amorphous silicate emission, size of the gap and the $F_{30}/F_{13.5}$ ratio

Transitional flaring disks which do show silicate emission are group Ia Herbig Ae/Be stars. The amorphous silicate features in these objects may originate in the inner edge of the outer disk. This may be the case for HD 100456 (e.g. Mulders et al. 2011) and HD 139614 (Matter et al., 2014), two transitional objects with the inner edge of the outer disk at respectively 13 and 5 AU. Alternatively, the amorphous silicate feature may originate in the inner disk. Examples are HD 142527 (Verhoeff et al., 2011), AB Aur (Honda et al., 2010) and HD 36112 (Isella et al., 2010). Also in these objects large gaps of several tens of AUs have been found. However, the inner disk may still contain a substantial amounts of small silicate grains producing the silicate features.

Group Ib Herbig Ae/Be stars do not show silicate emission features. Our study confirms that the weakness of silicate emission features is connected to the presence of large disk gaps in the critical temperature regime ($\gtrsim$160 K) responsible for emission of silicate features. HD 100453 has the smallest gap size in the sample of group Ib objects. Peculiarly, a closer look at the Spitzer/IRS spectrum of HD 100453 may show a tentative detection of very weak amorphous silicate features (Figure 4.2). Figure 4.5 shows that the $F_{30}/F_{13.5}$ ratio of HD100453 is on the border of a group Ia identification. We suggest that this is connected to the relatively small gap radius of 17 AU and thus higher temperature in the inner region of the outer disk. Our radiative transfer model of HD 100453 shows that the average temperature of the inner region of the outer disk (between $17-20$ AU) is $\sim$160 K. Because the inner edge of the outer disk is closer to the star, the temperature of the dust in the wall is higher than for HD 34282 and the other group Ib transitional disks studied in Maaskant et al. (2013). We can compare the temperature in the wall of HD 100453 to that of HD 100546 and HD 97048. HD 100546 is one of the best studied transitional disks which does show strong amorphous silicate features. Radiative transfer models presented in Mulders et al. (2011) show that the inner edge of the outer disk of HD 100546 is located at $\sim$13 AU and has a temperature of $\sim$200 K. For HD 97048, the typical temperature in the inner region of the outer disk ($34-37$ AU) is $\sim$110 K (Maaskant et al., 2013). HD 97048 does not show any sign of amorphous silicate emission. From this comparison, we infer that the temperature transition from $\sim$160 K to $\sim$200 K in the inner edge of the outer disk is critical for the strong enhancement of the amorphous silicate features originating in the wall. Possibly this is connected to the fact that grains of $\lesssim$160 K are icy and therefore grow to larger typical sizes (e.g. Sirono 2011, Okuzumi et al. 2012). The slow sublimation of ice in icy aggregates at $\sim$ 160 K, which are radially drifting inward in the disk, will lead to the formation of "pure" silicate aggregates which are thus more fragile and can readily fragment upon collision. In this scenario, an enhanced abundance of small fragmented silicate grains at temperatures of $\gtrsim$ 160 K, may contribute significantly to the amorphous silicate features.

4.6.3 Evolutionary link between transitional (flaring) and self-shadowed (flat) disks.

A key question in the study of protoplanetary disks is to determine the evolutionary link between gaps formation (group I) and grain growth and settling (group II). Disk gaps are found in an increasing number of group I Herbig stars and there is yet no evidence of large gaps in group II Herbig stars (Maaskant et al., 2013). Therefore, it is very unlikely that group I evolves to group II. There are now two possible evolutionary scenario's to understand the link between group I and II. First, as proposed by Maaskant et al. (2013), both groups may have evolved from a common ancestor (i.e., gapless flaring-disk structure). In transitional group I objects, gap formation has proceeded the collapse of the outer disk while grain growth and dust settling have flattened the outer disk in flat group II objects. Secondly, group II objects may be the precursors of group I objects. In that case, possibly planet formation is followed by the formation of a large gap that may produce a high vertical wall and stir up the dust in the outer disk.

4.7 Conclusions

We have used spatially resolved MIR observations and radiative transfer models. We fit the spectral energy distribution and the radial brightness profile of the Q-band images of the disks around two Herbig Ae/Be type Ib stars, HD 100453 and HD 34282. This work is compared to the results of Maaskant et al. (2013), where a similar analysis of four other Herbig stars, HD 97047, HD 169142, HD 135344 B and Oph IRS 48, is presented.

- We were not able to fit the spatially resolved Q-band imaging and SEDs considering a continuous disk (i.e. no gap). In contrast with a transitional disk consisting of a halo around the star, a gap and an hydrostatic outer disk, we successfully fit all the observations.
- Radiative transfer modelling constrains the inner radius of the outer disk at 17^{+2}_{-2} AU for HD 100453 and 79^{+31}_{-17} AU for HD 34282. This result confirms the conclusion by Maaskant et al. (2013) that group Ib Herbig Ae/Be stars are transitional disks with large gaps.
- The outer disk mass, surface density power law, and the opacity profile do not affect the Q-band size.
- We find no correlation between the halo masses, the disk masses and the sizes of the gaps in studied Herbig Ae/Be stars.
- The absence of the amorphous silicate emission in the spectra of these disks is consistent with the conclusions of Maaskant et al. (2013) that gaps in a critical temperature regime between $\sim 200 - 500$ K cause the silicate feature to disappear. In addition, grains are typically large in the outer disk.

- The temperature transition from ∼160 K to ∼200 K in the inner edge of the outer disk is critical for the strong enhancement of the amorphous silicate features originating in the wall

Acknowledgements: *The authors thank Rens Waters for inspiring discussions which helped to improve the analysis in this paper. The authors thank Michiel Min for providing his radiative transfer code MCMax. K.M. is supported by a grant from the Netherlands Research School for Astronomy (NOVA). Studies of interstellar chemistry at Leiden Observatory are supported through advanced-ERC grant 246976 from the European Research Council, through a grant by the Dutch Science Agency, NWO, as part of the Dutch Astrochemistry Network, and through the Spinoza premie from the Dutch Science Agency, NWO.*

4.8 Appendix A: parameter study

Figure 4.6 shows the results of a small parameter study to illustrate the degeneracy of SED modeling. HD 100453 is shown on the left and HD 34282 is shown on the right.

The top left plot in Figure 4.6 show the result of modelling different values for the inner radius of the outer disk (the wall radius). This value affects the MIR of the SED where the emission comes from the wall and the temperature is about ∼100-160 K. The gap size with the value of 17 AU fits the observed SEDs very well. This indicates a presence of a gap in between the halo and the outer disk. The exact size of this gap cannot be understood from modeling the SED alone, but must include fitting the size of the Qband image. The SED is degenerate because the structure of the inner halo (i.e. the optical depth, and scaleheigth), as well as the grain composition in the outer disk are not well known. As we will see, these parameters have a great influence on the SED as well.

The top right plot in Figure 4.6, shows a comparison of different disk radii. The outer radius is unknown and we try some values in the range of typical disk sizes and we find that a disk size with radius of 200 AU fits better the SED better. However, the changes of this value do not have a significant effect on the outcome of the modelling and therefore, it is not easy to estimate the size of the outer radius of the disk.

The bottom left plot in Figure 4.6 show variations in the dust mass. Higher mass means more material in the disk and therefore this would increase the thermal emission from the disk in the far-IR regions. Dust mass mainly affects the mm part of the SED. When the dust mass is taken to be lower than the best-fit value, the mm flux tends to shifts below the observation and when the mass is higher than the best fit, the mm flux shifts above the observation.

The bottom right plot in Figure 4.6 shows the result for different opacity profiles (i.e. different grain sizes and power law indices). The best-fit consists of grain size distribution of 0.5 μm to 1 mm with the power law index of -3.5. The change in this parameter affects the temperature and luminosity of the halo and the location of the wall of the outer disk.

This is especially noticeable in the NIR part of the SEDs. The red lines show the models with the highest abundance of small grains. Smaller grains have higher opacities, this means that more stellar radiation is absorbed the close to the star. Therefore the emission from the halo increases, but the stellar radiation decreases due to the higher optical depth. The other grain size populations show similar behaviours.

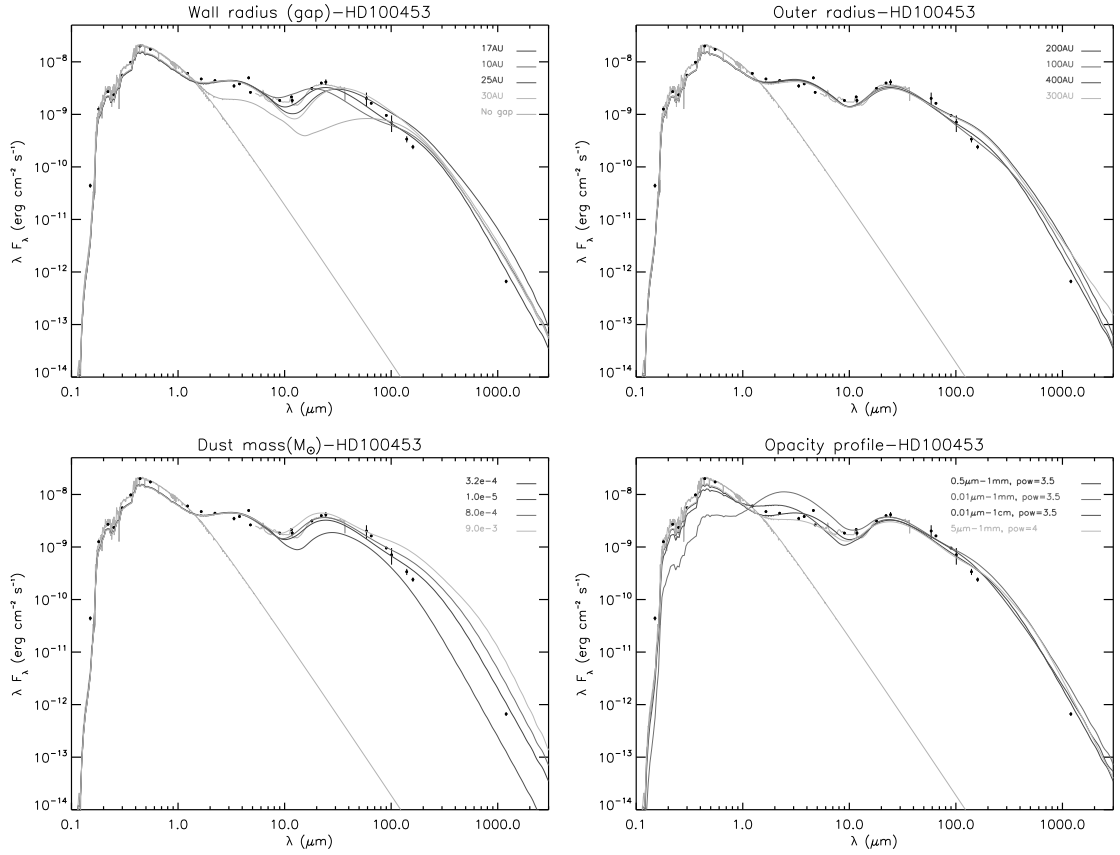

Figure 4.6: *Variations around the best-fit values for HD 100453. Top left: different gap sizes. Top right: different radii of outer disk. Bottom left: different total disk masses. Bottom right: different minimum and maximum grain sizes and power-laws of the grain size distribution.*

CHAPTER 5

Polycyclic aromatic hydrocarbon ionization as a tracer of gas flows through protoplanetary disk gaps

K. M. Maaskant, M. Min, L.B.F.M. Waters, and A.G.G.M. Tielens
Astronomy & Astrophysics, Volume 563 (2014)

Abstract

Planet-forming disks of gas and dust around young stars contain polycyclic aromatic hydrocarbons (PAHs). We aim to characterize how the charge state of PAHs can be used as a probe of flows of gas through protoplanetary gaps. In this context, our goal is to understand the PAH spectra of four transitional disks. In addition, we want to explain the observed correlation between PAH ionization (traced by the $I_{6.2}/I_{11.3}$ feature ratio) and the disk mass (traced by the 1.3 mm luminosity). We implement a model to calculate the charge state of PAHs in the Monte Carlo radiative transfer code MCMax. The emission spectra and ionization balance are calculated in the parameter space set by the properties of the star and the disk. A benchmark modeling grid is presented that shows how PAH ionization and luminosity behave as a function of star and disk properties. The PAH ionization is most sensitive to ultraviolet (UV) radiation and the electron density. In optically thick disks, where the UV field is low and the electron density is high, PAHs are predominantly neutral. Ionized PAHs trace low-density optically thin disk regions where the UV field is high and the electron density is low. Such regions are characteristic of gas flows through the gaps of transitional disks. We demonstrate that fitting the PAH spectra of four transitional disks requires a contribution of ionized PAHs in 'gas flows' through the gap. The PAH spectra of transitional disks can be understood as superpositions of neutral and ionized PAHs. For HD 97048, neutral PAHs in the optically thick disk dominate the spectrum. In the cases of HD 169142, HD 135344 B and Oph IRS 48, small amounts of ionized PAHs

located in the 'gas flows' through the gap are strong contributors to the total PAH luminosity. The observed trend in the sample of Herbig stars between the disk mass and PAH ionization may imply that lower-mass disks have larger gaps. Ionized PAHs in gas flows through these gaps contribute strongly to their spectra.

5.1 Introduction

The infrared (IR) spectra originating from protoplanetary disks are rich and diverse. Polycyclic aromatic hydrocarbons (PAHs) are observed in disks around Herbig Ae/Be stars (Meeus et al., 2001, Acke & van den Ancker, 2004, Keller et al., 2008, Acke et al., 2010) and T Tauri stars (Geers et al., 2007b, Bouwman et al., 2008). The strength of the PAH features decreases with stellar effective temperature. No T Tauri stars of the spectral type later than G8 shows the IR emission features in their spectra (e.g. Tielens 2008, Kamp 2011 and references therein). In addition, the strength of the IR emission features is generally much weaker relative to the total IR emission in the Herbig star spectra as compared to the diffuse ISM (Sloan et al., 2005, Keller et al., 2008, Acke et al., 2010, Boersma et al., 2008). Direct imaging observations taken in the PAH bands have shown that PAHs can be used as a tracer of the outer disk surface (Doucet et al., 2006, Lagage et al., 2006). Even so, the PAH emission is not dominated by PAHs on the surface of the outer disk in some transitional disks (Geers et al., 2007a, Maaskant et al., 2013).

After being electronically excited by ultraviolet (UV) photons, the PAHs cool by emission in the CH- and CC- stretching and bending modes. Laboratory studies and quantum chemical calculations show that many of the IR features shift in peak position, vary in width, and/or show substructure depending on ionization stage and detailed molecular structure (Hudgins & Allamandola, 1999, Allamandola et al., 1999, Bauschlicher et al., 2009, Ricca et al., 2012). An important parameter that influences the relative feature strength of the CH and CC modes is the effect of ionization with CC modes being carried predominantly by ions and CH modes by neutrals. Hence, the 6.2-μm (CC–mode) to 11.2-μm (CH–mode) ratio provides a good measure of the ionization balance of the emitting PAHs (Allamandola et al., 1999). This has been demonstrated in a variety of astrophysical environments (Hony et al., 2001, Peeters et al., 2002, Rapacioli et al., 2005, Galliano et al., 2008).

The intense radiation field of the central star may photo-dissociate the PAH molecules. As a result, the average PAH size increases, and the total abundance decreases (Visser et al., 2007, Siebenmorgen & Heymann, 2012). As a possible path for PAH-survival, Siebenmorgen & Krügel (2010) suggest that turbulent motions in the disk can replenish or remove PAHs from the reach of hard photons. Several modeling studies have been carried out to understand global trends in the composition and evolution of PAHs in relation to the disk (Habart et al., 2004, Dullemond et al., 2007a, Berné et al., 2009). However, none of them are focused on understanding PAH ionization.

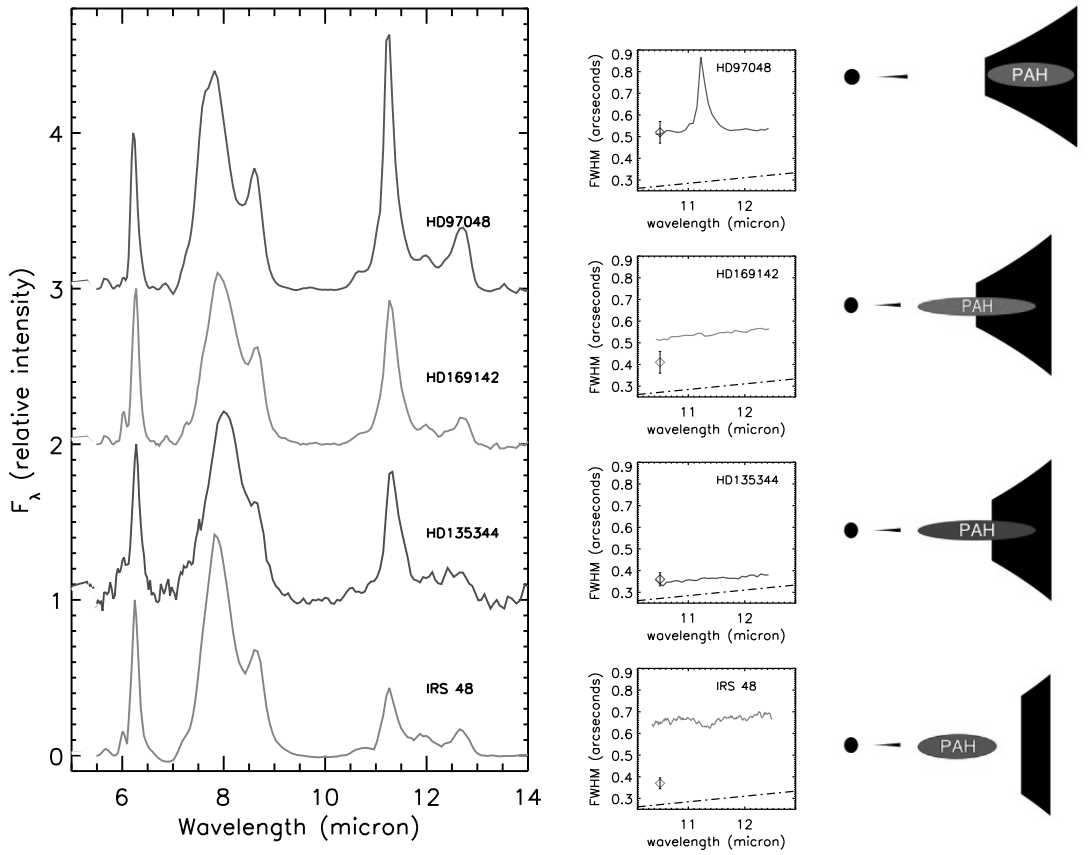

Figure 5.1: *Left: Spitzer/IRS spectra of the four transitional disks HD 97048, HD 169142, HD 135344 B and Oph IRS 48. The spectra are scaled relative to the 6.2-μm PAH peak flux and show a wide range in the $I_{6.2}/I_{11.3}$ ratio; most neutral in HD 97048 and most ionized in Oph IRS 48. Middle: VLT/VISIR observations show that FWHM as a function of wavelength. The size of the 11.3-μm feature is respectively larger, similar and smaller than the N-band continuum for HD 97048, HD 169142, HD 135344 B, and Oph IRS 48 (data from Maaskant et al. (2013)). The diamond symbols show the sizes of the point spread functions of the observations. The black dashed-dotted line is the diffraction limit of the telescope. Right: Sketches showing a qualitative interpretation of the spatial distribution of the dominant contribution of PAH emission, as shown by the ovals.*

In this paper, we investigate the effect of disk environments on PAH charge, spectra, and luminosity. The key question is: can we use the ionization balance of PAHs as a tracer of processes in protoplanetary disks? In Section 5.2, we first identify new observational trends seen in the $I_{6.2}/I_{11.3}$ PAH feature strength ratios. Section 5.3 describes the PAH model in the Monte Carlo radiative transfer tool MCMax. In Section 5.4, we show how the ionization of PAHs behaves as a function of star and disk properties. We use these results to demonstrate how we can understand the PAH spectra of four transitional disks in Section 5.5. In the discussion (Section 6.6), we discuss what we can learn about disk evolution from PAH ionization. The conclusions are given in Section 6.7.

5.2 New observational trends in PAH features of Herbig stars

In this section, we discuss new observational trends of PAH ionization in relation to the disk structure of Herbig stars. For a detailed observational overview of the four transitional disks in our sample, we refer to Maaskant et al. (2013). The PAH properties of all other Herbig stars are shown in Table 5.1 and are adopted from Acke et al. (2010).

5.2.1 Higher PAH ionization in dust depleted 'gaps'

For HD 97048, HD 169142, HD 135344 B, and Oph IRS 48, the IRS/Spitzer spectra are shown on the left of Figure 5.1. The intensity of the spectra is scaled relative to the peak flux of the 6.2-μm feature. While the general PAH profile is highly similar, a large spread is observed in the relative strength of the 11.3-μm to the central 6.2-μm feature. The $I_{6.2}/I_{11.3}$ ratio is lowest for HD 97048 and increases for HD 169142, HD 135344 B, and Oph IRS 48.

In contrast to HD 97048 (Lagage et al., 2006, Doucet et al., 2006), it was found using VLT/VISIR mid-infrared (MIR) imaging that PAH emission in Oph IRS 48 is not co-spatial to the dust continuum (Geers et al., 2007a). While the dust continuum at 18.8 μm shows a ring structure, the PAH emission at 8.6 μm peaks at the center. In a recent paper by Maaskant et al. (2013), observations show that PAH emission is also not dominated by the outer flaring disk for HD 169142 and HD 135344 B. These observations are shown in the middle of Figure 5.1, where the spatial full width at half maximum (FWHM) size of the 11.3-μm feature can be seen as imaged by VISIR (Geers et al., 2007a, Maaskant et al., 2013). For HD 97048, it is clear that the 11.3-μm feature originates in larger spatial scales than the continuum. The feature is not spatially resolved relative to the continuum in HD 169142 and HD 135344 B and is smaller than the continuum in Oph IRS 48. Using radiative transfer modeling, Maaskant et al. (2013) concluded that a significant contribution must come from close to the star and possibly from within the dust depleted 'gap' if the PAH feature is not larger than the continuum.

On the left of Figure 5.1 sketches are shown of the disk geometries which include colored ovals to indicate the origins of the dominant PAH contributions. The sizes of the disks are taken from the models of Maaskant et al. (2013), where the inner edge of the outer disk is set by MIR imaging. The inner disks represent the origins of near-infrared (NIR) emission in the spectral energy distributions (SEDs) though their structures are not well constrained.

The four transitional Herbig stars show a trend between the relative band strength ratio $I_{6.2}/I_{11.3}$ and the spatial origin in the disk. For HD 97048, where the PAH emission is dominated by the outer disk, the $I_{6.2}/I_{11.3}$ ratio is low: 0.87 ± 0.01. In HD 169142 and HD 135344 B, the 11.3-μm PAH features are not extended when compared to the continuum and have $I_{6.2}/I_{11.3}$ ratios of respectively 1.24 ± 0.01 and 1.42 ± 0.08. In Oph IRS 48, the PAHS are emitted from a location that is closer to the star than the outer disk,

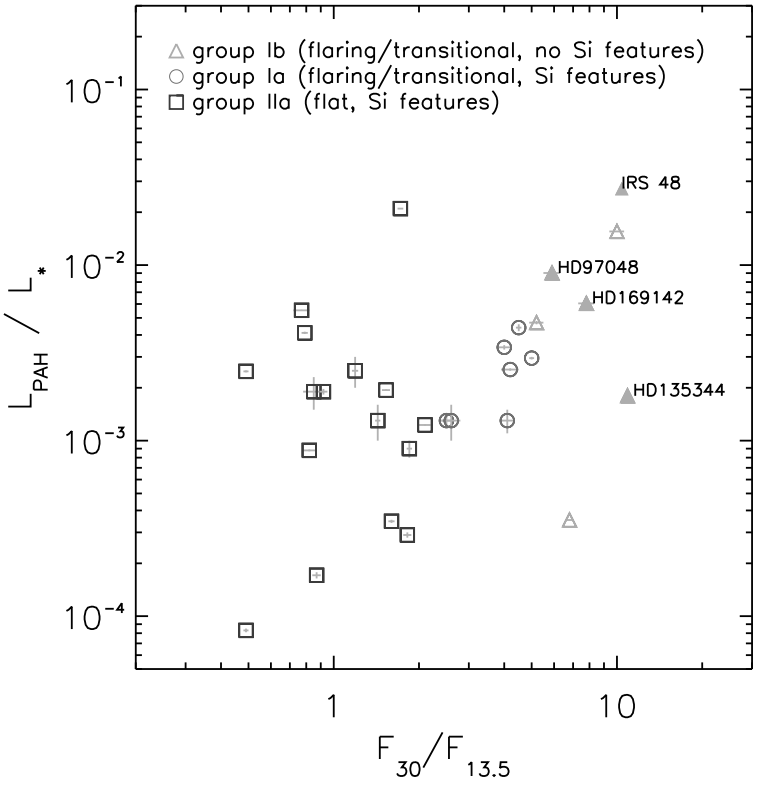

Figure 5.2: *The PAH luminosity ($L_{\rm PAH}/L_*$) of a sample of Herbig stars compared to the MIR spectral index ($F_{30}/F_{13.5}$). The MIR spectral index can be used as a tracer of disk gaps, as indicated by the symbols showing the flaring/transitional disks (group I) with silicate features (circles), without silicate features (triangles), and self-shadowed disks (group II) with silicate features (squares). While the PAH luminosities among the objects span ∼2–3 orders of magnitude, the averaged luminosities of the disk groups only differ by a factor of ∼2–3. The parameters of all the objects are listed in Table 5.1.*

and have a high $I_{6.2}/I_{11.3}$ ratio of 3.76 ± 0.01. Thus it seems the PAH emission which originate from the outer dusty disk has a lower $I_{6.2}/I_{11.3}$ ratio, while PAH emission from within the 'gap' has a high $I_{6.2}/I_{11.3}$ ratio. Since the $I_{6.2}/I_{11.3}$ ratio can be attributed to the charge state of the PAHs (Allamandola et al., 1999), we find that the PAHs in the optically thick dust disk are predominantly neutral, while the PAHs in the disk gap are ionized.

5.2.2 PAH ionization in Herbig stars

To better understand the behavior of the $I_{6.2}/I_{11.3}$ ratio for a broad range of disk geometries, we compare a large representative sample of IRS/Spitzer observations of Herbig objects (see Table 5.1). For 47 objects, IRS/Spitzer spectra are adopted from Acke et al. (2010). For 30 stars out of this sample, PAH luminosities were derived from detected features in the IRS/Spitzer spectrum. We discarded objects for which evidence of significant contamination from the surroundings exists in the literature. The objects are sorted by the

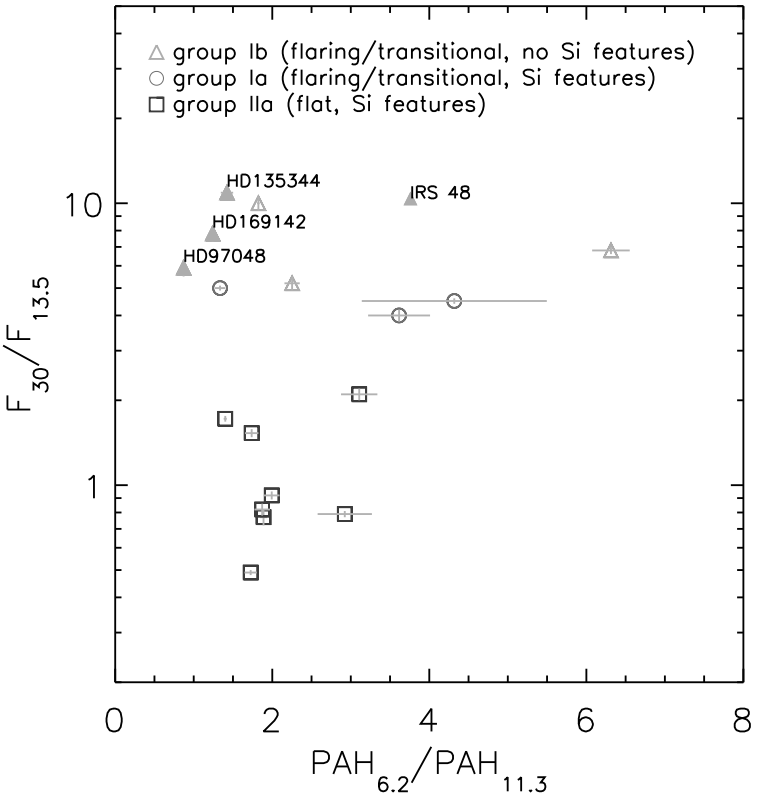

Figure 5.3: *The $I_{6.2}/I_{11.3}$ ratio compared to the MIR spectral index ($F_{30}/F_{13.5}$). Ionized PAHs are traced by a high $I_{6.2}/I_{11.3}$ ratio. The wider range in the $I_{6.2}/I_{11.3}$ ratio in flaring/transitional disks ($\langle I_{6.2}/I_{11.3}\rangle = 2.61 \pm 1.63$) suggests that the PAH emission originates in a wider range of physical environments while the origin of PAH emission in flat disks ($\langle I_{6.2}/I_{11.3}\rangle = 2.08 \pm 0.56$) seems to be more homogeneous. The parameters of all the objects are listed in Table 5.1.*

$F_{30}/F_{13.5}$ flux ratio between 30.0- and 13.5-μm. This flux ratio is indicative for the disk geometry as it may trace gap-sizes in the temperature range of ∼200–500 K and thus allows us to search for trends as a result of the geometry of the disk. The PAH luminosities and band-strength ratio 6.2/11.3 are included in Table 5.1. There is no evidence that the objects in Table 5.1, for which no PAH luminosity could be derived, represent a particular range in $F_{30}/F_{13.5}$ or L_{1300}/L_*.

For all the objects with PAH emission, Figure 5.2 shows the relative PAH luminosities (L_{PAH}/L_*) compared to the MIR spectral index $F_{30}/F_{13.5}$. The three different symbols indicate the SED group classifications from Meeus et al. (2001) and whether the object shows the amorphous 10- and 20-μm silicate features in the spectrum. The blue squares (group IIa) are interpreted as the 'flat', self-shadowed disks with silicate features. The red circles (group Ia) are 'flaring/transitional' objects with silicate features. The orange objects (group Ib) are 'flaring/transitional' objects without silicate features. The latter typically show prominent PAH spectra due to large gaps in the disk, which lower the continuum emission, thereby, increasing the contrast to the PAH features (Maaskant et al.,

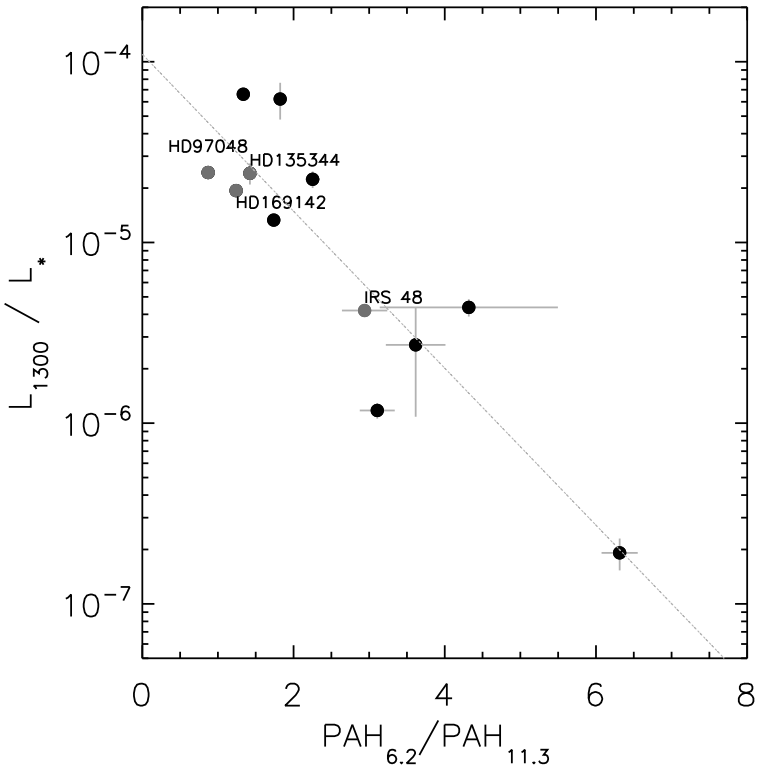

Figure 5.4: *An observational trend between the $I_{6.2}/I_{11.3}$ ratio as a function of the luminosity at 1.3 mm (L_{1300}/L_*). The grey dots show the objects studied in this paper. The dotted line gives the best fit to the data (Equation 5.1). The parameters of all the objects are listed in Table 5.1. For high mm luminosities, the $I_{6.2}/I_{11.3}$ ratio is lowest (tracing neutral PAHs), while the $I_{6.2}/I_{11.3}$ ratio is highest (tracing ionized PAHs) for low mm values.*

2013). Within the groups, $L_{\rm PAH}/L_*$ spans $\sim$2–3 orders of magnitude. The averaged difference between the groups is much smaller; flaring/transitional sources are, relatively speaking, only a factor of $\sim$2–3 more luminous in the fractional PAH luminosity than flat objects.

Figure 5.3 shows the $I_{6.2}/I_{11.3}$ ratio compared to the $F_{30}/F_{13.5}$ MIR spectral index. This figure shows that the averaged $\langle I_{6.2}/I_{11.3}\rangle$ ratio in flaring/transitional objects (2.61 ± 1.63) is higher and has a larger spread than in flat objects (2.08 ± 0.56). This may reflect that the PAH emission in flaring/transitional disks originates in more varied physical environments (with some cases, a strong contribution from ionized PAHs) while flat disks may be more homogeneous. In this paper we show that ionized PAH emission can arise from the gas inside the gap for transitional disks, which may arise in the gas flowing from the outer disk through the gap to the inner disk. For flat disks, there are few observational constraints on their disk geometries. However, for one particular case, there is evidence of extended PAH emission. Verhoeff et al. (2010) has shown for HD 95881 that PAHs have a spatial extent of $\sim$100 AU and are well resolved with respect to the continuum. They, thus, confirmed the presence of an illuminated gas surface. As discussed by Dullemond

et al. (2007a), the opacity in the upper layers of the disk decreases, causing a weaker far-infrared (FIR) flux when dust decouples from the gas and settles to the mid-plane. As a consequence, PAH emission from flat disks is predicted to be stronger because the gas is still flaring. However, as Figure 5.2 shows, this is not what is observed, suggesting that some mechanism is not only removing small grains but also the PAHs from the disk upper layers in flat disks.

5.2.3 PAH ionization and the millimeter luminosity

For most of the sources, the 1.3 millimeter (mm) photometry is collected from the literature. An overview of all available photometry is listed in Table 5.1. Since mm emission is optically thin and most prominently produced by cold mm-sized grains in the outer disk, its luminosity compared to the stellar luminosity can be used as a proxy of the total disk mass. Large uncertainties remain in the conversion of the sub-mm flux toward an estimate of the total disk mass, because of the unknown outer disk temperatures and the opacities of mm grains. Nevertheless, during the evolution of protoplanetary disks toward planetary systems, the disk loses most of the mass and the mm emission decreases. This makes it interesting to compare the mm fluxes of disks to other disk characteristics.

We report a new trend seen in the PAH $I_{6.2}/I_{11.3}$ flux ratio as a function of sub-mm brightness. Figure 5.4 shows the sub-mm luminosity at 1.3 mm (L_{1300}/L_*) compared to the $I_{6.2}/I_{11.3}$ PAH ratio for all Herbig stars with detected mm photometry. The $I_{6.2}/I_{11.3}$ flux ratio is higher for the sources with a lower mm flux. The gray line gives the best fit to the data. Using least squares minimization we find the following exponential best fit to the data for the disks of Herbig stars with mm luminosities between $10^{-7} \lesssim L_{1300}/L_* \lesssim 10^{-4}$

$$\frac{L_{1300}}{L_*} = 1.1 \times 10^{-4} \exp(-\frac{I_{6.2}}{I_{11.3}}). \tag{5.1}$$

The PAHs in massive disks are predominantly neutral (low $I_{6.2}/I_{11.3}$ flux ratio), while PAHs in lower mass disks are ionized (high $I_{6.2}/I_{11.3}$ flux ratio).

5.3 PAHs in the radiative transfer code MCMax

In this section we present our PAH ionization model and discuss how this is implemented in the radiative transfer code MCMax.

5.3.1 General description of PAH model

We model the disks using the radiative transfer code MCMax (see Min et al., 2009). MCMax is a code that not only solves for the radiative transfer but also solves the disk

Target	$F_{30}/F_{13.5}$ ▽	group	gap?	$L_{\rm PAH}/L_*$	$I_{6.2}/I_{11.3}$	L_* $L_\odot$	T_* K	d pc	F_{1300} mJy
HD35929	0.43 ± 0.01	IIa	…	…	…	131.2	6870	510	…
HD72106S	0.49 ± 0.01	IIa	…	$2.48 \pm 0.03 \times 10^{-3}$	1.72 ± 0.08	270.9	10750	277	…
HD58647	0.49 ± 0.01	IIa	…	$8.30 \pm 0.20 \times 10^{-5}$	…	270.9	10750	277	…
HD190073	0.75 ± 0.02	IIa	…	…	…	61.9	8990	290	…
HD98922	0.75 ± 0.03	IIa	…	…	…	855.7	10500	538	…
Wray1484	0.76 ± 0.02	Ia	…	…	…	1339.9	30000	750	…
HD95881	0.77 ± 0.05	IIa	…	$5.52 \pm 0.04 \times 10^{-3}$	1.88 ± 0.04	7.7	8990	118	…
NX Pup	0.78 ± 0.02	IIa	…	…	…	19.6	7290	450	…
HD50138	0.78 ± 0.04	IIa	…	…	…	423.5	12230	289	…
VV Ser	0.79 ± 0.02	IIa	…	$4.11 \pm 0.06 \times 10^{-3}$	2.92 ± 0.35	19.1	9000	330	…
HD85567	0.82 ± 0.04	IIa	…	$8.80 \pm 0.10 \times 10^{-4}$	1.87 ± 0.10	328.3	12450	480	…
HD37806	0.85 ± 0.07	IIa	…	$1.90 \pm 0.40 \times 10^{-3}$	…	145.3	9480	470	…
BF Ori	0.87 ± 0.03	IIa	…	$1.71 \pm 0.07 \times 10^{-4}$	…	34.1	8985	510	…
HD101412	0.92 ± 0.03	IIa	…	$1.90 \pm 0.07 \times 10^{-3}$	1.99 ± 0.10	5.1	9960	118	…
HD144668	0.96 ± 0.02	IIa	…	…	…	87.5	7930	208	20 ± 16 [o]
KK Oph	1.04 ± 0.02	IIa	…	…	…	0.74	8030	145	52 ± 15 [o]
HD37258	1.10 ± 0.03	IIa	…	…	…	36.2	8970	510	…
HD31648	1.19 ± 0.03	IIa	…	$2.50 \pm 0.50 \times 10^{-3}$	…	13.7	8720	131	250 ± 15 [r,†]
HD104237	1.28 ± 0.03	IIa	…	…	…	34.7	8405	116	92 ± 19 [o]
HD150193	1.42 ± 0.05	IIa	…	…	…	24.0	8990	150	45 ± 12 [r,†]
HD244604	1.43 ± 0.03	IIa	…	$1.30 \pm 0.30 \times 10^{-3}$	…	23.6	8730	340	…
HD142666	1.53 ± 0.05	IIa	$\surd$ [a]	$1.94 \pm 0.30 \times 10^{-3}$	1.74 ± 0.09	14.4	7580	145	127 ± 9 [m]
WW Vul	1.60 ± 0.04	IIa	…	$3.47 \pm 0.07 \times 10^{-4}$	…	15.8	8430	440	…
RR Tau	1.72 ± 0.04	IIa	…	$2.10 \pm 0.01 \times 10^{-2}$	1.40 ± 0.02	2.2	8460	160	…
HD144432	1.82 ± 0.06	IIa	$\surd$ [b]	$2.92 \pm 0.10 \times 10^{-4}$	…	10.1	7345	145	44 ± 10 [p]
HD37357	1.85 ± 0.04	IIa	…	$9.00 \pm 1.00 \times 10^{-4}$	…	85.1	9230	510	…
HD163296	2.00 ± 0.10	IIa	…	…	…	23.3	8720	122	743 ± 15 [o]
HD145263	2.00 ± 0.10	IIa	…	…	…	3.8	7200	116	…
HD35187	2.10 ± 0.10	IIa	…	$1.23 \pm 0.01 \times 10^{-3}$	3.11 ± 0.23	27.4	8970	150	20 ± 2 [t]
HD203024	2.30 ± 0.20	Ia	…	…	…	99.2	8200	620	…
HD179218	2.40 ± 0.20	Ia	…	…	…	79.2	9810	244	71 ± 7 [s]
HD250550	2.50 ± 0.10	Ia	…	$1.30 \pm 0.10 \times 10^{-3}$	…	20.9	10700	280	…
HD259431	2.55 ± 0.05	Ia	…	…	…	8294.5	25400	800	…
HD38120	2.60 ± 0.20	Ia	…	$1.30 \pm 0.30 \times 10^{-3}$	…	89.3	10500	510	…
HD100546	3.50 ± 0.20	Ia	$\surd$ [c]	…	…	32.9	10500	103	465 ± 20 [o]
HD37411	4.00 ± 0.20	Ia	…	$3.40 \pm 0.10 \times 10^{-3}$	3.62 ± 0.39	34.4	9100	510	5 ± 3 [o]
HD36112	4.10 ± 0.20	Ia	$\surd$ [d]	$1.30 \pm 0.20 \times 10^{-3}$	…	22.2	7850	205	72 ± 13 [s]
HD139614	4.20 ± 0.30	Ia	$\surd$ [e]	$2.54 \pm 0.04 \times 10^{-3}$	…	8.6	7850	140	242 ± 15 [m]
AB Aur	4.50 ± 0.10	Ia	$\surd$ [f]	$4.40 \pm 0.20 \times 10^{-3}$	4.32 ± 1.18	46.2	9520	144	136 ± 15 [r]
HD142527	5.00 ± 0.10	Ia	$\surd$ [g]	$2.95 \pm 0.05 \times 10^{-3}$	1.34 ± 0.07	50.6	6260	198	1190 ± 33 [p]
T CrA	5.00 ± 0.30	Ia	…	…	…	0.4	7200	130	219 ± 11 [o]
HD100453	5.20 ± 0.30	Ib	$\surd$ [h]	$4.70 \pm 0.10 \times 10^{-3}$	2.25 ± 0.10	8.0	7390	112	200 ± 21 [q,†]
HD97048	5.90 ± 0.40	Ib	$\surd$ [i]	$9.01 \pm 0.03 \times 10^{-3}$	0.87 ± 0.01	40.7	10010	158	452 ± 34 [o]
HD141569	6.80 ± 0.20	Ib	$\surd$ [j]	$3.53 \pm 0.02 \times 10^{-4}$	6.31 ± 0.24	18.3	9520	99	5 ± 1 [p]
HD169142	7.80 ± 0.50	Ib	$\surd$ [k]	$6.05 \pm 0.02 \times 10^{-3}$	1.24 ± 0.01	15.3	8200	145	197 ± 15 [m]
HD34282	10.00 ± 0.60	Ib	$\surd$ [h]	$1.55 \pm 0.01 \times 10^{-2}$	1.82 ± 0.02	3.1	8720	164	100 ± 23 [t]
Oph IRS 48	10.40 ± 0.30	Ib	$\surd$ [l]	$2.64 \pm 0.02 \times 10^{-2}$	2.94 ± 0.01	14.3	10000	120	60 ± 10 [n]
HD135344B	10.90 ± 0.30	Ib	$\surd$ [i]	$1.80 \pm 0.02 \times 10^{-3}$	1.42 ± 0.08	8.3	6590	140	142 ± 19 [m]

Table 5.1: *Stellar and disk parameters of the Herbig stars in our sample. The targets are sorted by the $F_{30}/F_{13.5}$ MIR spectral index which naturally splits most of the flat disks (group IIa) from the flaring/transitional disks (group Ia and Ib). The PAH characteristics and the stellar parameters are adopted from Acke et al. (2010). Complementary mm photometry is taken from the literature. The † indicates that the 1.3 mm flux is extrapolated from other (sub-)mm values using the spectral slope between the FIR and the (sub-)mm fluxes. References:* ***a)*** *Schegerer et al. 2013.* ***b)*** *Chen et al. 2012.* ***c)*** *Bouwman et al. 2003.* ***d)*** *Isella et al. 2010.* ***e)*** *Matter et al. 2013.* ***f)*** *Piétu et al. 2005.* ***g)*** *Fukagawa et al. 2006.* ***h)*** *Khalafinejad et al. 2014 (in prep.)* ***i)*** *Maaskant et al. 2013.* ***j)*** *Augereau et al. 1999.* ***k)*** *Honda et al. 2012.* ***l)*** *Geers et al. 2007a.* ***m)*** *Sylvester et al. 1996.* ***n)*** *Andrews & Williams 2007.* ***o)*** *Henning et al. 1994.* ***o)*** *Sylvester et al. 2001.* ***p)*** *Walker & Butner 1995.* ***q)*** *Meeus et al. 2002.* ***r*** *Sandell et al. 2011.* ***s)*** *Mannings & Sargent 2000.* ***t)*** *Natta et al. 2004.*

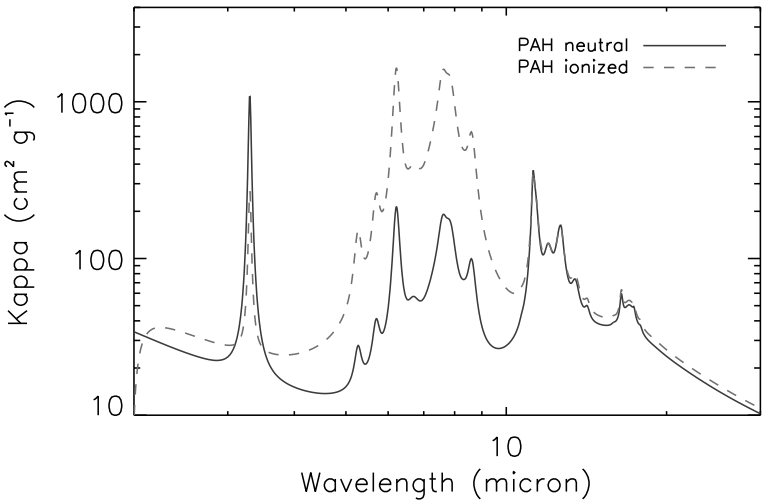

Figure 5.5: *Opacities for neutral PAHs (solid line) and ionized PAHs (dashed line) with* $N_C = 100$*. Computed using the method described by Draine & Li (2007)*

structure. For the continuum radiative transfer, it uses the Monte Carlo radiative transfer scheme of Bjorkman & Wood (2001b) with direct re-emission and temperature correction. This scheme cannot be directly applied to the PAH molecules, since they are not in thermal equilibrium. Therefore, we need to compute the emission spectra of the thermal equilibrium grains first and iterate the radiative transfer to include the radiative transfer effect on the emissivities of the PAHs.

The emission spectra of large molecules, like PAHs or very small dust grains, can be computed using the continuous thermal approximation (Guhathakurta & Draine, 1989, Draine & Li, 2001). In this approximation it is assumed that the emission is well described by a single temperature at any time. This temperature fluctuates strongly due to transient heating events and fast cooling. A PAH molecule cools down significantly before it is hit by the next energetic photon, which heats it again. These fluctuation, and the corresponding temperature distribution can be computed from the statistics of the radiation field and the heating and cooling properties of the particles. This method fully accounts for multi-photon heating events, or, the case where the particle is not yet cooled down completely before it is hit again. This is important for larger particles with higher heat capacities (i.e., longer cooling times) and for the intense radiation field close to the star. For the temperature distribution of the PAHs at each location in the disk is solved using a Monte Carlo method, simulating the transient heating events. An analytical method, using the solution of a set of linear equations to solve for the temperature distribution, is also implemented in MCMax (also used in Dullemond et al., 2007a). The two methods perfectly agree on the emerging PAH spectrum.

Once the spectral shape of the emissivity of the PAHs is computed using the temperature distribution, the PAHs can be included in the Monte Carlo radiative transfer in a very similar way to the other dust components. For ach time a photon package in the Monte

Carlo radiative transfer run is absorbed by a PAH molecule, we make sure that it is re-emitted with the same energy and with the spectral signature computed using the method above. In this way, we still strictly conserve energy, ensuring a quick convergence of the method.

The optical properties of the PAHs are computed using the method by Draine & Li (2001, 2007). The adopted opacities for neutral and ionized PAHs are shown in Figure 5.5 (with $N_C = 100$, the number of carbon atoms in the PAH molecule, and PAH radius $a_{PAH} = 6$ Å). The PAH optical properties are constructed from a number of laboratory and observational studies. Thus our PAH model represents the emission from various PAH molecules and is designed to conform to observed PAH properties in the ISM. We use a single sized (N_C=100) PAH molecule with two possible charge states. This PAH model is sufficient for the goal of our paper, which is to provide a tool to study the effect of the star and disk properties on the charge state of PAH molecules and its influence on the resulting IR spectra. PAH processing may also play a role in protoplanetary disks, either at the molecular level or in a disk environment. Specifically, the PAH destruction is predicted to act on the smallest PAH molecules (Visser et al., 2007), but the PAHs can be replenished from deeper layers of the disk by turbulence (Siebenmorgen & Heymann, 2012).

The $I_{6.2}/I_{11.3}$ μm band ratio may also be affected by dehydrogenation of the PAH molecule. The effect of ionization versus dehydrogenation on the $I_{6.2}/I_{11.3}$ ratio are reviewed in Tielens (2008). The hydrogen coverage on a PAH is a balance between dehydrogenation of highly excited PAHs following UV absorption and hydrogenation reactions with atomic hydrogen (Tielens et al., 1987, Le Page et al., 2003). Theoretically and experimentally, it has been well established that dehydrogenation is an 'on/off' switch; for example, when dehydrogenation becomes important, a PAH quickly loses all its hydrogens; over a small range of G_0/n_H (Ekern et al., 1997, Tielens, 2005, Berné & Tielens, 2012, Zhen et al., 2013). Hence, for any PAH, there is a critical G_0/n_H ratio and a PAH becomes fully hydrogenated (completely dehydrogenated) if the G_0/n_H ratio is less (larger) than this ratio. As the unimolecular dissociation rate depends exponentially on the internal excitation temperature and, therefore, in a given radiation field, on the size of the PAH, PAHs with a size smaller than a critical size are fully stripped of all their H (and do not contribute emission in any C-H mode), while PAHs larger than this size are fully hydrogenated. Small fully dehydrogenated PAHs are quickly destroyed through C_2 loss (or isomerized to cages and fullerenes) by further UV photon absorption (Joblin, 2003, Zhen et al., 2013) and this is expected to be the dominant photo destruction route for small PAHs (Berné & Tielens, 2012, Montillaud et al., 2013). Hence, as small dehydrogenated PAHs are quickly destroyed, the $I_{6.2}/I_{11.3}$ μm band ratio would show little variation. Moreover, if dehydrogenation were important, one would expect to see the solo/duo/trio ratio change in the direction of a larger solo/trio ratio (Schutte et al., 1993), which is not what is observed (Acke et al., 2010, Hony et al., 2001). For these reasons, the $I_{6.2}/I_{11.3}$ ratio have been widely accepted as variations in the ionization state of the emitting PAHs, and we follow this analysis here.

The PAH-to-dust mass fraction is difficult to constrain as PAHs may take part in various processes. The PAHs may be prone to photo-destruction (e.g. Guhathakurta & Draine

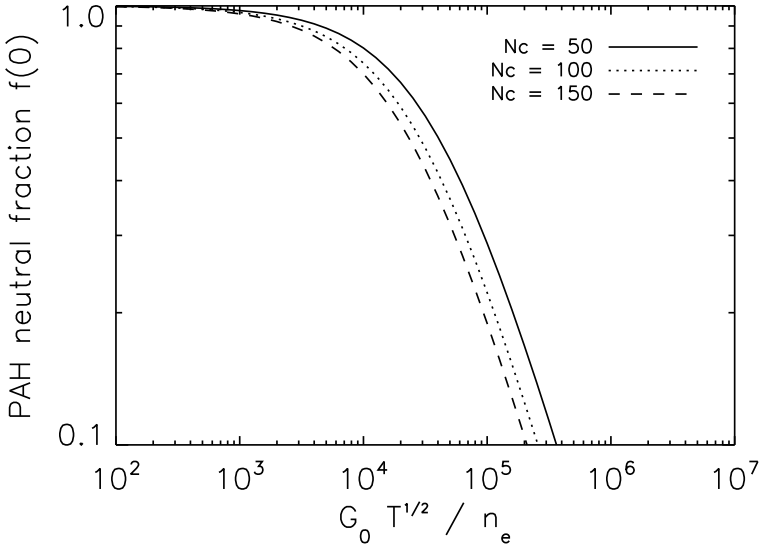

Figure 5.6: *The fraction of neutral PAH molecules $f(0)$ is given by the UV field, the temperature, and the electron number density and is controlled by the ionization parameter $G_0 T^{1/2}/n_e$. In our models, we assume a PAH size of $N_C = 100$.*

1989, Le Page et al. 2003, Visser et al. 2007). Moreover, it has been argued that PAHs may take part in the dust coagulation process (Dullemond et al., 2007a) or replenished by mixing processes in the disk (Siebenmorgen & Krügel, 2010). Observational evidence of the role of PAHs in these processes are not conclusive and it is presently unclear how important these routes are. As for PAH destruction, very small, catacondensed PAHs can also lose C_2H_2 through UV photon absorption while the H-loss channel dominates. However, the dominant photochemical destruction channel for the carbon skeleton for large pericondensed PAHs is through complete dehydrogenation followed by C_2 loss (Ekern et al., 1997, Joblin, 2003, Zhen et al., 2013). Larger PAHs are notoriously difficult to destroy (Jochims et al., 1994). Here, we treat the PAH/dust abundance ratio as a free parameter to be determined through our model fits of the observed SEDs.

5.3.2 The ionization balance

The charge of PAHs is determined by the balance between photo-ionization and electron recombination. The description of the ionization balance of PAHs is largely adopted from Bakes & Tielens (1994) and Tielens (2005). Here, we provide a brief summary. The ionization balance of PAHs is controlled by the parameter γ:

$$\gamma = G_0 T^{1/2}/n_e \tag{5.2}$$

with G_0 as the intensity of the radiation field between 6.0 and 13.5 eV in units of the Habing field u_{UV}^{Hab}, T the gas temperature, and n_e the electron density.

The intensity of the UV radiation field inside the disk can be characterized by $G_0 = u_{UV}/u_{UV}^{Hab}$, where

$$u_{UV} = \int_{6eV}^{13.5eV} u_\nu d\nu = \int_{6eV}^{13.5eV} (h/c) h\nu N_{ph} d\nu. \tag{5.3}$$

Here $u_{UV}^{Hab} = 5.33 \times 10^{-14}$ erg cm^{-3} is the energy density in the UV mean interstellar radiation field (Habing, 1968), and N_{ph} is the number of photons in units of cm^{-2} s^{-1} erg^{-1}. The contribution from the interstellar radiation field is also taken into account. Regions in the disk, where the optical depth is high may not receive enough photons between 6 and 13.6 eV to calculate G_0. In those cases, G_0 is set to a lower limit value of 10^{-6}. Because of their high temperatures, Herbig stars generate strong photospheric UV fluxes. Additional UV excess due to accretion is relatively unimportant for these stars because of the low accretion rates in most targets. The effective temperature can, therefore, be considered as a direct indicator of the stellar UV radiation field.

The surface layer of the disk is essentially a photodissociated region (Woitke et al., 2009, Kamp et al., 2010) and the electron abundance, $x_e = n_e/n_H$, can be set equal to the C^+ abundance, based on an equilibrium between the photoionization of neutral C and the recombination of C^+ (Tielens & Hollenbach, 1985). We adopt an ISM abundance of $n_C = 1.5 \times 10^{-4} n_0$ (Cardelli et al., 1996) with n_0 the gas density in cm^{-3}. The C / C^+ ratio changes with depth but carbon is largely ionized whenever there are UV photons around(Tielens, 2005). Therefore, we assume that ionized carbon with a fixed abundance is the dominant supplier of free electrons in the region where PAH emission originates,.

At higher altitudes in the disk surface, the gas temperature may exceed the dust temperature (e.g., Kamp & Dullemond 2004, Nomura & Millar 2005). However, it is beyond the scope of this paper to fully solve the thermo-chemistry balance. As the temperature only enters through a square root, we adopt $T_{gas} = T_{dust}$ in our model studies.

We consider PAH with only two accessible ionization stages, the neutral and the singly charged cation. The neutral fraction, $f(0)$ is given by

$$f(0) = [1 + \gamma_0]^{-1} \tag{5.4}$$

with γ_0 the ratio of the ionization rate over the recombination rate, which, adopting the classical expression, is is

$$\gamma_0 = 3.5 \times 10^{-6} N_c^{1/2} \frac{G_0 T^{1/2}}{n_e}. \tag{5.5}$$

Here, the constant 3.5×10^{-6} is derived from the probability that a colliding electron sticks (Tielens, 2005). The MCMax code calculates the neutral fraction $f(0)$ in each grid cell in the disk. For all grid cells with neutral fractions between $f(0) = 0$ (ionized) and $f(0) = 1$ (neutral), MCMax linearly interpolates between the neutral and ionized PAH emission profiles.

Figure 5.6 shows the relation between the neutral fraction and $G_0 T^{1/2}/n_e$ for different PAH sizes. We find that most PAHs are emitting in the physical range $G_0 T^{1/2}/n_e \sim$

$10^3 - 10^6$ in our disk models. Therefore, our two charge model covers the physical range of our interest.

The ultimate goal of our modeling is to understand the range of band strength ratios $I_{6.2}/I_{11.3}$ for the four transitional disks (HD 97048, HD 169142, HD135344 B, and Oph IRS 48) and to learn what differences in disk properties are responsible for neutral versus ionized PAH emission. In the next section we first describe a benchmark model and explore how PAHs behave as a function of the relevant parameter space. After that, we present PAH models of four transitional disks, which fit the $I_{6.2}/I_{11.3}$ ratio by combining contributions from neutral PAHs in the dusty outer disk and ionized PAHs in an optically thin gas flow through the gap.

5.4 Benchmark model

We study the behavior of the degree of ionization, the PAH luminosity, and the radial dependence of the PAH charge state throughout the disk. We focus on PAH emission from self-consistent disks models, which include high optical depth media. In this approach, the vertical density structure of the gas is set by hydrostatic equilibrium, and dust properties, such as scattering, grain sizes, and grain composition, are important input parameters for the radiative transfer. This allows us to evaluate how the charge state of PAH molecules in the disk translates to the spectrum. We start with a simple hydrostatic flaring disk model for which we adopt the stellar properties of HD 97048. All relevant star and disk parameters, as well as the results of the PAH characteristics, are given in Table 5.2.

We assume a dust composition of 80% silicate and 20% amorphous carbon. The dust composition with reference to the optical constants is 12% $MgFeSiO_4$ (Dorschner et al., 1995), 34% Mg_2SiO_4 (Henning & Stognienko, 1996), 32% $MgSiO_3$ (Dorschner et al., 1995), 2% $NaAlSi_2O_6$ (Mutschke et al., 1998) and 20% C (Preibisch et al., 1993). The shape of our particles is irregular and approximated using a distribution of hollow spheres (DHS, Min et al. 2005). A vacuum fraction of 0.7 has been used, which breaks the perfect symmetry of the spherical compact grain. Though we do not focus on detailed feature shapes this choice therefore does not influence our results.

The dust size range is from $a_{min} = 1$ µm up to $a_{max} = 1$ mm and follows a power-law distribution with $a_{pow} = -3.5$. The surface density of the gas and dust decreases proportional to r^{-1}. Typically in the ISM, the fraction of the mass locked up in PAHs relative to the total dust mass is 4×10^{-2} (Draine & Li, 2007). A comparison with the PAH abundance in protoplanetary disks may be misleading because gas and dust in disks are expected to be processed. Given the uncertainties in abundances, we find that a PAH-to-dust mass fraction of 5.0×10^{-4} fits the PAH luminosity of HD 97048. We use a single size PAH molecule with $N_C = 100$, which has a radius of $a_{PAH} = 6$ Å. The assumption of PAH-size may be arbitrary because the ionization depends weakly this choice. Though this paper only intends to demonstrate the effect of ionization, and the choice of a typical PAH of $N_C = 100$ therefore seems justified.

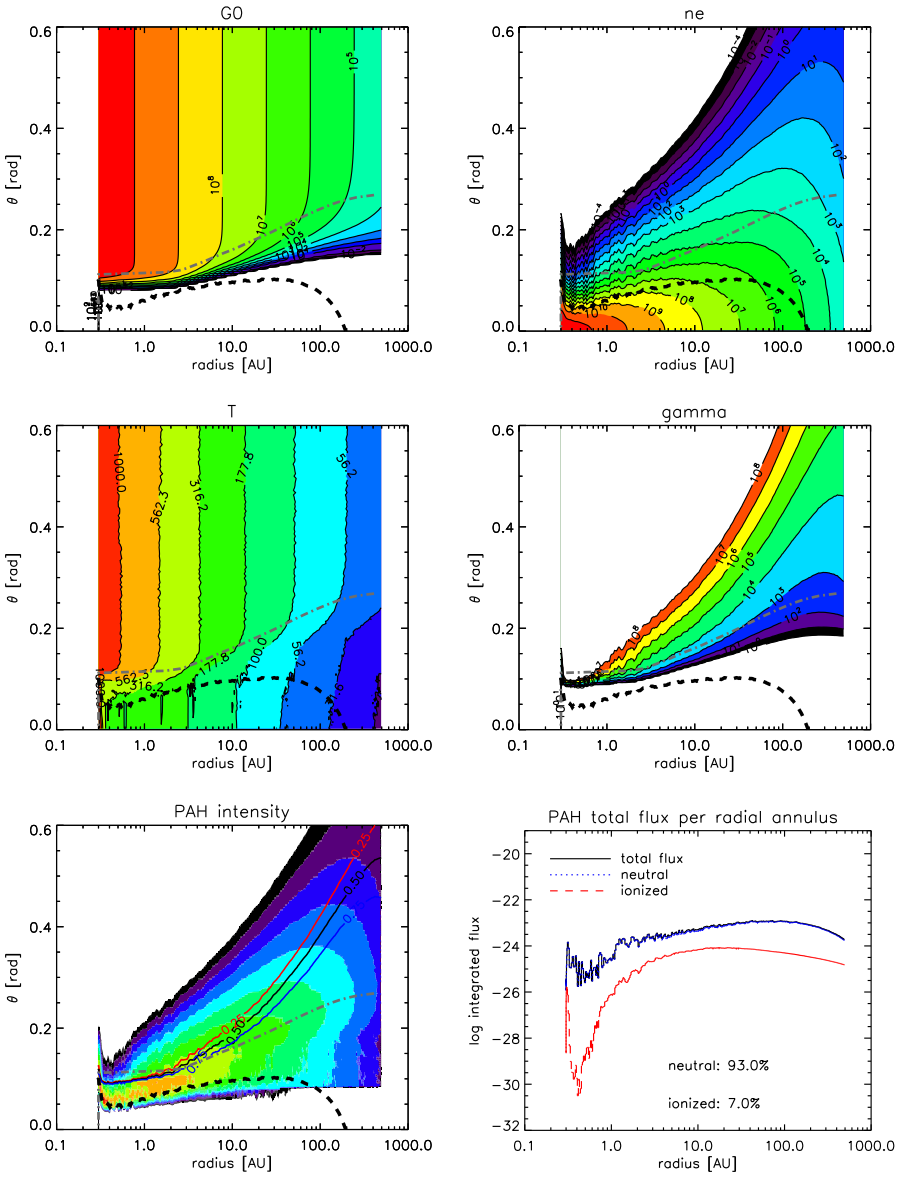

Figure 5.7: *Diagnostic plots of benchmark model. The black dashed line is the vertical $\tau_{\rm MIR} = 1$ surface at 10 μm, the grey dashed-dotted line gives the radial $\tau_{UV} = 1$ surface at 0.1 μm.* ***Upper left:*** *the strength of the UV field G_0.* ***Upper right:*** *the electron number density n_e.* ***Middle left:*** *the temperature distribution in the disk.* ***Middle right:*** *the ionization parameter γ given by $G_0 T^{1/2}/n_e$.* ***Bottom left:*** *the PAH intensity of a 2D cut through the disk. This diagnostic plot shows the origin of the PAH flux in the disk, i.e. the contributions of PAH emission to the final spectrum. The intensity of the PAH flux is shown in logarithmic scale (arbitrary scaling), where each colour spans an order of magnitude. The red, black and blue solid lines give the locations where the neutral fractions $f(0)$ are respectively 0.25, 0.5, 0.75. The neutral fractions are computed by equations 5.4 and 5.5 in each grid cell of the disk. PAHs in the surface of the disk are largely ionized, while PAHs in the mid-plane are neutral.* ***Bottom right:*** *the intensity of PAH emission per radial annulus (arbitrary units). The blue and red lines give the neutral and ionized contributions. 93% of the PAH molecules in the benchmark flaring disk model are neutral. The contribution from neutral PAHs dominate irrespective of the radial location in the disk. The noise is due to photon statistics. The height θ relates to Z by, $\theta = \tan(Z/r)$.*

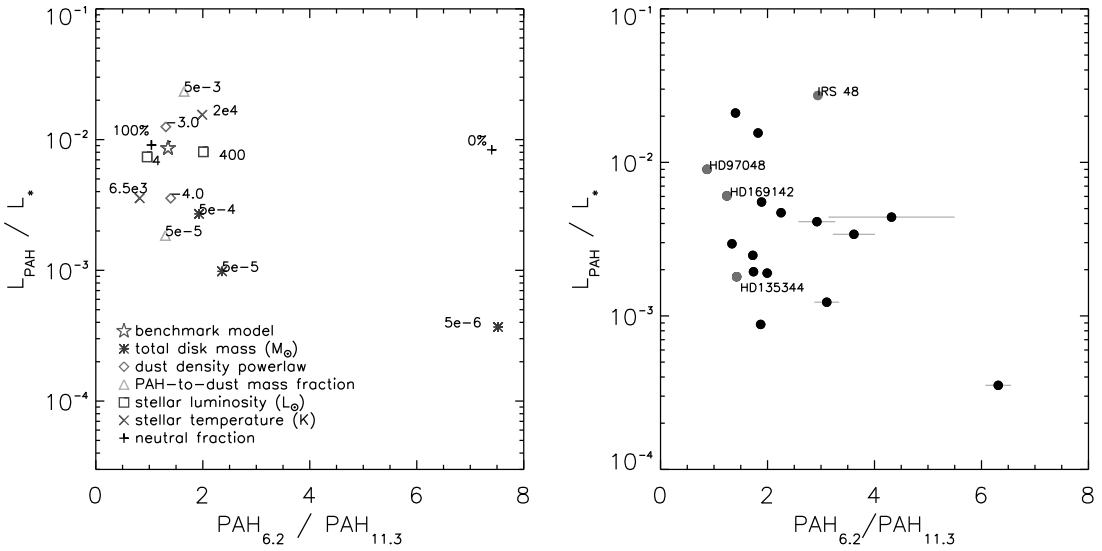

Figure 5.8: *PAH luminosities (L_{PAH}/L_*) compared to the $I_{6.2}/I_{11.3}$ ratio for the benchmark modeling grid (left) and the observations of Herbig stars (right). Several parameters of the benchmark model are varied and their effect to the PAH luminosity and $I_{6.2}/I_{11.3}$ ratio is shown. The main results of the benchmark modeling grid study is that in general the PAH neutral fraction is high and ionized PAHs originate from optically thin, low density environments. The red dots show the objects studied in this paper. The parameters of all the objects shown in this right plot are listed in Table 5.1.*

Figure 5.7 presents six diagnostic plots of the benchmark model. The black dashed-dotted line gives the radial $\tau_{UV} = 1$ surface at 0.1 μm. This is the location where UV-photons from the central star are scattered inward in the disk. The gray dashed line gives the vertical $\tau_{MIR} = 1$ surface at 10 μm. Above this line, MIR photons can escape the disk. Therefore, it shows the region of the disk where the PAH emission originates. The upper four plots give, respectively, the strength of the UV field G_0, the distribution of the electron number density n_e, the temperature T in the disk, and the ionization parameter γ given by $G_0 T^{1/2}/n_e$. The ionization parameter γ is a representation of the physical conditions, which control the ionization balance of PAHs. Thus, at the radial $\tau_{UV} = 1$ surface between 10 AU and 100 AU, $\gamma \sim 10^3 - 10^4$. The bottom left plot shows the PAH intensities (arbitrary scaling) responsible for the observed emission. The PAH intensity shows the relative contributions of PAH emission to the final spectrum. The region where the PAH contribution is highest lies between the radial $\tau_{UV} = 1$ and vertical $\tau_{MIR} = 1$ surfaces. The red, black and blue solid lines give the locations, where the neutral fractions $f(0)$ are, respectively 0.25, 0.5 and 0.75. The neutral fractions are computed in each grid cell of the disk using equations 5.4 and 5.5. From this, we can see that most of the PAH emission originates in values below the $f(0) = 0.75$ line and, thus, have a high neutral fraction. The bottom right plot shows the intensity of the integrated PAH emission per radial annulus (arbitrary units). The PAHs between ∼20–200 AU contribute most to the final spectrum. The blue and red lines give the decomposed neutral and ionized contributions. Of the PAH molecules, 93% in the benchmark flaring disk model are neutral.

An important insight from the benchmark model is that neutral PAHs dominate the emission at all radii in the disk. There is, thus, no gradient in the neutral fraction of PAHs as a function of radius in an optically thick disk. Only the surface layer of the disk produces ionized PAH emission but that contribution is ∼1–2 orders of magnitude smaller than the contribution from neutral PAHs from deeper layers in the disk. The effect of a higher UV field does not translate to a higher degree of ionization because the electron density is also higher closer to the star.

The PAH luminosity of the benchmark model is $L_{PAH}/L_* = 8.40 \times 10^{-3}$ and band strength ratio $I_{6.2}/I_{11.3} = 1.35$. The results are shown on the top of Figure 5.8, where a direct comparison can be made to the observations of our sample of Herbig stars, as shown on the bottom plot. As a next step, we investigate the effects of varying the star and disk parameters of the benchmark model on L_{PAH} and $I_{6.2}/I_{11.3}$. We discuss the parameters which have a significant effect on the charge state of the PAHs.

Table 5.2: *Characteristics of benchmark model and models of four transitional disks.*

Parameter		Unit	Benchmark	HD 97048	HD 169142	HD 135344 B	Oph IRS 48
Stellar temperature	T_*	K	10 000	10 000	8200	6590	9000
Stellar luminosity	L_*	$L_\odot$	40	40	15.3	8.26	14.3
Stellar radius	R_*	$R_\odot$	2.12	2.12	1.94	2.20	2.30
Stellar mass	M_*	$M_\odot$	2.50	2.50	2.28	3.30	2.25
inclination	i	°	45	43	13	11	48
Distance	d	pc	158	158	145	140	120
Carbon atoms in PAH	N_C	…	100	100	100	100	100
Silicate mass	M_{Si}	M_{dust}	0.8	0.8	0.8	0.8	0.8
Carbon mass	M_C	M_{dust}	0.2	0.2	0.2	0.2	0.2
Min dust size	a_{min}	µm	1	0.5	0.5	1	0.1
Max dust size	a_{max}	mm	1	1	1	1	1
Dust-size power-law index	a_{pow}	…	-3.5	-3.5	-3.5	-4.0	-4.0
Total, PAH neutral fraction	$< f(0)_{total} >$	…	0.93	0.97	0.92	0.91	0.54
Total, PAH ratio	$I_{6.2}/I_{11.3}$	…	1.35	1.27	1.36	1.42	3.30
Total, PAH luminosity	$L_{PAH,total}/L_*$	…	8.40×10^{-3}	9.13×10^{-3}	6.24×10^{-3}	3.45×10^{-3}	1.49×10^{-2}
Outer disk, PAH neutral fraction	$< f(0)_{disk} >$	…	0.93	0.97	1.00	1.00	0.98
Outer disk, PAH luminosity	$L_{PAH,disk}/L_{PAH,total}$	…	1	0.95	0.67	0.27	0.09
Outer disk, gas mass	$M_{gas,disk}$	$M_\odot$	5.0×10^{-2}	5.0×10^{-2}	8.0×10^{-3}	1.0×10^{-2}	3.0×10^{-3}
Outer disk, dust mass	$M_{dust,disk}$	$M_\odot$	5.0×10^{-4}	5.0×10^{-4}	8.0×10^{-5}	1.0×10^{-4}	3.0×10^{-5}
Outer disk, PAH mass	$M_{PAH,disk}$	$M_\odot$	2.5×10^{-7}	2.5×10^{-7}	4.0×10^{-8}	5.0×10^{-8}	1.5×10^{-8}
Outer disk, PAH-to-dust mass fraction	$f_{PAH,disk}$	…	5.0×10^{-4}	5.0×10^{-4}	5.0×10^{-4}	5.0×10^{-4}	5.0×10^{-4}
Outer disk, inner radius	$R_{in,disk}$	AU	0.3	34	23	30	63
Outer disk, outer radius	$R_{out,disk}$	AU	500	500	235	235	235
Disk gap, PAH neutral fraction	$< f(0_{gap}) >$	…	…	0.21	0.07	0.87	0.52
Disk gap, PAH luminosity	$L_{PAH,gap}/L_{PAH,total}$	…	…	0.05	0.33	0.73	0.91
Disk gap, gas mass	$M_{gas,gap}$	$M_\odot$	…	1.0×10^{-7}	1.4×10^{-8}	9.5×10^{-8}	1.9×10^{-6}
Disk gap, dust mass	$M_{dust,gap}$	$M_\odot$	…	1.0×10^{-9}	1.4×10^{-10}	9.5×10^{-10}	1.9×10^{-8}
Disk gap, PAH mass	$M_{PAH,gap}$	$M_\odot$	…	3.8×10^{-11}	5.8×10^{-12}	3.8×10^{-11}	7.7×10^{-10}
Disk gap, PAH-to-dust mass fraction	$f_{PAH,gap}$	…	…	4.0×10^{-2}	4.0×10^{-2}	4.0×10^{-2}	4.0×10^{-2}
Disk gap, inner radius	$R_{in,gap}$	AU	…	2.5	0.3	0.3	0.3
Disk gap, outer radius	$R_{out,gap}$	AU	…	34	23	30	63

5.4.1 Stellar properties

We varied the stellar temperatures and luminosities of the benchmark model. A decrease in stellar temperature and luminosity lowers the neutral fraction because the UV field G_0 decreases and fewer UV photons are available to excite the PAHs. Therefore, the $I_{6.2}/I_{11.3}$ ratio goes down. For a higher luminosity and/or stellar temperature, the UV field G_0 and, consequently, the $I_{6.2}/I_{11.3}$ ratio are higher. Figure 5.8 shows that our chosen range of stellar temperatures and luminosities result in band strength ratios $I_{6.2}/I_{11.3}$ between

$\sim 1-2.2$. This range covers 11 of the 18 Herbig stars shown on the right of Figure 5.8. None of the other 7 objects with higher $I_{6.2}/I_{11.3}$ ratios have temperatures and/or luminosities higher than 20 000 K and/or 400 $L_{\odot}$. Thus, for these objects, the stellar temperature and luminosity cannot explain the high band strength ratio $I_{6.2}/I_{11.3}$.

For stars with a lower temperature and/or luminosity, the UV density decreases and the contribution from PAHs heated by multi-photon events is lower. As PAHs heated by multi-photon events have a higher temperature, they also have a slightly higher $I_{6.2}/I_{11.3}$ ratio and vice versa. In the models with a lower stellar luminosity and temperature all the PAHs in the disk are neutral, although the $I_{6.2}/I_{11.3}$ ratio is slightly lower ($\sim 0.1-0.2$) than the 100% neutral benchmark model (see Figure 5.8). Thus, this difference is a result of the fraction of PAH emission heated by multi-photon versus single-photon events. However the difference is small and unimportant compared to the effect of ionization.

5.4.2 Grain properties

To test the effect of the grain size distribution, we change the dust density power-law to $a_{pow} = -3.0$ and $a_{pow} = -4.0$. For a relatively lower abundance of small grains ($a_{pow} = -3.0$), the average dust opacity is lower and the disk is less opaque. As a result, the PAH luminosity increases, since the optical depth in the disk is lower, and the region where PAHs can get excited is larger. For a higher abundance of small grains ($a_{pow} = -4.0$), the PAH luminosity decreases, since the optical depth in the disk is higher and the region where PAHs can get excited is smaller. The size distribution of dust grains has a strong effect on the PAH luminosity through the dust optical depth in the UV. If small dust grains are depleted, then the UV opacities in the disk are dominated by PAHs and a small amount of PAHs can give rise to a strong PAH luminosity. The effect on the degree of ionization is negligible since the ionization parameter γ and the neutral fraction $f(0)$ change accordingly to the optical depth and the fraction of ionized to neutral PAHs stays roughly similar.

5.4.3 PAH properties

Since evolutionary processes may affect the PAH composition in the disk, it is difficult to constrain PAH sizes and abundances. In our benchmark model, we assume a PAH mass of 5.0×10^{-4} M_{dust}. For an order of magnitude higher and lower PAH mass fraction, the PAH luminosities change by factors of 2.7 and 0.21 respectively. The PAH mass fraction may then explain the wide spread in PAH luminosity among Herbig stars ($\sim$3 orders of magnitude, see Table 5.1)

Figure 5.8 shows a small shift in the $I_{6.2}/I_{11.3}$ ratio for factor of 10 higher or lower PAH-to-dust mass fraction. This is also because the PAH-to-electron abundance is then altered, which changes the amount of electrons per PAH molecule available for recombination. Because PAH sizes in disks are expected to be in the order of $N_C \sim 50-150$

(Tielens, 2008), the difference in PAH sizes have a very small effect on the final spectra because the neutral fraction depends only on the square root of the PAH size in our ionization model (equation 5.5).

5.4.4 Disk mass

We test the effect of lower disk masses on the PAH characteristics by decreasing the total disk mass from 5×10^{-2} $M_\odot$, which is four orders of magnitude down to 5×10^{-6} $M_\odot$. For a less massive disk, the disk vertical height and, consequently, the fraction of the stellar luminosity captured by the disk are lower. Therefore, the PAH luminosity drops with decreasing disk mass, even when the disk is still optically thick.

The charge state increases when the mass of the disk becomes so small ($M_{disk} \lesssim 5 \times 10^{-5}$ $M_\odot$) that the disk becomes optically thin. At that point, the UV field G_0 is high even in the mid-plane of the disk, while the electron density n_e is lower. As a result, the fraction of ionized PAHs in the benchmark model with a disk mass of 5×10^{-6} $M_\odot$ is almost 100% and the $I_{6.2}/I_{11.3}$ ratio is 7.82. This low disk mass model and the Herbig star HD141569 have a similar L_{PAH} and $I_{6.2}/I_{11.3}$ (see also Table 5.1). This is consistent with our modeling result because HD 141569 is in the transition of a gas-rich protoplanetary disk to a gas-poor debris disk and largely optically thin (Li & Lunine, 2003, Thi et al., 2013).

5.4.5 Summary

The primary goal of our study is to identify the most important trends in the behavior of L_{PAH} and the $I_{6.2}/I_{11.3}$ ratio. We have presented a small parameter study around the benchmark model that investigates the behavior of PAH emission as a function of disk properties. We have covered the disk parameters which have a significant effect on the charge state and/or luminosity of the PAHs; the results are shown in Figure 5.8. The main insights are the following. **1)** The neutral fraction is high ($f(0) \sim 0.8 - 0.9$) for optically thick disks with properties typical for Herbig stars. **2)** The PAHs in an optically thick flaring disk are predominantly neutral at all radii. Thus the PAH neutral fraction shows no gradient with radius. **3)** The total PAH luminosity increases if the UV field is stronger if the PAH-to-gas mass fraction is higher and if the dust density is lower. **4)** The PAH ionization increases if the UV field is stronger and if the PAHs originate from low-density optically thin environments, where the electron density is low and the UV field is high.

5.5 Transitional disks

In this section, we show that fitting the PAH spectra of four transitional disks requires a significant contribution of ionized PAHs in gas flows through the gap. We perform quantitative fits to the PAH luminosities L_{PAH}/L_* and band strength ratios $I_{6.2}/I_{11.3}$ of four

transitional disks. We fit $I_{6.2}/I_{11.3}$ and L_{PAH}/L_* as close as possible to the observed values with a maximum discrepancy of a factor of 2. The presented PAH models demonstrate that a physical disk solution predicting an enhanced contribution of ionized PAHs from low-density, optically thin regions is successful in explaining the observed spectra. It is also consistent with the available spatial information shown in Figure 5.1.

We adopt the disk structures of HD 97048, HD 169142, HD 135344 B, and Oph IRS 48 derived by Maaskant et al. (2013) (see Table 5.2). All disks have large dust-depleted gaps and flaring outer disks. These large gaps are inferred from analysis of Q-band direct imaging. The absence of the 10- and 20-μm silicate feature indicates that the gaps are radially very large and empty in small dust grains. All disks show a NIR excess indicative of a hot (∼1500 K) component. To fit the SED at NIR wavelengths, an inner dust component has been added to the disk. For HD 97048, this inner disk is optically thick, is in hydrostatic equilibrium and is located from 0.3 – 2.5 AU. For HD 169142, HD 135344 B, and Oph IRS 48, optically thin spherical dust halos are added between 0.1–0.3 AU to account for an even stronger excess of NIR emission. For the outer disks, we assume that the vertical scale height is set by hydrostatic equilibrium. For the dusty disk, we assume a radial dependence of the surface density $\Sigma \propto r^{-1}$. Therefore, the density is highest in the mid-plane close to the star. If the inner disk is optically thick (as for HD 97048), the inner disk acts as a UV-shield and reduces the radiation field G_0 further out in in the disk.

We use the spatial information from the VLT/VISIR FWHM profile, as shown in Figure 5.1, to understand the distribution of PAHs throughout the disk. However, this information is only taken into account qualitatively, as we refrain from doing a detailed fit of the FWHM profile since there are issues with the point spread function (PSF) of the VISIR measurements. In addition, the origin of the N-band continuum is not well understood since it can be produced by very small grains or dust from the inner and/or outer disk (see Maaskant et al. 2013 for an extended discussion of this topic). A qualitative interpretation of the VLT/VISIR data is that the PAHs clearly come from larger scales than the N-band continuum for HD 97048; thus, PAH emission originates in the outer disk (in agreement with Lagage et al. 2006, Doucet et al. 2006). For HD 169142, HD 135344 B and Oph IRS 48, the FWHM in the PAH feature is equal and even smaller than the continuum. If PAH emission would originate only from the outer disk, than the 11.3-μm PAH feature would be resolved with respect to the FWHM of the continuum. Thus we interpret this as a significant contribution of PAH emission that comes from within the dust-depleted gap of the disk.

5.5.1 Adding low-density gas flows to the disk structure

Our model study in Section 5.4 has shown that the PAH emission from disks is predominantly neutral in character unless the disk mass is very low. In a more general sense, ionized PAHs are produced by high UV fields (or low dust densities) and low electron densities. The fitting of the observed $I_{6.2}/I_{11.3}$ ratio of PAHs in the integrated spectrum of the disk has been done by adding a low-density gaseous disk in the gap. In this way, PAH emission originates not only in predominantly neutral PAHs in the optically thick inner and outer

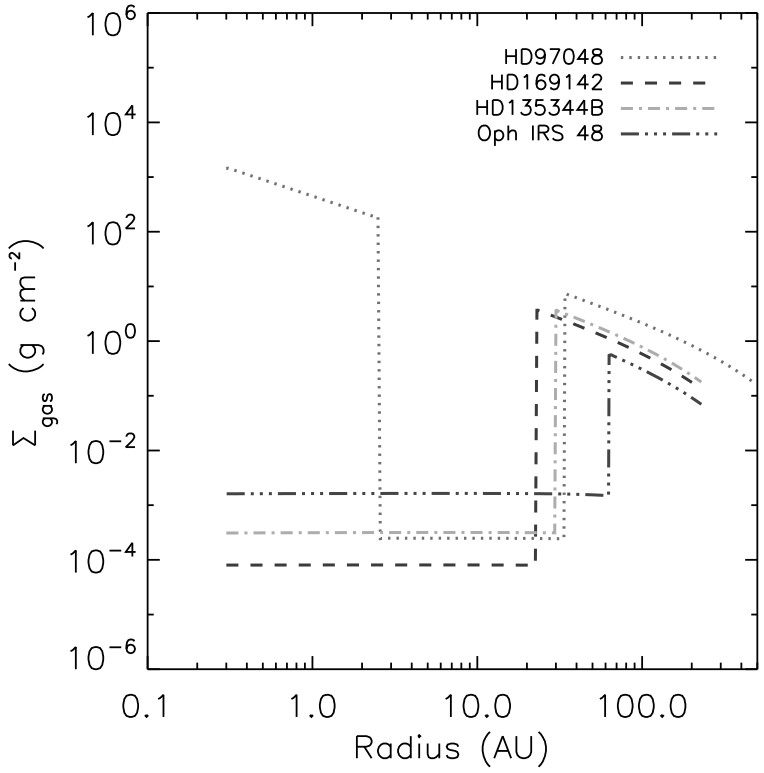

Figure 5.9: *The gas surface densities Σ_{gas} for the PAH models as a function of radius. Gas surface densities of $\Sigma_{gas} \sim 10^{-3} - 10^{-4}$ g cm^{-2} in the gaps are consistent with hydrodynamical planet formation models and represent gas flows through protoplanetary gaps. The PAHs in these low-density gaps have a high ionization fraction.*

disk but also in ionized PAHs in the disk gap. To model the gas flows though the gap and to prevent PAH self-shielding effects, we assume a radial dependence of the surface density of $\Sigma \propto r^0$ in the gap. The gas surface densities Σ_{gas} as a function of radius are shown in Figure 5.9. The required surface densities of the gas within the gap are on the order of $\Sigma_{gas} \sim 10^{-3} - 10^{-4}$ g cm^{-2}, which are consistent with hydrodynamical predictions of gas flows through planets opening a gap (e.g. Bryden et al. 1999, Dodson-Robinson & Salyk 2011, Zhu et al. 2012, Fung et al. 2013). The basic parameter assumptions and results of our best-fit models are given in Table 5.2. Figure 5.10 shows the PAH intensities of our derived PAH models as a function of the location in the disk.

5.5.2 PAH fit of the transitional disk HD 97048

The PAH luminosity of HD 97048 can be fitted with a PAH-to-dust mass fraction of 5.0×10^{-4} by giving a luminosity of $L_{PAH}/L_* = 9.13 \times 10^{-3}$, which is close to the observed $9.01 \pm 0.03 \times 10^{-3}$ in the IRS/Spitzer spectrum. The averaged neutral fraction is $f(0) = 0.97$; thus, only 3% of the PAHs in the disk are ionized. We note that the calculated $I_{6.2}/I_{11.3}$ ratio (1.27) is larger than the observed one (0.87). However, that may well be

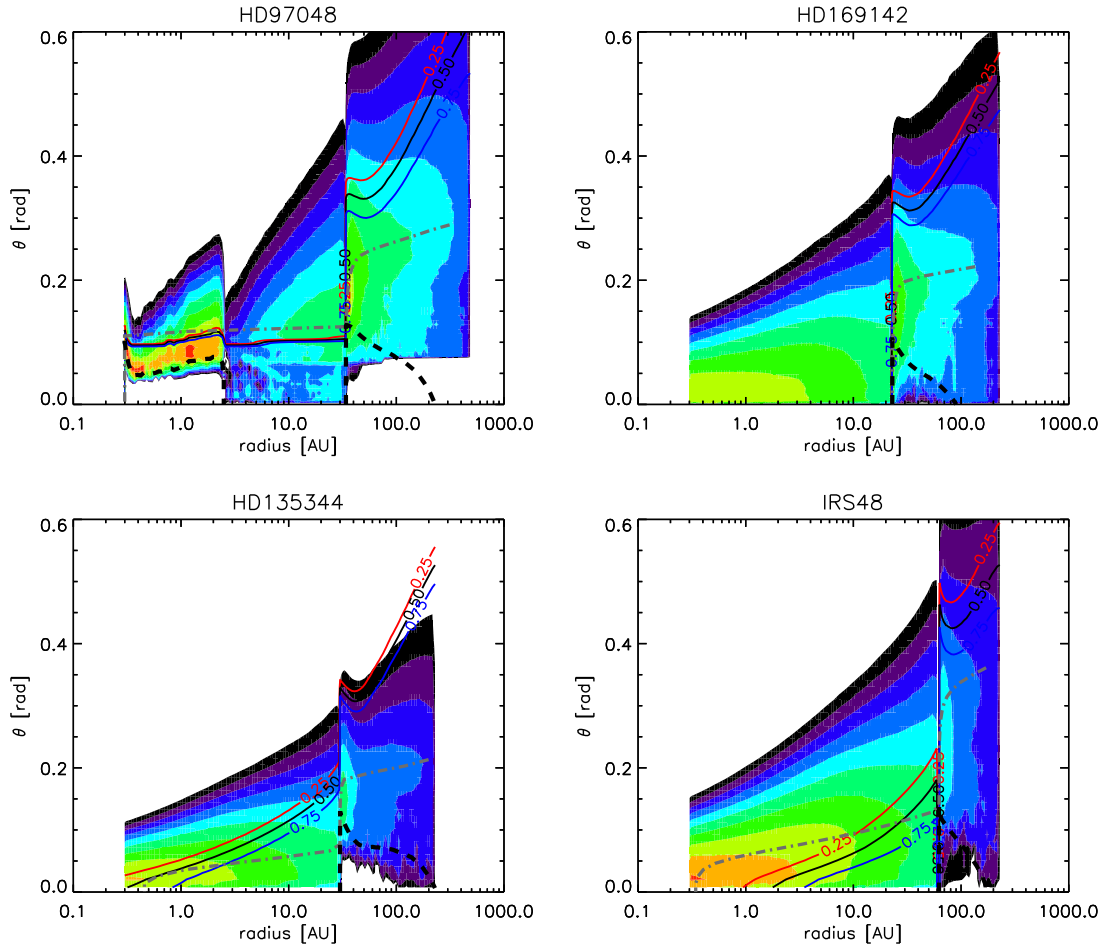

Figure 5.10: *Diagnostic plots showing the origin of the PAH flux in the disk, i.e. the contributions of PAH emission to the final spectrum. The intensity of the PAH flux is shown in logarithmic scale (arbitrary scaling), where each colour spans an order of magnitude. Top left: HD 97048, top right: HD 169142, bottom left: HD 135344 B, bottom right: Oph IRS 48. The red, black and blue solid lines give the locations where the neutral fractions $f(0)$ are respectively 0.25, 0.5, 0.75. The neutral fractions are computed by equations 5.4 and 5.5 in each grid cell of the disk. PAHs in the surface of the disk are largely ionized, while PAHs in the mid-plane are neutral. The black dashed line is the vertical $\tau_{\rm MIR} = 1$ surface at 10 μm, the grey dashed-dotted line gives the radial $\tau_{UV} = 1$ surface at 0.1 μm. The height θ relates to Z by, $\theta = \tan(Z/r)$.*

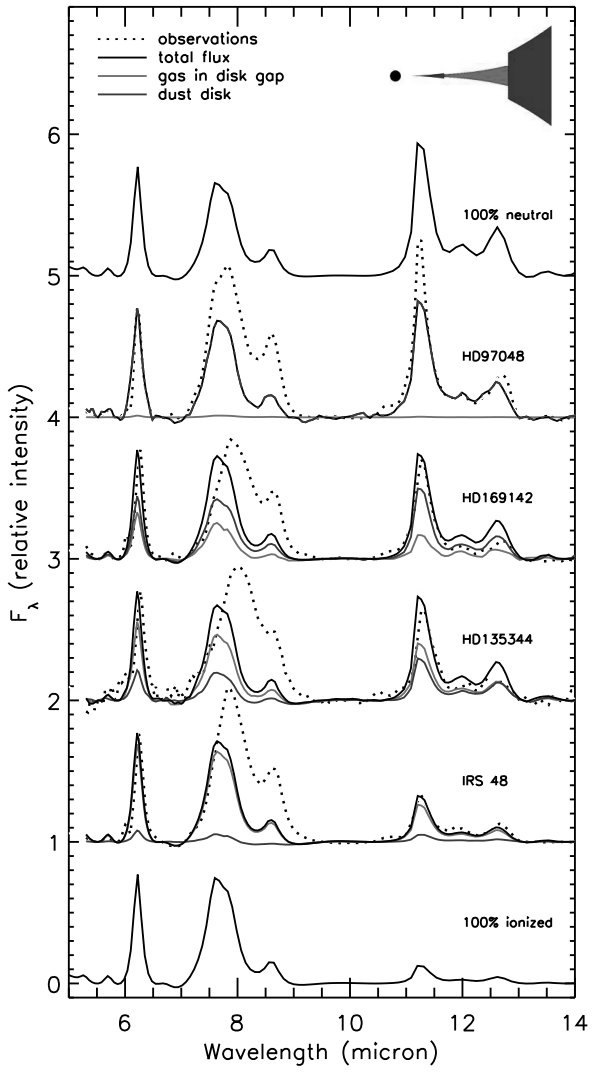

Figure 5.11: *The spectra at the top and the bottom represent the benchmark models with respectively 100% neutral and 100% ionized PAHs. The middle four spectra show transitional disks with the dotted line the Spitzer observations, the solid black lines the total fluxes of the best fit models, the solid grey line the contribution from PAHs in the dust disk, and the solid light grey line the contribution from the low density optically thin disk. Note that for HD 97048, there is no low density optically thin disk component thus the solid black and grey lines are merged into a black dashed line. For Oph IRS 48, the spectrum is dominated by ionized PAHs from the low density optically thin disk.*

an 'artefact' of our adopted PAH properties as the intrinsic $I_{6.2}/I_{11.3}$ ratio of neutral PAHs in the Draine & Li (2007) model is arbitrarily set. Figure 5.8 shows that the benchmark model in which 100% of the PAHs are neutral, which still has a higher $I_{6.2}/I_{11.3}$ fraction (0.94) than HD 97048. Thus, a better fit to the the observed $I_{6.2}/I_{11.3}$ ratio of HD 97048 is not possible because the adopted PAH properties do not cover lower $I_{6.2}/I_{11.3}$ ratios.

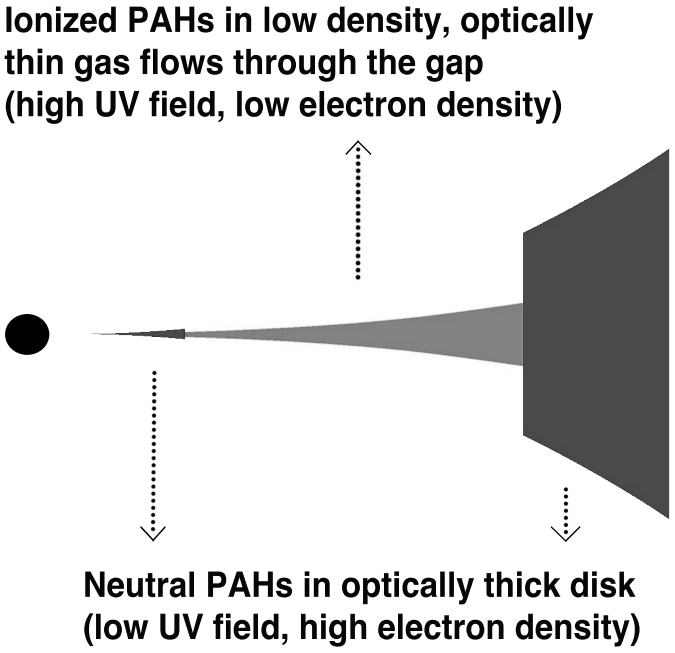

Figure 5.12: *Sketch of the main result of this paper. Neutral PAH emission originates in an optically thick disk (dark grey components) and ionized PAH emission from low density, optically thin gas flows through protoplanetary disk gaps (light grey component).*

The gap of HD 97048 may not be completely empty because no gap is seen in polarized scattered light (Quanz et al., 2012). Therefore, we fill the gap of HD 97048 with a gas surface density which of $\Sigma_{gas} = 2.5 \times 10^{-4}$ g cm^{-2}, which is similar to the solutions we find for the other transitional disks in our sample (in the next Section 5.5.3). Due to the optically thick inner disk, most of the material in the gap is in the shadow of the inner disk. Thus, the PAHs in the disk gap only contribute 5% to the total PAH luminosity. A small fraction of dust may also be present in the gap, which may explain the scattered light observations of Quanz et al. (2012). However, we do not further investigate that scenario since that is not the focus of our paper. The spectra of the PAH components from the optically thick dust disks are shown by the blue lines in Figure 5.11. The red lines show the PAH emission components from the low-density optically thin gas flows in the gaps.

There are two possibilities why HD 97048 is largely neutral. One explanation is because less (ionized) PAH emission originates in the gap. This occurs because they are in the shadow of the optically thick inner disk. The second explanation is because the contribution from PAHs in the large flaring outer disk is still large and dominating (compared to the other disks in our sample which have smaller outer disk radii). We have run several test models without optically thick inner disks, test models with a higher surface density in the gap, and test models with smaller outer disk radii. The results suggest that the first

explanation is most important, because models without an optically thick inner disk show a strong increase of L_{PAH} and $I_{6.2}/I_{11.3}$ due to the fact that (ionized) PAHs in the gap are now directly exposed to the UV emission. Since this is not observed, we suggest that the inner disk of HD 97048 is still optically thick.

5.5.3 PAH fits of the transitional disks HD 169142, HD 135344 B and Oph IRS 48

The model solution of HD 97048 does not work for HD 169142, HD 135344 B, and Oph IRS 48 for two reasons. First, the model is not consistent with the FWHM profiles because the observed PAH features are not extended compared to the continuum. Second, the observed $I_{6.2}/I_{11.3}$ ratios are too high to be fitted by neutral PAHs from the outer disk suggesting that a significant contribution comes from ionized PAHs. To fit the PAH spectra of HD 169142, HD 135344 B, and Oph IRS 48 we increase the contribution from the low density, optically thin gas in the disk gaps. We keep the PAH-to-dust fraction in the outer disk similar to that of HD 97048 ($f_{PAH,disk} = 5.0 \times 10^{-4}$).

To obtain a high PAH luminosity and low dust continuum, we assume that the opacities are dominated by the PAHs in the gap. For that reason, we assume that there are no small (~ 1 μm) grains and, thus, no dust is visible in the spectrum. To get a lower limit to the gas mass needed in the disk gap, we adopt a PAH mass fraction similar to the ISM of $f_{PAH,gap} = 4.0 \times 10^{-2}$. For HD 169142, HD 135344 B and Oph IRS 48, the luminosity L_{PAH}/L_* and the $I_{6.2}/I_{11.3}$ ratio are simultaneously fitted by adjusting the total amount of mass in the gas disk in the gap. The characteristics are given in Table 5.2. We have aimed to fit L_{PAH}/L_* and $I_{6.2}/I_{11.3}$ as close to the observed values as possible. We find that models could be found, which fit the observed L_{PAH}/L_* and $I_{6.2}/I_{11.3}$ within a factor of 2 for all the objects. Following this fitting procedure, PAHs in the gas flows through the gap produce respectively 33%, 73%, and 91% of the total PAH luminosity of HD 169142, HD 135344 B, and Oph IRS 48.

The diagnostic plots in Figure 5.10 show that the disk gap of HD 169142 has a high fraction of ionized PAHs, while the disk gap of HD 135344 B has a much larger fraction of neutral PAHs. This difference can be attributed to the lower stellar temperature of HD 135344 B ($T = 6590$ K) compared to HD 169142 ($T = 8200$ K) producing a lower UV-field.

5.5.4 Summary

We have found a model solution to fit L_{PAH} and the $I_{6.2}/I_{11.3}$ ratio of the transitional disks HD 97048, HD 169142, HD 135344 B, and Oph IRS 48. Observations constrain a contribution of ionized PAHs that arise from within the dust gap (see Figure 5.1). Our PAH models combine PAH contributions from the surface of a flaring dust disk and a gaseous disk component inside the gap where the ionization fraction can be high. The

density structure of gas and dust in the disk is key to the PAH charge state, since the UV field and electron density are the main parameters that determine the PAH ionization.

We stress that the scale height and surface densities as a function of radius are poorly constrained for the inner regions. However, the presented PAH model solutions do make a constraint that a particular abundance of ionized PAHs in an optically thin, low density environment is required to fit the spectra. We have chosen to present the models for which the vertical density structure is set by hydrostatic equilibrium. Alternatively we can parameterize the density structure in the disk gap and adopt a higher scale-height of the gas in the gap to obtain similar results. For example, an even better fit to the observed L_{PAH}/L_* can be obtained by artificially increasing the scale height of the gas in the gap for Oph IRS 48 (which may be an effect of a larger gas temperature due to UV irradiation). A fit to the observations is then found using a slightly higher mass $M_{PAH,gap} = 1.2 \times 10^{-9}$ $M_\odot$ and setting the vertical scale height $H_0 = 3.0$ AU at $R = 30$ AU where $H \propto r^{1.1}$. For comparison, the hydrostatic disk structure has a pressure scale height of $H_0 = 2.1$ AU at $R = 30$ AU.

5.6 Discussion

In the following section we discuss our results on PAH ionization in relation to the disk structure. First, we discuss observations and models of gas in protoplanetary disk gaps. Thereafter, we discuss our results in the context of disk evolution in Herbig stars.

5.6.1 Gas flows through protoplanetary gaps

To fit the observed PAH spectra of the transitional disks in our study, we find that a requirement is to add a 'gaseous' low-density, optically thin disk in the gap to account for a higher fraction of ionized PAHs. Observations of gas in disk gaps can be understood in the context of planet formation models. The disk should go through a gas-rich/dust-poor stage if planets form by a two-step process where grains first agglomerate into large rocky cores, followed by the accretion of a gaseous envelope (e.g. Lissauer 1993). As PAHs are small molecules, which are thought to travel along with the gas, we first compare PAHs to other gas diagnostics. Thereafter, we discuss our results in the context of theoretical modeling of gas flows through gaps.

Recent Herschel/PACS observations show that Herbig objects with pure rotational CO transitions have a strong UV luminosity and strong PAH emission (Meeus et al., 2013). However, for a number of other molecular lines, no connection to the PAH luminosity has been reported (Fedele et al., 2013). From these observations, it is difficult to deduce how PAHs and the gas are connected. On the other hand, there is ample evidence for (molecular) gas in disk gaps. In high-resolution M-band spectral studies of transitional disks, modeling of the rovibrational CO emission yields a great diversity of inner disk gas content and of gas/dust ratios (Salyk et al., 2007, 2009). Similar studies have been carried

out for HD 135344 B (Pontoppidan et al., 2008) and Oph IRS 48 (Brown et al., 2012a) where the respective authors find evidence for significant quantities of CO gas within the dust gap. Salyk et al. (2011) show that the detection efficiency of H_2O, OH, HCN, C_2H_2, and CO_2 depends on the disk color, $F_{30}/F_{13.5}$, Hα equivalent width, and, tentatively, the mass accretion rate, $\dot{M}$. This may suggest a connection between regions of lower dust/gas ratio in the disk and the strength of these molecular lines. Recent ALMA observations of HD 142527 have shown that reservoirs of gas are present in the dust depleted regions (Casassus et al., 2013). These observations show that gas flows through dust-poor regions are not uncommon in protoplanetary disks, which is consistent with our results.

Hydrodynamical simulations of the disk structure caused by planet formation predict the opening of an annular 'gap', where the structure and depth of the gap is dependent on the mass of the planet and disk viscosity (e.g., Bryden et al. 1999, Varnière et al. 2004). Mass can penetrate through the gap and flow onto the planet, or flow through the gap and replenish the inner disk (Lubow et al., 1999, Paardekooper & Mellema, 2004, Edgar & Quillen, 2008, Tatulli et al., 2011). Since pressure gradients at the outer edge of the gap, which are cleared by the planet, act as a filter, this process can also produce a very large gas-to-dust ratio in the inner disk, potentially explaining (pre-)transitional disks, which have optically thin inner cavities but still have relatively high accretion rates (Rice et al., 2006, Mendigutía et al., 2011). Recent work by Pinilla et al. (2012) demonstrates how dust particles are trapped further out than the location of the edge of the gap in the gas for a given planet. For example, the outer edge for the gas would be located at 37 AU in the specific case of a 15 M_{Jup} planet at 20 AU, while the dust ring would be at 54 AU. In these models, the surface densities of the gas in the gap can drop to $\Sigma_{gas} \sim 10^{-3} - 10^{-4}$ g cm^{-2}, which is similar to other studies on the gas densities in the gaps of transition disk caused by the presence of (multiple) planets (e.g., Bryden et al. 1999, Dodson-Robinson & Salyk 2011, Zhu et al. 2012, Fung et al. 2013). In a paper by de Juan Ovelar et al. (2013) using the models of Pinilla et al. (2012), it is demonstrated how multi-wavelength observations of the gap size (i.e., the location of the inner edge of the outer disk) may help to constrain the planet mass. The results of this paper may further help to constrain the physical properties of the gap. The required surface densities in the gaps of our models are $\Sigma_{gas} \sim 10^{-3} - 10^{-4}$ g cm^{-2}, which are consistent with the surface densities found in hydrodynamical simulations. The ionization balance of PAHs can, therefore, serve as an excellent diagnostic tool to characterize the gas flows through the gaps.

5.6.2 PAH ionization and Herbig star disk evolution.

Our study shows that neutral PAHs originate in optically thick environments where the UV field is low, and the electron density is high. Ionized PAHs originate in low density, optically thin gas flows where the UV field is high and the electron density is low. Figure 5.12 gives a summary sketch of these two disk environments in a transitional disk.

The two most extreme $I_{6.2}/I_{11.3}$ ratios among Herbig stars come from HD 141569, where the PAHs are likely almost all ionized, and HD 97048, where the PAH spectrum represents the highest neutral fraction (Table 5.1). In HD 141569, studies have shown

that the disk is largely optically thin (Li & Lunine, 2003, Thi et al., 2013), iwhich agrees with our result that ionized PAHs originate in optically thin environments. In HD 97048, neutral PAHs originating in the optically thick disk dominate. Even though there may be gas in the gap of HD 97048 due to the higher density of an optically thick inner disk, the PAHs in the low-density gap are not exposed enough to the UV field.

The effect of the disk geometry on the ionization balance may be visible in the $I_{6.2}/I_{11.3}$ ratio compared to the MIR spectral index $F_{30}/F_{13.5}$ (Figure 5.3). Flaring/transitional (group I) objects have a wider range in their degree of ionization compared to flat (group II) objects. This can be interpreted, as that PAH emission in flaring/transitional objects originates in more varied physical environments: those that are predominantly neutral in the optically thick disk and predominantly ionized in optically thin gaseous disk gaps. The PAH emission from flat disks show more similar $I_{6.2}/I_{11.3}$ ratios. This suggests that the disks of flat (group II) objects are more homogeneous. Possibly this could be due to the lack of large gaps in these objects. This would be consistent with the scenario that flaring (group I) objects are often (pre-)transitional, while self-shadowed (group II) objects lack any signatures of large dust gaps.

While ionized PAHs do trace low density gas flows, it is not always the case that gas flows have ionized PAHs. For example, the Herbig stars HD 135344 B and HD 142527 have rather low temperatures (respectively $T = 6590$ K and $T = 6260$ K), and, therefore, their UV fields are less efficient in ionizing the PAHs. Our models show that PAHs will be highly neutral in the disks of T Tauri stars. Thus, ionized PAHs are most likely found in low density gaps around Herbig stars with temperatures of $T \gtrsim 6000$K. Alternatively, if the gas density in the gas flow is high, then the PAHs may recombine more easily into the neutral state. This scenario may be part of the explanation why the spectrum of HD 97048 is still largely neutral.

A correlation is found between the mm luminosity and the $I_{6.2}/I_{11.3}$ ratio (Figure 5.4). Since the disk is optically thin at millimeter wavelengths, the mm luminosity may be a proxy of the disk mass in mm-sized dust grains. Therefore, for lower disk masses, the fraction of ionized PAHs seems to be higher. There are two possible ways to understand this trend. The first is that the inner region of the disk becomes optically thinner when accretion depletes most of the inner disk mass and less material from the outer disk is available to replenish the inner regions. As a consequence, the inner disk becomes optically thin, the low density gas flows become more irradiated by UV emission, and the ionization fraction is higher. Another possibility is that more planets are formed creating larger gaps over the course of time when the disk is loosing its mass. Consequently, more low density gas flows emerge with a high fraction of ionized PAHs.

5.7 Conclusions

We have modeled the charge state of PAHs in Herbig disks. We find that the neutral fraction of the disk is high for typical star and disk parameters. The key parameter to ionize the PAHs in the disk is to lower the gas density. The PAH luminosity is most influenced by competition from dust grains, either by an increased PAH mass fraction, or the removal of small dust grains. Our results can be summarised as follows:

- Emission from ionized PAHs trace low-density optically thin regions and has a high $I_{6.2}/I_{11.3}$ ratio.
- The PAHs in an optically thick disk are predominantly neutral and produce emission with a low $I_{6.2}/I_{11.3}$ ratio.
- The PAH spectra of transitional disks can be understood as superpositions of neutral PAHs from an optically thick disk and ionized PAHs from that of low density, optically thin gas flows through protoplanetary disk gaps.
- There is no gradient in the neutral fraction of PAHs as a function of radius in an optically thick disk.
- The PAH luminosity is not synonymous to the disk structure. As shown for the transitional disks in our sample, the total PAH mass in the low density, optically thin disk gap can be much smaller compared to the total PAH mass in the outer disk. Nevertheless, they give a dominating contribution to the total PAH luminosity.
- We find a trend in the $I_{6.2}/I_{11.3}$ ratio compared to the 1.3 millimeter luminosity. Since the 1.3 millimeter luminosity can be used as a proxy for the disk mass, the degree of ionization tends to be higher for lower disk masses. We suggest that the contribution to the PAH luminosity from ionized PAHs in low-density optically thin 'gas flows' becomes larger for lower mass disks.
- For a sample of 18 Herbig stars, the $I_{6.2}/I_{11.3}$ ratios indicates that PAH emission from flaring/transitional disks (group I) is higher and originates in a wider range of physical environments ($\langle I_{6.2}/I_{11.3}\rangle = 2.61 \pm 1.63$), while the origin of PAH emission in self-shadowed flat disks (group II) seems to be more homogeneous ($\langle I_{6.2}/I_{11.3}\rangle = 2.08 \pm 0.56$).

With superior mid-IR sensitivity and spatial resolution, observations by the Mid-InfraRed Instrument (MIRI) on the James Webb Space Telescope (JWST) will be able to probe more and fainter targets. This work shows that the ionization balance of PAHs provides an extra diagnostic tool to characterize the gaps of transitional disks and, thus, to study the process of planet formation.

Acknowledgements: *The authors thank the referee Ralf Siebenmorgen for useful comments which helped to improve the paper. The authors thank Bram Acke for providing the reduced data from his 2010 paper. The authors thank Carsten Dominik and Alessandra Candian for insightful comments and discussions which improved the analysis presented in this paper. The authors thank Lucas Ellerbroek for proof-reading and providing very useful comments. The authors thank the editor Malcolm Walmsley for providing useful comments on the final version of this paper. K.M. is supported by a grant from the Netherlands Research School for Astronomy (NOVA). M.M. acknowledges funding from the EU FP7-2011 under Grant Agreement No 284405. Studies of interstellar chemistry at Leiden Observatory are supported through advanced-ERC grant 246976 from the European Research Council, through a grant by the Dutch Science Agency, NWO, as part of the Dutch Astrochemistry Network, and through the Spinoza premie from the Dutch Science Agency, NWO.*

CHAPTER 6

Location and sizes of forsterite grains in protoplanetary disks. Interpretation from the Herschel DIGIT programme

K. M. Maaskant, B.L. de Vries, M. Min, L.B.F.M. Waters, C. Dominik, F. Molster, A.G.G.M. Tielens

Astronomy & Astrophysics, in press (2014)

Abstract

The spectra of protoplanetary disks contain mid- and far- infrared emission features produced by forsterite dust grains. The spectral features contain information about the forsterite temperature, chemical composition and grain size. We aim to characterize how the 23 and 69 μm features can be used to constrain the physical locations of forsterite in disks. We check for consistency between two independent forsterite temperature measurements: the I_{23}/I_{69} feature strength ratio and the shape of the 69 μm band. We perform radiative transfer modeling to study the effect of disk properties to the forsterite spectral features. Temperature dependent forsterite opacities are considered in self consistent models to compute forsterite emission from protoplanetary disks. Modeling grids are presented to study the effects of grain size, disk gaps, radial mixing and optical depth to the forsterite features. Independent temperature estimates derived from the I_{23}/I_{69} feature strength ratio and the 69 μm band shape are most inconsistent for HD 141569 and Oph IRS 48. A case study of the disk of HD 141569 shows two solutions to fit the forsterite spectrum. A model with T $\sim$ 40 K, iron rich ($\sim 0-1$ % Fe) and 1 μm forsterite grains, and a model with warmer (T $\sim$ 100 K), iron free, and larger (10 μm) grains. We find that for disks with low upper limits of the 69 μm feature (most notably in flat, self-shadowed disks), the forsterite must be hot, and thus close to the star. We find no correlation between disk gaps and the

presence or absence of forsterite features. We argue that the 69 μm feature of the evolved transitional disks HD 141569 and Oph IRS 48 is most likely a tracer of larger (i.e. $\gtrsim$ 10 μm) forsterite grains.

6.1 Introduction

Protoplanetary disks are thought to be the precursors of planetary systems. Disk evolution is therefore of great importance to understand how planets are being formed (e.g. Testi et al. 2014). Through analysis of the dust emission features at infrared (IR) wavelengths, both the chemical composition of dust and the size of grains can be constrained (e.g. Henning 2010). The characterisation of the dust provides evidence of physical and chemical processes in the disk.

Silicate dust undergoes significant processing in protoplanetary disks. Whereas dust in the interstellar medium (ISM) is largely amorphous (Kemper et al., 2004), i.e., characterized by a disordered network of silicates, enriched with O, Fe, and Mg, and to a lesser degree Ca and Al. In protoplanetary disks, silicate dust is also observed in crystalline phase (Malfait et al., 1998, Bouwman et al., 2001, Meeus et al., 2001). Forsterite (Mg_2SiO_4) is the most abundant observable crystalline constituent in disks around T Tauri and Herbig Ae/Be stars (Olofsson et al., 2009, Juhász et al., 2010). Forsterite formation requires temperatures of $\gtrsim$ 1000 K (Hallenbeck et al., 2000, Fabian et al., 2000). At these temperatures, crystalline silicates can be formed through gas-phase condensation, and annealing of preexisting amorphous silicates (see Wooden et al. 2005 for an overview). The required temperatures indicate that forsterite forms in the inner disk. High crystallinity fractions in the inner disk have been confirmed by interferometric observations (van Boekel et al., 2004).

Even-though dust crystals are formed at high temperature and therefore close to the star, they have also been observed much farther away from the star than expected (Malfait et al., 1998, Olofsson et al., 2009, Juhász et al., 2010, de Vries et al., 2012, Sturm et al., 2013). Also in our own solar system, comets and interplanetary dust particles include crystalline silicates (MacKinnon & Rietmeijer, 1987, Bradley et al., 1992). Silicate grains in long-period comets like Hale-Bopp can be crystalline (Crovisier et al., 1997, Wooden et al., 1999, Harker et al., 2002). Laboratory measurements of olivine crystals from unequilibrated bodies (e.g. such as comet 81P/Wild 2, Zolensky et al. 2006; and cometary interplanetary dust particles Zolensky et al. 2008) are generally iron poor. Iron fractions (by number) in olivine crystals found in the Itokawa asteroid and in ordinary chondrites can be up to $\sim$ 30% (Nakamura et al., 2011). This may reflect the lack of large scale mixing (Shu et al., 1994, Bockelée-Morvan et al., 2002, Gail, 2004, Jacquet, 2014) and indicate the importance of crystal formation (i.e. local heating events) associated with the inner and outer disk region (Urey, 1967, Huss et al., 2001, Harker & Desch, 2002, Desch et al., 2005, Ábrahám et al., 2009, Morlok et al., 2010, Tanaka et al., 2010).

The transition from amorphous to crystalline silicate dust leads to strong changes in the optical response function of the material (Hallenbeck & Nuth, 1998). Crystalline silicates have several sharp solid-state features. Detailed analysis of these features provide a wealth of information on the properties of the crystal grains (Koike et al., 2003, Suto et al., 2006). As these properties can potentially be linked to the specific circumstances required to crystallise the dust grains, crystalline silicates allow us to probe physical processes changing the chemical compositions in the disk.

The width and peak position of the 69 μm feature of forsterite is sensitive to the temperature (Bowey et al., 2002, Suto et al., 2006, Koike et al., 2006). In addition, the peak position of the feature becomes red shifted for higher fractions of iron (Koike et al., 1993, 2003). Herschel observations using the Photodetector Array Camera and Spectrometer (PACS) has allowed to study the 69 μm feature with high spectral resolution (Sturm et al., 2010, Mulders et al., 2011, de Vries et al., 2012, Sturm et al., 2013). A detailed analysis of the 69 μm feature shapes in protoplanetary disks is presented in Sturm et al. (2013). These authors found the following results. Most of the forsterite grains that give rise to the 69 μm bands are found to be $\sim 100 - 200$ K and iron-poor (less than $\sim$2% iron), supporting the hypothesis that the forsterite grains form through an equilibrium condensation process at high temperatures. The large width of the emission band in some sources has been interpreted to indicate the presence of forsterite reservoirs at different temperatures. It was also concluded that any model that can explain the PACS and the Spitzer IRS observations must take the effects of a wavelength dependent optical depth into account.

Only for HD 100546 (Mulders et al., 2011), radiative transfer modeling has been performed to study the consistency between the relative mid-infrared band strengths and the information contained in the shape of the 69 μm band. It was found that the best solution is given by a model with a high abundance of forsterite located in the inner edge of the outer disk. As protoplanetary disks are highly optically thick media, radiative transfer modeling is essential to investigate optical depth effects and to simultaneously study the effects of grain growth, protoplanetary gaps and, radial mixing.

In this paper, we perform an in-depth study of the 69 μm feature of Herbig Ae/Be stars using radiative transfer models. We find that forsterite shows a variety of spectral characteristics for different groups of protoplanetary disks and we find that the detection rate of the 69 μm feature increases for lower disk masses (Section 6.2). As the different groups can be linked to physical processes in the disk, it shows that forsterite is a valuable tracer of the disk evolution history. In Section 6.3 we introduce the radiative transfer code and the dust model used in this study. We study the behaviour of forsterite in different evolutionary scenarios in Section 6.4. In Section 6.5 we present a case study of the peculiar 69 μm band which may be indicative for large grains originating in the optically thin disk of HD 141569. The discussion and conclusions are presented in Section 6.6 and 6.7, respectively.

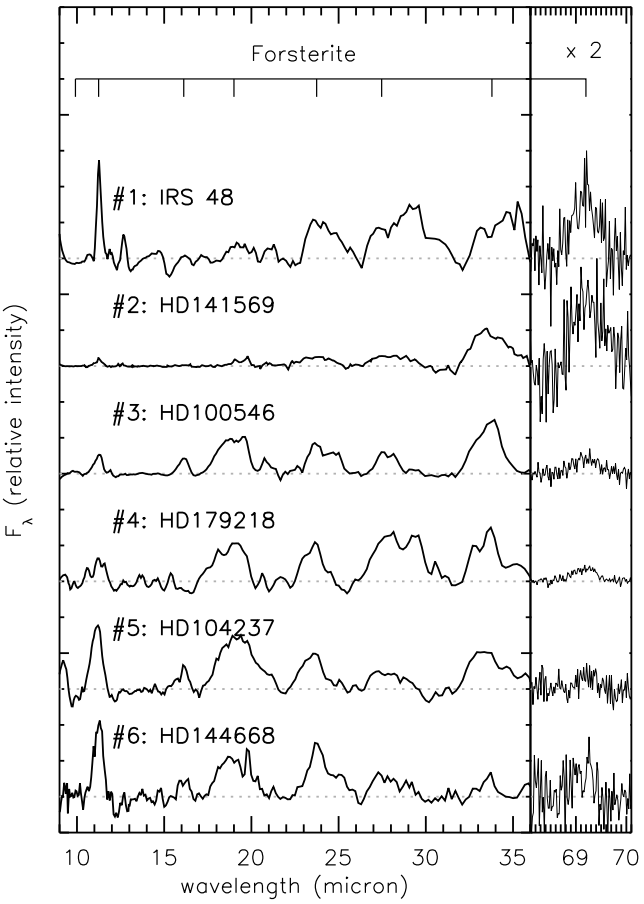

Figure 6.1: *Spectra of all sources with 69 μm detections. The continuum subtracted spectra are scaled relative to the strongest band. The objects are sorted by the $F_{30}/F_{13.5}$ ratio.*

6.2 Observations

In this section, we analyse the short and long wavelength forsterite features originating from protoplanetary disks. We compare the feature strength ratio I_{23}/I_{69} to the forsterite 69 μm shape and check for their consistency. In addition, we present trends between the I_{23}/I_{69} ratios and the millimetre (mm) luminosities of the disks. Note that throughout this paper, the integrated intensities are given by I_λ [erg cm^{-2} s^{-1}], the monochromatic flux by F_λ [erg cm^{-2} s^{-1} μm^{-1}], and the luminosity by L_λ [erg s^{-1}].

6.2.1 Data collection

We selected far-infrared (FIR) spectroscopic observations of Herbig stars (i.e. stars of spectral type F and higher) from the sample of Sturm et al. (2013). This allows us to identify trends in a sample of objects which are comparable in (stellar) properties. The observations were taken with the PACS instrument and are analysed as part of the Dust,

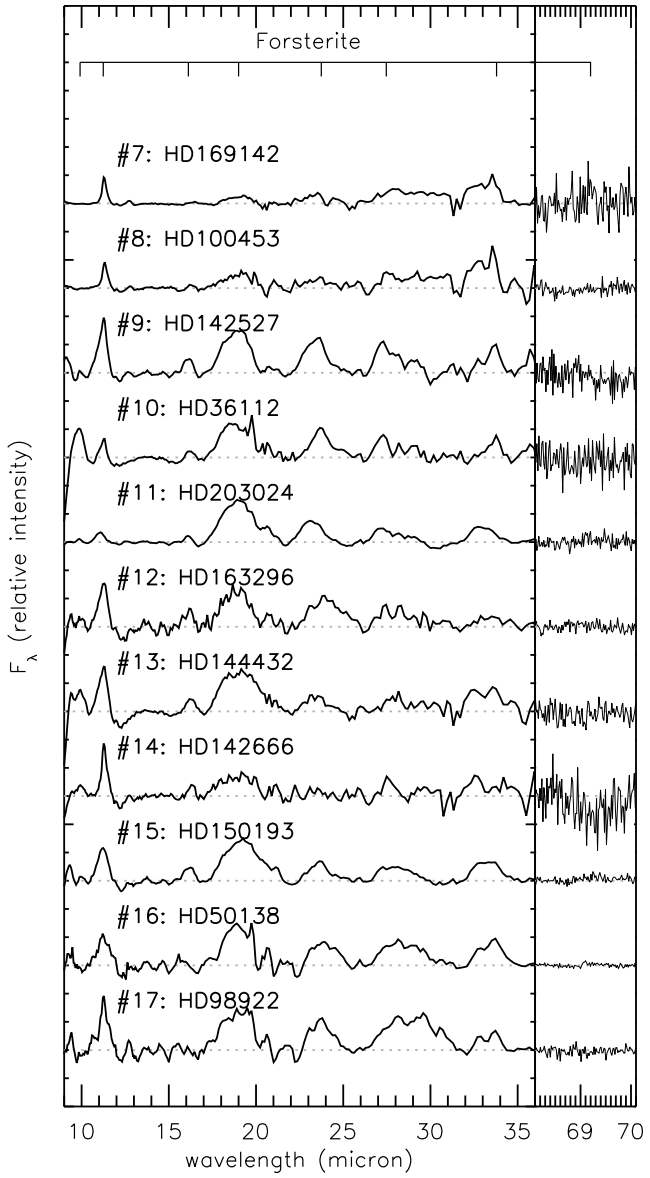

Figure 6.2: *Spectra of all sources with three or more forsterite features detected in the Spitzer/IRS spectrum. These objects have no detections at 69 μm. The continuum subtracted spectra are scaled relative to the strongest band and the objects are sorted by the $F_{30}/F_{13.5}$ ratio.*

Ice and Gas in Time (DIGIT) Herschel key programme. The data is processed using the Herschel Interactive Processing Environment (HIPE) using calibration version 42 and standard pipeline scripts. Table 6.1 shows the properties of the objects with forsterite 69 μm detections. Table 6.2 shows all Herbig Ae/Be objects which have been observed. For comparison with the spectral energy distributions (SEDs) we collected fluxes at 13.5 and 30 μm from Acke et al. (2010) and mm photometry for all sources from the literature. Identification of forsterite features in the wavelength range between $\sim 15-35$ μm is done using Spitzer/IRS spectra, which were first published by Juhász et al. (2010) and

re-reduced by the most recent calibration version (S18.18.0) for the study of Sturm et al. (2013).

Identification and measurements of the forsterite features are carried out after fitting and subtracting the continuum. The best fit to the continuum is obtained using a spline function, which is a polynomial between continuum wavelengths chosen just outside the features. The best results were obtained using the following wavelengths for the continuum. For the Spitzer/IRS wavelength domain: $\lambda_{\text{continuum}} = \{5.52, 5.83, 6.66, 7.06, 9.54, 10.32{,}12, 13.08, 13.85, 15.00, 17.00, 21.75, 26.00, 31.60, 35.10, 36.01\}$ μm. For the Herschel/PACS wavelength domain: $\lambda_{\text{continuum}} = \{65.50, 67.50, 68.55, 69.70, 70.00, 70.50, 71.00, 71.50\}$ μm. At each point we took the average continuum flux for a small wavelength range ($\Delta\lambda \sim 1\mu$m) around the feature. An extended discussion of this approach is given in Appendix B of Mulders et al. (2011). We visually checked that the continuum was properly fitted so that the strengths of the forsterite features could be accurately determined. We checked the spectra for detections of forsterite features. Almost all of the forsterite features we identify are also reported in Juhász et al. (2010) and Sturm et al. (2013). Table 6.2 gives an overview of all forsterite detections (for the short wavelength features, this implies that at least three bands are identified). Finally, the 23 μm feature is identified using a χ^2 Gaussian fitting routine and thereafter integrated to determine the band strengths. From all the short wavelength features we choose the 23 μm band for analysis because: 1) the band is relatively unaffected by the amorphous silicate feature, 2) it is a strong/prominent band, 3) there is minimal interference of other crystalline silicate bands (most notably enstatite) and 4) the Spitzer/IRS observations are reliable at that wavelength range. The error on the flux of the 23 μm band is dominated by the choice of the continuum points next to the features. This error calculation varies the position of the continuum points by a Monte Carlo based method and determines the 1 σ deviation to the mean flux. We derive a typical error of $\sim$20% to the feature strength.

Sturm et al. (2013) report the detection of the 69 μm feature in the PACS spectrum of AB Aur. However, several indications make the detection uncertain. The identification of the continuum between $\sim 65-75$ μm is arbitrary since the continuum of AB Aur shows several bumps in this wavelength range. Due to instrumental issues with PACS, it is not easy to identify for the indicated wavelength range if bumps are instrumental artefacts, real features or continuum. After analysis of the 69 μm the shape, the reported forsterite feature has a peculiar square-like shape, which is not seen in the other detections of the Herbig stars. In addition, the peak position is redshifted by 0.8 μm, while the other detections are all within a range of 0.2 μm. While this could be an effect of an iron fraction of $\sim$4 %, it is somewhat peculiar that AB Aur has this iron fraction, and the other detections not. Finally, unlike all other Herbig stars where the 69 μm feature is detected, AB Aur has no sign of forsterite detections in the Spitzer/IRS spectrum. Therefore, we choose not to classify the 69 μm feature of AB Aur as a detection of forsterite into our analysis. We emphasize that AB Aur is an outlier and better observations are needed to confirm the detection with sufficient confidence.

6.2.2 New Meeus group classication based on the $F_{30}/F_{13.5}$ continuum flux ratio

Meeus et al. (2001) showed that the SEDs of Herbig stars can be divided in two typical groups: sources with a strong mid-to far-infrared excess (group I) and sources which can be fitted by just one powerlaw (group II). A strong correlation between the $F_{30}/F_{13.5}$ continuum flux ratio and the group classification based on Meeus et al. (2001) has been shown in Maaskant et al. (2013, 2014). Group I and II sources have respectively high and low $F_{30}/F_{13.5}$ ratios and are easily distinguished by this parameter. Larger sizes of the gap in the disk temperature regime between $\sim 200-500$K causes the continuum flux at 13.5 μm to decrease. However, because the inner edge of the outer disk is a vertical wall with a high surface brightness, the flux at 30 μm increases. Therefore high values of $F_{30}/F_{13.5}$ are indicative of large gap sizes (Maaskant et al., 2013). As proposed by Khalafinejad (in prep.) the transitions between Meeus groups Ia, Ib and group IIa can be more easily classified using the $F_{30}/F_{13.5}$ ratio. With geometrically flat, full disks showing amorphous silicate features (group IIa): $F_{30}/F_{13.5} \leqslant 2.1$. For transitional/flaring objects with amorphous silicate features (group Ia): $2.1 < F_{30}/F_{13.5} < 5.1$. The transitional/flaring objects which do not have silicate features (group Ib) have: $F_{30}/F_{13.5} \geqslant 5.1$. The devision of these groups can be seen in Figure 6.3. The absence of the silicate feature is correlated with the highest values of $F_{30}/F_{13.5}$ because the disk gap is significantly depleted in small silicate dust grains. Due to the depletion of small dust grains, the optical depth also decreases, which enhances the flux from smaller PAH molecules which are thought to travel along with the gas (Maaskant et al., 2014). For our study we adopt this new classification scheme of the Meeus groups based on the $F_{30}/F_{13.5}$ ratio.

6.2.3 Properties of the forsterite features

Out of 23 sources observed with Herschel/PACS, 6 objects have a detection of the 69 μm feature. Their continuum subtracted Spitzer/IRS and Herschel/PACS spectra are shown in Figure 6.1. All objects without 69 μm feature detections are shown in Figure 6.2. In these figures, the continuum subtracted spectra are scaled relative to the strongest forsterite band and the objects are sorted by the continuum feature strength ratio of the 30 μm and 13.5 μm features (i.e. the $F_{30}/F_{13.5}$ ratio). We could not identify any parameters that could explain the lack of forsterite features for several sources (sources #18 – #23, see Table 6.2).

6.2.4 Observational trends

Since we only have a very small number of 69 μm detections, extracting trends is difficult and we should be careful drawing strong conclusions. Nevertheless, we searched for trends between the forsterite features and the stellar and photometric properties. The following tentative trends, related to the photometric properties (Figure 6.3) and to the forsterite features (Figure 6.4), could be identified in the data.

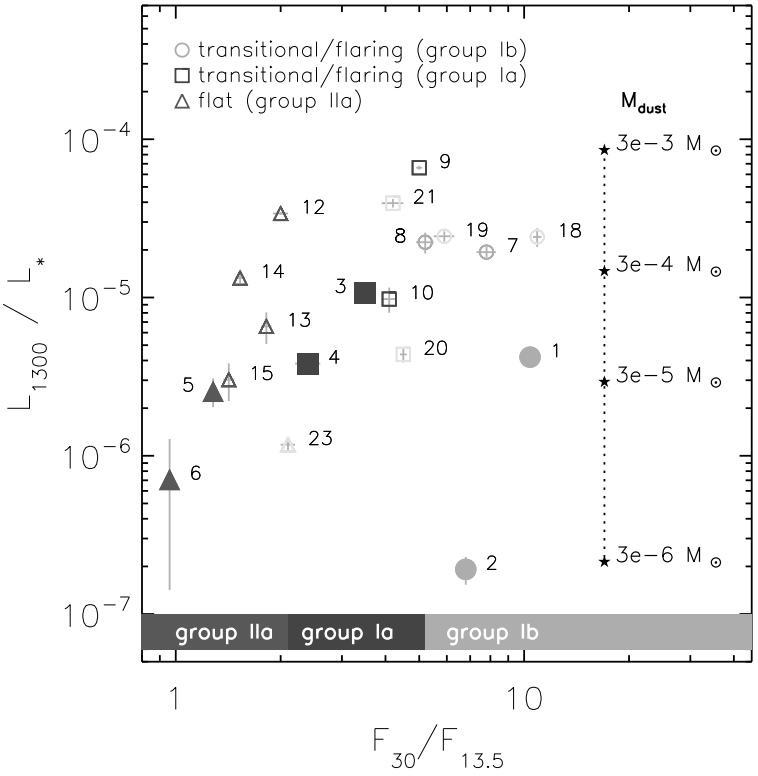

Figure 6.3: *The disk luminosity at 1.3 mm (L_{1300}/L_*) compared to the MIR spectral index $F_{13.5}/F_{30}$ ratio. Filled symbols indicate the objects for which the 69 μm feature has been detected. The 69 μm feature is often detected for disks with low L_{1300}/L_*. The MIR spectral index can be used as a tracer of large disk gaps. The symbols show flaring/transitional disks without silicate features (group Ib, circles, $F_{30}/F_{13.5} \geqslant 5.1$), with silicate features (group Ia, squares, $2.1 < F_{30}/F_{13.5} < 5.1$), and self-shadowed disks with silicate features (group IIa, triangles, $F_{30}/F_{13.5} \leqslant 2.1$). The numbers refer to the objects and are given in Table 6.2. The grey symbols show the objects with no forsterite detections at Spitzer/IRS and Herschel/PACS wavelengths.*

Figure 6.3 shows all the Herbig stars which have been observed with Spitzer/IRS and Herschel/PACS. This plot relates the 69 μm detections to the photometric properties of the Herbig stars. One of the main indicators of the protoplanetary disk mass is the 1.3 mm optically thin dust continuum emission. For comparison we have over-plotted mm luminosities of a radiative transfer modeling grid were the mass is varied by 4 orders of magnitude (section 6.4.5). This plot shows that the detection rate of the 69 μm forsterite features tends to be higher for lower 1.3 mm luminosities (L_{1300}/L_*). Thus for lower mass disks, the 69 μm feature seems to be more frequently detected (69 μm detections indicated by the filled symbols). We will discuss in Section 6.4 which disk evolutionary scenarios can explain this behaviour. Figure 6.3 also shows that there is no correlation between the 69 μm detections and the presence of large gaps as indicated by the MIR spectral index $F_{30}/F_{13.5}$ ratio.

Figure 6.4 shows all the sources with forsterite detections in the Spitzer/IRS and/or

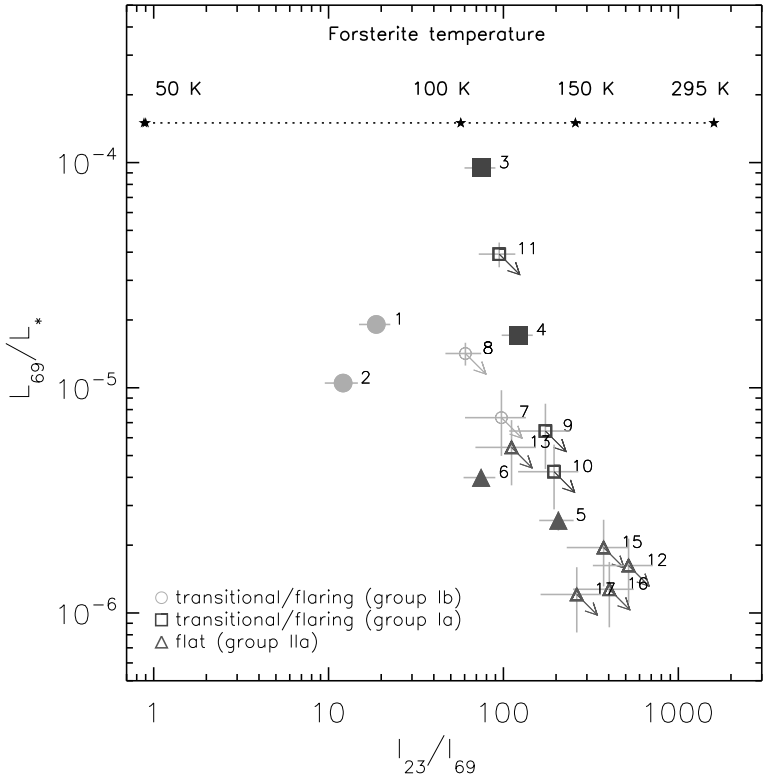

Figure 6.4: *The luminosity of the 69 μm feature (L_{69}/L_*) compared to the I_{23}/I_{69} ratio. Filled symbols indicate the objects for which the 69 μm feature has been detected. The numbers refer to the objects and are given in Table 6.2. The arrows indicate the upper limits of the 69 μm feature. The stars indicate band strength ratios of temperature dependent forsterite opacities multiplied by black bodies of corresponding temperatures. Thus the emission profile of optically thin dust emission is modelled and serves as a simple first comparison to the observed features ratios.*

Herschel/PACS wavelength range. It relates the 69 μm luminosity to the Meeus groups as well as to the forsterite temperature. Note that the absolute feature strength *alone* is a difficult diagnostic tool to search for processes in disks because the abundance differences are important for it and there is a large dispersion in the crystallinity fractions of Herbig stars. The I_{23}/I_{69} band strength *ratio* can be interpreted as a probe of the dominant forsterite temperature in the disk because it measures the shape of the underlying blackbody. Also overlaid are feature strength ratios for optically thin representative dust mixtures of different temperatures (20% forsterite, 20% amorphous carbon and 60% amorphous silicates, see Section 6.3.1 for the description of the dust model). In this mixture, temperature dependent opacities of forsterite are adopted (Suto et al., 2006). Hence, a high I_{23}/I_{69} ratio reflects a high forsterite temperature. We can learn from this plot that the luminosity of the 69 μm detections is stronger for transitional/flaring disks (group I) compared to the self-shadowed/flat (group II) objects. In addition, the forsterite temperature indicator I_{23}/I_{69} seems to be $\sim 1-2$ orders of magnitude lower for the group Ib objects (Oph IRS 48 and HD 141569) than for group Ia and IIa objects. The weakest detections of the 69 μm feature are found for the flat (group II) objects and have a similar I_{23}/I_{69} ratio as group Ia

objects. In the majority of objects, the 69 μm feature is not observed. The non-detection could be a consequence of insufficient sensitivity (such as for object #11: HD 203024). However, for the flat (group II) objects on the bottom right corner of Figure 6.4 (#12, #15, #16 and #17), the 23 μm feature is strong compared to the upper limit of the 69 μm feature. For these objects we can conclude that the forsterite temperature must be high.

The possible effects of these trends on the relative band strength I_{23}/I_{69} and the 69 μm width and peak position will be carefully examined in the remainder of this paper.

6.2.5 Consistency between feature strength ratio I_{23}/I_{69} and the 69 μm band shape

Another independent way of estimating the forsterite temperature relies on the analysis of the 69 μm feature shape. The features width and peak position contains information about the temperature, iron fraction and grain size. We will now check the consistency between both methods to derive a forsterite temperature estimate.

The feature strengths, widths and peak positions of the 69 μm feature are examined in Sturm et al. (2013). The feature properties are shown in Table 6.1. Lorentzian fits are also derived for the features to be able to compare them to the detection of the 69 μm feature in Beta Pictoris presented in de Vries et al. (2012). The forsterite in the debris disk of Beta Pictoris was found to be ∼80 K at a distance of ∼40 AU, and contains 1% iron. As gas rich disk may eventually evolve into debris disks, a comparison between the properties of the 69 μm feature in Herbig stars to that of Beta Pictoris may be relevant. The feature widths and positions for the sources in our sample are shown in Figure 6.5. The average width is ∼0.28 μm and the average peak position is ∼69.2 μm. Over-plotted are laboratory are measurements from Suto et al. (2006) with an iron fraction of 0% (right solid line). The right dashed line gives the widths and peak positions of 1% iron fraction; these are interpolated between 0% and 8% iron fractions using a linear trend fitted (de Vries et al., 2012) to the measured values between 0% and 16% iron fractions from Koike et al. (2003). The 69 μm feature shapes of protoplanetary disks are similar to laboratory measurements of $\sim 150-200$ K forsterite with an iron fraction between $0-1\%$.

The I_{23}/I_{69} ratio and the 69 μm band shapes are not consistent for HD 100546, HD 144668, HD 141569 and Oph IRS 48. Thus, a single temperature analysis can not explain the difference in the observational appearance of forsterite and more complex models have to be invoked. We will show in Sections 6.3 and 6.4 that the I_{23}/I_{69} ratio and the 69 μm band shape is sensitive to (distributions) of temperatures, iron fractions, grain sizes and optical depth effects. For HD 100546, it has been shown that the difference in temperature indicators can be explained by optical depth effects which increases the strength of the 69 μm feature compared to the 23 μm feature because the disk is optically thinner at longer wavelength (Mulders et al., 2011). Possibly a similar scenario may be the case for HD 144668. However, for the evolved transitional disks HD 141569 and Oph IRS 48, such optical depth effects are not sufficient since these disks are much more optically thin. Their very weak short wavelength features suggest that the forsterite must be cold ($T \lesssim 90$

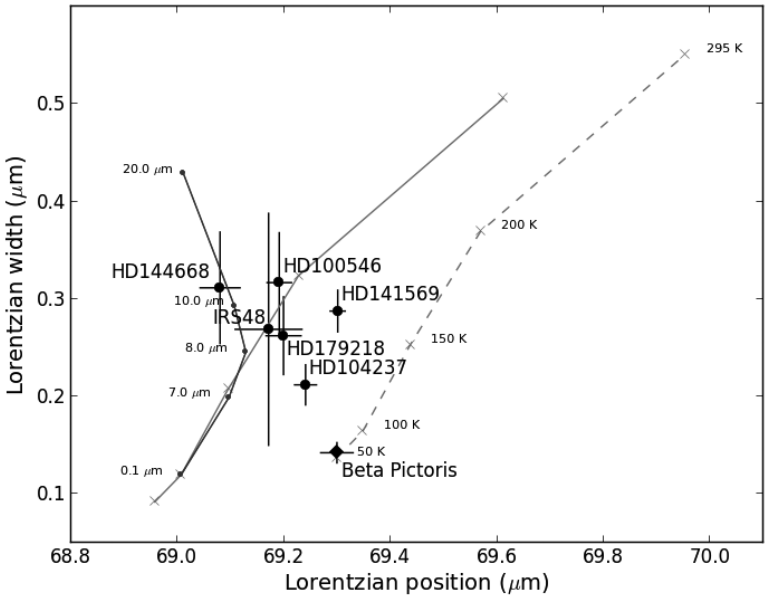

Figure 6.5: *Lorentzian width versus peak position diagram of 69 micron features (Gaussian values in Table 6.1). The left solid line shows the peak positions and widths for a T = 100 K grain with increasing size between 0.1* μm *and 20* μm*, computed with distribution of hollow spheres (DHS). The left solid grey line represents the peak positions and widths for iron free forsterite and increasing temperatures of 50 K, 100 K, 150 K, 200 K and 295 from laboratory measurements of Suto et al. (2006). The right dashed grey line shows the interpolated shift in peak position of the 69* μm *feature. The right dashed grey line shows the interpolated shift in peak positions and widths for the 69* μm *feature for 1% iron fraction(Koike et al., 2003).*

K). However, the band shape of their 69 μm features suggests much higher temperatures (respectively 174 K and 156 K, Sturm et al. 2013). In Section 6.5, we perform a case study of HD 141569 and present forsterite models which can fit the short and long wavelength spectra.

6.3 Radiative transfer and dust model

Many physical assumptions are made in models of dust features from protoplanetary disks. In this section we explain our modeling approach. First we discuss the dust model used for the analysis of forsterite features. Thereafter we briefly explain how forsterite is implemented in the radiative transfer code MCMax (Min et al., 2009) .

Table 6.1: *Peak positions and widths given for Lorentzian and Gaussian fits. For clarity, they are both given so that they are comparable to the Lorentzian values derived for Beta Pic (de Vries et al., 2012). Gaussian values are taken from Sturm et al. (2013). The difference between Lorentzian and Gaussian widths stems from their definition.*

ID	Object	p_L (μm)	w_L (μm)	p_G (μm)	w_G (μm)
1	Oph IRS 48	69.170	0.269	69.168	0.521
2	HD141569	69.300	0.288	69.303	0.600
3	HD100546	69.191	0.317	69.194	0.681
4	HD179218	69.199	0.262	69.196	0.502
5	HD104237	69.240	0.212	69.224	0.351
6	HD144668	69.079	0.312	69.088	0.599

Table 6.2: *The sample of Herbig stars studied in this paper. $\uparrow$ indicates upper limits. References of mm photometry are given in Table 1 of Maaskant et al. 2014.*

ID #	Target	Spitzer detections	69 µm detection	$F_{30}/F_{13.5}$ ∇	group	I_{23} erg cm^{-2} s^{-1}	I_{69} erg cm^{-2} s^{-1}	L_* $L_\odot$	T_* K	d pc	F_{1300} mJy
1	Oph IRS 48	√	√	10.40 ± 0.30	Ib	$1.14 \pm 0.21 \times 10^{-11}$	$6.11 \pm 0.21 \times 10^{-13}$	14.3	10000	120	60 ± 10
2	HD 141569	√	√	6.80 ± 0.20	Ib	$7.67 \pm 1.53 \times 10^{-12}$	$6.32 \pm 0.49 \times 10^{-13}$	18.3	9520	99	5 ± 1
3	HD 100546	√	√	3.50 ± 0.20	Ia	$7.08 \pm 1.40 \times 10^{-10}$	$9.46 \pm 0.13 \times 10^{-12}$	32.9	10500	103	465 ± 20
4	HD 179218	√	√	2.40 ± 0.20	Ia	$8.97 \pm 1.79 \times 10^{-11}$	$7.33 \pm 0.18 \times 10^{-13}$	79.2	9810	244	71 ± 7
5	HD 104237	√	√	1.28 ± 0.03	IIa	$4.41 \pm 0.88 \times 10^{-11}$	$2.14 \pm 0.21 \times 10^{-13}$	34.7	8405	116	92 ± 19
6	HD 144668	√	√	0.96 ± 0.02	IIa	$1.93 \pm 0.38 \times 10^{-11}$	$2.60 \pm 0.13 \times 10^{-13}$	87.5	7930	208	20 ± 16
7	HD 169142	√	…	7.80 ± 0.50	Ib	$1.68 \pm 0.34 \times 10^{-11}$	$\uparrow 1.73 \pm 0.56 \times 10^{-13}$	15.3	8200	145	197 ± 15
8	HD 100453	√	…	5.20 ± 0.30	Ib	$1.77 \pm 0.35 \times 10^{-11}$	$\uparrow 2.93 \pm 0.34 \times 10^{-13}$	8.0	7390	112	200 ± 31
9	HD 142527	√	…	5.00 ± 0.10	Ia	$4.64 \pm 0.92 \times 10^{-11}$	$\uparrow 2.67 \pm 0.86 \times 10^{-13}$	50.6	6260	198	1190 ± 33
10	HD 36112	√	…	4.10 ± 0.20	Ia	$1.40 \pm 0.28 \times 10^{-11}$	$\uparrow 7.20 \pm 2.30 \times 10^{-14}$	22.2	7850	205	72 ± 13
11	HD 203024	√	…	2.30 ± 0.20	Ia	$3.08 \pm 0.62 \times 10^{-11}$	$\uparrow 3.26 \pm 0.41 \times 10^{-13}$	99.2	8200	620	…
12	HD 163296	√	…	2.00 ± 0.10	IIa	$4.26 \pm 0.85 \times 10^{-11}$	$\uparrow 8.20 \pm 2.60 \times 10^{-14}$	23.3	8720	122	743 ± 15
13	HD 144432	√	…	1.82 ± 0.06	IIa	$9.36 \pm 1.90 \times 10^{-12}$	$\uparrow 8.40 \pm 2.70 \times 10^{-14}$	10.1	7345	145	44 ± 10
14	HD 142666	√	…	1.53 ± 0.05	IIa	$\uparrow 1.73 \pm 0.35 \times 10^{-12}$	$\uparrow 6.53 \pm 2.11 \times 10^{-13}$	14.4	7580	145	127 ± 9
15	HD 150193	√	…	1.42 ± 0.05	IIa	$2.50 \pm 0.50 \times 10^{-11}$	$\uparrow 6.70 \pm 2.20 \times 10^{-14}$	24.0	8990	150	45 ± 12
16	HD 50138	√	…	0.78 ± 0.04	IIa	$8.38 \pm 1.67 \times 10^{-11}$	$\uparrow 2.08 \pm 0.67 \times 10^{-13}$	423.5	12230	289	…
17	HD 98922	√	…	0.75 ± 0.03	IIa	$3.01 \pm 0.25 \times 10^{-11}$	$\uparrow 1.15 \pm 0.37 \times 10^{-13}$	855.7	10500	538	…
18	HD 135344 B	…	…	10.90 ± 0.30	Ib	$\uparrow 3.72 \pm 0.74 \times 10^{-13}$	$\uparrow 1.12 \pm 0.36 \times 10^{-13}$	8.3	6590	140	142 ± 19
19	HD 97048	…	…	5.90 ± 0.40	Ib	$\uparrow 9.80 \pm 1.90 \times 10^{-12}$	$\uparrow 1.96 \pm 0.63 \times 10^{-13}$	40.7	10010	158	452 ± 34
20	AB Aur	…	…	4.50 ± 0.10	Ia	$\uparrow 2.19 \pm 0.43 \times 10^{-11}$	$\uparrow 1.01 \pm 0.09 \times 10^{-12}$	46.2	9520	144	136 ± 15
21	HD 139614	…	…	4.20 ± 0.30	Ia	$\uparrow 2.18 \pm 0.43 \times 10^{-12}$	$\uparrow 7.50 \pm 2.40 \times 10^{-14}$	8.6	7850	140	242 ± 15
22	HD 38120	…	…	2.60 ± 0.20	Ia	$\uparrow 4.03 \pm 0.81 \times 10^{-12}$	$\uparrow 6.00 \pm 1.90 \times 10^{-14}$	89.3	10500	510	…
23	HD 35187	…	…	2.10 ± 0.10	IIa	$\uparrow 8.35 \pm 1.60 \times 10^{-13}$	$\uparrow 1.98 \pm 0.23 \times 10^{-13}$	27.4	8970	150	20 ± 2

6.3.1 Dust model

Throughout this paper, we make use of a standard dust composition responsible for the continuum radiation of 80% silicate and 20% amorphous carbon. This is the dust component without forsterite. To be consistent with previous radiative transfer modeling by Mulders et al. (2011), the adopted amorphous dust composition with reference to the optical constants, is 32% $MgSiO_3$ (Dorschner et al., 1995), 34% Mg_2SiO_4 (Henning & Stognienko, 1996), 12% $MgFeSiO_4$ (Dorschner et al., 1995), 2% $NaAlSi_2O_6$ (Mutschke et al., 1998), 20% C (Preibisch et al., 1993). The shape of our particles is irregular and approximated using a distribution of hollow spheres (DHS, Min et al. 2005) using a maximum vacuum fraction $f_{max} = 0.7$. In DHS, f_{max} is the parameter which controls the shape of the particle and can be regarded as the 'irregularity' parameter, as there is no observable difference between porosity and irregularity.

Forsterite features are analysed using the optical constants from laboratory data of Suto et al. (2006) and using irregular DHS particles with a maximum vacuum fraction of $f_{max} = 0.7$, which has been found to be a good representation of observed short wavelength crystalline silicate profiles in Spitzer data (Juhász et al., 2010). The effects of temperature on the width and peak position of the 69 μm feature are also illustrated in Figure 6.5. The forsterite opacities of Suto et al. (2006) are temperature dependent, and are the best opacities available to use in radiative transfer modeling of protoplanetary disks where the temperatures are below $\lesssim$ 1500 K. Figure 6.6 shows the opacities of several forsterite grains. The top figure shows 1 μm grains for 50 K and 295 K. The short wavelength features are very similar, while the peak strength, peak position, and width of the 69 μm feature are very sensitive to the temperature in this range. The integrated feature strength of the 69 μm feature is ∼3 times higher for 50 K compared to 295 K forsterite. The bottom figure shows the opacities of 1 and 10 μm grains. Due to the larger grain size, the grain model predicts that the shorter wavelength features become weaker, and that the 69 μm feature broadens. A more detailed discussion on the emission characteristics of larger (∼ 10 μm) forsterite grains is given in Min et al. (2004). The temperatures of amorphous silicates and carbonaceous grains are calculated from radiative equilibrium. It is assumed that the forsterite grains are in thermal contact with the other dust constituents. Where relevant, we evaluate in the next sections whether this assumption is reasonable. See Mulders et al. (2011) for an extended discussion on the assumption of thermal contact between the dust grains in radiative transfer modeling of protoplanetary disks.

6.3.2 Radiative transfer model

We use the Monte Carlo radiative transfer code MCMax to compute full radiative transfer models. With a given set of star and disk input parameters, MCMax can compute the temperature and the vertical density structure of highly optically thick disks self-consistently. From these models it produces a range of observables such as the resulting SED and the forsterite features which are calculated by integrating the formal solution to the equation of radiative transfer by ray-tracing.

6.4 Benchmark modeling

In this section, we construct a benchmark model for a typical disk around a Herbig star. This model is used to investigate the key parameters that change the feature strength ratio of forsterite in protoplanetary disks. The aim is to provide a qualitative description for the behaviour of the feature strength ratio I_{23}/I_{69}. Thereby, we derive estimates of the minimum and maximum I_{23}/I_{69} ratios and compare them to the observed values in the spectra of the objects in our sample. We start by introducing the properties of a benchmark disk model. We study four evolutionary disk scenarios that control the I_{23}/I_{69} band strength ratio: **1)** grain growth, **2)** transitional disk, **3)** radial mixing and **4)** optical depth effects.

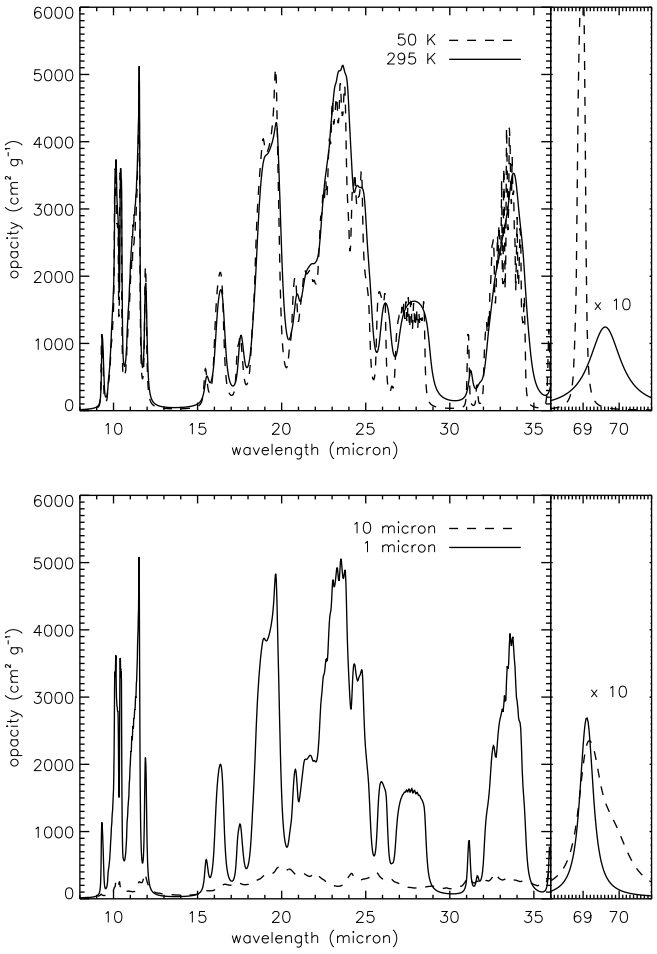

Figure 6.6: *Top: calculated opacities of 1 μm forsterite grains at 50 K and 295 K. Bottom: calculated opacities for 1 and 10 μm forsterite grains (T = 150 K).*

6.4.1 Benchmark disk model

We model a hydrostatic flaring disk with stellar properties from HD 97048 (see parameters in table 6.2). The parameters of this model are taken from the study of Maaskant et al. (2014) and summarized here (see Table 6.3). The chosen stellar properties ($L_* = 40.7 L_\odot$, $T_* = 10010$ K) are typical for Herbig Ae/Be stars. By this choice, the influence of the stellar radiation to the thermal structure of the disk can be assumed to represent the objects in our sample. The inner and outer radii of the disk are set at respectively 0.1 and 250 AU. The radial dependence of the surface density is parametrised by a power law with index -1. The dust mass is $M_{dust} = 3 \times 10^{-4}$ $M_\odot$, where we assume a gas-to-dust ratio of 100. The dust size ranges from $a_{min} = 0.01$ μm up to $a_{max} = 1$ mm and follows a power-law distribution with $a_{pow} = -3.5$.

The standard benchmark model described above does not yet contain forsterite. The models presented in the following sections are different from the benchmark model because forsterite is added to the disk between given radii. This is done by replacing a mass fraction of 10% of the standard dust component by forsterite grains. Note that the total

dust mass at any radius is therefore conserved and that the forsterite grains used in the models are all one size and iron free. Additionally, in the scenarios *transitional disk* and *optical depth*, also the disk parameters $R_{in,disk}$ (inner radius of the disk) and $M_{dust,disk}$ (disk mass in dust) are changed to better mimic the disk evolutionary scenarios. All other parameters are held constant so that the effect of the changed parameter is best visible.

Table 6.3: *Characteristics of the benchmark model.*

Parameter		Unit	Benchmark
Stellar temperature	T_*	K	10 010
Stellar luminosity	L_*	$L_\odot$	40.7
Stellar radius	R_*	$R_\odot$	2.12
Stellar mass	M_*	$M_\odot$	2.50
inclination	i	$^\circ$	45
Distance	d	pc	158
Disk, inner radius	$R_{in,disk}$	AU	0.1
Disk, outer radius	$R_{out,disk}$	AU	250
Silicate fraction	f_{Si}	...	0.8
Carbon fraction	f_C	...	0.2
Min dust size	a_{min}	µm	0.01
Max dust size	a_{max}	mm	1
Dust-size power-law index	a_{pow}	...	-3.5
Disk, gas mass	$M_{gas,disk}$	$M_\odot$	3.0×10^{-2}
Disk, dust mass	$M_{dust,disk}$	$M_\odot$	3.0×10^{-4}

6.4.2 Scenario 1: grain growth

In the scenario *grain growth*, the dependence of the relative features strengths on the grain size is studied. We compare forsterite grains of 1, 5 and 10 µm in size. In this modeling grid, forsterite is mixed in the region between $0-50$ AU. As shown by the opacities in Figure 6.6, for grains $\gtrsim 1$ µm, the shorter wavelength features get weaker compared to the 69 µm feature. Thus I_{23}/I_{69} also decreases. For grains smaller than a few micron, the relative band strength is constant. Because the features between $25-35$ µm change in position, the points where the continuum is subtracted is changed from 21.75 and 26.4 µm to 23.5 and 29 µm.

6.4.3 Scenario 2: transitional disk

The scenario *transitional disk* highlights the temperature dependence of the feature strength ratios. To model this, we create disk models with increasingly larger inner holes (50, 100, and 150 AU). We then assume in each transitional disk that forsterite is present (10 %) in

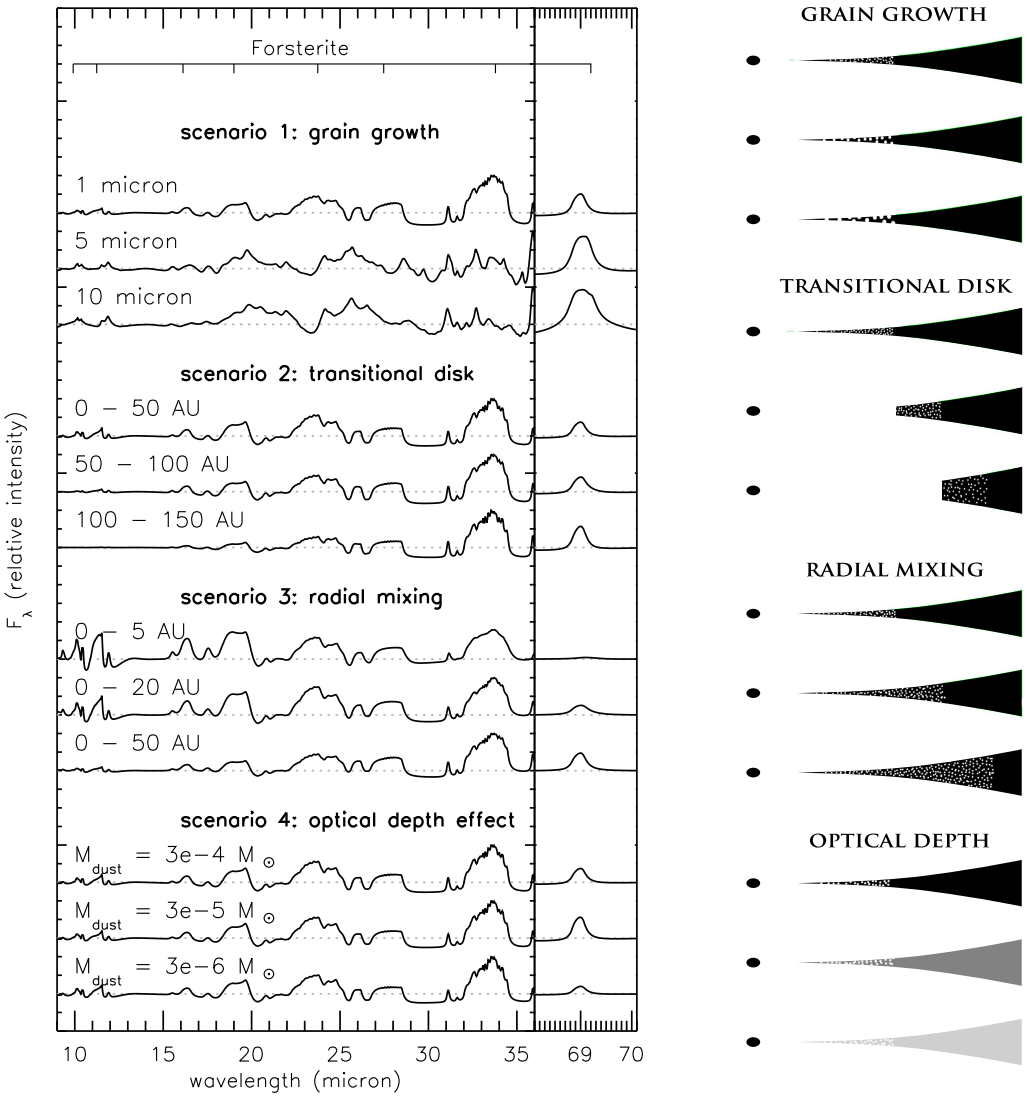

Figure 6.7: *Grain size scenario, transitional disk scenario, radial mixing scenario, optical depth effect. The continuum subtracted spectra are scaled relative to the strongest band so that the effect on the forsterite temperature is presented best. The right panel shows sketches to illustrate the structure of the disk and the location and sizes of forsterite grains.*

the 50 AU-wide region just outside of the gap. For the disk as a whole this means that an increasing amount of near infrared continuum is missing. The dominant effect for the forsterite feature ratios is the temperature selection that is taking place.

6.4.4 Scenario 3: radial mixing

The effect of forsterite being gradually mixed towards larger radii is studied in the scenario *radial mixing*. To model this scenario, a forsterite mass abundance of 10% is mixed in

the disk between 0.1 AU up to 5, 20 and 50 AU. When forsterite is mixed with a constant mass abundance ratio up to 50 AU in the disk, the feature strength ratio is $I_{23}/I_{69} = 1.2$. If forsterite is only present in the inner disk within 5 AU, than the 69 μm feature is relatively weak and $I_{23}/I_{69} = 15.2$.

6.4.5 Scenario 4: optical depth effects

The scenario *optical depth effects* investigates the feature strength ratio as a result of the differences in dust continuum optical depth. The optical depth is lower at longer wavelengths, therefore the $\tau = 1$ surface at 69 μm lies deeper in the disk than the $\tau = 1$ surface at 23 μm. Hence, the regions in the disk producing the 23 and 69 μm features have different volumes. Thus the feature strength ratio can be altered if the optical depth changes in the disk (as shown for HD 100546 in Mulders et al. 2011). We model this scenario adopting a mass abundance of 10% of forsterite within $0-50$ AU in the disk, and by varying the mass of the disk between 3×10^{-4} $M_\odot$ and 3×10^{-6} $M_\odot$. By decreasing the total mass in the disk, the disk goes stepwise from optically thick at both 23 and 69 μm to optically thin at 69 μm, and on to optically thin in both features. The 1.3 mm luminosity values of these disk models are over-plotted on Figure 6.3 and cover the range of observed 1.3 mm continuum detections for our sample of Herbig stars.

6.4.6 Summary of modelling scenarios

Comparing the results in this section to the observations as presented in Table 6.2 and Figures 6.4 and 6.3 we obtain the following results.

Since grains grow in protoplanetary disks, the *grain growth* scenario may be important to explain the observed forsterite feature strength ratios. Figure 6.7 shows the relative band strengths for different grain sizes. We find that for 1 μm grains the I_{23}/I_{69} band strength ratio is highest. For grains larger than a few micron, we find that the 23 μm band disappears and thus that the I_{23}/I_{69} ratio decreases to zero. For one particular object, HD 141569, it is demonstrated in Section 6.5, that the grain size is a plausible explanation for the feature strength ratio. Dust settling and grain growth of the standard dust component are not included. In reality, other grains also grow in size, and larger grains settle towards the midplane leaving relatively more small dust grains in the surface layers of the disk. These effects mainly affect the optical depth of the disk. Therefore, grain growth and settling change the ratio of flux contributions from small and larger grains. Thus the final spectrum may be expected to be a balance between small and large grains, set by the specific disk parameters.

In the *transitional disk* scenario, dust is cleared from the inner region and the forsterite is gradually mixed at larger radii. So basically these models show the effect of a decreasing average forsterite temperature. This scenario is limited in understanding the origin of the gap and the forsterite in the outer disk. E.g. it is yet not understood if the presence

of cold forsterite is due to in situ formation in the outer disk or is radially mixed outward. Figure 6.7 shows that if the forsterite is at larger radii in the disk, the I_{23}/I_{69} ratio decreases. Since the temperature is lower in the outer disk, the peak of the disk emission shifts towards longer wavelengths and the strength of the 69 μm feature increases in strength compared to that of the 23 μm feature. This may partly explain the forsterite spectra of transitional disks with known large gaps such as Oph IRS 48 and HD 141569.

An important insight follows from the *radial mixing* modeling grid for objects with strong forsterite features detected in the Spitzer/IRS spectrum, but no 69 μm feature detections. Figure 6.7 shows that if forsterite is only present in the inner disk, the 69 μm feature is much weaker than the 23 μm feature. There are two reasons for this effect. The first is based on the temperature. Even if the forsterite is hot, the 69 μm feature may not be visible in the spectrum because continuum emission from colder regions of the disk (where no forsterite is present) dominates. The second effect is that the integrated strength of the 69 μm band is three times weaker for 295 K compared to 50 K forsterite (see Section 6.3.1). In addition, because the feature gets broader towards higher temperatures, the peak flux of the 69 μm feature decreases almost an order of magnitude (see Figure 6.6). It is thus expected that the 69 μm feature will further broaden and decrease in strength for temperatures above 295 K. The low upper limits of the 69 μm detections typically show very large values of $I_{23}/I_{69} \sim 100$ (most notably for Group II sources). Since a forsterite abundance of 10 % between 0–5 AU gives a $I_{23}/I_{69} = 15.2$, this suggests that forsterite must be even closer to the star ($\sim 1-2$ AU). Because forsterite only resides in these hot inner regions of the disk, radial mixing is likely not an efficient process.

We find that within a limited mass range, *optical depth* effects can enhance the 69 μm feature as it becomes optically thin while the disk is still optically thick at 23 μm. This may explain the higher detection rate of the 69 μm feature for disks with a lower mm luminosity (Figures 6.3). There are three principal cases for the relative optical depth at 23 and 69 μm. The first situation is that the disk is optically thick at both 23 and 69 μm. This is the case for a disk mass of $M_{dust} = 3 \times 10^{-4}$ $M_{\odot}$. The optical depths scale relative to the density. So under the assumption that forsterite is vertically well mixed, the feature strength ratio is quite constant. The second situation is that the disk becomes optically thin at 69 μm while it is still optically thick at 23 μm ($M_{dust} = 3 \times 10^{-5}$ $M_{\odot}$). In this case, the 69 μm feature becomes stronger and the feature strength ratio decreases. Thirdly, the disk mass is so low that the disk is optically thin at both wavelengths. In this situation, all forsterite is visible to the observer and the feature strength ratio increases again.

Models predicting strong 69 μm features and weak features at shorter wavelengths are the grain growth scenario (where the emission is dominated by larger $\gtrsim 1$ μm forsterite dust), the transitional disk scenario (where only cold forsterite is left in the disk), and the optical depth scenario (the mass of small dust grains decreases and the disk becomes optically thin at 69 μm while it is still optically thick at 23 μm).

The opposite case where the 69 μm feature is weak compared to strong short wavelength forsterite bands can be explained due to inefficient radial mixing. In this scenario, forsterite is only present in the inner disk within a few AU. The location in the disk where the forsterite is hot depends on the stellar properties and geometry of the inner disk. For the

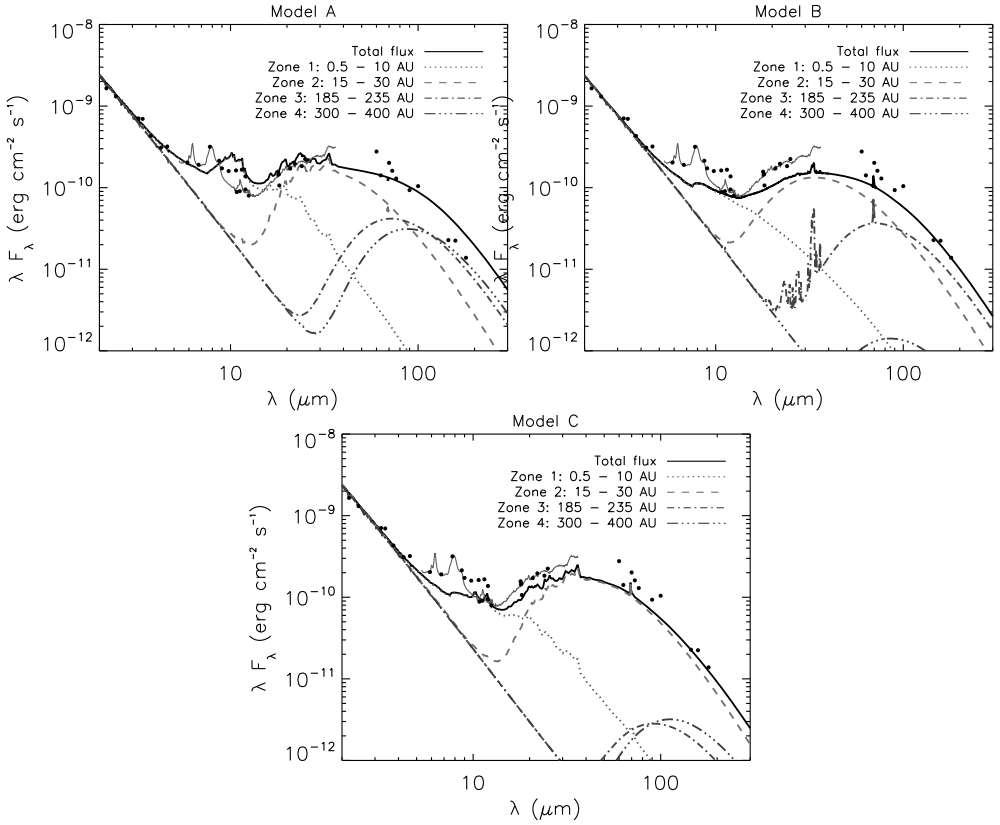

Figure 6.8: *SEDs of three models of HD141569. Top left: model A, small (1 μm) forsterite grains. Top right: model B, small (1 μm), cold, iron rich forsterite grains. Bottom: model C, large (10 μm) forsterite grains.*

continuous disk models presented in this section, the surface temperature of the disk is $\gtrsim$ 200 K at radii $\lesssim$ 3 AU. If the grains in the disk are mixed outward, then the 69 μm feature rapidly increases in strength. A mixing of 10 % forsterite in the inner 5 AU would result in a I_{23}/I_{69} ratio of 15.2. Since flat disks have an order of magnitude higher I_{23}/I_{69} ratios (Figure 6.4), we conclude that mixing is not efficient in flat disks.

6.5 The strong and broad 69 micron band of HD141569

In this section, detailed radiative transfer models of HD141569 are presented. HD141569 is selected for a case-study because we found in Section 6.2 that it is the most extreme outlier in the comparison between the forsterite temperature derived from the I_{23}/I_{69} feature strength ratio (T $\lesssim$ 70 K), and the temperature estimate obtained from the shape of the 69 μm feature (T $\sim$ 174 K).

6.5.1 Disk modeling approach

We focus on the dust mineralogy to constrain the size and location of forsterite. We first derive the geometry of the disk responsible for the dust continuum emission. Thereafter, we explore the properties of the grains that can fit the forsterite spectrum. We search for solutions which can reproduce the relative band strength I_{23}/I_{69}, the shape of the 69 μm feature and simultaneously fit the SED.

From earlier studies of the disk of HD141569, it is known that the disk of HD141569 is gas rich and is in the transition to a debris disk system (e.g. Augereau et al. 1999, Fisher et al. 2000, Clampin et al. 2003, Thi et al. 2014). Since we focus on the properties of the dust, our first step is to construct a geometrical model of the dust disk of HD 141569. We use the stellar properties derived in van den Ancker et al. (1998), with temperature $T_* = 9520$ K, luminosity $L_* = 18.3$ $L_\odot$ and distance $d = 99$ pc. The radiative transfer and dust model are described in Section 6.3. The modeling approach is largely similar to the benchmark model described in Section 6.4. The radial dependence of the surface density is parametrised by a power law with index -1. We assume a gas-to-dust ratio of 100. The dust size ranges from $a_{\rm min}$ up to $a_{\rm max}$ and follows a power-law distribution with $a_{\rm pow} = -3.5$. The maximum grain size $a_{\rm max}$ is set at 1 mm. The minimum grain size of the amorphous dust, as wel as the forsterite grains, is determined through simultaneously fitting of the forsterite features and the SED. The disk mass is also derived by fitting of the SED. We assume an amorphous dust composition of 80% silicate and 20% carbon for the dust emitting the continuum emission. Forsterite of either 1 or 10 μm size grains is mixed in the disk at certain radii in order to fit the forsterite spectrum.

6.5.2 The geometry of the disk

We construct a disk model that is based on available imaging data and the SED. In order to successfully fit the continuum emission of the SED, we find that it is required to break up the disk into four zones, with the following characteristics. Zone 1, between $0.5-10$ AU, is the innermost disk and is derived by a fit to the SED between $\sim 5-12$ μm. Therefore, zone 1 has a typical dust temperature between $\sim 150-1000$ K. Note that the continuum emission between the PAH features does not originate from the PAHs (Maaskant et al., 2013). We do not fit the PAH features in this model. Disk zone 2, between $15-30$ AU, accounts for the MIR emission bump between ~ 12 μm up to at least ~ 100 μm. The presence of this disk zone is inferred due to the bump in the SED, which is indicative of a high vertical disk wall that produces a strong single temperature emission component at ∼100 K. MIR imaging observations by Fisher et al. (2000) are consistent with the presence of such a disk zone, since quadratic deconvolution of the source with the PSF gives FWHM sizes of 34 AU at 10 μm and 62 AU at 18 μm for the extended emission near the star. However, we do not model the MIR observations, so we cannot accurately determine the inner and outer location of disk zone 2. Therefore we arbitrarily set zone 2 between $15-30$ AU, which results in typical dust temperatures between $\sim 70-100$ K. The presence of disk zone 3 and zone 4, located between respectively $185-235$ AU and $300-400$ AU, are inferred from direct scattered light observations (Augereau et al.,

1999, Clampin et al., 2003). From our model, we derive typical temperatures in zone 3 and 4 of $\sim$ 40 K and $\sim$30 K respectively.

Figure 6.8 shows three SEDs of forsterite models which we present in the next section. A degeneracy which follows from the SED fit is whether the outermost zones 3 and 4 dominate the continuum at long wavelengths. The observed photometry can be fitted by the Rayleigh Jeans tails of disk zones 2, 3 and 4 as shown in Figure 6.8. Millimetre imaging is needed to lift this degeneracy.

6.5.3 Fitting the forsterite

We want to reproduce the low forsterite I_{23}/I_{69} band strength ratio as well as the shape (i.e. the width and peak position) of the 69 μm feature. We do not aim to derive a perfect fit. Instead, we identify the most important parameters that play a role in fitting the forsterite spectrum. Referring back to the parameter study presented in the previous section, we can already indicate in what regions of the parameter space we can find solutions. In general, a low I_{23}/I_{69} ratio can be explained by cold forsterite (as in the transitional disk scenario), or larger grains. Optical depth effects do not play a role because we find in our models that because of the low mm luminosity, the disk mass is also very low and therefore the disk is optically thin.

To be consistent with the shape of the forsterite 69 μm feature, we need to include an effect that broadens the band while the forsterite is cold (i.e. to ensure a low I_{23}/I_{69} ratio). There are two effects that can produce that result. The first solution is by including an iron distribution. This has been done in detail by Sturm et al. (2013), who find that an iron fraction between 0–1.2 % (derived by interpolation between laboratory measurements between 0–8 %) of forsterite can fit the 69 μm feature of HD 141569. The second solution is by including forsterite grain size larger than a few micron (Section 6.4.2).

There are only two locations in the disk from which forsterite emission can observed the spectrum. From disk zone 2, which dominate the SED at MIR wavelengths, and from disk zone 3, which has a smaller contribution to the SED because the dust is colder. Forsterite emission from disk zones 1 and 4 is respectively too hot and cold to be observed.

In the next sections we present three forsterite models. Model A shows that 1 μm forsterite grains in disk zone 2 do not fit the observed spectra. Then we present two different models which do give a fit to the spectrum. Model B, with very cold, 1 μm, iron containing, forsterite in disk zone 3, and Model C, with forsterite grains of 10 μm mixed in disk zone 2. The parameters of the three models that are used to fit the forsterite spectrum, as well as the SED, are shown in Table 6.4. Spectra and sketches of these models are shown in Figure 6.9. In the discussion (Section 6.6.3) we evaluate the model solutions, discuss which formation histories are required for both scenarios, and argue that model C, using larger 10 μm grains, is favoured.

Table 6.4: *Characteristics of three HD 141569 models.*

Parameter	Unit	Model A	Model B	Model C
Disk total dust mass	$M_\odot$	3.1×10^{-6}	1.2×10^{-6}	9.5×10^{-6}
Disk zone 1				
Disk location	AU	0.5 – 10	0.5 – 10	0.5 – 10
Disk, dust mass	$M_\odot$	5×10^{-10}	7×10^{-10}	7×10^{-10}
Forsterite fraction	...	0	0	0
Min. dust size	μm	1	10	10
Disk zone 2				
Disk location	AU	15 – 30	15 – 30	15 – 30
Disk, dust mass	$M_\odot$	1×10^{-7}	1×10^{-7}	5×10^{-7}
Forsterite fraction	...	0.07	0	0.07
Min. dust size	μm	1	10	10
Disk zone 3				
Disk location	AU	185 – 235	185 – 235	185 – 235
Disk, dust mass	$M_\odot$	1×10^{-6}	1×10^{-6}	3.0×10^{-6}
Forsterite fraction	...	0	0.2	0
Min. dust size	μm	1	1	10
Disk zone 4				
Disk location	AU	300 – 400	300 – 400	300 – 400
Disk, dust mass	$M_\odot$	2×10^{-6}	1×10^{-7}	6.0×10^{-6}
Forsterite fraction	...	0	0	0
Min. dust size	μm	1	1	10

6.5.3.1 Model A: small forsterite grains

Model A incorporates (iron-free) 1 μm forsterite grains in disk zone 2. A mass abundance of 7% forsterite in zone 2 of the disk was needed to fit the peak flux of the 69 μm flux. This model gives several problems. As Figure 6.9 shows, the forsterite features at short wavelengths are over-predicted and the shape of the 69 μm band does not match the observation because the forsterite is too warm. The peak position of the 69 μm feature is too blue and the width is too narrow. As the peak position is sensitive to the iron content of forsterite, this could be alleviated by including a distribution of iron (Section 6.5.3.2).

The upper plot of Figure 6.8 shows that the SED of the disk is not well fitted. Because we assume that the minimum size of the amorphous silicate dust grains are equal to the forsterite grains, the 10 μm amorphous silicate features shows up in the spectrum. This feature originates from zone 1, thus we find that the innermost disk zone 1 is depleted of small ($\lesssim$1 μm) dust grains. Second, if the outermost zones 3 and 4 contribute $\sim$50 % of the emission at 69 μm, the SED at mm wavelengths is over predicted. Thus, we learn that

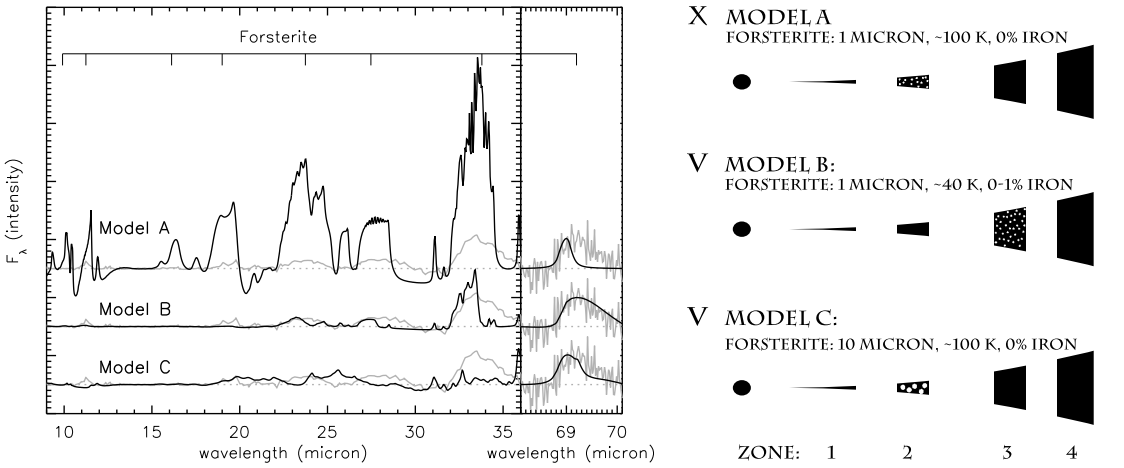

Figure 6.9: *The forsterite spectra of model A, B and C to HD141569. The black line is the model and the grey line is the data. Model A fails to fit the data, while model B and C give reasonable good fits. See text for model details. The right panel gives schematic representations of the disk structures. Four disk zones are needed to fit the SED and direct imaging observations. The 'X' symbol means that the model fails to fit the spectrum, the 'V' symbols shows the best fitting models.*

disk zone 2 dominates the continuum emission in the MIR and FIR from $\sim$ 14 μm up to at least $\sim$100 μm, and that the contribution from disk zones 3 and 4 at these wavelengths is small.

The assumption of thermal contact between the forsterite grains and the other disk components has consequences for the emission spectrum of forsterite. For this model, we have tested the scenario where the forsterite is not in thermal contact with the amorphous dust. We find that the temperature and more noticeably, the luminosity of forsterite decreases. Nevertheless, after scaling the abundance up to fit the 69 μm feature again, the forsterite is still too warm (i.e. the short wavelength features are still over-predicted).

6.5.3.2 Model B: small, cold, iron rich forsterite grains

In model B, 1 μm forsterite grains are mixed in zone 3, where they are further away from the star and thus colder. In order to fit the 69 μm feature, an abundance of 20 % forsterite in zone 3 is needed to fit the strength of the 69 μm feature. Because of the lower temperature in zone 3, the short wavelength features are much weaker. To prevent the model from producing the amorphous 10 and 20 μm silicate features, the minimum grain sizes in the innermost zones 1 and 2 are set at 10 μm. Note that this model implies that there is no contribution from warmer crystalline silicate grains in zone 2.

The shape of the 69 μm feature is fitted by assuming that the forsterite has a Gaussian distribution of different iron fractions. It has been shown by laboratory measurements that already an iron fraction of 8 % shifts the position of the 69 μm feature from 69 to 72 μm (Koike et al., 2003). Since iron increases the peak wavelength to the red, a Gaussian

distribution between 0 and 1 % iron can broaden the feature significantly. In Figure 6.9 it is shown that a distribution of iron fractions between $0-1$ % fits the feature well. The shape of the 69 μm has been calculated using weighted interpolations of different iron fractions. The method of interpolation is described in de Vries et al. (2012).

6.5.3.3 Model C: large forsterite grains

Model C presents a solution using iron-free forsterite grains of 10 μm in disk zone 2, using a mass abundance of 7% to fit the strength of the 69 μm feature. Similar to the grain size of the forsterite, the minimum grain size of the amorphous dust in the innermost zone 1 and 2 are set at 10 μm. For consistency, the minimum grain size in disk zones 3 and 4 are also set at 10 μm. The increased grain size influences the opacity profile of forsterite (see Figure 6.6). The shorter wavelength features are much weaker and the width of the 69 μm feature is naturally fitted, though the peak position of the model is slightly too blue (~ 0.2 μm) compared to the observed feature. Because the features between $25-35$ μm seem to change in position, the points where the continuum is subtracted for this model is changed from 21.75 and 26.4 μm to 23.5 and 29 μm.

6.5.4 Summary of HD 141569 modeling

Two models reasonably fit the observed spectrum of HD 141569, model B using respectively iron rich, ~ 40 K, 1 μm forsterite in zone 3, and model C, using iron free ~ 100 K, 10 μm forsterite in zone 2. Note that any model combining the parameter sets of these two cases would likely also fit the observations. For example, the short wavelengths forsterite features are not well fitted in model C, but this issue may be resolved by adding a small amount of small 1 μm forsterite grains (while the 69 μm feature is still dominated by the larger ~ 10 μm forsterite grains). Forsterite formation scenarios will have to explain how forsterite can be present at large distances from the central star and why they are either iron rich, or depleted of small grains. In Section 6.6.3 we will discuss both scenarios.

6.6 Discussion

The composition and sizes of forsterite grains are results of physical processes that take place during the evolution of protoplanetary disks. In the inner regions of disks where temperatures are high ($\gtrsim 1000$ K), forsterite can be formed through gas phase condensation and/or thermal annealing. The crystals may then be transported to the cooler outer parts of the disk. Scenarios include radial mixing in the disk (e.g., Bockelée-Morvan et al. 2002, Gail 2004, Davoisne et al. 2006, Jacquet 2014) and disk winds (e.g. Shu et al. 1994). Alternatively, crystalline silicates can be formed in-situ in the outer disk by shock waves (Harker & Desch, 2002, Desch et al., 2005), lightning (e.g. Pilipp et al. 1998), parent body collisions (Urey, 1967, Huss et al., 2001, Morlok et al., 2010), and stellar outbursts

(Juhász et al., 2012). To understand the significance of these scenarios, it is important to characterize the location, composition and sizes of forsterite grains in protoplanetary disks.

6.6.1 Forsterite in flat disks

We find that the I_{23}/I_{69} ratios of flat disks in our sample indicate high ($\gtrsim$ 200 K) forsterite temperatures. Since such temperatures are only found in the inner $\lesssim$ 5 AU of a continuous disk (i.e. no gaps), this shows that forsterite emission predominantly originates from the inner region in flat disks. Hence, the observations suggest that for flat disks, forsterite formation occurs in the hot inner region of the disk.

We find by radiative transfer models in Section 6.4 that the 69 μm feature is weakest if forsterite is only present in the inner few AU of the disk. If forsterite becomes abundant in colder regions of the disk, than the 69 μm feature rapidly increases in strength and should have been detectable. As the radial size of the T $\gtrsim$ 1000 K zone, where forsterite can form by annealing or vapor condensation, is small, the presence of forsterite features at short wavelengths imply that forsterite have diffused outward somewhat. However, the absence of the 69 μm features indicates that the diffusion process does not efficiently transport forsterite grains to the outer disk further than ∼5 AU.

The presence of (weak) 69 μm features in HD 104237 and HD 144668 and their absence in the other flat disks, may reflect optical depth effects. Among all flat disks, HD 104237 and HD 144668 have the lowest mm brightness and have the lowest I_{23}/I_{69} (besides HD 144432, but this is an upper limit). Since mm emission is optically thin, the low mm luminosities may imply lower disk masses. When the disk mass is lower, the disk is also more optically thin. In that case, the region where the forsterite is located may become optically thin at 69 μm while it is still optically thick at MIR wavelengths. Alternatively, forsterite grains may have been diffused outward to colder regions of the disk, or may have grown to larger sizes. All of these effects enhance the strength of the 69 μm feature and lower the I_{23}/I_{69} ratio. Although we cannot determine which evolutionary model is favourable, they all suggest that the detection of the 69 μm feature in flat disks is connected with disk evolution.

6.6.2 Forsterite in transitional disks

Many, if not all Herbig disks with disk classification group I are disks with large gaps and can be characterized as (pre-)transitional. An evolutionary path from the observed group I to the observed group II sources seems no longer likely. Instead, both might derive from a common ancestor, or group I objects may originate from group II sources (Maaskant et al., 2013). The variety in the results of our study for transitional disks (group I sources) is puzzling, in particular in connection with the fact that cold forsterite appears to be absent in flat disks (group II sources). For the transitional disks, we find that the majority of these disks do not have a detectable amount of cold forsterite (measured by

the presence or absence of the 69 μm feature). However, for a few sources, significant amounts of forsterite are present in the cold outer regions. The high crystalline mass fraction in the inner edge of the outer disk of HD 100546 (Mulders et al., 2011) seems to indicate that the cold forsterite is connected to the formation of the gap. As suggested by Bouwman et al. (2003), forsterite grains may be blown outwards on the wall by radiation pressure. However, this scenario would not work efficiently if significant amounts of gas resides in the gaps (as is the case for the transitional disks of Oph IRS 48, HD 141569 and HD 100546, Bruderer et al. 2014, Thi et al. 2014, Acke & van den Ancker 2006. Also for HD 100546, the non-negligible accretion rate derived by Deleuil et al. (2004) argues against outward radial mixing through the gap.

A possibility to explain the cold forsterite would be that the mixing in an earlier evolutionary state is more efficient than we derive, and that the forsterite is hidden in the disk and only exposed and made visible when the gap opens and the disk rim is illuminated. Perhaps the forsterite grains hide in the midplane after growing and settling and become visible when the disk mass decreases due to optical depth effects. Another option is that the forsterite is locally produced in the transitional disks where it is observed. This would also suggest a connection to the gap forming process, but is clearly not a process that is always linked to the formation of gaps.

When looking at this result in the terms of an evolutionary picture, the following scenarios and questions arise. If we assume that transitional disks are the evolutionary successor to flat disks, then we would in the first instance not expect significant amount of forsterite in the outer disk. Since radial mixing does not appear to be effective in flat disks, the situation just before the opening of a big gap would be that little or no forsterite present at low temperatures in the outer disk. Direct radial mixing would become infeasible in a disk with a large gap. If, however, the transitional disks and flat disks have evolved from a common ancestor, but represent different paths of disk evolution, than the large dispersion in abundances of cold forsterite in transitional disks still remains to be explained in this framework.

6.6.3 Larger grains in group Ib transitional disks

HD 141569 and Oph IRS 48 are transitional disk which lack the 10 and 20 μm amorphous silicate features, but instead show prominent PAH emission bands in their spectra. This is an indicator of large gaps which have depleted the population of small ($\lesssim 1$ μm) dust grains in the temperature region of the disk where amorphous silicate features are produced (Maaskant et al., 2013). The 69 μm features of HD141569 and Oph IRS 48 are remarkably strong and have large widths indicating temperatures of $\sim 150-200$ K. This is however not consistent with the temperature derived from the I_{23}/I_{69} ratio ($\sim 50-100$ K). We have found by detailed modeling of HD 141569 that there are two scenarios that fit the forsterite spectra. In the first scenario (model B), the forsterite is located in the outer disks at ~ 200 AU where temperatures are below $\lesssim 40$ K, an iron distribution has been used to fit the width of the 69μm feature. In the second scenario (model C), the forsterite is modelled by larger (10 μm) grains in the disk zone which also produces the mid- to

far-infrared continuum emission. The larger grain size broadens the 69 μm feature and decreases the strength of the features at lower wavelength. Combinations of these two extreme models may also fit the spectra.

We now discuss the forsterite formation histories required to explain both model solutions. For model B, it is difficult to understand that there is a mass abundances of ∼20 % in the disk at ∼ 200 AU, while no forsterite grains are present in the innermost disk zones. If shock heating, parent body collisions or radial mixing are responsible for the cold forsterite, we may expect this to be more efficient closer to the star due to higher densities and relative velocities. Also the Gaussian distribution of iron fractions between $0-1$ % has no clear origin. The shape of the 69 μm feature of HD 141569 is comparable to that of Oph IRS 48. The inner edge of the outer disk of Oph IRS 48 has a temperature ∼120 K and is located at ∼60 AU (Maaskant et al., 2013). However, there is yet no observational evidence of a large colder ($T \lesssim 50$ K) outer disk at $\gtrsim 200$ AU for Oph IRS 48. A model with a dominant contribution of cold, iron rich forsterite (model B) seems much more difficult to construct for Oph IRS 48. Model C, the scenario with a dominant contribution of larger (i.e. 10 μm) grains, does not have these difficulties. In addition, our solution of larger forsterite grains in the disks of HD 141569 and Oph IRS 48 seems to be consistent with significant depletion of small grains in group Ib sources. For all these reasons, we consider model C to be a more likely scenario to explain the forsterite spectrum of HD 141569 and Oph IRS 48. In this scenario, the larger width of the forsterite 69 μm feature can be used as an independent indicator of larger grains sizes in protoplanetary disks.

6.7 Conclusions

We have performed a detailed radiative transfer study to examine the observational behaviour of forsterite spectra under several evolutionary scenarios. In particular we check for consistency between the forsterite I_{23}/I_{69} feature strength ratio, and the shape of the 69μm feature and study HD 141569 in detail as it is the most extreme outlier in the sample. Our findings are:

- Forsterite in flat (group II) disks is located in the inner few AU. This indicates that radial mixing is an inefficient process, at least in flat disks, or that local production does not take place.
- The detection rate of the 69 μm forsterite feature is higher for objects with lower millimeter luminosity. This may indicate that as disks evolve toward lower masses, optical depth effects or increased production/transportation of forsterite in/to cold regions of the outer disk enhance the strength of the 69 μm feature.
- The I_{23}/I_{69} ratio is an independent forsterite temperature indicator, and is most inconsistent with the observed 69 μm shapes of HD 141569 and Oph IRS 48.

- The large widths of the 69 μm features of HD 141569 and Oph IRS 48 can be explained by forsterite grains with sizes above a few micron, or by a distribution of iron fractions between $\sim 0-1$ %.
- The weak 23 μm feature compared to the 69 μm band strength in the evolved transitional objects HD 141569 and IRS 48 can be explained by very cold, or larger grains.
- The innermost disk of HD 141569, responsible for the continuum emission between $\sim 4-14$ μm, does not contain small ($\lesssim 1$ μm) amorphous and crystalline silicate grains.
- Radiative transfer models show two solutions to fit the larger width of the forsterite 69 μm band, consistently with the low I_{23}/I_{69} feature strength ratio of HD 141569. A model with iron rich ($\sim 0-1$ % Fe fraction), ∼40 K, 1 μm grains (model B) and a model using iron free, ∼100 K, 10 μm grains (model C). We argue that the model with larger ($\gtrsim 10$ μm) forsterite seems to be most likely.

Acknowledgements: *The authors thank the anonymous referee for his/her excellent comments and constructive feedback. The authors thank Neal Evans, Gwendolyn Meeus, Thomas Henning, Jeroen Bouwman, and the members of the Herschel DIGIT team for useful discussions which improved the analysis presented in this paper. The authors thank Gijs Mulders and Inga Kamp for useful comments on the manuscript. K.M. is supported by a grant from the Netherlands Research School for Astronomy (NOVA). M.M. acknowledges funding from the EU FP7-2011 under Grant Agreement No 284405. Studies of interstellar chemistry at Leiden Observatory are supported through advanced-ERC grant 246976 from the European Research Council, through a grant by the Dutch Science Agency, NWO, as part of the Dutch Astrochemistry Network, and through the Spinoza premie from the Dutch Science Agency, NWO.*

Bibliography

Ábrahám, P., Juhász, A., Dullemond, C. P., et al. 2009, Nature, 459, 224

Acke, B., Bouwman, J., Juhász, A., et al. 2010, ApJ, 718, 558

Acke, B., Min, M., van den Ancker, M. E., et al. 2009, A&A, 502, L17

Acke, B., & van den Ancker, M. E. 2004, A&A, 426, 151

Acke, B., & van den Ancker, M. E. 2006, A&A, 449, 267

Acke, B., van den Ancker, M. E., & Dullemond, C. P. 2005, A&A, 436, 209

Adams, F. C., Lada, C. J., & Shu, F. H. 1987, ApJ, 312, 788

Alexander, R. D., Clarke, C. J., & Pringle, J. E. 2006, MNRAS, 369, 216

Allamandola, L. J., Hudgins, D. M., & Sandford, S. A. 1999, ApJ, 511, L115

Allamandola, L. J., Tielens, A. G. G. M., & Barker, J. R. 1985, ApJ, 290, L25

Allamandola, L. J., Tielens, A. G. G. M., & Barker, J. R. 1989, ApJS, 71, 733

Andrews, S. M., & Williams, J. P. 2005, ApJ, 631, 1134

Andrews, S. M., & Williams, J. P. 2007, ApJ, 671, 1800

Andrews, S. M., Wilner, D. J., Espaillat, C., et al. 2011, ApJ, 732, 42

Armitage, P. J. 2007, ArXiv Astrophysics e-prints, arXiv:astro-ph/0701485

Armitage, P. J. 2011, ARA&A, 49, 195

Artymowicz, P., & Lubow, S. H. 1994, ApJ, 421, 651

Augereau, J. C., Lagrange, A. M., Mouillet, D., & Ménard, F. 1999, A&A, 350, L51

Augereau, J. C., & Papaloizou, J. C. B. 2004, A&A, 414, 1153

Bakes, E. L. O., & Tielens, A. G. G. M. 1994, ApJ, 427, 822

Ballester, G. E., Sing, D. K., & Herbert, F. 2007, Nature, 445, 511

Bauschlicher, Jr., C. W., Peeters, E., & Allamandola, L. J. 2009, ApJ, 697, 311

Benisty, M., Tatulli, E., Ménard, F., & Swain, M. R. 2010, A&A, 511, A75

Benisty, M., Renard, S., Natta, A., et al. 2011, A&A, 531, A84

Bergin, E. A., & Tafalla, M. 2007, ARA&A, 45, 339

Berné, O., Joblin, C., Fuente, A., & Ménard, F. 2009, A&A, 495, 827

Berné, O., & Tielens, A. G. G. M. 2012, Proceedings of the National Academy of Science, 109, 401

Bjorkman, J. E., & Wood, K. 2001a, ApJ, 554, 615

Bjorkman, J. E., & Wood, K. 2001b, ApJ, 554, 615

Bockelée-Morvan, D., Gautier, D., Hersant, F., Huré, J.-M., & Robert, F. 2002, A&A, 384, 1107

Boersma, C., Bouwman, J., Lahuis, F., et al. 2008, A&A, 484, 241

Boley, A. C., Payne, M. J., Corder, S., et al. 2012, ApJ, 750, L21

Bontemps, S., André, P., Kaas, A. A., et al. 2001, A&A, 372, 173

Boss, A. P. 1997, Science, 276, 1836

Bouwman, J., de Koter, A., Dominik, C., & Waters, L. B. F. M. 2003, A&A, 401, 577

Bouwman, J., de Koter, A., van den Ancker, M. E., & Waters, L. B. F. M. 2000, A&A, 360, 213

Bouwman, J., Meeus, G., de Koter, A., et al. 2001, A&A, 375, 950

Bouwman, J., Henning, T., Hillenbrand, L. A., et al. 2008, ApJ, 683, 479

Bowey, J. E., Barlow, M. J., Molster, F. J., et al. 2002, MNRAS, 331, L1

Bradley, J. P., Humecki, H. J., & Germani, M. S. 1992, ApJ, 394, 643

Brown, J. M., Blake, G. A., Qi, C., et al. 2009, ApJ, 704, 496

Brown, J. M., Herczeg, G. J., Pontoppidan, K. M., & van Dishoeck, E. F. 2012a, ApJ, 744, 116

Brown, J. M., Rosenfeld, K. A., Andrews, S. M., Wilner, D. J., & van Dishoeck, E. F. 2012b, ApJ, 758, L30

Bruderer, S., van der Marel, N., van Dishoeck, E. F., & van Kempen, T. A. 2014, A&A, 562, A26

Bryden, G., Chen, X., Lin, D. N. C., Nelson, R. P., & Papaloizou, J. C. B. 1999, ApJ, 514, 344

Calvet, N., D'Alessio, P., Watson, D. M., et al. 2005, ApJ, 630, L185

Cardelli, J. A., Meyer, D. M., Jura, M., & Savage, B. D. 1996, ApJ, 467, 334

Carmona, A., van den Ancker, M. E., Thi, W.-F., Goto, M., & Henning, T. 2005, A&A, 436, 977

Carmona, A., van der Plas, G., van den Ancker, M. E., et al. 2011, A&A, 533, A39

Carmona, A., Pinte, C., Thi, W. F., et al. 2014, ArXiv e-prints, arXiv:1403.6193

Casassus, S., van der Plas, G., M, S. P., et al. 2013, Nature, 493, 191

Charbonneau, D., Allen, L. E., Megeath, S. T., et al. 2005, ApJ, 626, 523

Chen, L., Kreplin, A., Wang, Y., et al. 2012, A&A, 541, A104

Chiang, E., & Murray-Clay, R. 2007, Nature Physics, 3, 604

Chiang, E. I., & Goldreich, P. 1997, ApJ, 490, 368

Cieza, L. A., Schreiber, M. R., Romero, G. A., et al. 2012, ApJ, 750, 157

Cieza, L. A., Padgett, D. L., Allen, L. E., et al. 2009, ApJ, 696, L84

Cieza, L. A., Schreiber, M. R., Romero, G. A., et al. 2010, ApJ, 712, 925

Clampin, M., Krist, J. E., Ardila, D. R., et al. 2003, AJ, 126, 385

Collins, K. A., Grady, C. A., Hamaguchi, K., et al. 2009, ApJ, 697, 557

Crovisier, J., Leech, K., Bockelee-Morvan, D., et al. 1997, Science, 275, 1904

Currie, T. 2010, ArXiv e-prints, arXiv:1002.1715

Currie, T., & Sicilia-Aguilar, A. 2011, ApJ, 732, 24

Cutri, R. M., Skrutskie, M. F., van Dyk, S., et al. 2003, 2MASS All Sky Catalog of point sources.

Davoisne, C., Djouadi, Z., Leroux, H., et al. 2006, A&A, 448, L1

de Juan Ovelar, M., Min, M., Dominik, C., et al. 2013, A&A, 560, A111

de Vries, B. L., Acke, B., Blommaert, J. A. D. L., et al. 2012, Nature, 490, 74

de Winter, D., van den Ancker, M. E., Maira, A., et al. 2001, A&A, 380, 609

de Zeeuw, P. T., Hoogerwerf, R., de Bruijne, J. H. J., Brown, A. G. A., & Blaauw, A. 1999, AJ, 117, 354

Deleuil, M., Lecavelier des Etangs, A., Bouret, J.-C., et al. 2004, A&A, 418, 577

Dent, W. R. F., Greaves, J. S., & Coulson, I. M. 2005, MNRAS, 359, 663

Desch, S. J., Ciesla, F. J., Hood, L. L., & Nakamoto, T. 2005, in Astronomical Society of the Pacific Conference Series, Vol. 341, Chondrites and the Protoplanetary Disk, ed. A. N. Krot, E. R. D. Scott, & B. Reipurth, 849

Di Francesco, J., Johnstone, D., Kirk, H., MacKenzie, T., & Ledwosinska, E. 2008, ApJS, 175, 277

Dodson-Robinson, S. E., & Salyk, C. 2011, ApJ, 738, 131

Doering, R. L., Meixner, M., Holfeltz, S. T., et al. 2007, AJ, 133, 2122

Dong, R., Rafikov, R., Zhu, Z., et al. 2012, ApJ, 750, 161

Dorschner, J., Begemann, B., Henning, T., Jaeger, C., & Mutschke, H. 1995, A&A, 300, 503

Doucet, C., Habart, E., Pantin, E., et al. 2007, A&A, 470, 625

Doucet, C., Pantin, E., Lagage, P. O., & Dullemond, C. P. 2006, A&A, 460, 117

Draine, B. T. 2003, ARA&A, 41, 241

Draine, B. T., & Li, A. 2001, ApJ, 551, 807

Draine, B. T., & Li, A. 2007, ApJ, 657, 810

Dullemond, C. P., Apai, D., & Walch, S. 2006, ApJ, 640, L67

Dullemond, C. P., & Dominik, C. 2004a, A&A, 417, 159

Dullemond, C. P., & Dominik, C. 2004b, A&A, 421, 1075

Dullemond, C. P., & Dominik, C. 2005, A&A, 434, 971

Dullemond, C. P., & Dominik, C. 2008, A&A, 487, 205

Dullemond, C. P., Dominik, C., & Natta, A. 2001, ApJ, 560, 957

Dullemond, C. P., Henning, T., Visser, R., et al. 2007a, A&A, 473, 457

Dullemond, C. P., Hollenbach, D., Kamp, I., & D'Alessio, P. 2007b, Protostars and Planets V, 555

Dullemond, C. P., & Monnier, J. D. 2010, ARA&A, 48, 205

Dunkin, S. K., Barlow, M. J., & Ryan, S. G. 1997, in Astrophysics and Space Science Library, Vol. 215, Infrared Space Interferometry : Astrophysics the Study of Earth-Like Planets, ed. C. Eiroa, 9

Edgar, R. G., & Quillen, A. C. 2008, MNRAS, 387, 387

Ekern, S. P., Marshall, A. G., Szczepanski, J., & Vala, M. 1997, ApJ, 488, L39

Engelke, C. W., Price, S. D., & Kraemer, K. E. 2006, AJ, 132, 1445

Espaillat, C., Calvet, N., D'Alessio, P., et al. 2007, ApJ, 670, L135

Fabian, D., Jäger, C., Henning, T., Dorschner, J., & Mutschke, H. 2000, A&A, 364, 282

Fedele, D., van den Ancker, M. E., Acke, B., et al. 2008, A&A, 491, 809

Fedele, D., Bruderer, S., van Dishoeck, E. F., et al. 2013, A&A, 559, A77

Fisher, R. S., Telesco, C. M., Piña, R. K., Knacke, R. F., & Wyatt, M. C. 2000, ApJ, 532, L141

Fitzpatrick, E. L. 1999, PASP, 111, 63

Fujiwara, H., Honda, M., Kataza, H., et al. 2006, ApJ, 644, L133

Fukagawa, M., Tamura, M., Itoh, Y., et al. 2006, ApJ, 636, L153

Fung, J., Shi, J.-M., & Chiang, E. 2013, ArXiv e-prints 1310.0156, arXiv:1310.0156

Gail, H.-P. 2004, A&A, 413, 571

Galliano, F., Madden, S. C., Tielens, A. G. G. M., Peeters, E., & Jones, A. P. 2008, ApJ, 679, 310

Garcia Lopez, R., Natta, A., Testi, L., & Habart, E. 2006, A&A, 459, 837

Geers, V. C., Pontoppidan, K. M., van Dishoeck, E. F., et al. 2007a, A&A, 469, L35

Geers, V. C., van Dishoeck, E. F., Visser, R., et al. 2007b, A&A, 476, 279

Gezari, D. Y., Pitts, P. S., & Schmitz, M. 1999, VizieR Online Data Catalog, 2225, 0

Gorti, U., Dullemond, C. P., & Hollenbach, D. 2009, ApJ, 705, 1237

Grady, C. A., Woodgate, B. E., Bowers, C. W., et al. 2005, ApJ, 630, 958

Grady, C. A., Schneider, G., Hamaguchi, K., et al. 2007, ApJ, 665, 1391

Grady, C. A., Muto, T., Hashimoto, J., et al. 2013, ApJ, 762, 48

Greaves, J. S., Mannings, V., & Holland, W. S. 2000, Icarus, 143, 155

Guhathakurta, P., & Draine, B. T. 1989, ApJ, 345, 230

Habart, E., Natta, A., & Krügel, E. 2004, A&A, 427, 179

Habart, E., Natta, A., Testi, L., & Carbillet, M. 2006, A&A, 449, 1067

Habing, H. J. 1968, Bull. Astron. Inst. Netherlands, 19, 421

Hallenbeck, S., & Nuth, J. 1998, Ap&SS, 255, 427

Hallenbeck, S. L., Nuth, III, J. A., & Nelson, R. N. 2000, ApJ, 535, 247

Harker, D. E., & Desch, S. J. 2002, ApJ, 565, L109

Harker, D. E., Wooden, D. H., Woodward, C. E., & Lisse, C. M. 2002, ApJ, 580, 579

Hartmann, L., Calvet, N., Gullbring, E., & D'Alessio, P. 1998, ApJ, 495, 385

Hellyer, B. 1970, MNRAS, 148, 383

Henning, T. 2010, ARA&A, 48, 21

Henning, T., Launhardt, R., Steinacker, J., & Thamm, E. 1994, A&A, 291, 546

Henning, T., & Stognienko, R. 1996, A&A, 311, 291

Honda, M., Inoue, A. K., Okamoto, Y. K., et al. 2010, ApJ, 718, L199

Honda, M., Maaskant, K., Okamoto, Y. K., et al. 2012, ApJ, 752, 143

Hony, S., Van Kerckhoven, C., Peeters, E., et al. 2001, A&A, 370, 1030

Howard, A. W., Marcy, G. W., Johnson, J. A., et al. 2010, Science, 330, 653

Hudgins, D. M., & Allamandola, L. J. 1999, ApJ, 516, L41

Hughes, A. M., Wilner, D. J., Qi, C., & Hogerheijde, M. R. 2008, ApJ, 678, 1119

Huss, G. R., MacPherson, G. J., Wasserburg, G. J., Russell, S. S., & Srinivasan, G. 2001, Meteoritics and Planetary Science, 36, 975

Isella, A., Carpenter, J. M., & Sargent, A. I. 2009, The Astrophysical Journal, 701, 260

Isella, A., Natta, A., Wilner, D., Carpenter, J. M., & Testi, L. 2010, ApJ, 725, 1735

Jacquet, E. 2014, ArXiv e-prints, arXiv:1402.0533

Joblin, C. 2003, in SF2A-2003: Semaine de l'Astrophysique Francaise, ed. F. Combes, D. Barret, T. Contini, & L. Pagani, 175

Jochims, H. W., Ruhl, E., Baumgartel, H., Tobita, S., & Leach, S. 1994, ApJ, 420, 307

Juhász, A., Bouwman, J., Henning, T., et al. 2010, ApJ, 721, 431

Juhász, A., Dullemond, C. P., van Boekel, R., et al. 2012, ApJ, 744, 118

Kamp, I. 2011, in EAS Publications Series, Vol. 46, EAS Publications Series, ed. C. Joblin & A. G. G. M. Tielens, 271–283

Kamp, I., & Dullemond, C. P. 2004, ApJ, 615, 991

Kamp, I., Tilling, I., Woitke, P., Thi, W.-F., & Hogerheijde, M. 2010, A&A, 510, A18

Kasting, J. F., Whitmire, D. P., & Reynolds, R. T. 1993, Icarus, 101, 108

Kataza, H., Okamoto, Y., Takubo, S., et al. 2000, in Society of Photo-Optical Instrumentation Engineers (SPIE) Conference Series, Vol. 4008, Optical and IR Telescope Instrumentation and Detectors, ed. M. Iye & A. F. Moorwood, 1144–1152

Keller, L. D., Sloan, G. C., Forrest, W. J., et al. 2008, ApJ, 684, 411

Kemper, F., Vriend, W. J., & Tielens, A. G. G. M. 2004, ApJ, 609, 826

Kenyon, S. J., & Hartmann, L. 1987, ApJ, 323, 714

Koike, C., Chihara, H., Tsuchiyama, A., et al. 2003, A&A, 399, 1101

Koike, C., Shibai, H., & Tuchiyama, A. 1993, MNRAS, 264, 654

Koike, C., Mutschke, H., Suto, H., et al. 2006, A&A, 449, 583

Krijt, S., & Dominik, C. 2011, A&A, 531, A80

Kuhn, J. R., Potter, D., & Parise, B. 2001, ApJ, 553, L189

Kusakabe, N., Grady, C. A., Sitko, M. L., et al. 2012, ApJ, 753, 153

Lagage, P. O., Pel, J. W., Authier, M., et al. 2004, The Messenger, 117, 12

Lagage, P.-O., Doucet, C., Pantin, E., et al. 2006, Science, 314, 621

Lagrange, A.-M., Bonnefoy, M., Chauvin, G., et al. 2010, Science, 329, 57

Le Page, V., Snow, T. P., & Bierbaum, V. M. 2003, ApJ, 584, 316

Leger, A., & Puget, J. L. 1984, A&A, 137, L5

Leinert, C., van Boekel, R., Waters, L. B. F. M., et al. 2004, A&A, 423, 537

Li, A., & Lunine, J. I. 2003, ApJ, 594, 987

Li, H., Colgate, S. A., Wendroff, B., & Liska, R. 2001, ApJ, 551, 874

Lissauer, J. J. 1993, ARA&A, 31, 129

Lisse, C. M., VanCleve, J., Adams, A. C., et al. 2006, Science, 313, 635

Loinard, L., Torres, R. M., Mioduszewski, A. J., & Rodríguez, L. F. 2008, ApJ, 675, L29

Lubow, S. H., Seibert, M., & Artymowicz, P. 1999, ApJ, 526, 1001

Lyo, A.-R., Ohashi, N., Qi, C., Wilner, D. J., & Su, Y.-N. 2011, AJ, 142, 151

Maaskant, K. M., Min, M., Waters, L. B. F. M., & Tielens, A. G. G. M. 2014, A&A, 563, A78

Maaskant, K. M., Honda, M., Waters, L. B. F. M., et al. 2013, A&A, 555, A64

MacKinnon, I. D. R., & Rietmeijer, F. J. M. 1987, Reviews of Geophysics, 25, 1527

Malfait, K., Bogaert, E., & Waelkens, C. 1998, A&A, 331, 211

Mamajek, E. E. 2009, in American Institute of Physics Conference Series, Vol. 1158, American Institute of Physics Conference Series, ed. T. Usuda, M. Tamura, & M. Ishii, 3–10

Mannings, V., & Sargent, A. I. 1997, ApJ, 490, 792

Mannings, V., & Sargent, A. I. 2000, ApJ, 529, 391

Mariñas, N., Telesco, C. M., Fisher, R. S., & Packham, C. 2011, ApJ, 737, 57

Marois, C., Macintosh, B., Barman, T., et al. 2008, Science, 322, 1348

Marois, C., Zuckerman, B., Konopacky, Q. M., Macintosh, B., & Barman, T. 2010, Nature, 468, 1080

Martin-Zaïdi, C., Lagage, P.-O., Pantin, E., & Habart, E. 2007, ApJ, 666, L117

Mathis, J. S., Rumpl, W., & Nordsieck, K. H. 1977, ApJ, 217, 425

Matter, A., Labadie, L., Kreplin, A., et al. 2013, in Protostars and Planets VI, Heidelberg, July 15-20, 2013. Poster #2B014, 14

Matter, A., Labadie, L., Kreplin, A., et al. 2014, A&A, 561, A26

McClure, M. K., Furlan, E., Manoj, P., et al. 2010, ApJS, 188, 75

Meeus, G., Bouwman, J., Dominik, C., Waters, L. B. F. M., & de Koter, A. 2002, A&A, 392, 1039

Meeus, G., Bouwman, J., Dominik, C., Waters, L. B. F. M., & de Koter, A. 2003, A&A, 402, 767

Meeus, G., Waters, L. B. F. M., Bouwman, J., et al. 2001, A&A, 365, 476

Meeus, G., Pinte, C., Woitke, P., et al. 2010, A&A, 518, L124

Meeus, G., Montesinos, B., Mendigutía, I., et al. 2012, A&A, 544, A78

Meeus, G., Salyk, C., Bruderer, S., et al. 2013, A&A, 559, A84

Meijer, J. 2007, PhD thesis, University of Amsterdam

Mendigutía, I., Calvet, N., Montesinos, B., et al. 2011, A&A, 535, A99

Mennella, V., Brucato, J. R., Colangeli, L., & Palumbo, P. 1999, ApJ, 524, L71

Merín, B., Montesinos, B., Eiroa, C., et al. 2004, A&A, 419, 301

Min, M., Dominik, C., & Waters, L. B. F. M. 2004, A&A, 413, L35

Min, M., Dullemond, C. P., Dominik, C., de Koter, A., & Hovenier, J. W. 2009, A&A, 497, 155

Min, M., Hovenier, J. W., & de Koter, A. 2005, A&A, 432, 909

Momose, M., Morita, A., Okamoto, Y., et al. 2013, in Astronomical Society of the Pacific Conference Series, Vol. 476, Astronomical Society of the Pacific Conference Series, ed. R. Kawabe, N. Kuno, & S. Yamamoto, 389

Montillaud, J., Joblin, C., & Toublanc, D. 2013, A&A, 552, A15

Morlok, A., Koike, C., Tomioka, N., Mann, I., & Tomeoka, K. 2010, Icarus, 207, 45

Mulders, G. D., Dominik, C., & Min, M. 2010, A&A, 512, A11

Mulders, G. D., Min, M., Dominik, C., Debes, J. H., & Schneider, G. 2012, ArXiv e-prints, arXiv:1210.4132

Mulders, G. D., Waters, L. B. F. M., Dominik, C., et al. 2011, A&A, 531, A93

Muto, T., Grady, C. A., Hashimoto, J., et al. 2012, ApJ, 748, L22

Mutschke, H., Begemann, B., Dorschner, J., et al. 1998, A&A, 333, 188

Najita, J. R., Strom, S. E., & Muzerolle, J. 2007, MNRAS, 378, 369

Nakamura, T., Noguchi, T., Tanaka, M., et al. 2011, Science, 333, 1113

Natta, A., Testi, L., Calvet, N., et al. 2007, Protostars and Planets V, 767

Natta, A., Testi, L., Neri, R., Shepherd, D. S., & Wilner, D. J. 2004, A&A, 416, 179

Nomura, H., & Millar, T. J. 2005, A&A, 438, 923

Okamoto, Y. K., Kataza, H., Yamashita, T., et al. 2003, in Society of Photo-Optical Instrumentation Engineers (SPIE) Conference Series, Vol. 4841, Instrument Design and Performance for Optical/Infrared Ground-based Telescopes, ed. M. Iye & A. F. M. Moorwood, 169–180

Okuzumi, S., Tanaka, H., Kobayashi, H., & Wada, K. 2012, ApJ, 752, 106

Oliveira, I., Merín, B., Pontoppidan, K. M., & van Dishoeck, E. F. 2013, ApJ, 762, 128

Olofsson, J., Augereau, J.-C., van Dishoeck, E. F., et al. 2009, A&A, 507, 327

Olofsson, J., Benisty, M., Le Bouquin, J.-B., et al. 2013, A&A, 552, A4

Paardekooper, S.-J., & Mellema, G. 2004, A&A, 425, L9

Panić, O., Hogerheijde, M. R., Wilner, D., & Qi, C. 2008, A&A, 491, 219

Peeters, E., Hony, S., Van Kerckhoven, C., et al. 2002, A&A, 390, 1089

Piétu, V., Dutrey, A., Guilloteau, S., Chapillon, E., & Pety, J. 2006, A&A, 460, L43

Piétu, V., Guilloteau, S., & Dutrey, A. 2005, A&A, 443, 945

Pilipp, W., Hartquist, T. W., Morfill, G. E., & Levy, E. H. 1998, A&A, 331, 121

Pinilla, P., Benisty, M., & Birnstiel, T. 2012, A&A, 545, A81

Pinte, C., Harries, T. J., Min, M., et al. 2009, A&A, 498, 967

Pollack, J. B., Hubickyj, O., Bodenheimer, P., et al. 1996, Icarus, 124, 62

Pontoppidan, K. M., Blake, G. A., van Dishoeck, E. F., et al. 2008, ApJ, 684, 1323

Preibisch, T., Ossenkopf, V., Yorke, H. W., & Henning, T. 1993, A&A, 279, 577

Puget, J. L., & Leger, A. 1989, ARA&A, 27, 161

Qi, C., D'Alessio, P., Öberg, K. I., et al. 2011, ApJ, 740, 84

Quanz, S. P., Avenhaus, H., Buenzli, E., et al. 2013, ArXiv e-prints, arXiv:1302.3029

Quanz, S. P., Birkmann, S. M., Apai, D., Wolf, S., & Henning, T. 2012, A&A, 538, A92

Raman, A., Lisanti, M., Wilner, D. J., Qi, C., & Hogerheijde, M. 2006, AJ, 131, 2290

Rapacioli, M., Joblin, C., & Boissel, P. 2005, A&A, 429, 193

Reche, R., Beust, H., & Augereau, J.-C. 2009, A&A, 493, 661

Ricca, A., Bauschlicher, Jr., C. W., Boersma, C., Tielens, A. G. G. M., & Allamandola, L. J. 2012, ApJ, 754, 75

Rice, W. K. M., Armitage, P. J., Wood, K., & Lodato, G. 2006, MNRAS, 373, 1619

Sako, S., Okamoto, Y. K., Kataza, H., et al. 2003, PASP, 115, 1407

Salyk, C., Blake, G. A., Boogert, A. C. A., & Brown, J. M. 2007, ApJ, 655, L105

Salyk, C., Blake, G. A., Boogert, A. C. A., & Brown, J. M. 2009, ApJ, 699, 330

Salyk, C., Pontoppidan, K. M., Blake, G. A., Najita, J. R., & Carr, J. S. 2011, ApJ, 731, 130

Sandell, G., Weintraub, D. A., & Hamidouche, M. 2011, ApJ, 727, 26

Sandford, S. A., Aléon, J., Alexander, C. M. O. ., et al. 2006, Science, 314, 1720

Schegerer, A. A., Ratzka, T., Schuller, P. A., et al. 2013, A&A, 555, A103

Schutte, W. A., Tielens, A. G. G. M., & Allamandola, L. J. 1993, ApJ, 415, 397

Shakura, N. I., & Sunyaev, R. A. 1973, A&A, 24, 337

Shu, F., Najita, J., Ostriker, E., et al. 1994, ApJ, 429, 781

Siebenmorgen, R., & Heymann, F. 2012, A&A, 543, A25

Siebenmorgen, R., & Krügel, E. 2010, A&A, 511, A6

Sirono, S.-i. 2011, ApJ, 735, 131

Sitko, M. L., Day, A. N., Kimes, R. L., et al. 2012, ApJ, 745, 29

Sloan, G. C., Keller, L. D., Forrest, W. J., et al. 2005, ApJ, 632, 956

Smith, J. D. T., Draine, B. T., Dale, D. A., et al. 2007, ApJ, 656, 770

Snow, T. P., & Witt, A. N. 1995, Science, 270, 1455

Strom, K. M., Strom, S. E., Edwards, S., Cabrit, S., & Skrutskie, M. F. 1989, AJ, 97, 1451

Sturm, B., Bouwman, J., Henning, T., et al. 2010, A&A, 518, L129

Sturm, B., Bouwman, J., Henning, T., et al. 2013, A&A, 553, A5

Suto, H., Sogawa, H., Tachibana, S., et al. 2006, Monthly Notices of the Royal Astronomical Society, 370, 1599

Sylvester, R. J., Dunkin, S. K., & Barlow, M. J. 2001, MNRAS, 327, 133

Sylvester, R. J., Skinner, C. J., Barlow, M. J., & Mannings, V. 1996, MNRAS, 279, 915

Tanabe, T., Nakada, Y., Kamijo, F., & Sakata, A. 1983, PASJ, 35, 397

Tanaka, K. K., Yamamoto, T., & Kimura, H. 2010, ApJ, 717, 586

Tatulli, E., Benisty, M., Ménard, F., et al. 2011, A&A, 531, A1

Testi, L., Birnstiel, T., Ricci, L., et al. 2014, ArXiv e-prints, arXiv:1402.1354

Thi, W.-F., Pinte, C., Pantin, E., et al. 2013, ArXiv e-prints, arXiv:1309.5098

Thi, W.-F., Pinte, C., Pantin, E., et al. 2014, A&A, 561, A50

Tielens, A. G. G. M. 2005, The Physics and Chemistry of the Interstellar Medium

Tielens, A. G. G. M. 2008, ARA&A, 46, 289

Tielens, A. G. G. M., Allamandola, L. J., Barker, J. R., & Cohen, M. 1987, in NATO ASIC Proc. 191: Polycyclic Aromatic Hydrocarbons and Astrophysics, ed. A. Leger, L. D'Hendecourt, & N. Boccara, 273–285

Tielens, A. G. G. M., & Hollenbach, D. 1985, ApJ, 291, 722

Urey, H. C. 1967, Icarus, 7, 350

van Boekel, R., Min, M., Waters, L. B. F. M., et al. 2005, A&A, 437, 189

van Boekel, R., Waters, L. B. F. M., Dominik, C., et al. 2004, A&A, 418, 177

van den Ancker, M. E., de Winter, D., & Tjin A Djie, H. R. E. 1998, A&A, 330, 145

van der Marel, N., van Dishoeck, E. F., Bruderer, S., et al. 2013, Science, 340, 1199

van der Plas, G., van den Ancker, M. E., Acke, B., et al. 2009, A&A, 500, 1137

van der Veen, W. E. C. J., Habing, H. J., & Geballe, T. R. 1989, A&A, 226, 108

Varnière, P., Quillen, A. C., & Frank, A. 2004, ApJ, 612, 1152

Verhoeff, A. 2009, PhD thesis, Sterrenkundig Instituuut "Anton Pannekoek", University of Amsterdam

Verhoeff, A. P., Min, M., Acke, B., et al. 2010, A&A, 516, A48

Verhoeff, A. P., Min, M., Pantin, E., et al. 2011, A&A, 528, A91

Verhoeff, A. P., Waters, L. B. F. M., van den Ancker, M. E., et al. 2012, A&A, 538, A101

Visser, R., Geers, V. C., Dullemond, C. P., et al. 2007, A&A, 466, 229

Waelkens, C., Bogaert, E., & Waters, L. B. F. M. 1994, in Astronomical Society of the Pacific Conference Series, Vol. 62, The Nature and Evolutionary Status of Herbig Ae/Be Stars, ed. P. S. The, M. R. Perez, & E. P. J. van den Heuvel, 405

Walker, H. J., & Butner, H. M. 1995, Ap&SS, 224, 389

Weidenschilling, S. J. 1980, Icarus, 44, 172

Williams, J. P., & Cieza, L. A. 2011, ARA&A, 49, 67

Wisniewski, J. P., Clampin, M., Grady, C. A., et al. 2008, ApJ, 682, 548

Woitke, P., Kamp, I., & Thi, W.-F. 2009, A&A, 501, 383

Wooden, D. H., Harker, D. E., & Brearley, A. J. 2005, in Astronomical Society of the Pacific Conference Series, Vol. 341, Chondrites and the Protoplanetary Disk, ed. A. N. Krot, E. R. D. Scott, & B. Reipurth, 774

Wooden, D. H., Harker, D. E., Woodward, C. E., et al. 1999, ApJ, 517, 1034

Wyatt, M. C. 2005, A&A, 440, 937

Zacharias, N., Monet, D. G., Levine, S. E., et al. 2004, in Bulletin of the American Astronomical Society, Vol. 36, American Astronomical Society Meeting Abstracts, 1418

Zhen, J., Paardekooper, D., Candian, A., Linnartz, H., & Tielens, A. 2013, Chemical Physics Letters,

Zhu, Z., Nelson, R. P., Dong, R., Espaillat, C., & Hartmann, L. 2012, ApJ, 755, 6

Zolensky, M., Nakamura-Messenger, K., Rietmeijer, F., et al. 2008, Meteoritics and Planetary Science, 43, 261

Zolensky, M. E., Zega, T. J., Yano, H., et al. 2006, Science, 314, 1735

Zubko, V. G., Mennella, V., Colangeli, L., & Bussoletti, E. 1996, MNRAS, 282, 1321

Curriculum vitae

Koen Maarten Maaskant (2013)

I was born on the fourth of July, 1985, in a small hospital in the picturesque village Naarden. My childhood, where I played football up to my 18th birthday, took place in Muiden, famous for its medieval castle 'Muiderslot'. In Bussum, I went to the high-school 'Goois Lyceum'. This was an important period as my future interest drastically changed from architecture to physics. Key for this early career shift was the first moment where I held my physics book, learned the physics behind cathode ray tubes, and thought: this is amazing. Between 2003 and 2010, I studied physics & astronomy at the University of Amsterdam. In these vivid years, I explored student life in optima forma, including rowing at student society Skøll, working in the planetarium of the Amsterdam zoo Artis, and other typical activities. After an internship at the Amsterdam Medical Center, and some interesting psychology and epistemological philosophy courses, I came to realize that I really wanted to do astrophysics. I was fortunate to carry out my master research with dr. L.B.F.M. Waters, with who I studied stellar evolution in high mass star forming regions using VLT/Sinfoni integral field spectroscopic data. During my PhD, I worked with dr. A.G.G.M. Tielens at Leiden Observatory, and studied the evolution of protoplanetary disks of Herbig stars. I focussed on comparing data from telescopes such as Spitzer, Herschel, VLT and Subaru, with numerical radiative transfer models, in order to understand observational signatures of molecules and silicate dust around young stars and exoplanets. As a next step in my career, I will work as a researcher in the high-tech industry.

Publications

- de Vries, B. L., **Maaskant, K.M.** et al. 2014. First evidence for large forsterite grains around evolved stars: using spectral features to probe the grain size of forsterite around the pre-planetary nebula IRAS 17150. To be submitted to Astronomy & Astrophysics
- Ellerbroek, L. E., ... **Maaskant, K.M.**, et al. 2014. A resolved, au-scale gas disk around the B[e] star HD 50138. Submitted to Astronomy & Astrophysics
- Khalafinejad, S., **Maaskant, K. M.**, et al. 2014. *Large gaps in the transitional disks of HD 100453 and HD 34282: connecting the gap size to the spectral energy distribution*. Submitted to Astronomy & Astrophysics
- **Maaskant, K. M.**, et al. 2014. *Location and sizes of forsterite grains in protoplanetary disks: interpretation from the Herschel DIGIT programme*. Astronomy & Astrophysics
- **Maaskant, K. M.**, et al. 2014. *Polycyclic aromatic hydrocarbon ionization as a tracer of gas flows through protoplanetary disk gaps*. Astronomy & Astrophysics
- Meeus, G., ... **Maaskant, K. M.**, et al 2013. *DIGIT survey of far-infrared lines from protoplanetary discs. II. CO*. Astronomy & Astrophysics
- Ellerbroek, L. E., ... **Maaskant, K. M.**, et al. 2013. *RCW36: characterizing the outcome of massive star formation*. Astronomy & Astrophysics
- **Maaskant, K. M.**, et al. 2013. *Identifying gaps in flaring Herbig Ae/Be disks using spatially resolved mid-infrared imaging. Are all group I disks transitional?*. Astronomy & Astrophysics
- Sturm, B., ... **Maaskant, K.M.**, et al. 2013.*The 69 μm forsterite band in spectra of protoplanetary disks. Results from the Herschel DIGIT programme*. Astronomy & Astrophysics
- Honda, M., **Maaskant, K. M.**, et al. 2012. *Mid-infrared Imaging of the Transitional Disk of HD 169142: Measuring the Size of the Gap*. Astrophysical Journal
- **Maaskant, K. M.**, et al. 2011. *Sequential star formation in IRAS 06084-0611 (GGD 12-15). From intermediate-mass to high-mass stars*. Astronomy & Astrophysics

Conference proceedings

- **Maaskant, K. M.**, et al. 2013
  Are all flaring Herbig disks transitional?
- Ellerbroek, L.E., ... **Maaskant, K. M.**, et al. 2012
  The Star Formation History of RCW 36
- Mulders, G, ... **Maaskant, K. M.**, et al. 2012
  Locating dust crystals in protoplanetary disks with Herschel PACS

Positions and diplomas

- PhD Astronomy & Astrophysics
  (2010 - 2014), Leiden University
  The Netherlands
- MSc Astronomy and Astrophysics
  (2008-2010), University of Amsterdam
  The Netherlands
- BSc Physics and Astronomy
  (2003-2008), University of Amsterdam
  The Netherlands
- Highschool, Voorbereidend Wetenschappelijk Onderwijs
  (1997-2003), Bussum
  The Netherlands

Nederlandse samenvatting

De afgelopen decennia is er een revolutie in de sterrenkunde teweeg gebracht door de ontdekkingen van nieuwe planeten buiten ons zonnestelsel. Dit soort planeten noemen we ook wel exoplaneten; planeten net zoals onze eigen Aarde, Mars of Jupiter, alleen dan draaien ze rondom andere sterren. Exoplaneten staan op vele lichtjaren afstand. Dat betekent dat het licht (ondanks een snelheid van ongeveer 299 792 458 meter per seconde) er jaren over doet om ons te bereiken. Ze staan daarom te ver weg om er naar toe te reizen, met de snelste raketten zouden we tienduizenden jaren onderweg zijn. Gelukkig kunnen we de exoplaneten wel bestuderen met behulp van telescopen. Planeten vinden is niet gemakkelijk. Dat komt omdat het reflecterende licht erg zwak is ten opzichte van de ster. Desondanks bestaan er geavanceerde waarneem technieken die in staat zijn om exoplaneten alsnog te detecteren. Met indrukwekkende resultaten: momenteel zijn er al meer dan duizend exoplaneten gevonden[1]. Voorspellingen gebaseerd op extrapolaties van de bestaande waarnemingen laten zien dat er waaschijnlijk miljarden exoplaneten in onze Melkweg zijn (Howard et al., 2010). Zelfs de samenstelling van atmosferen van exoplaneten wordt al onderzocht. Het nieuwe tijdperk van exoplanetaire wetenschap, dat door de talloze nieuwe ontdekkingen in een stroomversnelling is gekomen, roept dan ook talrijke nieuwe vragen op. Wat voor soort exoplaneten zien we? Zijn ze groot zoals Jupiter, of klein zoals Mercurius? Zijn er nog andere bewoonbare exoplaneten zoals de Aarde? Hoe ontstaan planeten? Het beantwoorden van deze grote vragen vergt geduld en vereist de gezamenlijke inspanning van vele wetenschappers die werkzaam zijn in verschillende disciplines, zoals sterrenkunde, maar ook natuurkunde, scheikunde en informatica. Er kan een belangrijke bijdrage worden geleverd in het onderzoek naar het ontstaan van planeten door de vroegste fase van de vorming van een planetenstelsel te bestuderen: de *protoplanetaire schijf*.

Ongeveer 4.57 miljard jaar geleden is de planeet Aarde gevormd uit een ronddraaiende protoplanetaire schijf. Hoe dat precies ging is moeilijk te achterhalen, omdat al het materiaal van de protoplanetaire schijf is samengeklonterd en gesmolten tot planeten en andere hemellichamen. Daarbij is veel 'bewijs' verloren gegaan dat ons iets kan vertellen over de geboorteplaats van het zonnestelsel. Gelukkig hebben telescopen wel andere protoplanetaire schijven gevonden rondom jonge sterren in de Melkweg. Zo kunnen we er toch indirect achterkomen hoe ons zonnestelsel moet zijn ontstaan. In dit proefschrift wordt het infrarood licht van gas en stof in zulke protoplanetaire schijven bestudeerd. Daarbij

[1]NASA exoplaneet archief: http://exoplanetarchive.ipac.caltech.edu/

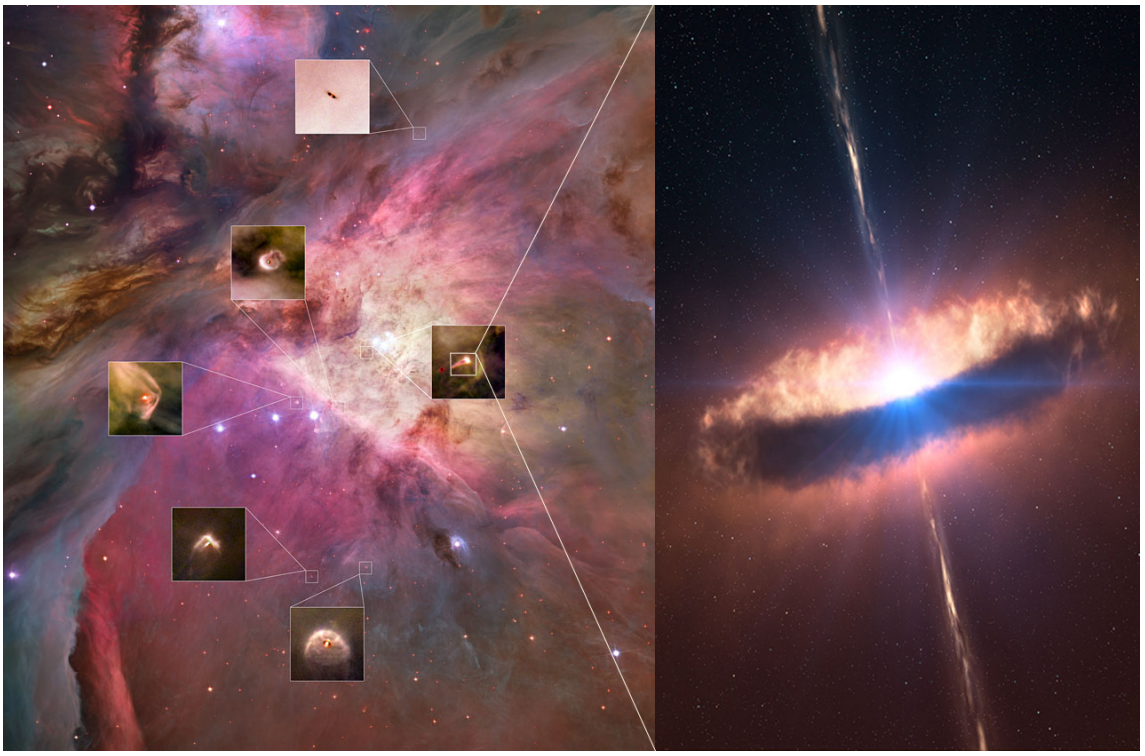

Figure 6.10: ***Links:*** *Hubble telescoop waarneming van de Orion Nevel. In deze wolk van gas en stof worden honderden nieuwe sterren en planeten gevormd. Uitvergroot op dit plaatje zijn enkele 'proplyds' te zien. In 'proplyds' zitten protoplanetaire schijven waaruit sterren en planeten vormen.* ***Rechts:*** *Een grafische weergave van een protoplanetaire schijf rondom een jonge ster. In ongeveer 10 miljoen jaar evolueert de schijf, daarbij kan het materiaal samen klonteren en planeten vormen. Maar daarnaast kan het materiaal ook op de ster vallen of worden weggeblazen door jets, zoals te zien is aan de straalstroom loodrecht op de schijf.*

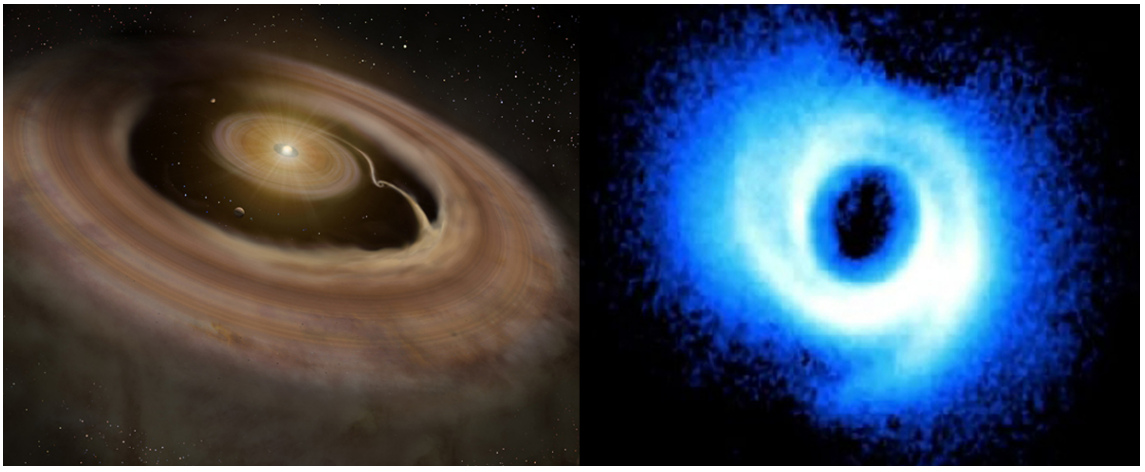

Figure 6.11: ***Links:*** *Een grafische weergave van een transitionele schijf waarin planeten vormen.* ***Rechts:*** *Waarnemingen van de transitional schijf HD 135344 B die genomen zijn met het instrument HiCiAO op de Subaru telescoop in Hawaii (Muto et al., 2012).*

komen vernieuwende technieken en inzichten naar voren waardoor we de evolutie van protoplanetaire schijven naar planetenstelsels beter in kaart kunnen brengen.

Jonge sterren en planeten worden geboren in wolken van gas en stof die ook wel stervormingsnevels worden genoemd (zie bijvoorbeeld de Orionnevel op Figuur 6.10 links). Door de zwaartekracht trekken gedeeltes van deze wolk in elkaar. Het meeste materiaal valt naar het midden en daar vormt zich dan een nieuwe ster. Maar een gedeelte van de wolk kan niet direct op de ster vallen omdat het materiaal een te hoge draaiingssnelheid om de ster heeft. Dit gedeelte slaat neer in een protoplanetaire schijf rondom de ster. In deze protoplanetaire schijf kunnen vervolgens nieuwe planeten vormen.

Een protoplanetaire schijf bestaat uit een verzameling van atomen, moleculen, microscopische zandkorreltjes, meteorieten, kometen (zie Figuur 6.10 rechts). Dit materiaal kan uiteindelijk uitgroeien tot planeten. De natuurkundige en chemische eigenschappen van het materiaal bepalen wat voor soort licht het uitstraalt. Als bijvoorbeeld de temperatuur hoog is, dan straalt het materiaal licht uit met een hogere frequentie (een 'blauwere' kleur), is het materiaal koud, dan straalt het licht uit met een lagere frequentie (en kleurt het 'rood'). De dichtheid en samenstelling van het materiaal zijn andere essentiële eigenschappen die bepalen welk licht het uitzendt.

Het licht van protoplanetaire schijven kan worden waargenomen door gebruik te maken van telescopen. Deze telescopen maken waarnemingen waarbij de sterkte en de kleur van het licht heel nauwkeurig bepaald worden. Vervolgens wordt deze informatie geanalyseerd en vergeleken met modellen. Een model is een analytische 'interpretatie' van een protoplanetaire schijf. Met behulp van computers worden de natuurkundige en chemische eigenschappen van een protoplanetarie schijf gesimuleerd, daardoor kan worden uitgerekend hoe het licht er door een telescoop uit zou moeten zien. Als deze simulatie overeenkomt met de echte waarneming, dan is er bewijs geleverd dat het model (de 'interpretatie') van de protoplanetaire schijf, juist is. Deze methode beschrijft de kern van het werk dat in dit proefschrift wordt gepresenteerd.

In dit proefschrift is de evolutie van protoplanetaire schijven naar planetenstelsels op drie verschillende manieren onderzocht. Ten eerste is de geometrie van protoplanetaire schijven bestudeerd in de hoofdstukken 2, 3 en 4. Hierin is ontdekt dat een heleboel protoplanetaire schijven eigenlijk bestaan uit ringen met lege ruimtes daartussen. Deze lege ruimtes zouden ontstaan kunnen zijn doordat daar planeten zijn gevormd. Deze schijven worden ook wel transitionele schijven genoemd omdat ze in de overgang zijn naar planetenstelsels (zie figuur 6.11 voor een voorbeeld van een transitionele schijf).

Ten tweede is de ionisatie van polycyclische aromatische koolwaterstof (PAK) moleculen onderzocht. Een voorbeeld van een PAK is naftaleen ($C_{10}H_8$). Op Aarde zijn PAKs ook wel bekend als uitlaatgassen en zijn dus schadelijk voor de gezondheid en het milieu. PAKs zijn belangrijke bouwstenen van protoplanetaire schijven. Ze hebben door efficiënte absorptie van ultraviolet straling een groot effect op de energie balans in de schijf. Daarnaast kunnen PAKs, door verschillende chemische reacties, naar complexere organische moleculen worden getransformeerd. Het is daarom mogelijk dat PAKs de eerste stap vertegenwoordigen op weg naar aminozuren en nucleotiden, de grondstoffen van eiwitten en DNA. In hoofdstuk 5 is beschreven hoe de kleur van het licht van een PAKs

molecuul verandert in de omgeving waar een planeet ontstaat. Dat is erg handig aangezien de planeet zelf te klein is om te detecteren. In plaats daarvan kan het licht van de PAKs worden gebruikt om de planeetvorming te traceren.

Ten slotte wordt in hoofdstuk 6 besproken waar microscopische forsteriet deeltjes zich in de schijven bevinden. Forsteriet (Mg_2SiO_4) is een gekristalliseerde silicaat en is een belangrijk mineraal in de sterrenkunde. Silicaten vormen ook een belangrijk deel van het materiaal waaruit de Aarde is opgebouwd. Forsteriet vormt een onderdeel van de mineraalgroep olivijnen. Het groene zand van de Papakolea strand op Hawaï bestaat uit olivijnen kristallen die zijn geërodeerd uit lavastenen.Ook kometen en meteorieten bestaan grotendeels uit silicaten. In dit onderzoek zijn de chemische samenstellingen en de locaties van het forsteriet in protoplanetaire schijven onderzocht. Hieruit is onder andere naar voren gekomen dat de forsteriet deeltjes groter worden naar mate de schijf verder evolueert. Dit is belangrijk aangezien dit de eerste stap kan zijn van de groei van microscopische zandkorrels naar planeten.

Het onderzoek naar protoplanetaire schijven boekt snel vooruitgang. Het verband tussen protoplanetaire schijven en het ontstaan van de aarde wordt steeds beter begrepen. Wellicht komen we er snel achter of er ook exoplaneten zijn waarop leven mogelijk is. Ieder jaar worden er vele onderzoeken gepubliceerd die, net zoals dit proefschrift, kunnen bijdragen aan de kennis over de evolutie en het ontstaan van exoplaneten in protoplanetaire schijven. Met geavanceerde telescopen en de uitstekende samenwerking tussen wetenschappers over de hele wereld, ziet ook de toekomst er veelbelovend uit.

Dankwoord

Met een kop koffie en een zonnig uitzicht over de skyline van Santiago kan ik mij geen betere inspiratie wensen om het dankwoord van mijn thesis te schrijven. Ik heb het geluk dat ik kan gaan promoveren met vele inspirerende collega's, vrienden en familieleden naast mij. Het doet mij veel plezier nu eindelijk iedereen goed te kunnen bedanken.

Tijdens mijn promotie heb ik zeer intensief gebruik gemaakt van verschillende numerieke codes. Michiel, jouw algoritmes om analyses op protoplanetaire schijven uit te kunnen voeren zijn van grote waarde geweest voor de inhoud van deze thesis. Je bent ijzersterk als het gaat om het begrijpen van optische eigenschappen van stof in circumstellair materiaal. Ik dank je zeer voor het aanleggen van dit fundament, en voor jouw inspanning en scherpe blik op de fysische details in onze onderzoeken.

Afgelopen vier jaar heb ik veel collega's leren kennen met wie ik veel heb kunnen samenwerken. Arjan (Bik), bedankt voor jouw gastvrijheid in Heidelberg en begeleiding tijdens (het schrijven van een artikel van) mijn master onderzoek. Arjan (Verhoeff), jouw VISIR data is de grote inspiratie bron geweest voor mijn studie naar PAHs in Herbig sterren. Gijs, ik ben blij dat jij op het API rondliep toen ik begon aan mijn PhD. Bedankt voor de vele discussies over Herbig sterren en MCMax. *Mitsuhiko, it was a great pleasure to collaborate with you on the mid-infrared imaging data. It has become an important part of my thesis and I would like to acknowledge your significant role in these papers. Sara, thanks for being a great student. I have much respect for your motivation to work on our project.* Ben, geweldig dat we naast talloze filosofische gesprekken ook nog echt hebben kunnen samenwerken aan forsterite, Stockholm was top. Gerrit, dank je voor je geweldige gastvrijheid in Santiago. De nieuwe ALMA data leveren vast en zeker mooie papers op. Ik zie er naar uit om de 'gaps' erin te zien zitten.

Lucas, Sjors en Arjen. Tijdens onze studie en promotie hebben we, vaak onder het genot van bier en vlees, onze passie voor natuur- en sterrenkunde kunnen delen. Lucas, je bent een bijzondere gozer, het is fijn samenwerken en ik bewonder je tomeloze energie in alles wat je doet. Sjors, ook met jou heb ik, tussen de bedrijven door, altijd over alles kunnen praten. Altijd gezellig om in recalcitrante buien met jou te sparren. Arjen, nog voordat we gingen studeren leerden we elkaar al kennen tijdens de zomer vakantie in Frankrijk. Je bent een van de meest getalenteerde sterke verhalen vertellers die ik ken. Ik heb met jullie drie alle mooie en moeilijke momenten tijdens mijn promotie kunnen delen en daarvoor ben ik zeer dankbaar.

Sterrenkunde is een teamsport. Het werken in wetenschappelijke consortia is daarom vanzelfsprekend. Een prettig neveneffect is dat collega's snel vrienden worden. In Amsterdam is de cookie groep een geweldige groep om je eigen werk aan een kritische inspectie te onderwerpen. Rik, Saskia, Sebastiaan, Bram, Mihkel, Tomas, Theo, Maria, Caroline, Christian, bedankt! In Leiden vormt de ISM groep een leger aan kennis en skills, Ainil, Isabel, Alessandra, Lynn, Pablo, Heather, Suklima, Annemieke, Marissa, Sylvia, Frank, bedankt! Lex, Alex, Ralph, Michiel, Rudy, Sera en Huib, bedankt voor jullie gedegen API onderwijs en goede adviezen tijdens mijn promotie. Kamergenoten Diego, Thijs, Willem, Jos, Renske en Wendy, bedankt voor de dagelijkse gezelligheid. *Tim, Emanuele, Carl en Mher, thanks for you ingenious, daedalian sense of humor. Outside the Netherlands, I have been fortunate to be involved in two international group of excellent researchers. In the DIGIT group, working on data from the Herschel space telescope, Neal, Thomas, Ewine, Jeroen, Gwendolyn, Davide, Simon, Johan, Joel, Daniel, Irene and others, and the DIANA group working on modeling of protoplanetary disks, Peter, Inga, Wing-Fai, Armin, Andres and others, thank you all for the meetings, the many discussions, and for making the social events very enjoyable.*

Hoewel mijn referentiekader misschien nog niet heel breed is heb ik het idee dat zaken op de Amsterdamse en Leidse sterrenkunde instituten vaak ontzettend goed geregeld zijn. Omdat dat ook voor mij belangrijk is geweest wil ik graag expliciet de instituut managers en secretariaten in Amsterdam en Leiden bedanken. Lidewijde, Evelijn, Milena, Minou, Susan, Anita en anderen, bedankt, jullie doen geweldig werk.

Vriendschappen zijn heel waardevol en vormen voor mij een belangrijke basis om met plezier te werken. Ondanks dat een promotie inhakt op de beschikbare tijd voor een social life, wil ik de volgende vrienden heel erg bedanken. Uit het ouderlijk dorp: Ben, Govert, Brian, Olga, Layla, Wouter, Simon, Lars, Roeli en alle andere vrienden uit Muiden en omstreken. Van de middelbare school: Levi, Wouter, Steven, Nick, Joel, Wiebe, Martijn, Jan Joost, Tim, Merel, Astrid en jullie betere wederhelften. Uit de studententijd in Amsterdam: Daan, Thomas, Jannes, Rik, Atilla, Ruben, Robert en Zoli. Van het planetarium in Artis: Charifa, Reino, Eveline, Anthony, Ammar, Jolanda, Tessa, Milo en Bas. Van de bier en vlees traditie, Bram, Wiebe, Mathijs. Uit het zwembad: Hanneke, Pieter, en andere USC zwembuddies. Van de natuurkunde studie: Ido, Bouwe, Sjoert, Freek, Peter, Pieter. Vrienden, super bedankt voor al jaren gezelligheid, mijn proefschrift heeft daar zeker van geprofiteerd.

Ik ben ontzettend blij met mijn familie. Een bijzondere dank gaat uit naar wijlen mijn opa Leo, die mij nauwkeurig bijles in de wis- en natuurkunde gaf en bijdroeg aan mijn enthousiasme voor natuurkunde. Broers, zussen en aanhang, Gijs, Daphne, Anne, Pablo, Geerte, Joost, Dimitri en Fahiem en kleine neefjes en nichtjes, Sabijn, Isabel, Max en Pepijn, bedankt, jullie zijn top. Mia, John, Martijn, een betere schoonfamilie kan ik mij niet voorstellen. Jeroen, Anja, Stefan, Saskia, Elsbeth, Godfried, Njal, Therese, Rangvi, Gustaf, Elsa, ik hoop dat we de Sinterklaas traditie nog lang zullen voortzetten. Maar bovenal, pap en mam, bedankt voor al het vertrouwen en de onvoorwaardelijke steun.

Ten slotte, Astrid, je bent het mooiste in mijn leven. Bedankt voor alle liefde en support. Samen met jou heb ik veel zin in alles wat er verder nog op ons pad kan komen.

And in the end, the love you take is equal to the love you make.

THE END – THE BEATLES